NANYANG TECHNOLOGICAL UNIVERSITY

EFFECT OF EXCAVATION ON PERFORMANCE OF ADJACENT BUILDINGS

EFFECT OF EXCAVATION ON PERFORMANCE OF ADJACENT BUILDINGS

DARWID HALIM

DARWID HALIM

SCHOOL OF CIVIL AND ENVIRONMENTAL ENGINEERING

2008

2008

Effect of Excavation on Performance of Adjacent Buildings

Darwid Halim

School of Civil and Environmental Engineering

A thesis submitted to the Nanyang Technological University
in fulfilment of the requirement for the degree of
Doctor of Philosophy

2008

ACKNOWLEDGEMENTS

This research is impossible to be accomplished without the help from many individuals. First and foremost, the author would like to express his appreciation and gratitude to his supervisor, Associate Professor Wong Kai Sin. His suggestions, guidance, encouragement, and constructive criticisms are sincerely appreciated. The author would like to thank Professor Harianto Rahardjo for his help during the admission process to NTU.

The author would also like to express his gratitude to Mr. James Nicholas Shirlaw from Golder Associate of Singapore who previously working in Land Transport Authority of Singapore. His suggestions, guidance and help in obtaining the valuable field data from the construction of MRT North East Line are sincerely appreciated.

At the same time, the author would also like to express his gratitude to the following persons from Land Transport Authority of Singapore: Mr. Seetoh Hon Hoy for his very helpful guidance in extracting the data from the Geotechnical Database System; Mr. Chen Din Chong for his help in providing drawings regarding MRT North East Line; Mr. Joshua Ong Cho Whatt for his advise and help in providing the data; Mr. William Tan and Mr. Rajeev Iyengar for their assistance in the data collection process. The author would also like to thank his fellow students in the graduate research room at N1-B4b-06 in NTU.

Finally, the author would like to acknowledge the financial support from Nanyang Technological University in the form of research scholarship and teaching assistantship.

ABSTRACT

Deep excavations in urban area can damage surrounding buildings. The current practice in assessing building damage is based on greenfield settlement computed from 2-D finite element analysis. This is less than satisfactory for situations where 3-D effect is prominent. In this case, a 3-D analysis is preferred. Unfortunately, the 3-D finite element analysis is a fairly complex and demanding task. A simple method has been developed to estimate 3-D settlement from 2-D analysis. The conventional method also assumed that the building would settle the same amount as the ground. This assumption is reasonable for buildings supported on individual footings without ground beams. For frame structures and buildings supported on rafts, the differences in building and ground settlements can be significant. A new method has been developed to integrate the soil-structure interaction into the analysis so that the structure stiffness can be taken into consideration. A new chart for damage assessment of frame structures has also been developed. The chart divides the damage into several categories.

This study also investigated the potential causes of post-excavation settlement in deep excavations in soft clay. Results indicate that there are two major causes. The first one is leakage in the retaining wall and the base slab. The second one is under-drainage into a pervious layer that extends into the excavated area and exposed at the formation level.

This research is numerical based with the aid of the computer programs ABAQUS and Sage Crisp. The proposed methods and charts have been validated against hypothetical problems and case records.

TABLE OF CONTENTS

LIST OF TABLES

LIST OF FIGURES

LIST OF SYMBOLS

Symbol	Description
α	Angular strain
β	Angular distortion or relative rotation
δ_{column}	Differential settlement between two columns
δ_{ρ}	Relative or differential settlement
δ_{ij}	Differential settlement between point i and j
δ_{ij}/l_{ij}	Distortion between point i and j
δ_{tilt}	Differential settlement due to tilt between two columns
δ_{v}	Differential Settlement ; Vertical ground settlement
ε_{b}	Maximum direct tensile strain
ε_{crit}	Critical tensile strain
ε_{d}	Diagonal tensile strain
ε_{h}	Average horizontal strain
ε_{le}	Lateral extension strain
ε_{M}	Bending strain at top of wall
ε_{p}	Principal tensile strain
ε_{t}	Cumulative maximum tensile strain along top of wall
ϕ'	Soil friction angle
ϕ'_{cs}	Critical state friction angle
γ	Total unit weight of soil; Shear strain
κ	Slope of swelling and recompression line
λ	Slope of normally consolidated line;
	Distance from bottom of building to its neutral axis divided by H
μ_{d}	Wall penetration factor
μ_{t}	Clay thickness factor
μ_{w}	Wall stiffness factor
ν	Poisson’s ratio
ν'	Rotation slope

Symbol	Description
$\nu'_{(M)}$	Proporsion of deformation due to moment
$\nu'_{(V)}$	Proporsion of deformation due to shear
ν_{max}	Maximum curve deflection
θ	Rotation or slope; Angle between height and length of building
ρ_i	Settlement at any point i
σ'_v	Vertical effective stress
σ'_3	Minor Principal Stress
ω	Tilt
Δ	Relative deflection
Δ/L	Deflection ratio
e_Γ	Void ratio on the critical state line at p' equals to 1 kPa
a	Percentage of open area in wall
c_u	Undrained shear strength of clay
c_{u1}	Cohesion of soil above excavation depth
c_{u2}	Cohesion of soil below excavation depth
c_t	Diagonal crack total
c_p	Cumulative diagonal crack width
c_t	Cumulative tensile crack width
g	Slope
h	Horizontal movement
h_i	Distance from bottom of building to floor i
k	Permeability; Ratio of crack width due to horizontal movement and crack total; Spring stiffness
l_{ij}	Distance between point i and j
m	Average slope at particular mode of deformation
p'_c	Maximum past pressure in terms of mean effective stress
q	Surcharge pressure
t	Rigid-body tilt
y_i	Story height
A	Area of spring

Symbol	Description
A_i	Area of floor slab contributing to bending resistance
Av_i	Shear area of wall i
B	Width of excavation
C_c	Coefficient of normally consolidated line
C_{ur}	Coefficient of recompression line
D	Distance from excavation edge
D_{max}	Distance to point where settlement to lateral movement is zero
D_r	Relative density
E	Young's modulus of building component
E_{ave}	Average stiffness of soil
E_c	Young's modulus of the column
E_{ur}	Unloading Reloading Soil Stiffness
E'_i	Tangent Modulus
E'_s	Secant Modulus
E'_{50}	Elastic stiffness of soil at 50% of the failure stress
E/G	Ratio of elastic to shear modulus
F	Nodal force
G	Shear modulus of building component
G_s	Specific Gravity
H	Building height; Depth of excavation
I	Moment of inertia
I_c	Moment of inertia of the column in the plane of wall
K	Modulus number
K_{nc}	Coefficient of in-situ earth pressure at normally consolidated state
K_o	Coefficient of earth pressure at rest
L	Original length of building; Length of spring; Length of a particular mode of deformation either sagging or hogging;
LL	Liquid Limit
LocMax	Distance from excavation wall to maximum ground settlement
Loc0.75	Distance from excavation wall to 75% location of normalized ground settlement

Symbol	Description
L/H	Ratio of length to height of the building
M	Slope of critical state line projected to q versus p' plane
N_{corr}	Corrected blow count of SPT
N_c	Bearing capacity coefficient for cohesion effect
N_h	Excavation shape factor
N_S	Stability number
N_{SPT}	Blow count of SPT
OCR	Over-Consolidation Ratio
P_a	Atmospheric pressure
PI	Plasticity Index
R_f	Failure ratio
R_M	Radius of bending
S_{max}	Maximum settlement at excavation edge
S	Settlement
S_L	Stress level
V_i	Shear in each story
V	Total shear in the laminate beam

CHAPTER 1
INTRODUCTION

1.1 Research Background

During a deep excavation, ground movement will occur and affect the performance of buildings surrounding it. Different types of building, foundation support and soil conditions make the assessment of building damage very difficult. Currently, the greenfield settlement together with the charts by Burland and Wroth (1974) or Boscardin and Cording (1989) are commonly used in the assessment. This approach is simple and can be used for preliminary assessment purpose. Under the greenfield condition, the building is assumed to settle the same amount as the ground which may not be appropriate in many cases.

Conceptually, the most accurate approach is to conduct a 3-D finite element analysis so that the soil-structure interaction can be taken into consideration. Unfortunately, this is not an easy task. It takes considerably more time to set up the problem when compared to the 2-D analysis. Another hindrance is the slow speed and the meager memory capacity of the present day personal computer.

The main thrust of this research is to develop a method that enables one to predict building damage based on the results from 2-D finite element analysis. This method takes into consideration the 3-D effect and raft stiffness. This process involves four steps.

The first step is to develop the ability to model deep excavation properly using the finite element method. The biggest uncertainty in the finite element analysis is usually in choosing the right soil parameters. There are many empirical correlations available for the Modified Cam Clay and Mohr-Coulomb soil models. The aim of this study is to examine the reliability of these correlations in excavation analysis and to validate them against case records.

The second step is to adopt or establish a simple way to classify building damage. Currently, there are several charts published in the literature which are based on different criteria. The aim of this study is to develop a new chart that is effective and easy to use.

The third step is to establish a procedure that enables one to predict 3-D greenfield settlement from 2-D finite element analysis. Up to present, no such method is available. Therefore, a new method is needed. The proposed method is only limited to excavations of rectangular shape.

The last step is to develop a method to determine building settlement based on greenfield soil displacement that takes into consideration the soil-raft interaction. This step requires a separate raft analysis.

These four steps enable one to estimate building settlement at the end of excavation. It is well known that under certain circumstances, the post-excavation settlement will continue for a long time. The last part of this study is to investigate the causes of post-excavation settlement and to find ways to limit this settlement.

All of these problems and challenges form the background for this research. This research aims to produce a practical solution to these problems.

1.2 Objective

This research has two main objectives. They are:

1. To establish a method or procedure to assess the effect of excavation on the performance of adjacent buildings; and
2. To obtain a better understanding on the causes of post-excavation settlement.

1.3 Scope of Work

The scope of work includes:

1. A comprehensive literature review on ground movements due to excavation and building damages owing to ground movements.

2. Validation of soil parameters for finite element analysis.
3. Development of a chart for assessment of building damage due to deep excavation.
4. Development of a procedure to estimate 3-D greenfield settlement from 2-D finite element analysis.
5. Development of a procedure to predict building settlement from the 3-D greenfield settlement.
6. Investigation on the sources of post-excavation settlement.

1.4 Organization of Dissertation

This dissertation consists of nine chapters. Chapter 1 is an introduction to this research.

Chapter 2 summarizes the literature reviews. Factors affecting the performance of deep excavation are presented here. The main focus is on ground and water movements in deep excavations.

Chapter 3 reviews the present knowledge in the assessment of building damage. It covers building response, damage category, mechanism of development of building cracks, and published charts to predict building damage.

Chapter 4 describes the verification of soil parameters from empirical correlations for Modified Cam Clay and Mohr-Coulomb soil models based on 10 case studies. New correlations are also proposed.

Chapter 5 presents the development of a new chart to predict building damage. It covers the development process of the chart, the building damages in Singapore during the construction of MRT North-East Line project, and verification of the chart using data from building damage in Singapore and other published data.

Chapter 6 presents a method for converting results of 2-D analysis into 3-D greenfield settlement. The proposed method is validated using hypothetical studies of different dimensions and soil conditions as well as one case study.

Chapter 7 presents a method to predict building settlement based on the greenfield soil displacements. The building stiffness is represented by an equivalent raft stiffness. The proposed method uses the 3-D greenfield settlement together with an appropriate raft stiffness as input into a raft analysis. This method is only applicable to raft on stiff (elastic) soil.

Chapter 8 investigates the main sources of post-excavation settlement. Factors affecting it are highlighted.

Chapter 9 summarizes the results of this research.

CHAPTER 2
DEEP EXCAVATION

2.1 Introduction

According to Terzaghi and Peck (1967), a deep excavation is classified as an excavation with a depth of more than 6 m. Harris and O'Rourke (1983) defined shallow trenches and deep trenches as excavations with depths up to 1.8 m and 6 m, respectively. These definitions are illustrated in Figure 2.1.

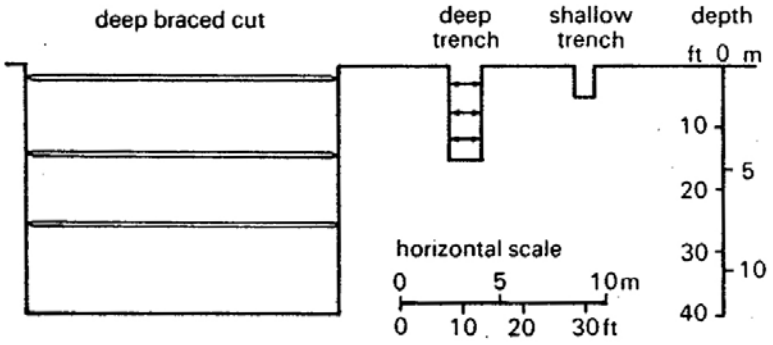

Figure 2.1 Illustration of Excavation Definition (Harris and O'Rourke, 1983)

In deep excavation construction, the stability and ground movements are the major concerns as they are inter-related. It means that factors affecting the performance of deep excavation will also affect ground settlement. Therefore, it is important to know what these factors are and how they affect the performance.

2.2 Factors Affecting Performance of Deep Excavation

When a layer of soil is excavated, the stresses and strains within the soil mass will change. The wall will deflect and the ground will settle. The basic mechanism is depicted in Figure 2.2.

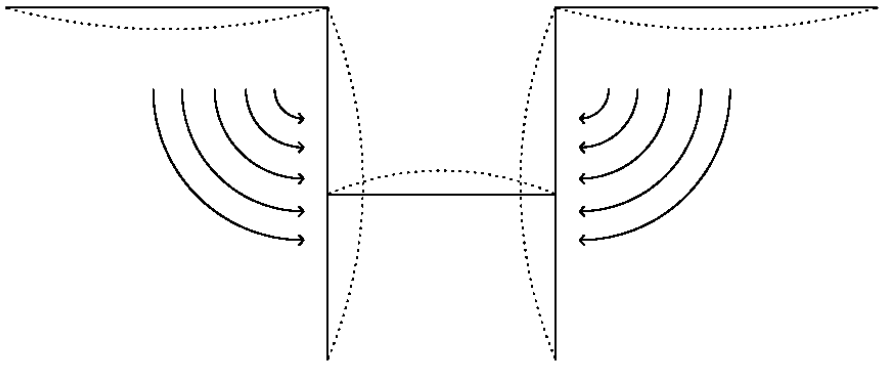

Figure 2.2 Basic Mechanisms of Wall and Ground Movement

There are many factors affecting the performance of a deep excavation. Some of them are soil shear strength, soil stiffness, support system stiffness, support spacing, preloading, construction delay, construction sequence, workmanship, initial lateral stress of soil, wall type, consolidation, anisotropy, excavation shape, temperature, the depth of hard stratum, embedment of excavation wall, and construction activity.

2.2.1 Basal Heave Stability

The excavation base stability or basal heave stability can be expressed in terms of factor of safety, FS, and stability number, N_S. In sand, basal heave is usually not a problem since the shear strength of soil is strong. However in clay, especially in soft clay, basal heave can be a major problem. It is primarily caused by low strength of soil below the excavation base which can lead to large ground settlement. Jet grouting can be used to increase the stability (Wong et al., 1990).

Terzaghi (1943) proposed Equation 2.1 to compute the factor of safety for basal heave stability under plane strain condition. The failure plane is assumed to extend vertically up to the ground surface. This equation does not take into account the effect of wall penetration, shape of excavation, and wall stiffness. This method is only applicable to shallow excavation with $H/B < 1$.

$$FS = \frac{1}{H}\frac{5.7c_{u2}}{\left(\gamma - \frac{c_{u1}\sqrt{2}}{B}\right)} \tag{2.1}$$

where H : depth of excavation

B : width of excavation

γ : total unit weight of soil

c_{u1} : cohesion of soil above excavation depth

c_{u2} : cohesion of soil below excavation depth

Experience by Bjerrum and Eide (1956) in Oslo shows that for narrow excavation where H/B≥1, the failure zone is a deep seated local failure similar to that of an end bearing failure around a pile tip. Bjerrum and Eide (1956) proposed Equation 2.2. The N_c value can be determined from Figure 2.3.

$$FS = N_c \frac{c_u}{\gamma H + q} \tag{2.2}$$

where N_c : a coefficient depending upon the dimensions of excavation

c_u : undrained shear strength of clay

q : surcharge pressure

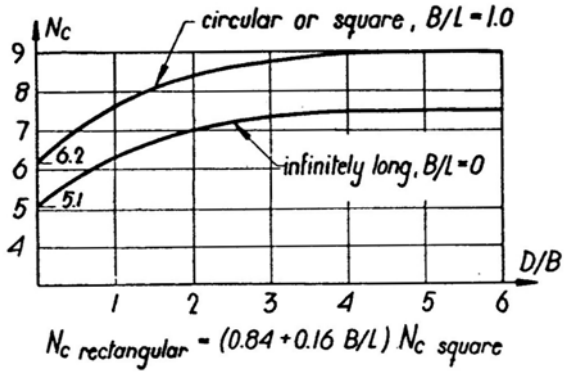

Figure 2.3 N_c Value (Bjerrum and Eide, 1956)

Goh (1994) proposed a method that takes into consideration the effect of wall penetration and wall stiffness. The new approach is developed based on several series of finite element analysis as shown in Equation 2.3. Charts for the correction factors are shown in Figure 2.4.

$$FS = \frac{c_u N_h}{\gamma H + q} \mu_t \mu_d \mu_w \tag{2.3}$$

where μ_t : clay thickness factor

μ_d : wall penetration factor

μ_w : wall stiffness factor

N_h : excavation shape factor

Peck (1969) shows that the basal heave stability can also be expressed in terms of the stability number, N_s, as shown in Equation 2.4.

$$N_S = \frac{\gamma H}{c_{u2}} \tag{2.4}$$

Clough and Schmidt (1981) showed that N_s can also be used to show roughly the degree of mobilization of the shear strength of clay using the chart in Figure 2.5. Each zone represents a different state of stability of the excavation. A stability number between 2 and 4 represents Zones II and III where the behavior of clay is largely elastic. Zone IV represents a limited plastic zone. Zones V and VI indicate significant plastic behavior of the clay where large deformation may occur.

Mana (1977) showed that there is a relationship between basal heave stability with wall deflection. It implies that ground movement is also affected. When a factor of safety of basal heave falls below 1.5, the soil rapidly moves into a plastic state. As a consequence, large wall movements may occur as shown in Figure 2.6.

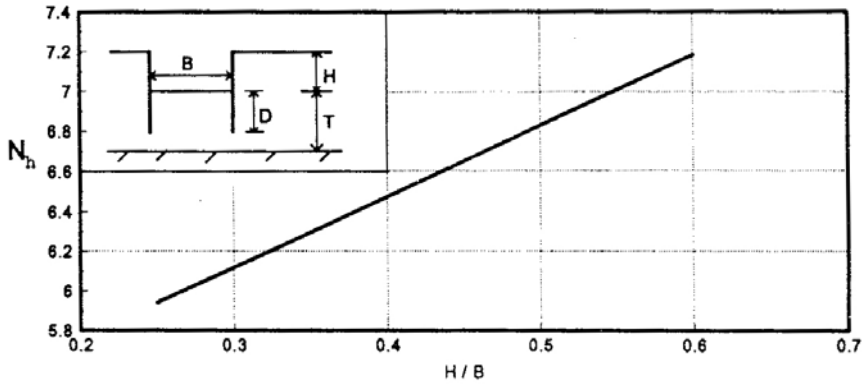

(a) N_h: Excavation Shape Factor

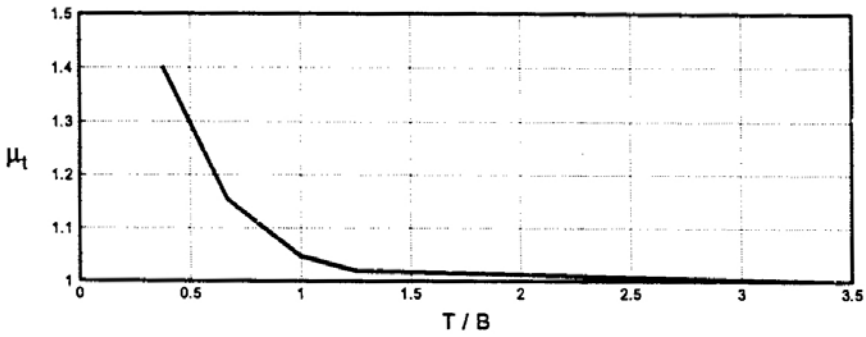

(b) μ_t: Clay Thickness Factor

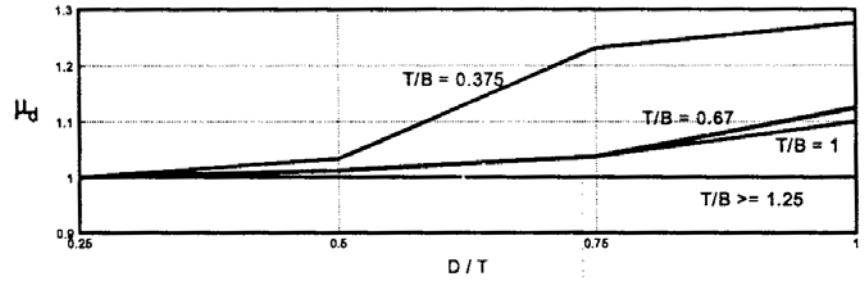

(c) μ_d: Wall Penetration Factor

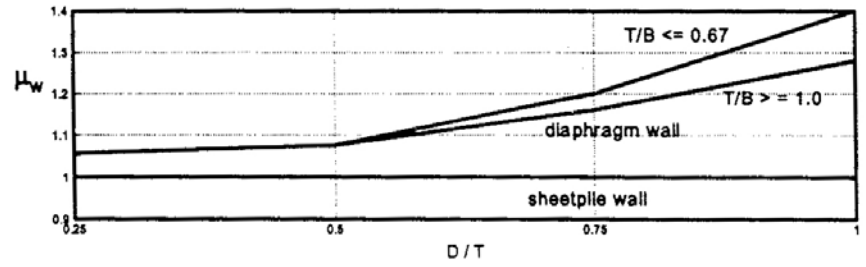

(d) μ_w: Wall Stiffness Factor

Figure 2.4 N_h, μ_t, μ_d, and μ_w (Goh, 1994)

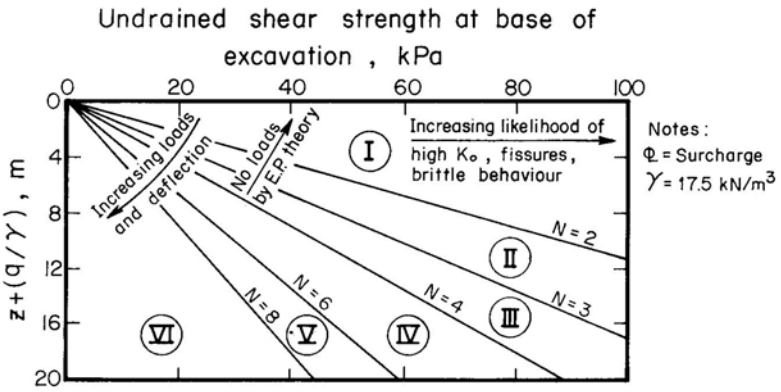

Figure 2.5 Stability Number Classifications (Clough and Schmidt, 1981)

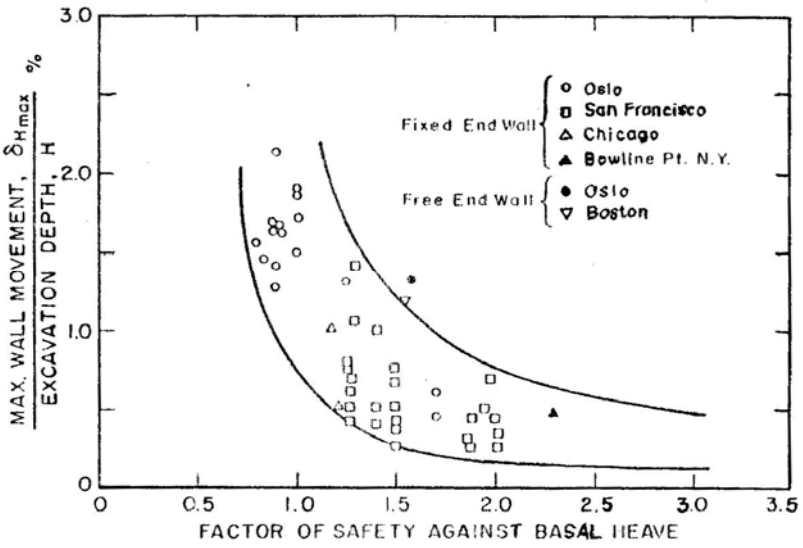

Figure 2.6 Factor of Safety Against Basal Heave Versus Maximum Wall Movement (Mana, 1977)

The displacement and yield patterns at different values of factor of safety against basal heave (Mana, 1977) are shown in Figure 2.7. Local yield is first observed when the factor of safety is about 1.5 with the depth of excavation at 5 m. As the factor of safety decreases, the yield zone increases.

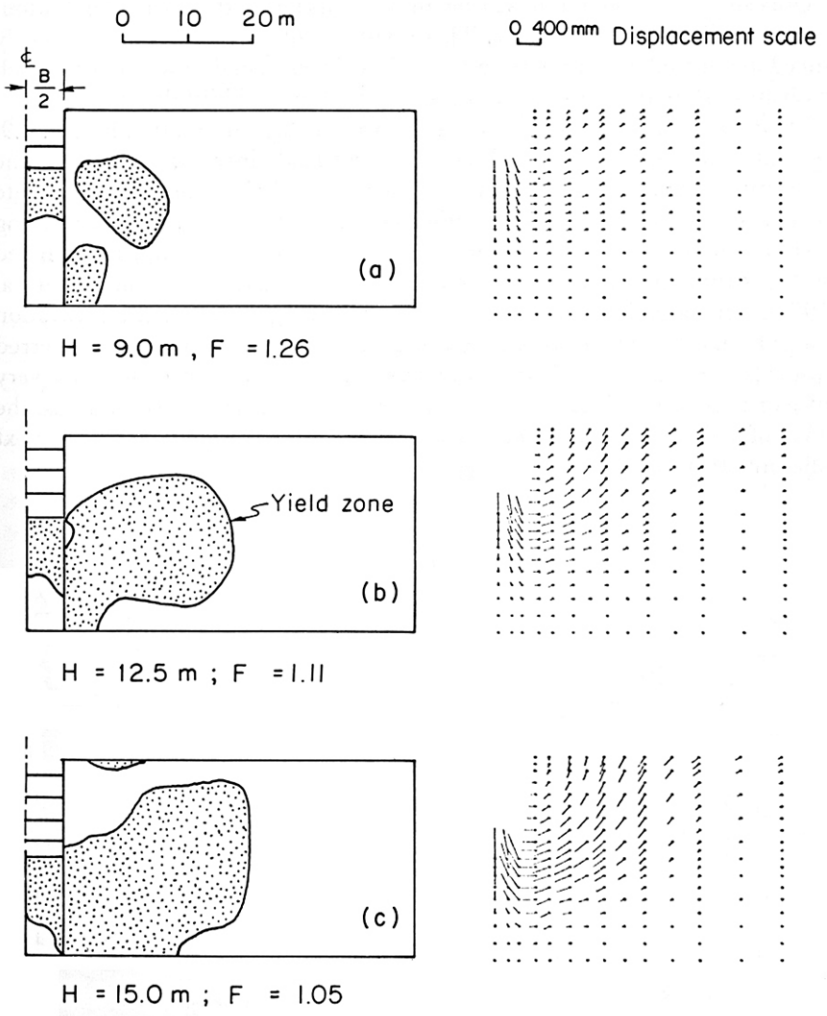

Figure 2.7 Displacement and Yielding Patterns for Deep Excavation in Soft Clay (Mana, 1977)

2.2.2 Soil Shear Strength

Soil shear strength is the most important parameter in deep excavation analysis especially in soft clay. Wong and Broms (1989) studied the effect of undrained shear strength on wall deflection based on finite element analysis as shown in Figure 2.8. It is easy to understand that the wall deflection decreases with

increasing soil strength. However, when the factor of safety against basal heave drops below 2, the wall deflection will increase exponentially regardless the soil shear strength.

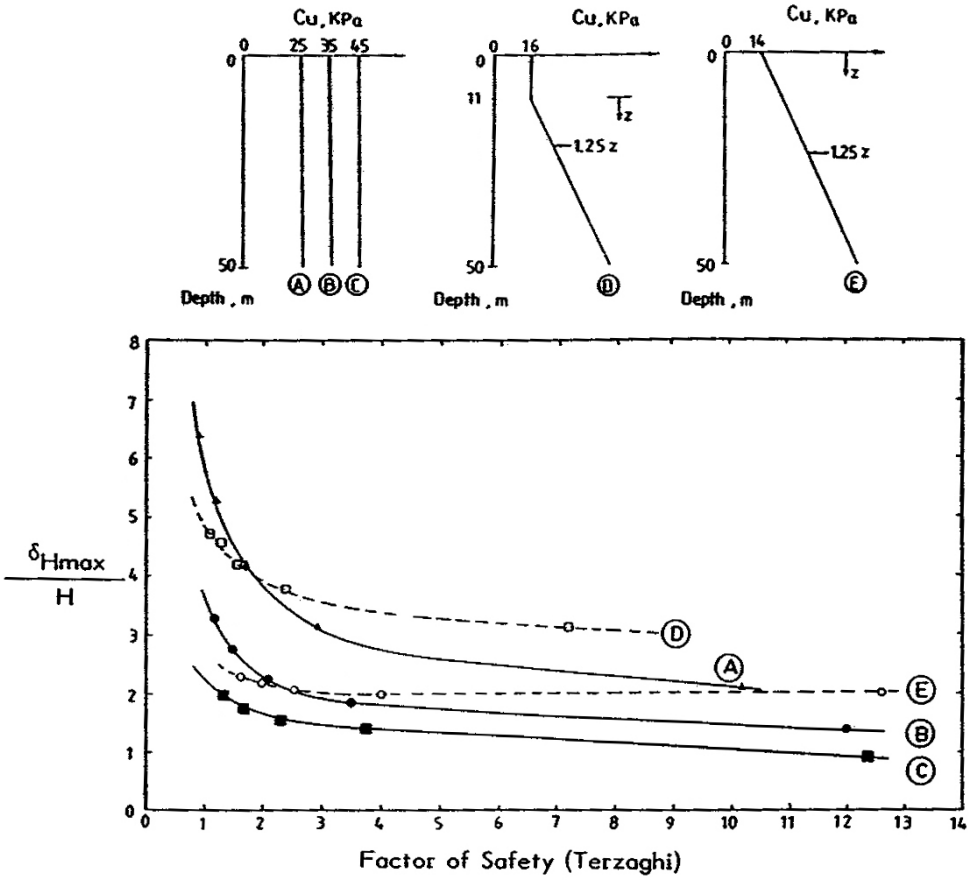

Figure 2.8 Effect of Soil Shear Strength on Wall Deflection
(Wong and Broms, 1989)

In 2-D finite element analysis, the excavation is modeled as a plane strain problem. However, most of the test results are obtained from triaxial rather than plane strain tests. The difference in shear strength between triaxial and plane strain conditions can be very different (Kjellman, 1936, Taylor, 1939, Leussink and Wittke, 1964, Henkel and Wade, 1966). For most cases, the denser or stiffer is the soil, the higher the soil shear strength under plane strain condition (Lee, 1970). For dense sand, the friction angle of plane strain can be 8° higher than the loose sand. For compacted clay, it can be 4°. However, for loose or soft soil, the

difference is only 1° less. Therefore, it is conservative to use shear strength parameters from triaxial tests in most cases.

2.2.3 Soil Stiffness

Deformation at relatively low shear stress level is governed by soil stiffness. For clay, the stiffness can be expressed as a modulus multiplier, M, times the cohesion, c_u (Ladd et al., 1977). A stiff soil would yield smaller wall deflection and ground settlement. Clough et al. (1979) pointed out that the effect of soil stiffness to wall deflection is crucial in the case of marginal stability where the factor of safety against basal heave is less than 1.5.

2.2.4 Support System Stiffness

Goldberg et al. (1976) defined the support system stiffness as EI/h^4, where EI is the wall stiffness and h is the vertical distance between supports. Slightly different of support system stiffness was defined by Clough, et al. (1979) as $EI/\gamma_w h^4$ where γ_w is the unit weight of water. The effect of support stiffness becomes significant when the factor of safety against basal heave falls below 1.5 (Clough, et al., 1979) as shown in Figure 2.9.

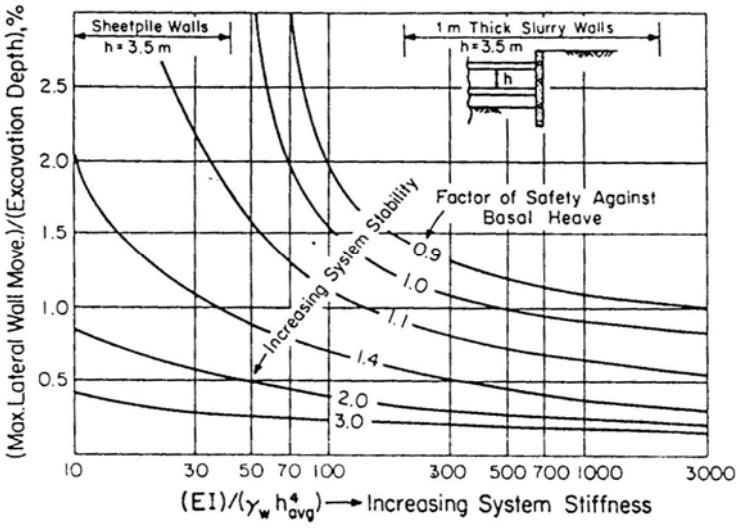

Figure 2.9 Effect of System Support Stiffness to Wall Deflection (Clough et al., 1979)

Poh et al. (1997) studied the effect of prop stiffness on wall deflection in stiff residual soil. Two scenarios were used. One is the excavation with one strut and another is with two struts. The results show the wall deflection decreases with strut stiffness in general. However, in stiff residual soil, this effect is not very significant as shown in Figure 2.10.

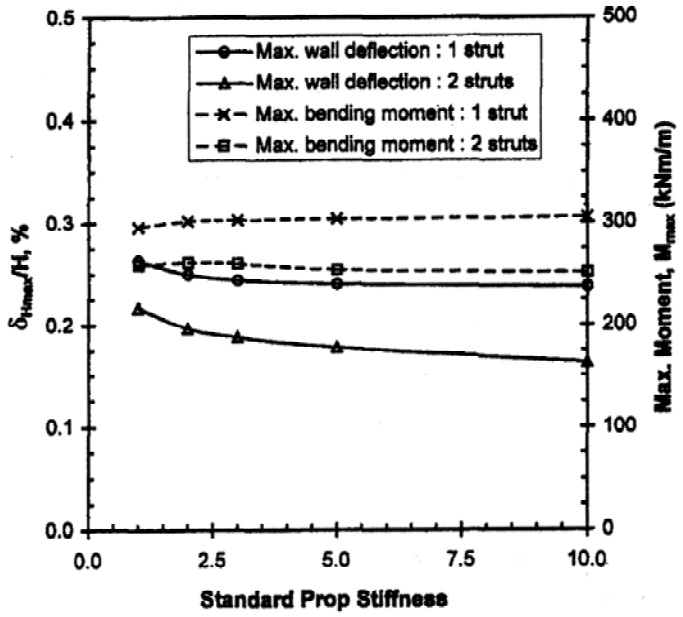

Figure 2.10 Effect of Struts Stiffness on Lateral Wall Deflection (Poh et al., 1997)

2.2.5 Support Spacing

Using closer strut spacing in soft soil can reduce substantially lateral wall deflection (Peck, 1969, Goldberg et al., 1976, Clough and O'Rourke, 1990). In Figure 2.11, Clough et al. (1979) normalized the actual depth of excavation at each step to the critical depth, ΔH_C. As the spacing strut increases, the wall deflection also increases. When $\Delta H/\Delta H_C$ exceeds 0.8, the maximum horizontal wall starts to increase exponentially.

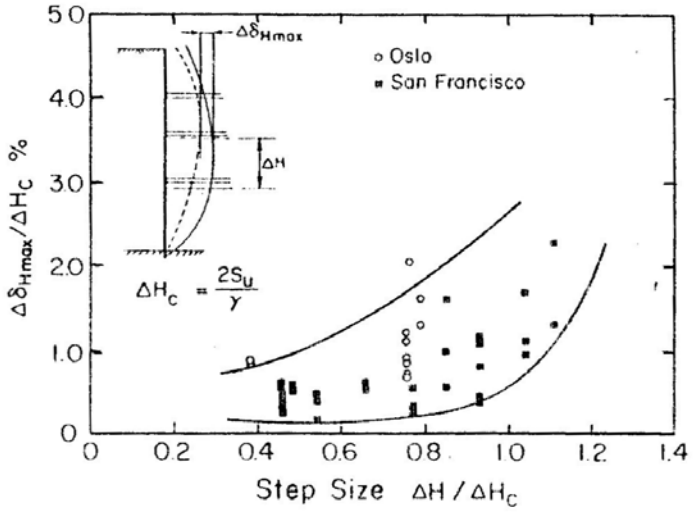

Figure 2.11 Effect of Support Spacing to Wall Deflection (Clough et al., 1979)

2.2.6 Preloading

Preloading generally improves the performance of a deep excavation. The main purpose is to remove any slack in the strutting system (O'Rourke, 1981). High preloading can cause high bending moment to the wall since the wall is restraint from deflection. In most cases, a preload equal to 50% of the design load (based on Peck's apparent pressure diagram), is sufficient to close the gap and avoid overstressing of the wall.

Another effect of preloading is to produce a stiffer response of the soil because it forces the soil to go through a cycle of loading and reloading (Clough and Davidson, 1977). As the strut is preloaded, the shear stress in the soil will reduce. When the excavation goes deeper, the shear stress in the soil mass will increase again. Subsequent preloading will reduce the shear stress again. This unloading-reloading results in a stiffer soil response although the affected areas are localized.

2.2.7 Construction Delay

Clough and Davidson (1977) illustrated one case in San Francisco where the workers were on strike. At the time when the base slab had to be cast, the strike was on. The delay increased the wall deflection by two folds as shown in Figure

2.12. Since the deformation of soil is also time dependent due to consolidation and creep, it is important not to delay the excavation activities, especially in crucial time like casting of the base slab.

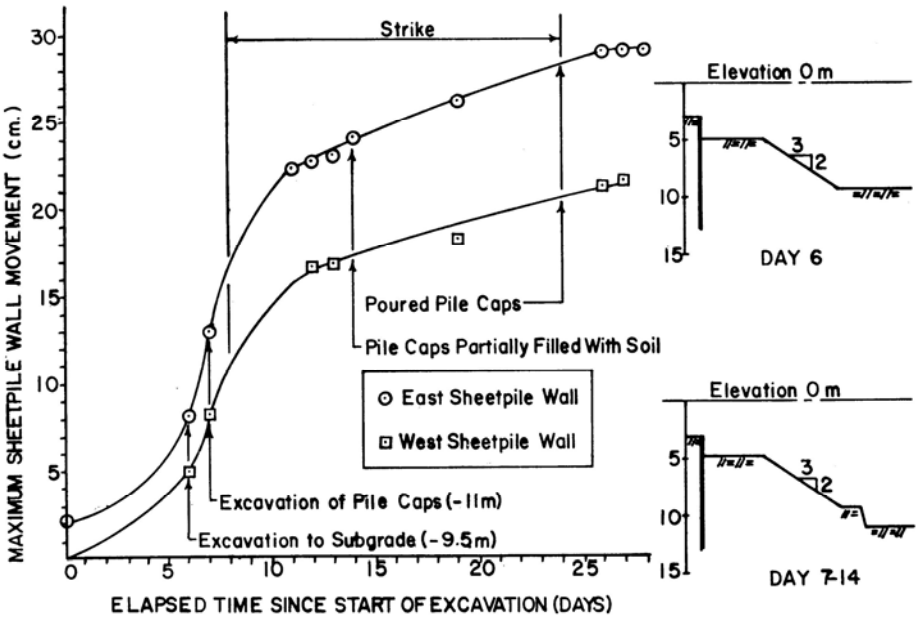

Figure 2.12 Maximum Sheetpile Movement in San Francisco
(Clough and Davidson, 1977)

2.2.8 Construction Sequence

Clough and Davidson (1977) reported a case history in San Francisco. The excavation was carried out in two phases located side by side. Since the soil conditions were the same and the support systems very similar, differences in performance most likely are due to differences in construction sequences. The wall deflections are shown in Figure 2.13. In Phase 1, construction of first braces was placed when the excavation was 5 m deep. In Phase 2, it was 8 m. The result was larger wall deflection in Phase 2. It highlights the adverse effect of over-excavation. Broms et al. (1986) also reported similar observation. The struts were not installed until the excavation had proceeded two to three meters below the intended strut level. The consequence was an increase in ground settlement by 50 to 100%.

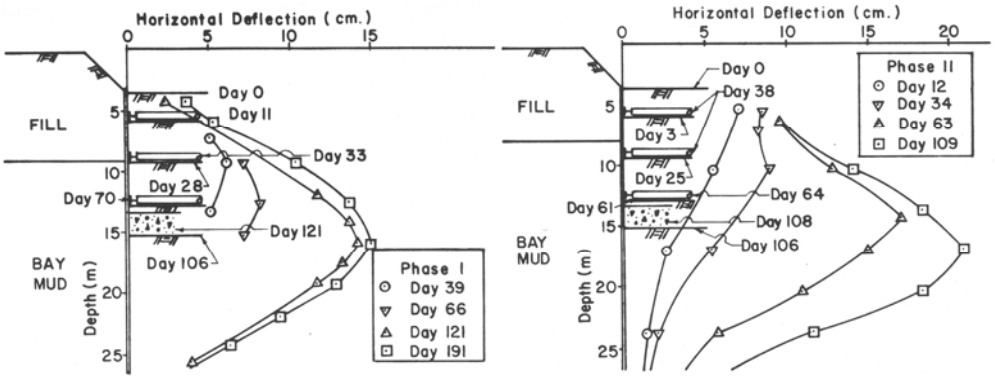

Figure 2.13 Wall Deflections for Two Similar Phases in San Francisco (Clough and Davidson, 1977)

Finno et al. (1989) described a case history at HDR 4 Test Section in Chicago. There were four levels of struts. The third level of struts was installed before the second level of struts because of over-excavation. At the time when the first level of struts was installed, the wall deflection at a depth of 4 m below ground level was only 50 mm. When the third level of struts was installed, the maximum wall deflection had increased to 250 mm. It is much larger than anticipated according to the design. Therefore, it is important to exercise stringent construction control so that the design construction sequence is followed closely.

2.2.9 Workmanship

Peck (1969) emphasized the importance of workmanship in his three settlement profile zones. This settlement profile is shown later in Figure 2.39. He observed that poor workmanship, such as late installation of support, could lead to large movement. Since this is a human factor, it is difficult to control and anticipate which makes the prediction of wall and ground movement much more difficult.

2.2.10 Initial Lateral Stresses of Soil

In the overconsolidated crustal zones or layers, the influence of initial state of lateral earth pressure should be considered. Pott and Fourie (1985) did a hypothetical study to investigate the effect of K_o on wall deflection. Figure 2.14

shows that wall deflection is higher for K_o equals to 2 as compared to 0.5. It is because the relief of horizontal pressure increases with increasing K_o.

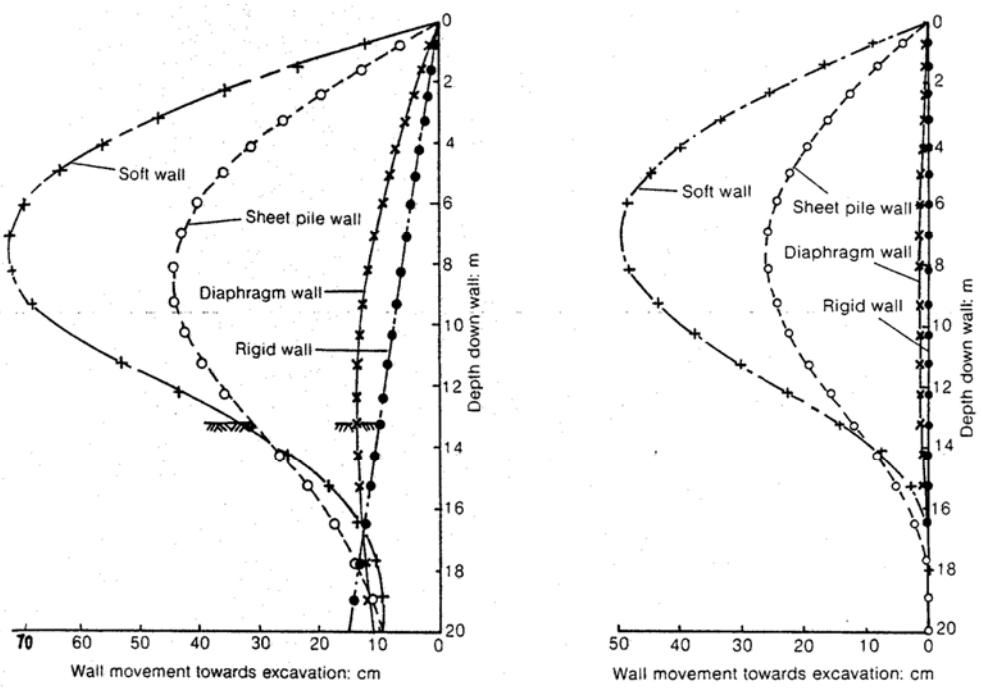

(a) $K_o = 2$ (b) $K_o = 0.5$

Figure 2.14 Lateral Wall Movement with Different K_o Value

(Potts and Fourie, 1985)

2.2.11 Wall Type

At South Cove in Boston, a deep excavation was dug for a subway project. Diaphragm wall was used in the section closest to an existing 7-storey building. Other sections used sheetpile wall. Lambe et al. (1972) observed that the concrete wall moved only 25 mm as compared to 178 mm for the sheetpile wall. Goldberg et al. (1976) reported similar experience using diaphragm walls in weak soil. The movement of diaphragm wall is only about a quarter of the sheetpile movement. However, Poh et al. (1997) reported that in the case of very stiff soil, such as weathered rock or residual soil, the effect of wall type is not important as shown in Figure 2.15. It is only the bending moment that is highly affected. The stiffer wall causes higher bending moment.

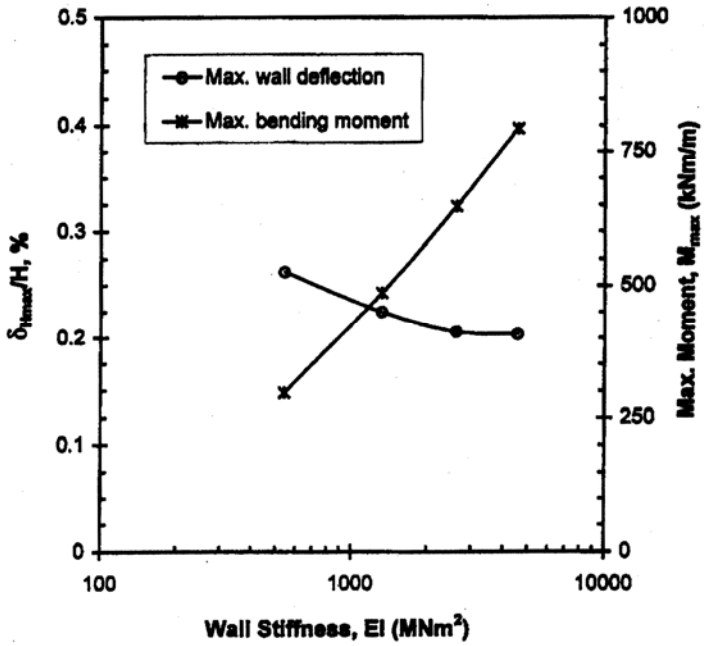

Figure 2.15 Effect of Wall Stiffness on Lateral Wall Deflection for Stiff Residual Soils (Poh et al., 1997)

2.2.12 Consolidation

Osaimi and Clough (1979) reported that some consolidation is likely to occur at the end of construction even for excavations in clay with very low permeability. This consolidation can affect the ground settlement.

In practice, diaphragm walls are usually extended to a competent soil stratum (N_{SPT} > 50). However, there is no guarantee that it will provide an effective cut-off (Wen et al., 2001). Seepage can still occur. Lambe et al. (1970) showed that two-thirds of the total settlement occurred due to seepage during a deep excavation project along Accolon Way in Boston. Experiences in the MRT North East Line in Singapore showed that post-excavation settlement could be 55 to 60% of the total settlement (Wen et al., 2001 and Li, 2002).

Another cause for consolidation is leakage. It is usually caused by cracks in the diaphragm walls, imperfections of the diaphragm wall construction and joints

between wall panels. Sliwinski and Fleming (1975) reported a case in London where most leakages occurred at locations of maximum differential deflections of wall panels. This location is usually at the corner of diaphragm wall as shown in Figure 2.16.

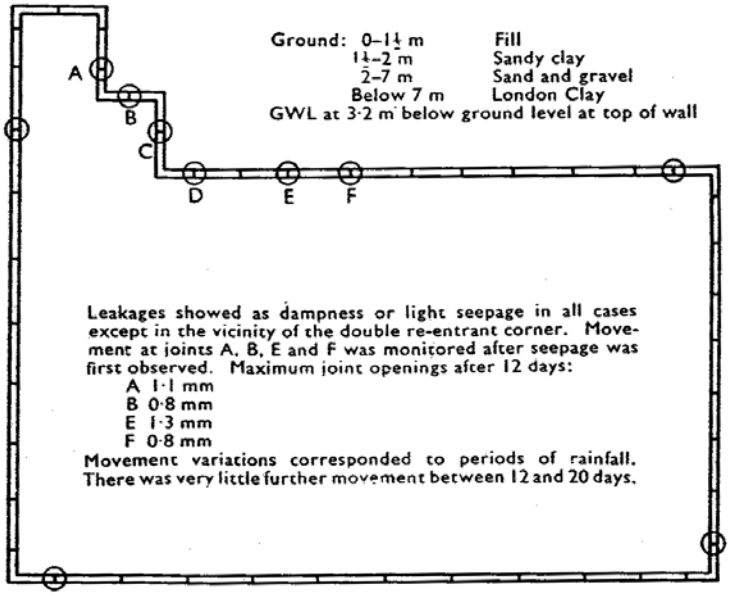

Figure 2.16 Leakage at Panel Joints on a London Site
(Sliwinski and Fleming, 1975)

2.2.13 Anisotropy

Most clays are anisotropic in material properties by nature. The shear strength may vary with the direction of major principal stress. Figure 2.17 shows the shear strength of an isotropic clay independent of the direction of principal stresses. However, for an anisotropic clay, the shear strength is related to the direction of principal stresses. Before excavation, the initial major principal stress is in the vertical direction. As excavation progresses, the direction of major principal stress at the bottom of excavation will change from vertical to horizontal. It means that the shear strength of a normally consolidated clay at the bottom of excavation will decrease. This anisotropy effect may reduce the available passive resistance of clay in front of the excavation wall which can lead to large wall movement and ground settlement.

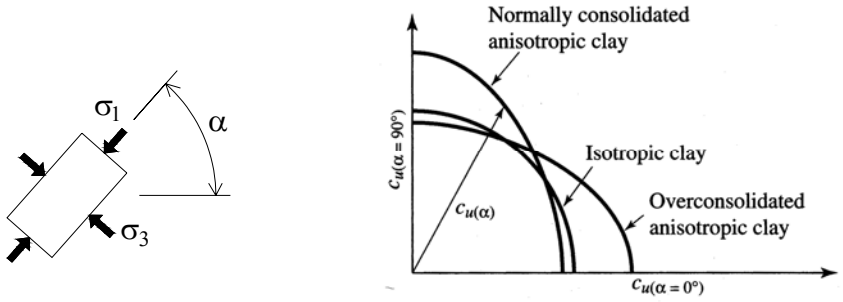

(a) (b)

Figure 2.17 Anisotropic Effect on Shear Strength of Saturated Clay (Das, 2002)

Clough et al. (1979) conducted a hypothetical study of deep excavation with anisotropy effect. Figure 2.18 shows that an anisotropic soil yields higher wall deflection as compared to that of an isotropic soil. It is because the soil resistance at the passive side of anisotropic soil has yielded while the isotropic soil has not. Therefore, the anisotropic soil offers less resistance to the lateral wall movements. The study also reveals that when the factor of safety against basal heave falls below 1.5, the anisotropy effect becomes more prominent. Finno and Harahap (1991) reported similar findings. They recommended that soil anisotropy should be considered when evaluating potential ground movements for excavation in soft to medium clay.

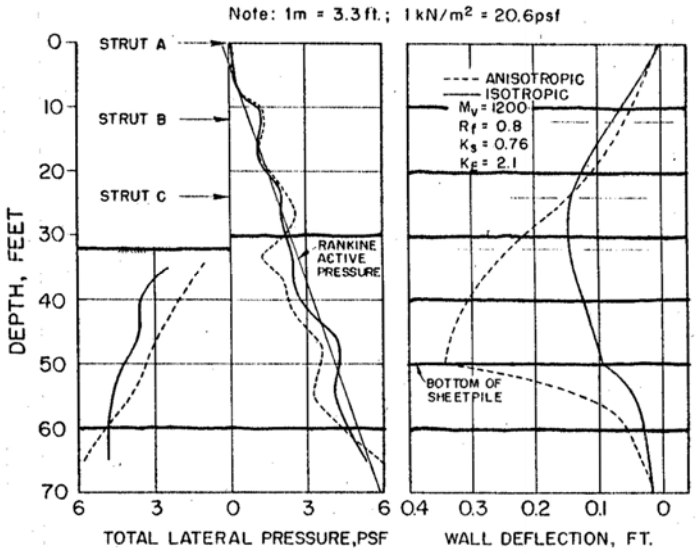

Figure 2.18 Anisotropy in Deep Excavation (Clough et al., 1979)

2.2.14 Excavation Shape

Bono et al. (1992) reported that the corner of an excavation will cause significant reduction in deformation and ground settlement as shown in Figure 2.19. Ou et al. (1996) reported similar findings. Lee et al. (1998) concluded that the corner effect would depend on the support system stiffness, the length to depth ratio of the excavation, and the depth to competent stratum.

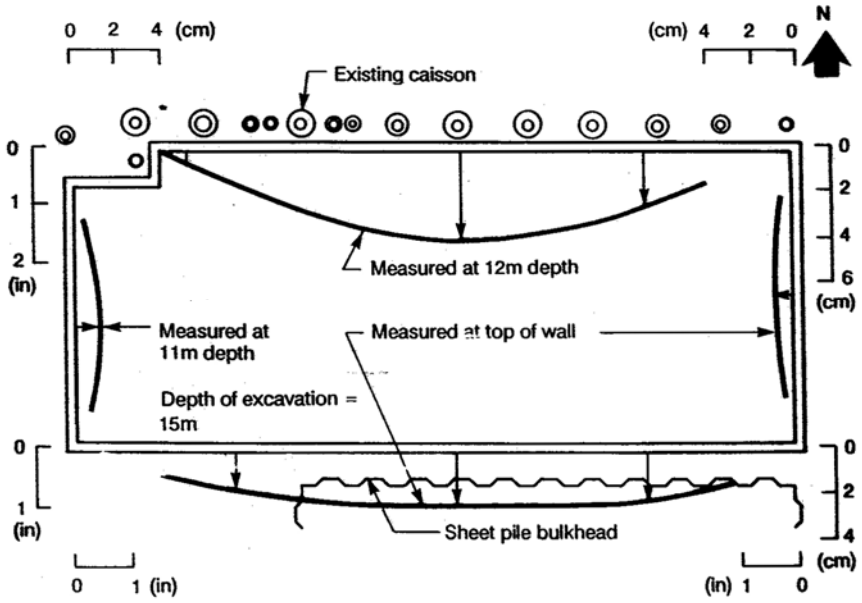

Figure 2.19 Corner Effect on Wall Deflection (Bono et al., 1992)

Wong and Broms (1989) investigated the effect of depth and width of excavation based on a finite element study. When the excavation goes deeper, the factor of safety against basal heave will become smaller resulting in an increase in wall deflection as shown in Figure 2.20. Figure 2.21 shows that the wall deflection increases proportionally with the increase in excavation width.

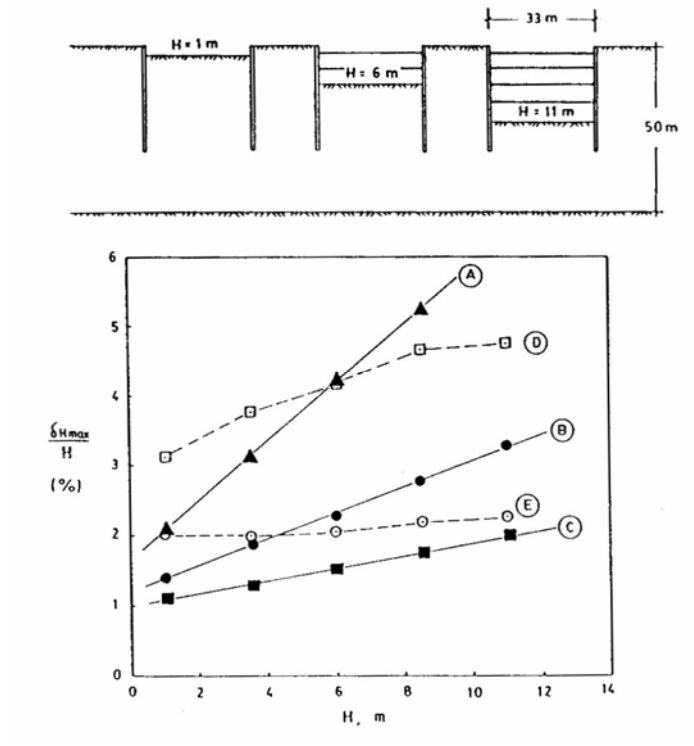

Fig. 2.20 Effect of Excavation Depth on Wall Deflection (Wong & Broms, 1989)

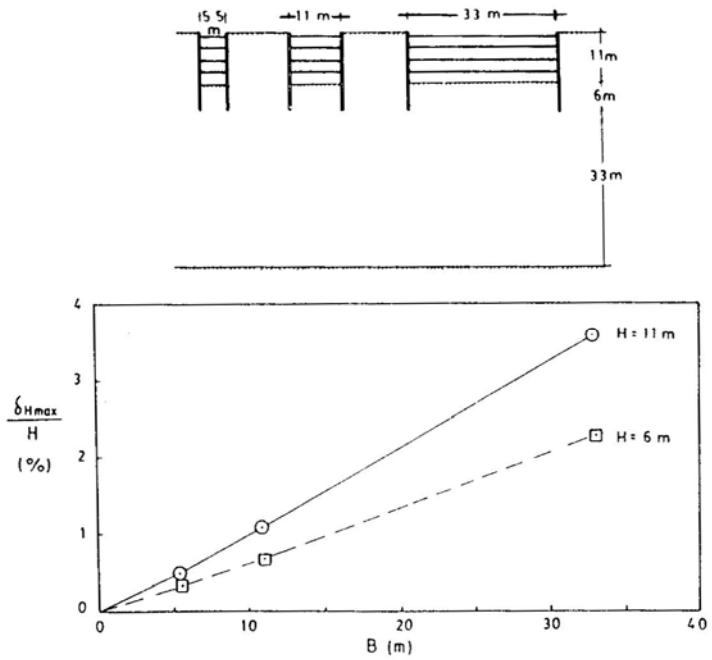

Fig. 2.21 Effect of Excavation Shape on Wall Deflection (Wong & Broms, 1989)

2.2.15 Temperature

In region where the temperature fluctuation is high, such as Boston, the temperature effect on struts should be considered. Whittle et al. (1993) reported a case in Boston where an increase of 25°C caused thermal expansion to the structural floors. This force later pushed the wall that caused the top of the diaphragm wall to move outward about 5 to 10 mm.

Some overstressing in the jacking boxes was also reported by Bono et al. (1992). The thermal effect on struts caused overstressing in some of the jacking boxes. Since strut failure could lead to a collapse of the excavation, the contractor made an emergency repair on the strut to reinforce the jacking boxes. Batten et al. (1996) showed that the temperature not only influences the axial loads, it can also generate high bending stress on the wall. The increase of temperature will increase the strut force. This force would push the wall and prevent the wall to deflect any further. Hence, the bending stress in wall would increase.

Niu et al. (2005) showed an interesting plot between temperature and wall deflection at different time. As shown in Figure 2.22, when the temperature was high, the wall deflected less. It is because the increase of temperature increased the strut length and pushed the wall back.

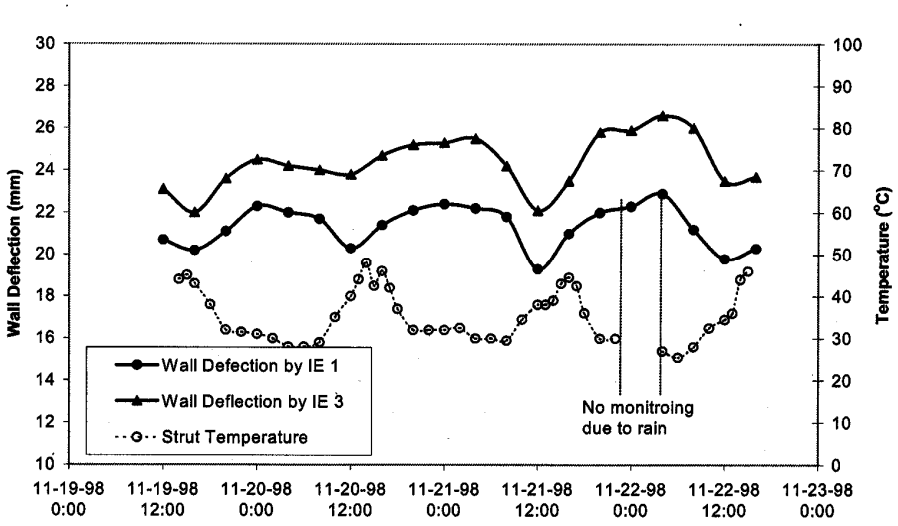

Figure 2.22 Effect of Temperature on Wall Deflection (Niu et al., 2005)

2.2.16 Depth of Hard Stratum

Wong and Broms (1989) studied the effect of depth to hard stratum on wall deflection. Figure 2.23 shows that the deeper the hard stratum, the higher is the wall deflection. It occurs until the T/B ratio is greater than 1.2. Beyond it, the effect of hard stratum depth becomes insignificant.

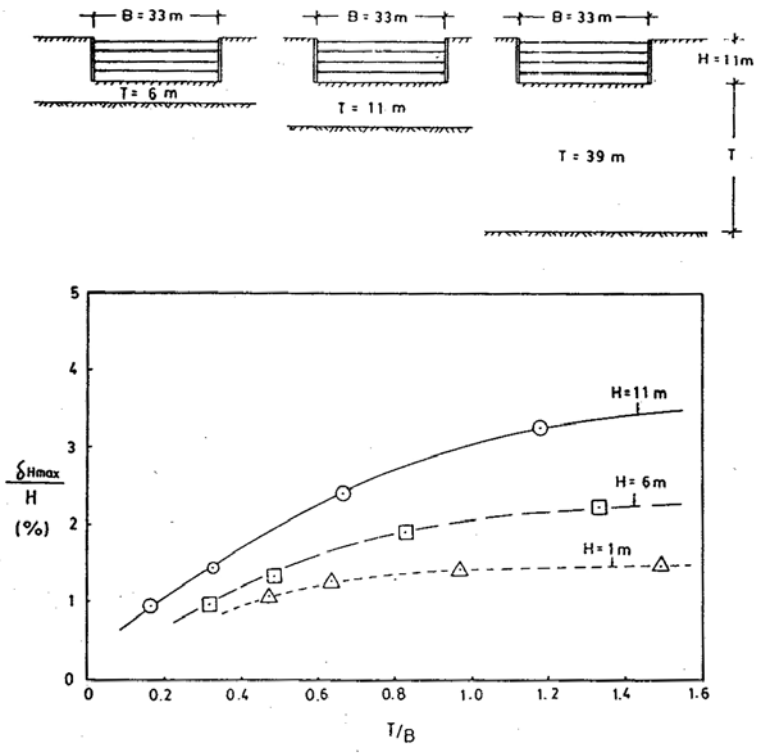

Figure 2.23 Effect of Depth of Hard Stratum to Wall Deflection
(Wong and Broms, 1989)

2.2.17 Embedment of Excavation Wall

Peck (1969) and Broms et al. (1986) reported that very little benefit can be gained by driving the sheetpiles far below the bottom of the excavation in a deep stratum of soft to medium stiff clay provided the stability of the excavation with respect to bottom heave is sufficient. Wong and Broms (1989) illustrated this problem in Figure 2.24. As shown by the results from Cases A and B, the difference in maximum wall deflection between no wall penetration to full penetration is small.

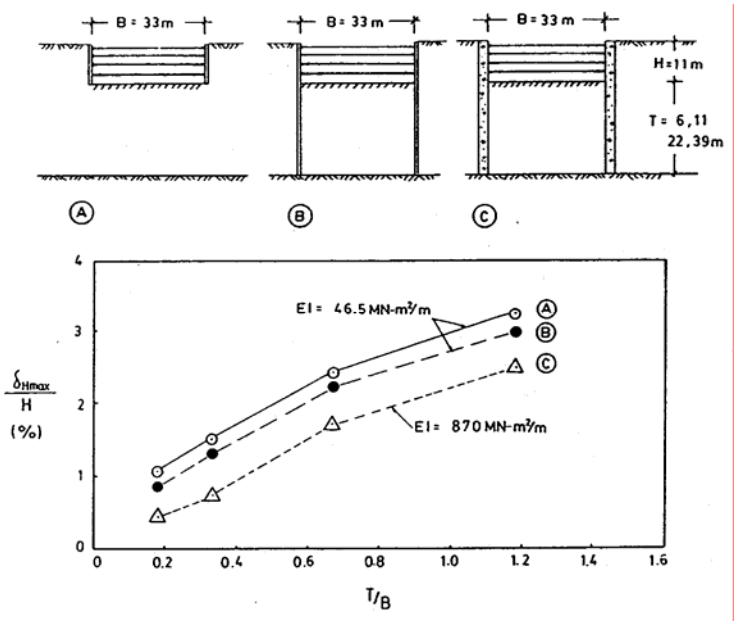

Figure 2.24 Effect of System Support Stiffness and Penetration to Wall Deflection (Wong and Broms, 1989)

In the case of lightly overconsolidated clay, this effect can also be minor as reported by Whittle and Hashash (1993). Poh et al. (1997) studied similar problems for stiff residual soils. As shown in Figure 2.25, the maximum wall deflection is not affected by the length of diaphragm wall.

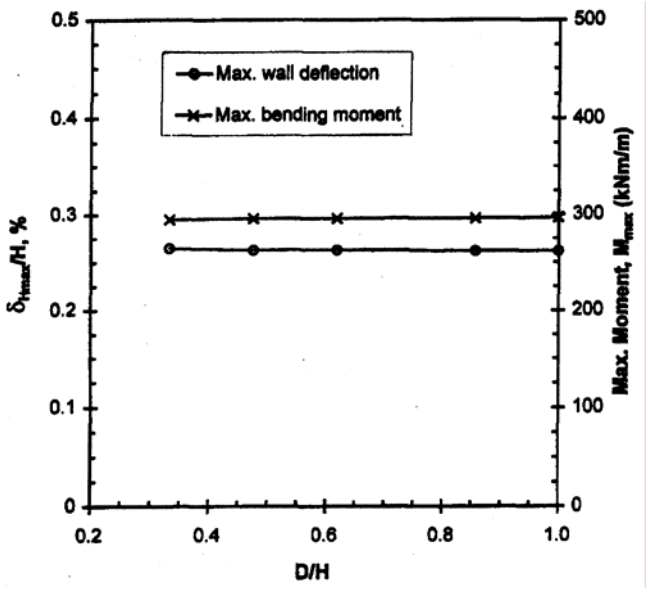

Figure 2.25 Effect of Wall Length on Wall Deflection (Poh et al., 1997)

2.2.18 Construction Activity

Some construction activities during excavation can greatly affect the soil movements. During the construction of drilled shafts and caisson in Chicago, Lambe et al. (1970) showed that it caused 50% to 70% of the total settlement. Horizontal ground movements can also occur due to wall construction. Finno et al. (1988) showed that 13 mm of horizontal ground movement occurred during the installation of sheetpile at HDR-4 project in Chicago. Studies done by Clough and O'Rourke (1990) showed that a slurry wall construction with 37 m depth in Hong Kong had generated settlement more than 50 mm. However, in most cases, the maximum settlements are in the range of 5 to 15 mm as shown in Figure 2.26.

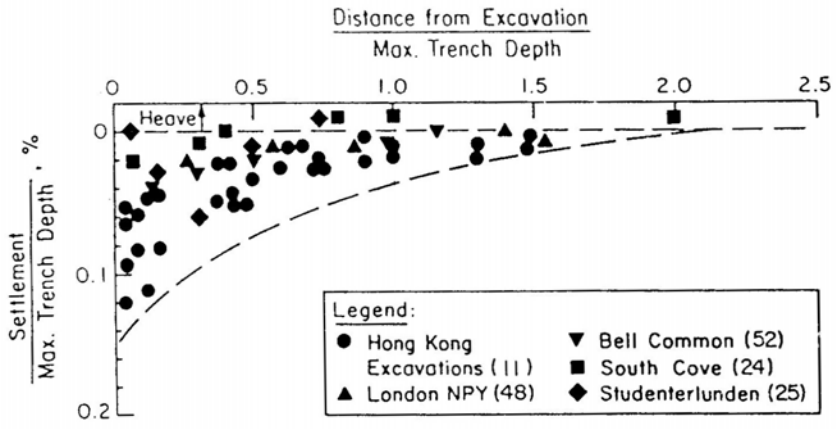

Figure 2.26 Ground Movement Due To Slurry Wall Construction (Clough and O'Rourke, 1990)

Poh et al. (2001) reported lateral soil movement during the construction of wall panels at Singapore Post Office. The soil moved inward up to 39.2 mm as shown in Figure 2.27. However, during the concreting process, the soil was pushed back again due to the pressure of fresh concrete.

2.3 Relationship between Ground Settlement and Wall Movements

The ground settlement due to excavation can be divided into two parts. The first part is during excavation which is essentially an undrained deformation. The second part is post-excavation settlement due to seepage.

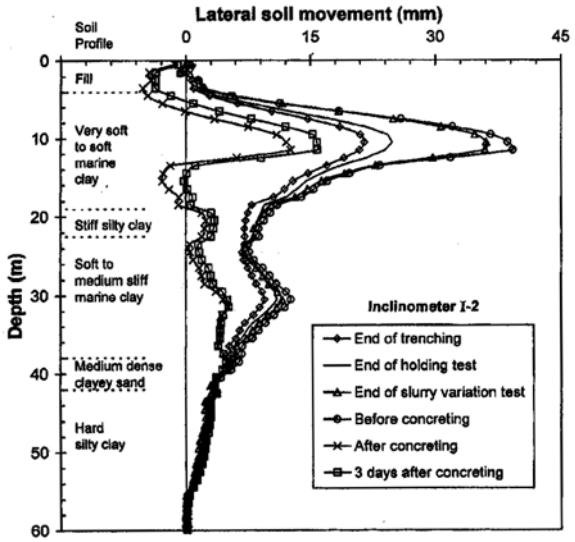

Figure 2.27 Effect of Panel Construction on Wall Deflection (Poh et al., 2001)

Ground settlements and wall movements are interrelated with each other. As the wall deflects inward, the ground behind the wall will settle. The ratio of areas between ground settlement and wall deflection is almost same (NGI, 1962) as depicted in Figure 2.28. This is true if there is no significant ground water drawdown as reported by Miyoshi (1977). Figure 2.29 shows that when the ground water level is constant as in Site A, the ratio of areas between wall deflection and ground settlement is more or less one. When the ground water level drops as in Site B, the ratio also drops. The difference is caused by consolidation settlement due to lowering of water table.

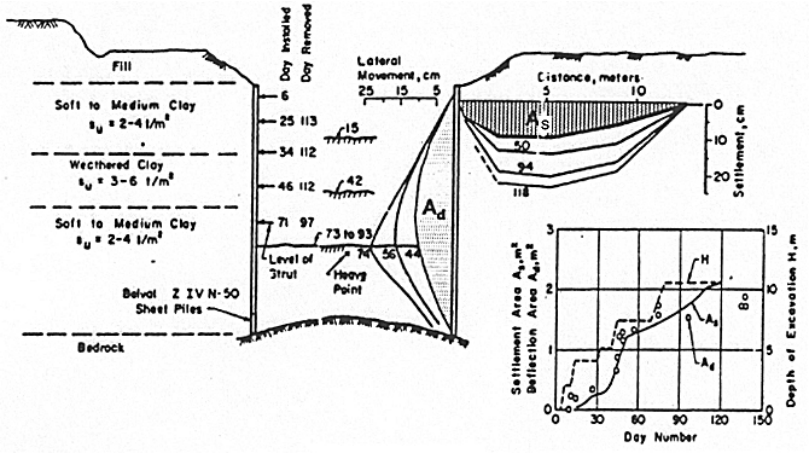

Figure 2.28 Areas of Wall Deflection and Ground Settlement at Oslo (NGI, 1962)

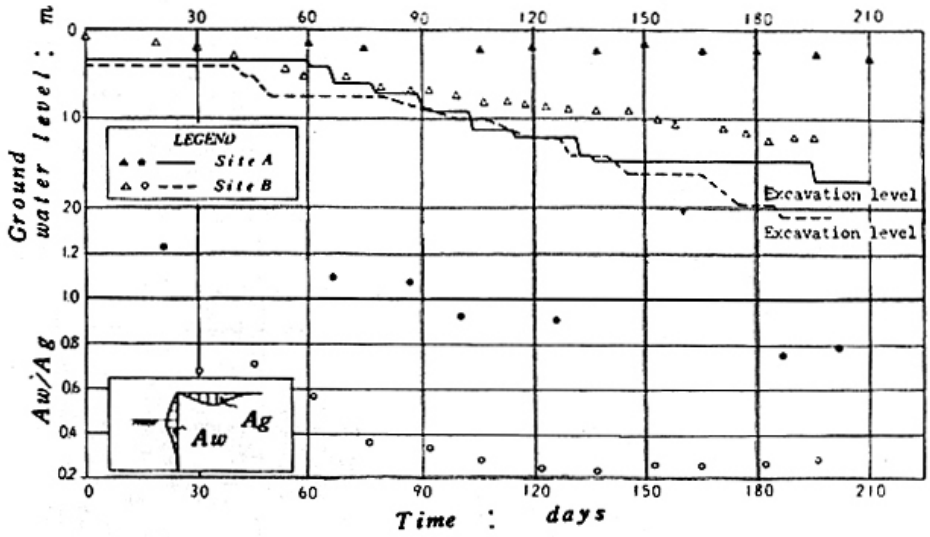

Figure 2.29 Ratio of Wall Deflection to Ground Settlement (Miyoshi, 1977)

Osaimi and Clough (1979) studied the soil movement pattern between high and low permeability of an elastic soil shown in Figure 2.30. The soil movement patterns between them are different. The high permeability soil has a larger upward movement near the bottom of excavation and more horizontal movement at the vertical excavation face.

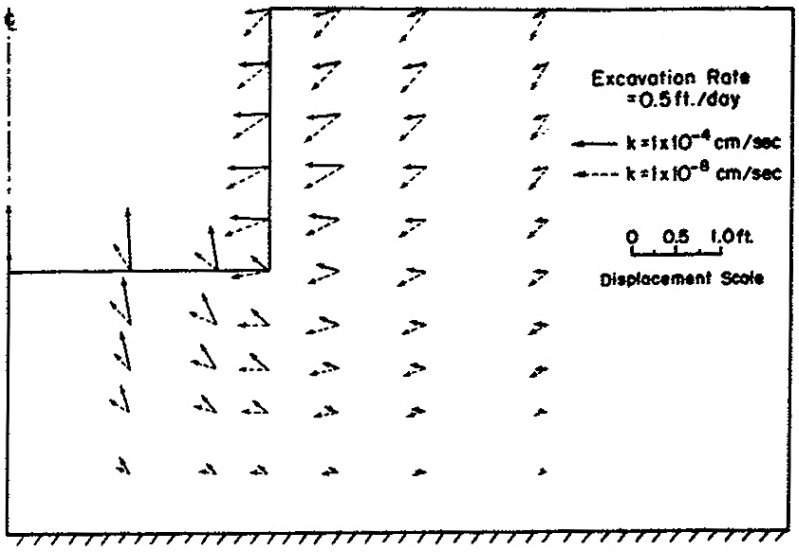

Figure 2.30 Displacement Vectors for Unsupported Elastic Soil (Osaimi and Clough, 1979)

2.4 Shape of Ground Settlement and Wall Deflection

Generally, there are two modes of ground movements and two modes of wall deflection. The ground settlement profile can be of spandrel or concave type as shown in Figure 2.31. According to Ou et al. (1993), if a large wall deflection occurs at the first stage of excavation and the wall deflection is relatively small at subsequent excavations, the spandrel type of settlement profile usually occurs. On the other hand, once a relatively small amount of wall deflection occurs at the initial stage of excavation when compared with that at greater depths, the concave ground settlement profile will occur. It should be noted that in a braced excavation, spandrel type usually occurs first since the soil need to be excavated first before first strut level can be installed.

Based on the study done by O'Rourke et al. (1976), the horizontal ground movements can be larger than the ground settlements in spandrel type. On the contrary, the horizontal ground displacements will normally be significantly less than the ground settlements in the concave type. Similar pattern was also reported by Ou et al. (1993). Therefore, in order to minimize the horizontal movement, Peck (1969) and Wong et al. (1997) suggested that the first prop level should be kept close to the ground surface. The maximum ground settlement for the spandrel type usually occurs very close to the wall face. In the case of concave type, studies by Ou et al. (1993) showed that it is about half of the final excavation depth.

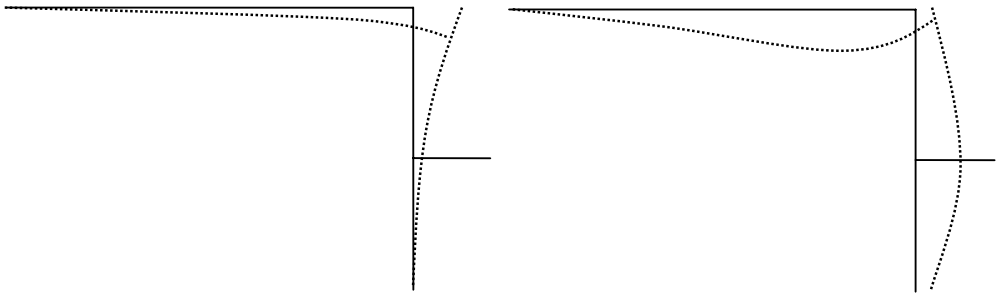

(a) Spandrel Ground Movement and Cantilever Wall Movement

(b) Concave Ground Movement and Deep Seat Wall Movement

Figure 2.31 Ground and Wall Movement Types

2.4.1 Ground Settlement in Stiff Clay, Residual Soils and Sands

Clough and O'Rourke (1990) reported that for excavations in stiff clay, residual soils and granular soil, the maximum settlement is typically less than 0.5% of the depth of excavation with an average of 0.15% regardless of wall type as shown in Figure 2.32. This finding is consistent with the studied by Goldberg et al. (1976) and Li and Wong (2001).

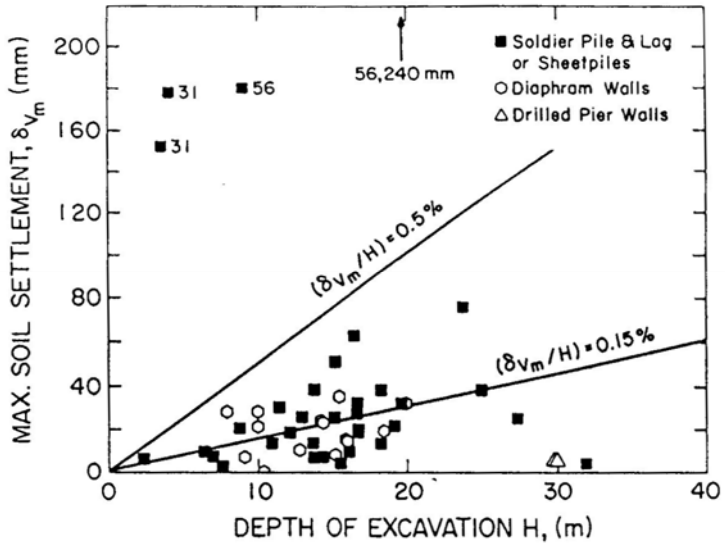

Figure 2.32 Ground Movement on Stiff Clay, Residual Soils and Sands (Clough and O'Rourke, 1990)

Figure 2.33 shows the distribution of ground settlement for stiff to very hard clay (Clough and O'Rourke, 1990). Heaving was reported in some cases. Figure 2.34 shows the distribution of ground settlement for excavations in sand. The maximum ground settlement envelope is about 0.3% of the maximum excavation depth. The settlement zone extends to a distance equal to two times the maximum excavation depth for sand and three times for stiff to very hard clay.

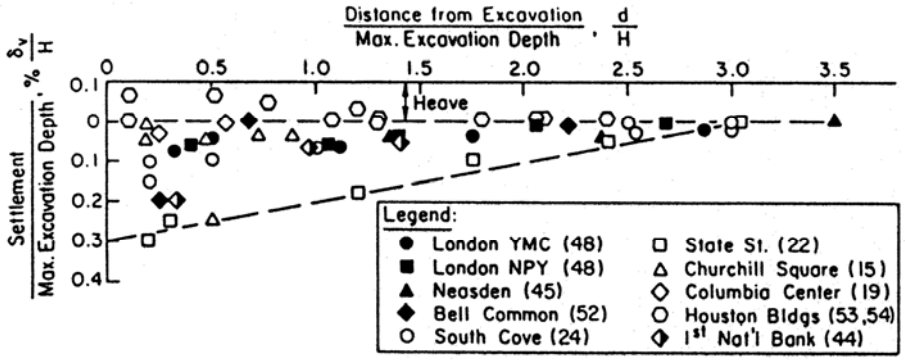

Figure 2.33 Ground Movement Distribution on Stiff to Very Hard Clay
(Clough and O'Rourke, 1990)

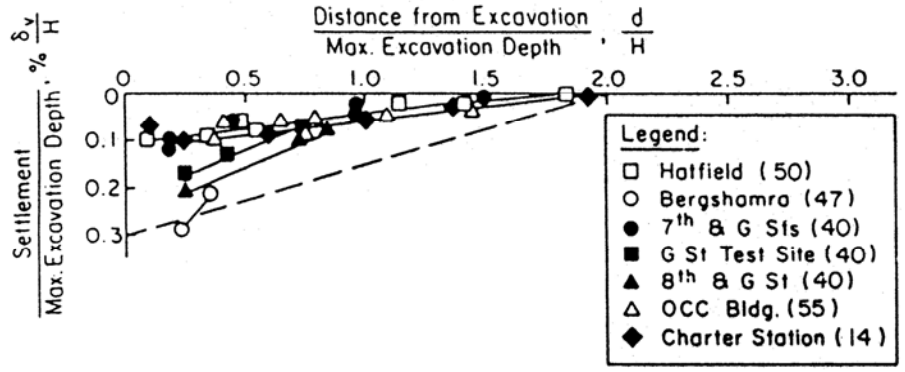

Figure 2.34 Ground Movement Distribution on Sand
(Clough and O'Rourke, 1990)

2.4.2 Ground Movement in Soft and Medium Clay

Ground movements in soft to medium clay are governed mainly by basal heave stability. Peck (1969) pointed out that if the stability number, N_s, is between 6 and 9, the ground movement can become large. It is because when the stability number reached this value, extensive plastic yielding has occurred in the soil around the base of excavation. Figure 2.35 shows that the maximum ground settlement envelope is about 2.5% of the maximum excavation depth. The zone extends to about 3 times the excavation depth from the wall.

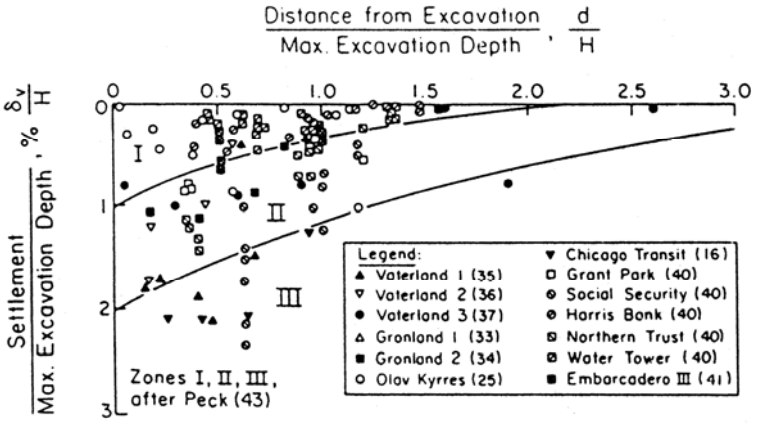

Figure 2.35 Ground Movement Distribution on Soft to Medium Clay (Clough and O'Rourke, 1990)

2.4.3 Wall Movements in Stiff Clay, Residual Soils, and Sand

Clough and O'Rourke (1990) proposed a chart to predict the maximum wall movement based on the data collected from excavation in stiff soil and for soft soil. Figure 2.36 shows that for stiff soil, the average horizontal wall movement is 0.2% of the depth of excavation with a maximum of 0.5%. However, it should be noted that the maximum wall deflections of soldier pile and sheetpile walls are more scattered.

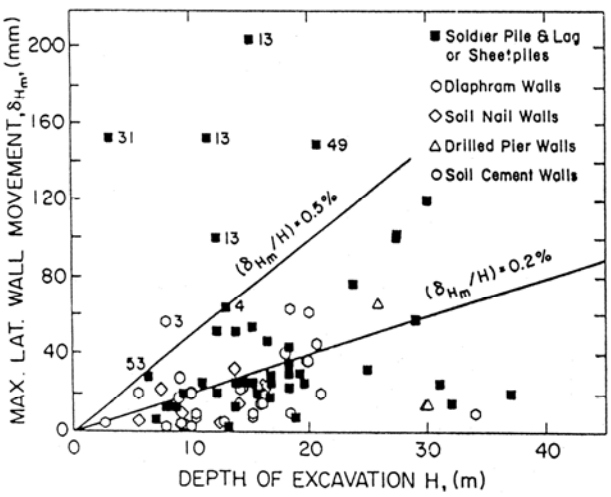

Figure 2.36 Observed Maximum Wall Movements for Stiff Clay, Residual Soil and Sand (Clough and O'Rourke, 1990)

2.4.4 Wall Movements in Soft and Medium Clay

The magnitude of wall movement is related to the factor of safety on basal heave. When the factor of safety falls below 1.5, more and more soil moves into the plastic state resulting in large wall movements as shown in Figure 2.6.

2.5 Prediction of Ground Settlement Profile

Peck (1969) divided the settlement data into three categories according to soil types and workmanship as shown in Figure 2.37. It should be noted that the chart is based largely on data from soldier pile and sheetpile walls. This chart may not be appropriate for use with diaphragm wall. Clough and O'Rourke (1990) reported a case involving 36 m of excavation in stiff clay for the Columbia Center in Seattle, Washington. The maximum ground movement was only about 0.1% of the excavation depth. According to Peck's chart, the maximum movement in category I is 1% of the excavation depth. Therefore, using Peck's chart to estimate the ground movement with diaphragm wall can be very conservative.

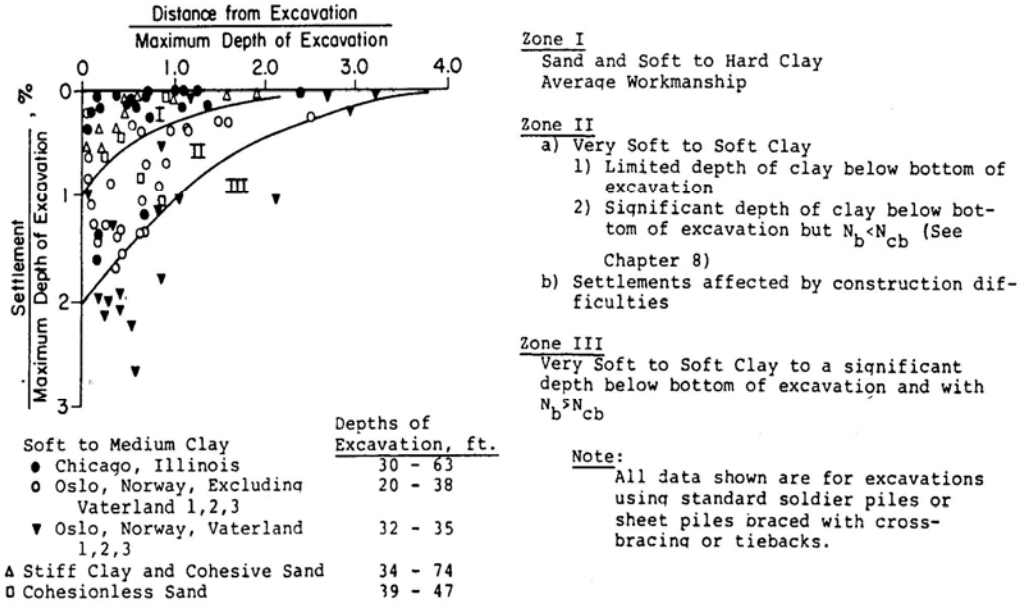

Figure 2.37 Ground Settlement Distribution (Peck, 1969)

Clough and O'Rourke (1990) proposed three ground settlement envelope profiles which are divided into sands, stiff to very hard clays, and soft to medium clays. They are shown in Figure 2.38. The data included various types of walls and supports, such as sheetpiles with tiebacks or a concrete diaphragm wall with cross-lot struts. For soft to medium clay, the settlement profile is divided into two zones. One is the maximum settlement zone and the other is the transition zone.

Another ground settlement prediction comes from Hsieh and Ou (1998). Based on 10 case histories in Taipei, Taiwan, they observed that the vertical movements of soil behind the wall may extend to a considerable distance. The settlement at a limited distance behind the wall is not uniform like those proposed by Clough and O'Rourke (1990). It increases with the excavation depth. They proposed a tri-linear line for predicting the spandrel type settlement profile, based on an average value of the observed settlement profiles as shown in Figure 2.39. Line a-b is termed as 'primary influence zone', which has a relatively steep slope. If a building falls within this zone, its safety should be checked since the angular distortion can be relatively large. The second zone, line b-c, is termed settlement influence zone where the building may be less affected.

Osman and Bolton (2006) proposed another method to predict ground settlement within the framework of plasticity theory. It incorporates the actual stress-strain data and the undrained shear strength profile of the soil. The soil behaviour is represented by a direct simple shear test curve of mobilized stress and strain. The soil is also assumed to shear and deform compatibly and continuously with no relative sliding at the boundaries. A fairly tedious procedure involving complex equations was proposed for the prediction of ground settlement which is expressed as a cosine function. This method is more difficult to use as compared to previous methods.

2.6 Pore Water Pressure and Seepage due to Deep Excavation

In a deep excavation, a huge amount of soil is removed which cause the wall to deflect and the ground to settle. All of these stress changes will change the pore

water regime. It is important to understand how the pore water pressure changes. Lambe et al (1972) reported that the permeability of soil and rate of construction can greatly affect the pore water pressure regime.

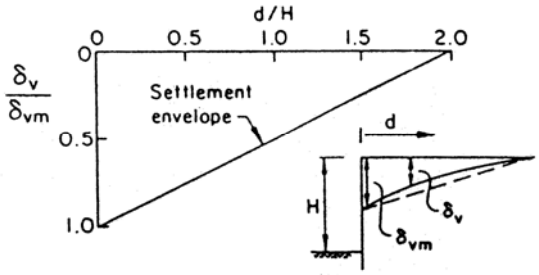

(a) Sand

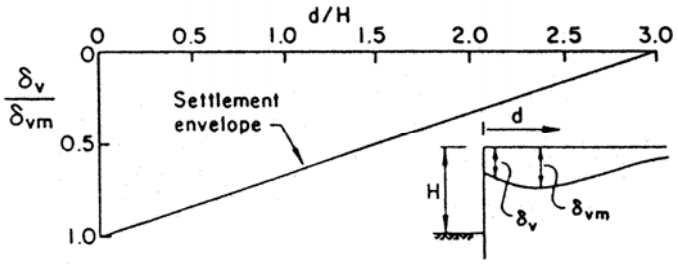

(b) Stiff to Very Hard Clay

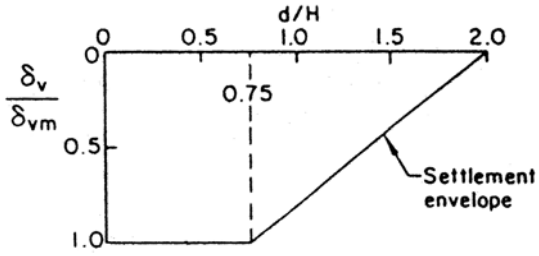

(c) Soft to Medium Clay

Figure 2.38 Ground Movement Envelopes (Clough and O'Rourke, 1990)

Pore water pressure starts to change during the installation of the walls. Finno et al. (1989) reported that positive excess pore water pressure increased significantly during the construction of HDR-4 in Chicago as shown in Figure 2.40. However, as the excavation progressed, it began to drop again. Similar experience was also recorded by Koutsoftas et al. (2000) during the construction of SPTC wall for MUNI Metro Turnback project in San Francisco as shown in Figure 2.41.

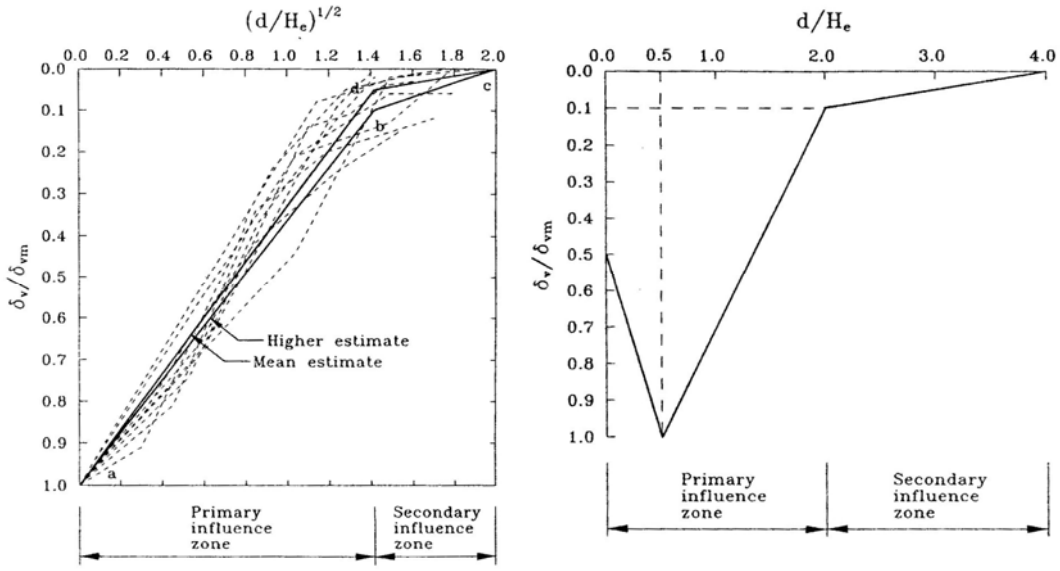

(a) Spandrel Settlement (b) Concave Settlement

Figure 2.39 Ground Settlement Distribution (Hsieh and Ou, 1998)

If leakage occurs, the ground will continue to settle. Nevertheless, if leakage can be minimized which is usually the case when the project has been completed, the negative excess pore pressures tend to dissipate with time. Consequently, the ground will heave rather than settle. Ward (1961) and Ward and Burland (1973) showed that in long term, the ground settlement outside the 12 m deep excavation for Shell Centre in London started to heave rather than continuing to settle.

The amount of leakage will affect the distribution of pore water pressure around the excavation. Therefore, the contour of pore water pressure between excavation with diaphragm wall and sheetpile are very different. Figures 2.42 and 2.43 show this phenomenon. Figure 2.42 is for a project involving sheetpile along Accolon Way in Boston (Lambe et al., 1970). Figure 2.43 is for a project involving diaphragm wall for the Taipei National Enterprise Center (Ou et al., 1998).

Sheetpile walls are definitely more permeable as compared to diaphragm walls. A drop in ground water level with this type of wall is likely to occur. Seng (1985) reported one case in Singapore with sheetpile wall. Measurements from the standpipe indicated a drop in water level due to leakage in the sheetpile adjacent

to the standpipe. Once the leakage had been sealed, the reading of standpipe indicated a recovery of the ground water level.

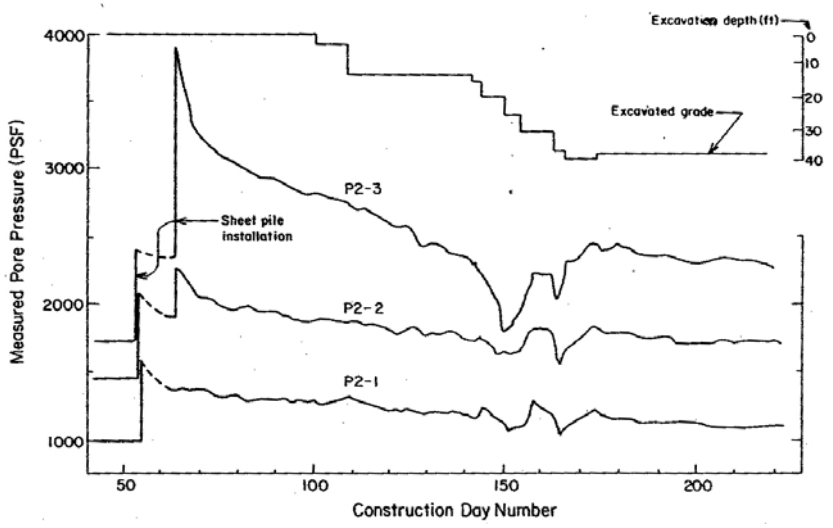

Figure 2.40 Pore Water Pressure at HDR-4 in Chicago (Finno et al., 1991)

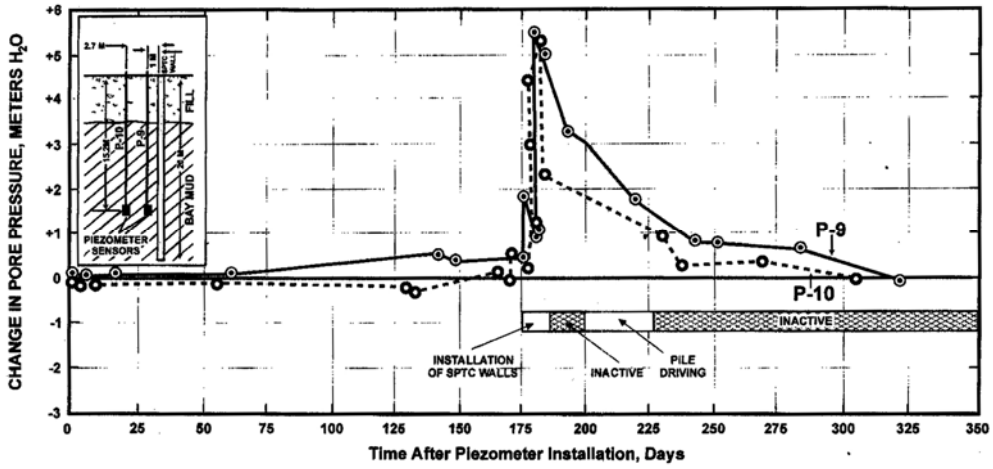

Figure 2.41 Pore Water Pressure Increment due to Wall Construction (Koutsoftas et al., 2000)

Figure 2.43 shows that the ground water level was relatively constant in the excavation using diaphragm wall. Even though diaphragm wall is not impermeable, it is much better than the sheetpile wall. The corresponding ground water level is essentially hydrostatic. Seepage should not be a problem if there are no adjacent buildings surrounding the excavation. The major problem of seepage

is ground settlement that damages buildings. If seepage can be minimized, damage on building can also be minimized. Minimizing seepage on the diaphragm wall is not an easy task. Nearly all basements in Singapore constructed of diaphragm walls have experienced problems with wetness on or moisture ingress through the walls (Wong, 1997).

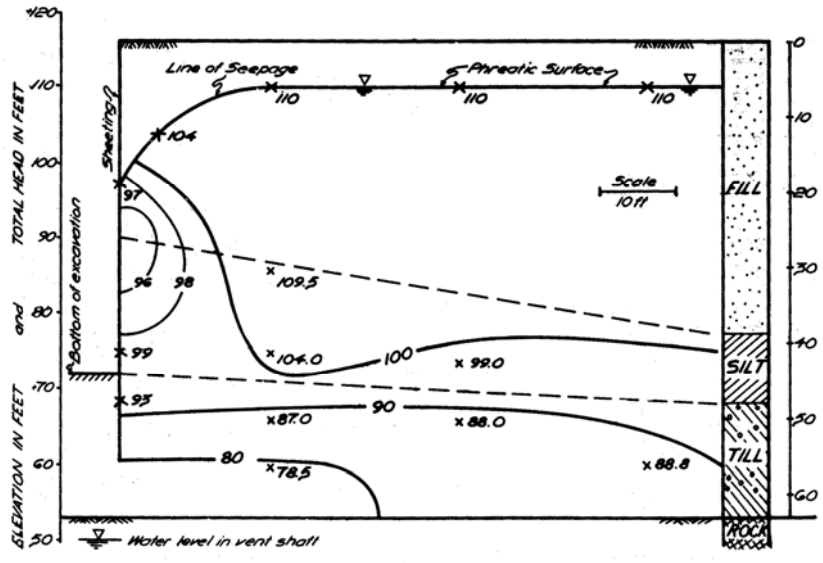

Figure 2.42 Pore Water Pressure Contour with Sheet-Pile Wall
(Lambe et al., 1970)

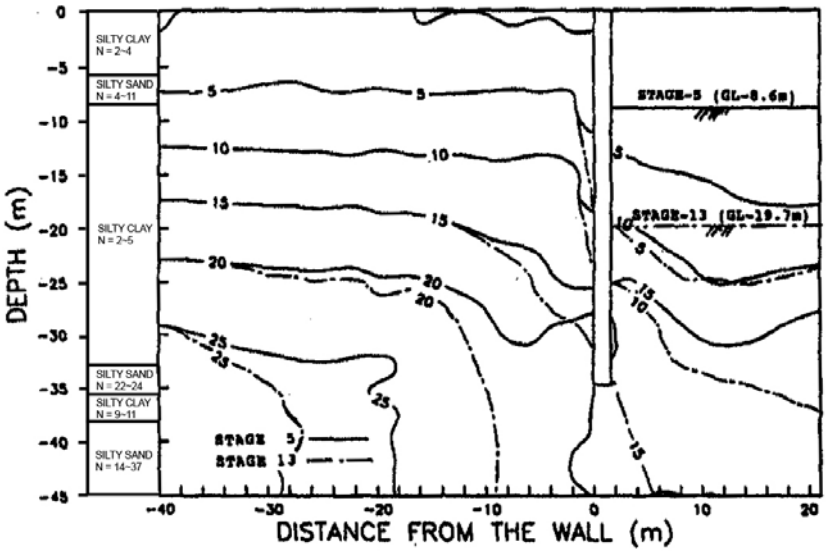

Figure 2.43 Pore Water Pressure Contour with Diaphragm Wall
(Modified from Ou et al., 1998)

2.7 Waterproofing on Diaphragm Wall

In Singapore according to Wong (1997), methods of waterproofing the basement walls fall into three categories. The first method is to construct a false wall with a drained cavity next to the interior face of a basement wall, for example, in the Ngee Ann City complex. This method will only result in a dry looking basement wall, but would not solve the problem of seepage through the diaphragm walls.

The second method is to rely on the water tightness of the concrete itself. It is done by adding some additives to increase water tightness of the concrete. These additives could reduce but not eliminate the wet or damp spots on the wall.

The third method is to apply an impervious membrane on the interior face of the basement wall, such as High Density Polyethylene (HDP), mastic asphalt, bentonite clay layer, polyurethane membrane, or a thick concrete cover. At Newton MRT Station, the concrete cover was 800 mm thick which is the same thickness as the diaphragm walls. Unfortunately, the thick concrete cover did not stop the wall leakage completely. All these waterproofing methods can only minimize seepage but not totally eliminate it.

2.8 Summary

Several factors affecting the performance of deep excavation have been discussed. They are soil shear strength, soil stiffness, support system stiffness, support spacing, preloading, construction delay, construction sequence, workmanship, initial lateral stress of soil, wall type, consolidation, anisotropy, excavation shape, temperature, the depth of hard stratum, embedment of excavation wall, and construction activity. These factors greatly affect the ground settlement and wall deflection. Another important factor is wall leakage. It mainly affects ground settlement and to a less degree the wall deflection. All these factors should be carefully considered during the design and construction phases in order to minimize ground settlement, wall deflection, and building damage. Several methods proposed by researchers to predict ground settlement envelopes have also been discussed. These methods can be used to predict building damage.

CHAPTER 3
BUILDING DAMAGE

3.1 Introduction

Excavation and tunneling will cause changes in soil stresses and ground losses. These changes will lead to soil movements. In an urban environment, these changes can have large impact on the structures and utilities adjacent to the excavation and tunneling. The structures may settle, distort or deform which can result in cracking and structural damages.

An excavation or a tunneling project cannot be considered successful if it resulted in collapse or damage to adjacent structures or utilities. Little (1969) has estimated that the cost of preventing any cracking could exceed 10% of the total building cost. Therefore, the ability to predict and ensure the safety of structures or utilities adjacent to the excavation or tunneling is very important. Different approaches have been proposed to assess the degree of damage to a building due to soil movements. This chapter summarizes the published methods of assessing building damage due to soil movement.

3.2 Definition of Building Damage Parameters

Burland and Wroth (1974) proposed some definitions describing the types of movement and deformation experienced by a foundation. The following are the proposed definitions. The symbols are shown in Figure 3.1.

1. ρ = settlement. It defines the settlement of a point.
2. δ_ρ = relative or differential settlement. It defines the relative settlement between two points.
3. θ = rotation or slope. It defines the gradient of a line connecting two points.
4. α = angular strain. The angular strain α at point B (for example) is defined as

$$\alpha_B = \frac{\delta_{\rho BA}}{l_{AB}} + \frac{\delta_{\rho BC}}{l_{BC}} \tag{3.1}$$

It is positive for sagging and negative for hogging as shown in Figure 3.1a

5. Δ = relative deflection. It defines the displacement of a point relative to the line connecting two reference points.
6. Δ/L = deflection ratio. It defines the ratio between the relative deflection (Δ) and the length of two reference points (L) defining Δ.
7. ω = tilt. It defines the rotation of a rigid superstructure.
8. β = angular distortion or relative rotation. It defines an angle between tilt and the line connecting two reference points.
9. ε_h = average horizontal strain. It defines a change in length in the horizontal direction.

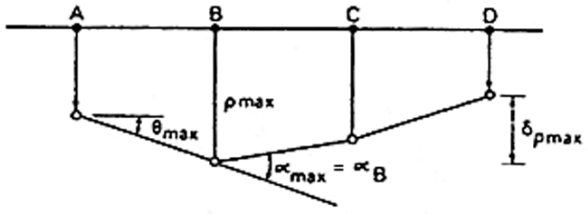

(a) Definitions of Settlement ρ, Relative Settlement δ_ρ, Rotation θ, and Angular Strain α

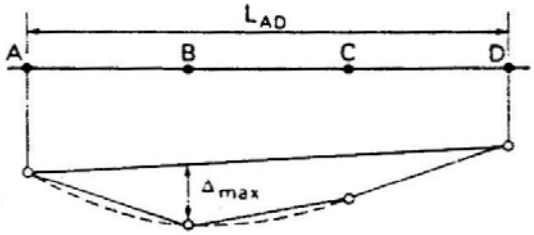

(b) Definitions of Relative Deflection Δ and Deflection Ratio Δ/L

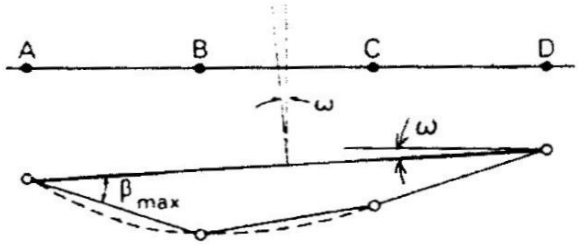

(c) Definitions of Tilt ω and Relative Rotation (Angular Distortion) β

Figure 3.1 Definitions of Foundation Movement (Burland, 1997)

The settlement of a building can be divided into three components (Padfield and Sharrock, 1983). They are total settlement, tilt, and distortion as illustrated in Figure 3.2.

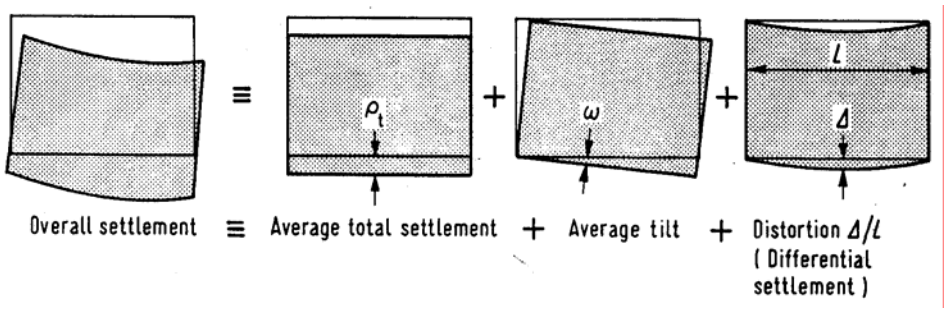

Figure 3.2 Three Components of Settlement (Padfield and Sharrock, 1983)

3.3 Type of Building and Its Responses to Excavation

Buildings can be categorized into frame and load bearing wall structures. They respond differently to soil movements.

3.3.1 Frame Structures

There are two types of frames structures: (a) frames with infill panel wall and (b) frames without infill. In the case of frames with infill panel wall, differential vertical movement of columns will induce shear deformation rather than bending. It causes diagonal tensile strain to develop. As a result, cracks will occur as illustrated in Figure 3.3.

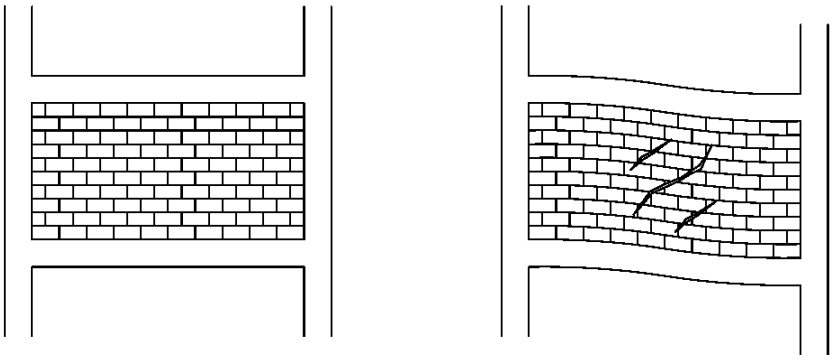

Figure 3.3 Cracks in Infill Frame

Boscardin and Cording (1989) showed that a taller building is more resistant to shear because it is more rigid. This structure will tend to tilt rather than distort. On the contrary, a wide building with many bays is likely to experience large distortion.

Leonard (1975) observed that for frame structures supported on isolated footings, tilting should be included in the distortion calculation. It is unlikely that each individual footing would rotate through the same angle as the building as depicted in Figure 3.4. Tilting in Figure 3.4a will cause no strains in the framing only if the footings are free to rotate. However, this condition most likely will not occur in practice. In the usual practice for designing framed structures which assumes fixity of the foundation similar to Figure 3.4b, tilting would contribute to the stresses and strains in the frame. Therefore, tilting should be included in the distortion calculations. Burland et al. (1977) suggested similar opinion that removing tilt in the frame buildings on separate footings might be inappropriate.

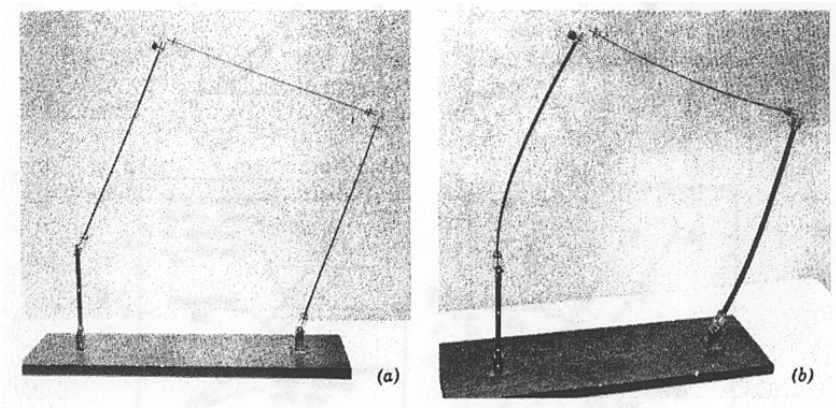

Figure 3.4 Tilting in Frame Structure with Different Support Rotation (Leonards, 1975)

3.3.2 Load Bearing Walls

Cracking in load bearing walls can be caused by hogging or sagging type of settlement as illustrated in Figure 3.5. In reinforced or unreinforced load bearing structures with panel walls, cracks due to sagging are less intense than those due to hogging. This is because in the sagging mode, there is friction between the foundation and panel wall which will restrain continuous cracking. However, even

rare, if this friction is insufficient, continuous cracking may occur. This phenomenon is reported by Ward (1956) about a brick building founded on continuous strip footing where slip had occur along the bitumen damp course. In the hogging mode, there is usually no constraint on top of the panel wall. It means that nothing will prevent the panel wall to crack, so continuous crack can propagate from top to bottom and finally to the foundation. The structure behaves as two separate walls and very wide cracks can develop. It also implies that cracks in hogging settlement are easier to occur as compared to sagging settlement.

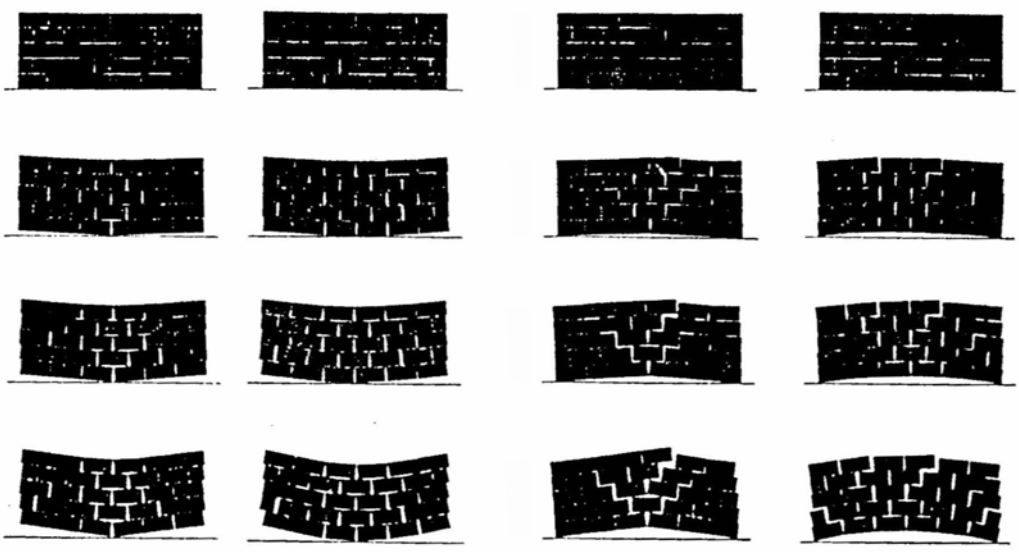

(a) Crack in Sagging Mode (b) Crack in Hogging Mode

Figure 3.5 Crack in Load Bearing Wall (after Burland and Wroth, 1974)

Cording et al. (1978) studied the deformations of brick bearing walls adjacent to excavations in Washington D. C. and New York. Three types of cracks were typically observed as shown in Figure 3.6.

1. Inclined cracks and separations occurring at the mortar joints concentrated near windows. Usually they are the largest cracks and most extensively developed.
2. Vertical or nearly vertical cracks occurring near the roofs of the buildings appears to have been related to the hogging bending that tends to cause cracking in the upper portion of a structure.

3. Vertical or nearly vertical cracks occurred near the base of a building are generally extended from the ground surface to heights of 1.5 to 3 m. Their general orientation and location suggest that they were influenced by lateral ground strain.

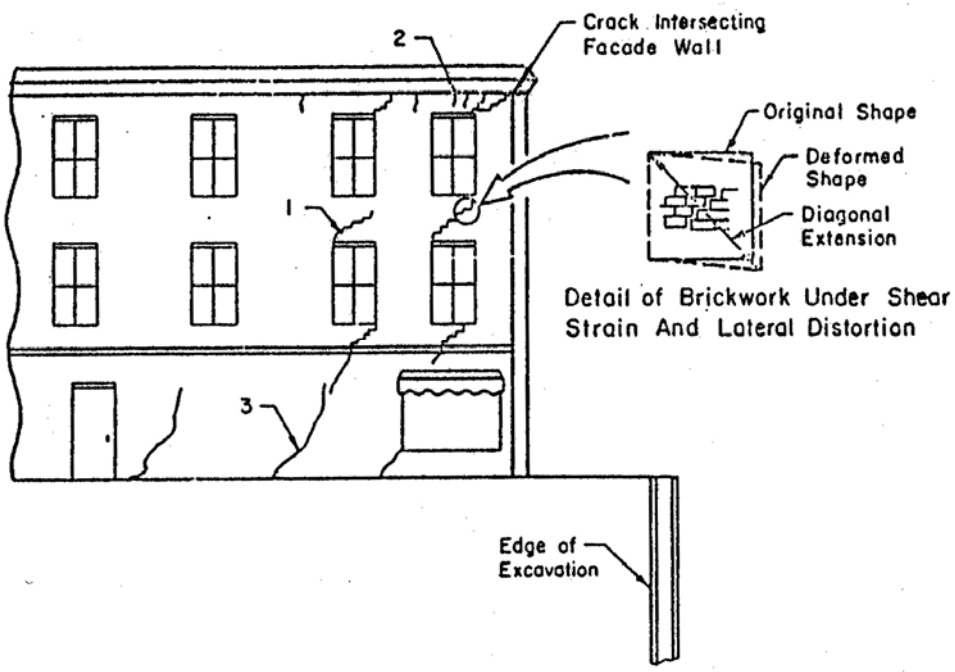

Figure 3.6 Typical Fracture Patterns Observed in Brick-Bearing Wall (Cording et al., 1978)

3.3 Building Damage Category

Skempton and MacDonald (1956) classified building damage into three categories. They are:

1. Architectural damage
2. Functional damage
3. Structural damage

Architectural damage will affect the appearance of a structure, such as tilt, total settlement, cracks or separations in panel walls, floors, and finishes. On the other hand, functional damage will affect the serviceability of structures, such as jammed

doors or windows, falling plaster, tilting of floors or walls, and other damages that do not require structural repair. Finally, structural damage will affect the stability of structures, such as distortion of beams, columns or other primary support elements.

However, this classification has no clearly defined limits and is highly subjective. By combining the work done by Jennings and Kerrich (1962), the U.K. National Coal Board (1975) and MacLeod and Littlejohn (1974), a new classification system was proposed by Burland et al. (1977) which is basically based on the ease of repair of plaster and brickwork of masonry. This classification is shown in Table 3.1.

It has an advantage which gives clearer limit between one damage categories with others. Approximate width of cracks can be also used as a damage indicator. However, it was pointed out that the key factor in determining the category should be the ease of repair, not the width of cracks. The clear distinction of this chart makes it the popular choice until now.

Burland (1997) pointed out that the dividing line between Category 2 and 3 is particularly important. Damage up to Category 2 can result from a variety of causes, either from shrinkage or thermal effects within the structure or associated with the ground. Therefore, the identification is usually very difficult because it is frequently the result from a combination of causes. If the damage exceeds Category 2, the cause is easier to identify since it is usually associated with ground movement.

Limit of Building Damage

Skempton and MacDonald (1956) recommended a safe limit of angular distortion to avoid cracking in panel walls to be 1/300. However, according to Bjerrum (1963), damage criteria should be based on the function of building as shown in Figure 3.7. Industrial buildings may be more sensitive to cracking because of the machinery being very sensitive to settlement although the building itself suffered only architectural damage. According to Cording et al. (1978), architectural damage is likely to occur if angular distortion exceeds 1/1000 for brick-bearing wall structures and 1/750 for frame structures.

Table 3.1 Classification of Visible Damage (Burland, 1997)

Category	Class of damage	Description of damage[a]	Approximate width of cracks[b] mm
0	Negligible	Hairline cracks.	< 0.1
1	Very Slight	Fine cracks which can easily be treated during normal decoration. Perhaps isolated slight fracturing in building. Cracks in external brickwork visible on close inspection.	< 1
2	Slight	Cracks easily filled. Redecoration probably required. Several slight fractures inside of building. Cracks are visible externally and some repointing may be required externally to ensure weathertightness. Doors and windows may stick slightly.	< 5
3	Moderate	The cracks require some opening up and can be patched by a mason. Recurrent cracks can be masked by suitable linings. Repointing of external brickwork and possibly a small amount of brickwork to be replaced. Doors and windows sticking. Service pipes may fracture. Weathertightness often impaired.	5 to 15 or several cracks > 3
4	Severe	Extensive repair involving breaking out and replacing sections of walls, especially over doors and windows. Window and door frames distorted, floor sloping noticeably. Walls leaning or bulging noticeably, some loss of bearing in beams. Services pipes disrupted.	15 to 25 also depends on number of cracks
5	Very Severe	This requires a major repair job involving partial or complete rebuilding. Beams lose bearing, walls lean badly and require shoring. Windows broken with distortion. Danger of instability.	usually > 25 but depends on number of cracks

[a]Location of damage in the building or structure must be considered when classifying degree of damage.

[b]Crack width is only one aspect of damage and should not be used alone as a direct measure of it.

Bjerrum (1963) proposed two charts showing the relationship between maximum differential settlement and maximum settlement of a building in clay and another one in sand as shown in Figure 3.8. These charts exclude cases with load intensity or thickness of the compressible strata varied at different parts of the building. Figure 3.8a shows that the maximum differential settlement of a rigid structure is smaller than that of a flexible structure in clay. The figure also shows that the maximum settlement on clay is more than that in sand.

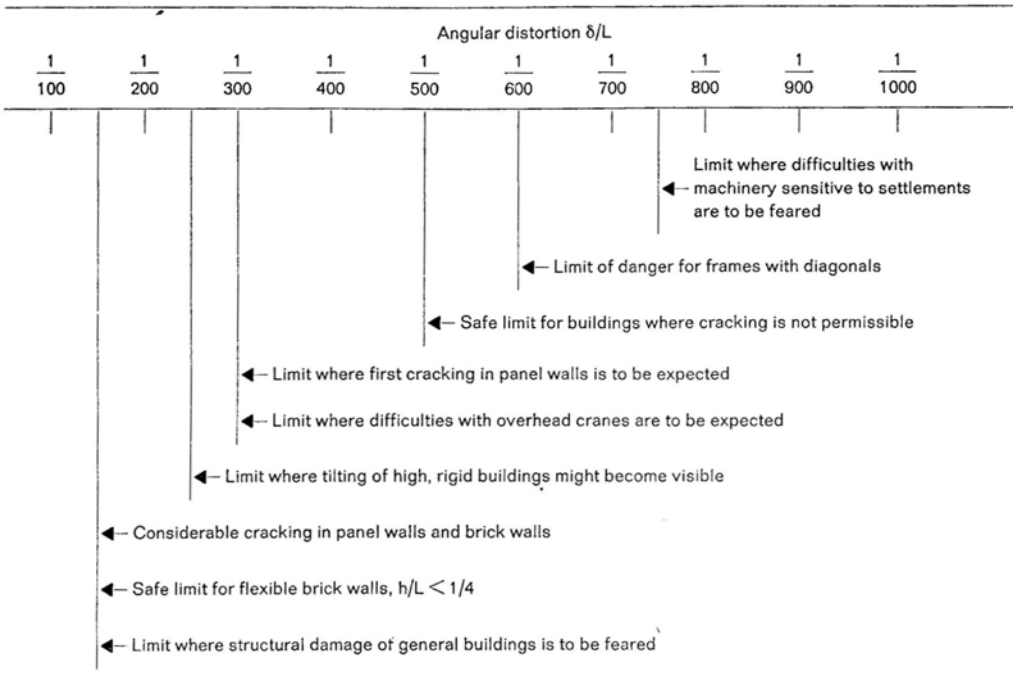

Figure 3.7 Damage Criteria (Bjerrum, 1963)

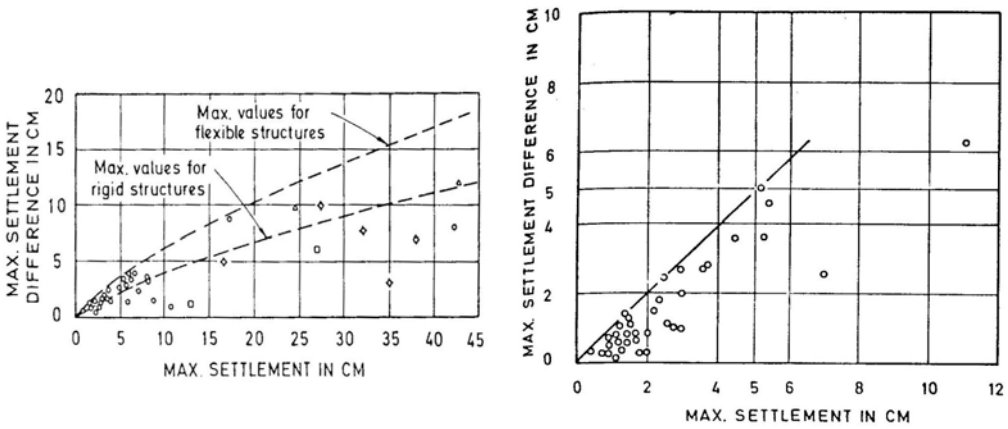

(a) Buildings on Clay (b) Buildings on Sand

Figure 3.8 Max. Settlement versus Max. Settlement Difference (Bjerrum, 1963)

Burland et al. (1977) plotted similar problems for frame buildings on isolated foundation and building with raft foundation on clayey soils as shown in Figure 3.9. Bjerrum's upper limit curves for flexible and rigid structures were also incorporated. Several conclusions were reported as follows:

1. The ratio between maximum differential settlement and the maximum settlement is less for buildings founded on a stiff overlying layer than for those founded directly on clay.
2. Bjerrum's upper limit curves for flexible and rigid structures appear to be confirmed for undamaged buildings. It is also interesting to note that many of the results for damaged buildings lie above the curve.
3. Some cases of slight damage to buildings on isolated foundations are reported for differential settlements in excess of 50 mm and total settlements in excess of 150 mm.
4. In contrast, damage to buildings on rafts has not been reported for differential settlements and total settlements less than 125 mm and 250 mm, respectively.
5. It is very clear from Figure 3.9b, that many buildings on rafts have undergone substantial total settlements with no reported damage.

If the settlement occurs gradually with time, the building may be able to adjust to it. Study done by Grant et al. (1974) supports this hypothesis. They studied the performance of 66 buildings. Twenty-six buildings that underwent slow settlement (more than 2 years) indicated higher angular distortion before cracking as compare to the others which underwent fast settlement (less than 2 years). However, the increase of angular distortion is not significant. Buildings, which underwent slow settlement, could sustain angular distortion between 1/250 and 1/200 whereas the others were able to sustain an angular distortion of 1/300.

In terms of cracking, there is a difference between a building that settles under its own weight and one that is subjected to excavation-induced damage. In the first case, there are no cracks prior to settlement. Therefore, the damage limits discussed earlier can be applied directly. However, in the second case, there may be pre-existing strain in the building prior to excavation. Therefore, the damage limits for these two cases are quite different. Unfortunately, the pre-existing strain in a building is not known in most cases. Hence, it is very difficult to set the damage limit for buildings located next to an excavation.

3.5 The Mechanism of Cracking of the Building

The angular distortion is an important index. However, there are other important indices, such as the ratio of length and width of the building and the limiting tensile strain before cracking (Polshin and Tokar, 1953). These two important indices were used by Burland and Wroth (1974) to give a fundamental understanding in the mechanism of cracking of building. The building was modeled as a simple high beam as shown in Figure 3.10.

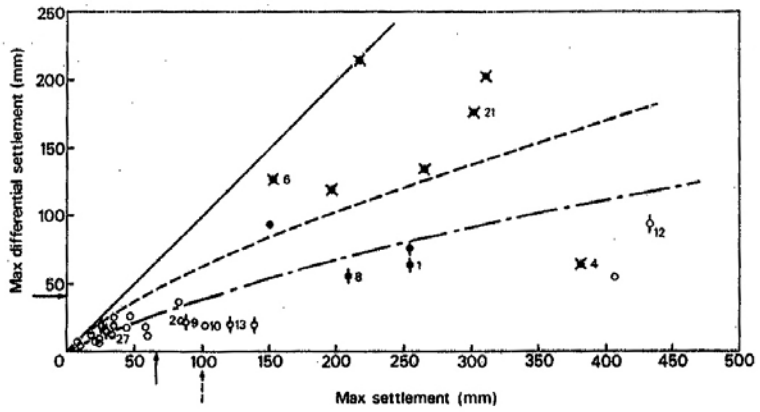

(a) Frame Buildings on Isolated Foundations

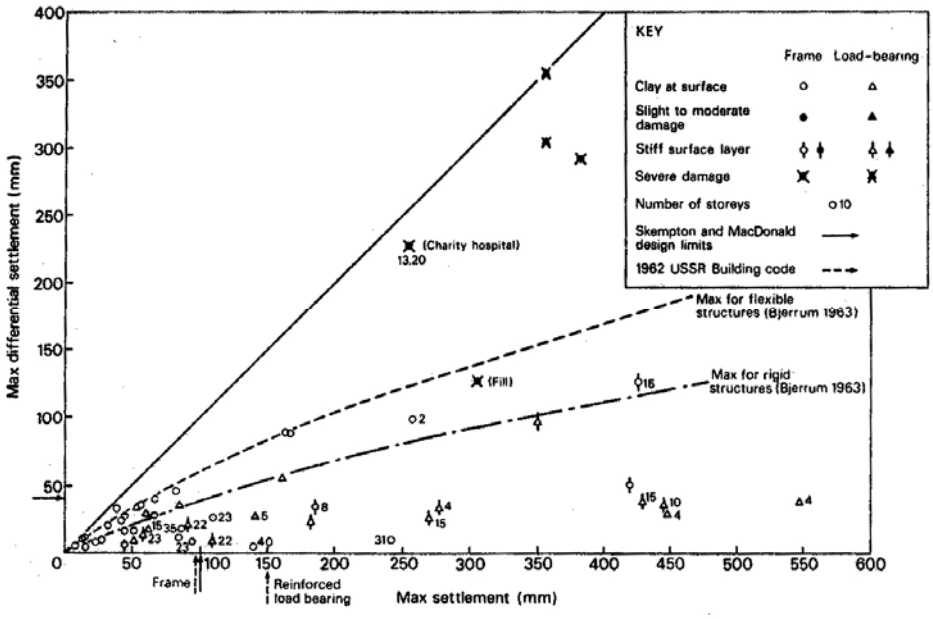

(b) Buildings on Raft Foundations

Figure 3.9 Performance of Buildings on Clayey Soils (Burland et al., 1977)

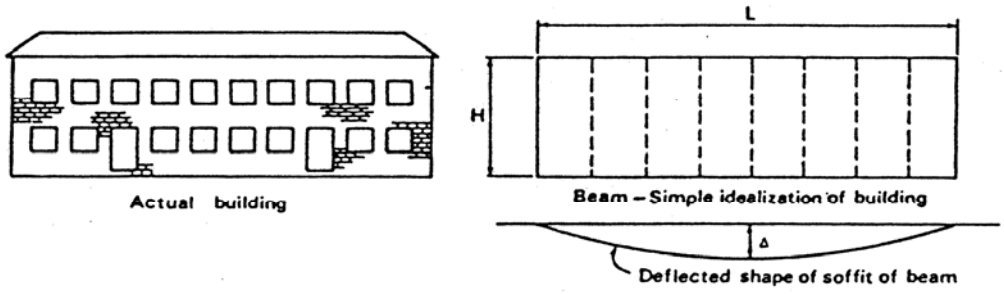

Figure 3.10 Rectangular Beam Analogy for Building (Burland and Wroth, 1974)

Using an elastic deflection theory for rectangular beam from Timoshenko (1957), Burland and Wroth expressed the relative deflection (Δ/L) in terms of the ratio of length to height of the building (L/H) and maximum direct tensile strain (ε_b) or diagonal tensile strain (ε_d). Equation of total deflection of a beam due to moment and shear generated by a point load at the middle of a beam as proposed by Timoshenko is shown in Equation 3.2.

$$\Delta = \frac{PL^3}{48EI}\left(1 + \frac{18I}{L^2 H}\frac{E}{G}\right) \tag{3.2}$$

Using a ratio of elastic to shear modulus (E/G) equals to 2.6 and a neutral axis at the middle of a beam, a relationship between Δ/L, L/H, and ε_b or ε_d can be derived as shown in Equations 3.3 and 3.4. Both equations are plotted in Figure 3.11. On the other hand, Equation 3.5 shows a relationship between Δ/L, L/H, and ε_b with the neutral axis at the bottom of a beam.

$$\frac{\Delta}{L} = \left(0.167\frac{L}{H} + 0.65\frac{H}{L}\right)\varepsilon_{b(\max)} \tag{3.3}$$

$$\frac{\Delta}{L} = \left(0.25\frac{L^2}{H^2} + 1\right)\varepsilon_{d(\max)} \tag{3.4}$$

$$\frac{\Delta}{L} = \left(0.083\frac{L}{H} + 1.3\frac{H}{L}\right)\varepsilon_{b(\max)} \tag{3.5}$$

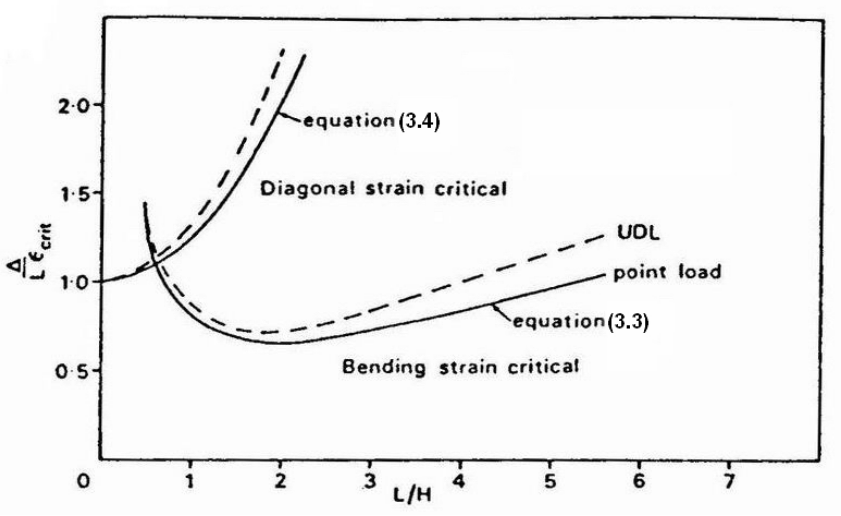

Figure 3.11 Relationship between L/H and $\Delta/L\varepsilon_{crit}$ for Rectangular Beam (Burland and Wroth, 1974)

Four important conclusions can be derived from Figure 3.11. They are:

1. The deflection ratio is affected by the L/H ratio of the beam and the critical tensile strain, ε_{crit}.
2. The limit value of Δ/L is proportional to the ε_{crit} for a given value of L/H.
3. Structures with a lower value of L/H are sensitive to diagonal crack if the diagonal tensile strain is greater than the critical value.
4. Lateral crack will develop for structures with high value of L/H if the direct tensile strain is exceeded.

Some structures may be very stiff in shear but weak in longitudinal stiffness, such as precast concrete units held together with dowels. Others may have little shear stiffness, such as walls with many openings. By expressing the longitudinal stiffness as an elastic modulus, E, and the shear stiffness as a shear modulus, G, Burland and Wroth (1974) showed the effect of E/G to Δ/L in Figure 3.12.

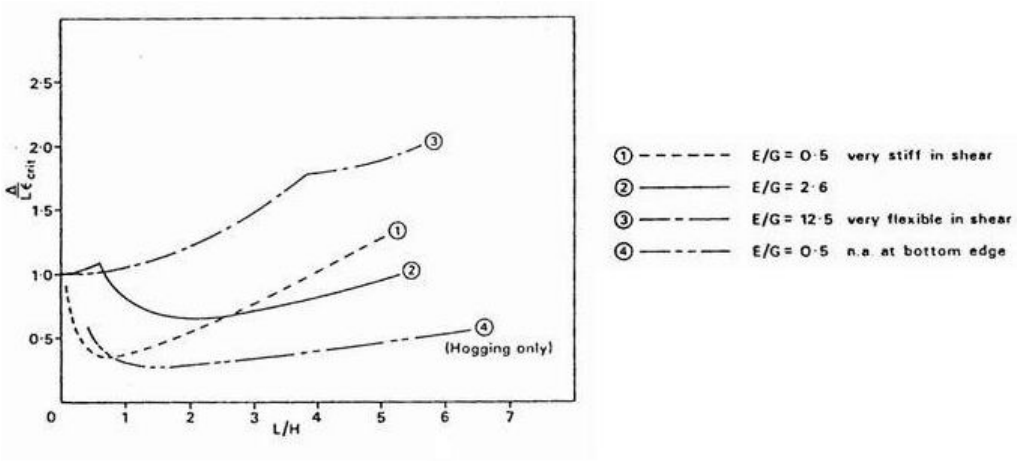

Figure 3.12 Effect of E/G between $\Delta/L\varepsilon_{crit}$ and L/H for Rectangular Beam

Figure 3.12 shows that for framed structures and reinforced load bearing walls, which are relatively flexible in shear and stiff in direct tension (high E/G), the diagonal strain will be more critical (curve 3). For unreinforced masonry walls, bending or direct tensile strain can be critical since these structures have a relatively low tensile resistance as reflected by curve 2. Since bending can be caused by sagging and hogging deflection, Burland and Wroth (1974) proposed two different criteria. The tolerable deflection ratio is smaller when those structures deflect in hogging mode as compared to sagging mode. It is expressed by curve 4.

Another important parameter on building damage is horizontal strain, especially around mining, tunneling, and open excavation. Studies conducted by Boscardin and Cording (1989) showed that the lateral strain should be considered in assessing building damage since increasing lateral strains will decrease the tolerance of differential settlement.

3.6 Existing Building Damage Prediction

Five building damage prediction methods will be present here. They are proposed by Burland and Wroth (1974), Rankin (1988), Boscardin and Cording (1989), Boone (1996), and Finno et al. (2005).

3.6.1 Building Damage Prediction from Burland and Wroth (1974)

Burland and Wroth (1974) published three charts for prediction of building damage potential as shown in Figures 3.13 to 3.15. One chart is for frame buildings, the other two are for load bearing walls in sagging and hogging deflection mode, respectively. It is based on L/H ratio and deflection ratio according to Equations 3.3 to 3.5. The critical tensile strain (ε_b and ε_d) used in the chart is 0.075%. It is a strain that most likely causes visible cracks in the brick wall. It is not a strain that causes loss of tensile strength which occurs at a much smaller value. Therefore, the line in the charts represents an area where visible cracks on the wall will most likely occur.

Figure 3.13 shows a chart for building damage prediction for frame buildings. A frame building tends to shear rather than to bend as shown in Figure 3.3. Because of this, Burland and Wroth used Equation 3.4 to predict building damage for the frame building. Figure 3.9 shows that as the ratio of length to height of the building increases, the relative deflection (Δ/L) also increases which means it is more tolerable with ground settlement.

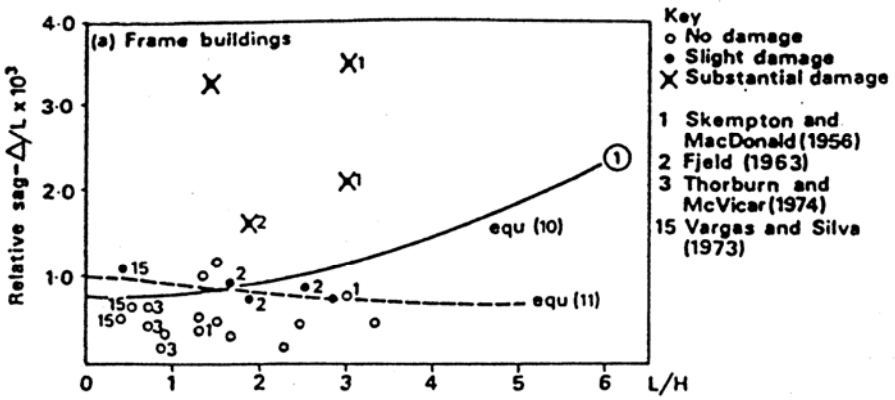

Figure 3.13 Building Damage Prediction for Frame Buildings
(Burland and Wroth, 1974)

Figures 3.14 and 3.15 are charts for building damage prediction for load bearing walls. Figure 3.14 is for walls which deflect in sagging mode and Figure 3.15 is for hogging mode. Load bearing walls, which deflect in hogging mode, are more critical than those in sagging mode. These figures show that for the same L/H, a

load bearing wall that deflects in sagging mode has a larger relative deflection before cracks started to occur as shown in Figure 3.15.

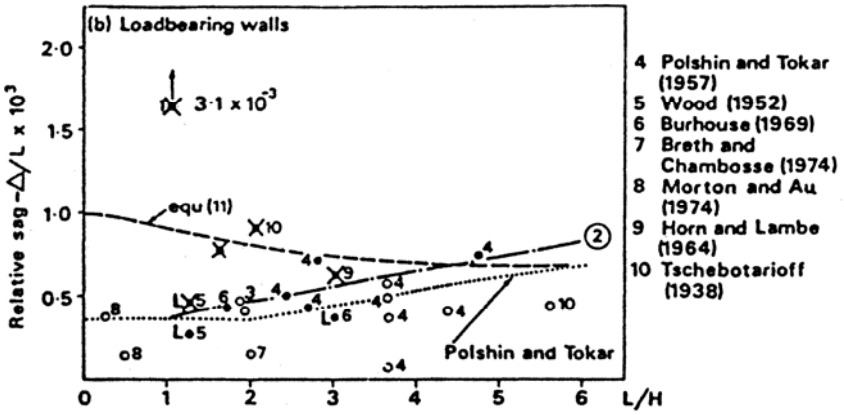

Figure 3.14 Building Damage Prediction for Load Bearing Walls in Sagging Deflection (Burland and Wroth, 1974)

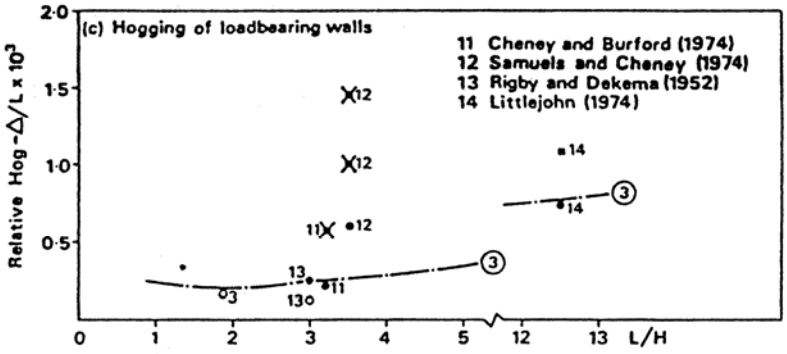

Figure 3.15 Building Damage Prediction Chart for Load Bearing Walls in Hogging Deflection (Burland and Wroth, 1974)

3.6.2 Building Damage Prediction from Rankin (1988)

Rankin (1988) proposed four risk categories based on the maximum slope and maximum settlement of building as shown in Table 3.2. The application of this method requires experience and judgment because of insufficient case records. This approach is very simple and can be used as a preliminary assessment of building damage without complex and unnecessary calculations.

Table 3.2 Building Damage Prediction (Rankin, 1988)

Risk Category	Maximum Slope of Building	Maximum Settlement of Building (mm)	Description of Risk
1.	Less than 1/500	Less than 10	*Negligible*: superficial damage unlikely.
2.	1/500 to 1/200	10 to 50	*Slight*: Possible superficial damage which is unlikely to have structural significance.
3.	1/200 to 1/50	50 to 75	*Moderate*: Expected superficial damage and possible structural damage to buildings, possible damage to relatively rigid pipelines
4.	Greater than 1/50	Greater than 75	*High*: Expected structural damage to buildings. Expected damage to rigid pipelines, possible damage to other pipelines.

3.6.3 Building Damage Prediction from Boscardin and Cording (1989)

The method by Boscardin and Cording (1989) includes the effect of horizontal strain on building damage. They proposed a chart based on two parameters, angular distortion (β) and horizontal strain (ε_h) as shown in Figure 3.16. The curve is based on deep beam analysis where L/H equals to one. Therefore, it cannot account for the effect of building dimension which was considered important by Burland and Wroth (1974). Burland (1995) commented that the criterion for moderate to severe damage in this chart should be considered as moderate only because none of the cases exhibited severe damage for within that range.

In predicting the horizontal strain, Geddes (1991) suggested that it is not appropriate to assume similar horizontal strain between ground and structure. The horizontal strain is negligible for a rigid structure that remains intact under the induced load regardless of the ground strain. Therefore, the horizontal strain in the structure should be used rather than that of the ground.

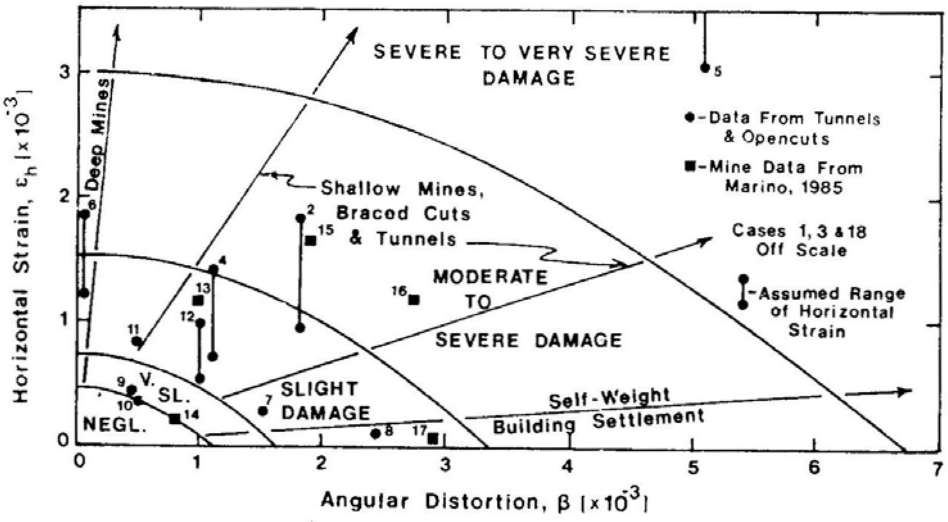

Figure 3.16 Building Damage Prediction Chart (Boscardin and Cording, 1989)

3.6.4 Building Damage Prediction from Boone (1996)

Boone (1996) proposed a chart to predict building damage for both load bearing wall and frame structures as shown in Figure 3.17. It was first proposed in 1996 which then modified in 1999 (Boone et al., 1999). It is assumed that the building will deform as a simply supported deep beam that is uniformly loaded. It considers the ground movement profile, location of the building, building dimension, bending and shear stiffness of building, and degree of slip between the ground and the foundation. Some calculations (Table 3.3) are required before using the chart. This method gives an estimate of the cumulative crack width due to cumulative maximum tensile strain along top of wall (ε_t) and principal tensile strain (ε_p).

3.6.5 Building Damage Prediction from Finno et al. (2005)

Finno et al. (2005) tried to improve Equations 3.3 to 3.5 developed by Burland and Wroth (1974). A building is simplified as a rectangular beam with unit thickness, the moment of inertia (I) depends only on the building height (H). This method also assumed that the ratio of E/G is equal to 2.6. In reality, a building consists of floors and walls. Both of them affect the building deformation. Their contribution to the building stiffness should be calculated separately. In order to take into account the

effect of floor and beam, a laminate beam was proposed. It assumed that floors restrain bending deformations and walls resist shear deformations.

Table 3.3 Equations for Estimation Building Damage

Parameter	Equations
Settlement, S, and horizontal movement, h	$S = S_{max}[(D_{max} - D)/D_{max}]^2$; $h = h_{max}[(D_{max} - D)/D_{max}]^2$
Slope, g	$g = 2S_{max}(D_{max} - D)/(D_{max})^2$
Rigid-body tilt, t	$t = (S_1 - S_2)/L$
Rotation slope, v'	$v' \approx g_1 - t$
Maximum curve deflection, v_{max}	$v_{max} = v'L/4$
Proportion of deformation due to moment, $v'_{(M)}$, $v_{max(M)}$	$v_{max(M)} = v_{max}/(1 + 2.88H^2/L^2)$; $v'_{(M)} = v'/(1 + 2.88H^2/L^2)$
Proportion of deformation due to shear, $v'_{(V)}$, $v_{max(V)}$	$v_{max(V)} = v_{max} - v_{max(M)}$; $v'_{(V)} = v' - v'_{(M)}$
Radius of bending, R_M	$R_M = L/[2 \sin(\tan^{-1}v'_{(M)})]$
Bending strain at top of wall, ε_M	$\varepsilon_M = H/(2R_M)$
Lateral extension strain, ε_{le}	$\varepsilon_{le} = (h_1 - h_2)/L$
Shear strain, γ	$\gamma = \tan^{-1}v'_{(V)}$
Cumulative maximum tensile strain along top of wall, ε_t	$\varepsilon_t = \varepsilon_M + \varepsilon_{le}$
Principal tensile strain, ε_p	$\varepsilon_p = 0.25\varepsilon_t + [(0.25\varepsilon_t)^2 + (0.5\gamma)^2]^{1/2}$
Cumulative tension crack width, C_t	$C_t = \varepsilon_t L$
Cumulative diagonal crack width, C_p	$C_p = \varepsilon_p[(0.5L)^2 + H^2]^{1/2}$

Definitions: S_{max} = Maximum settlement at excavation edge
D = Distance from excavation edge
D_{max} = Distance to point where settlement - lateral movement is zero
L = Original length of building
H = Depth of excavation and retaining system

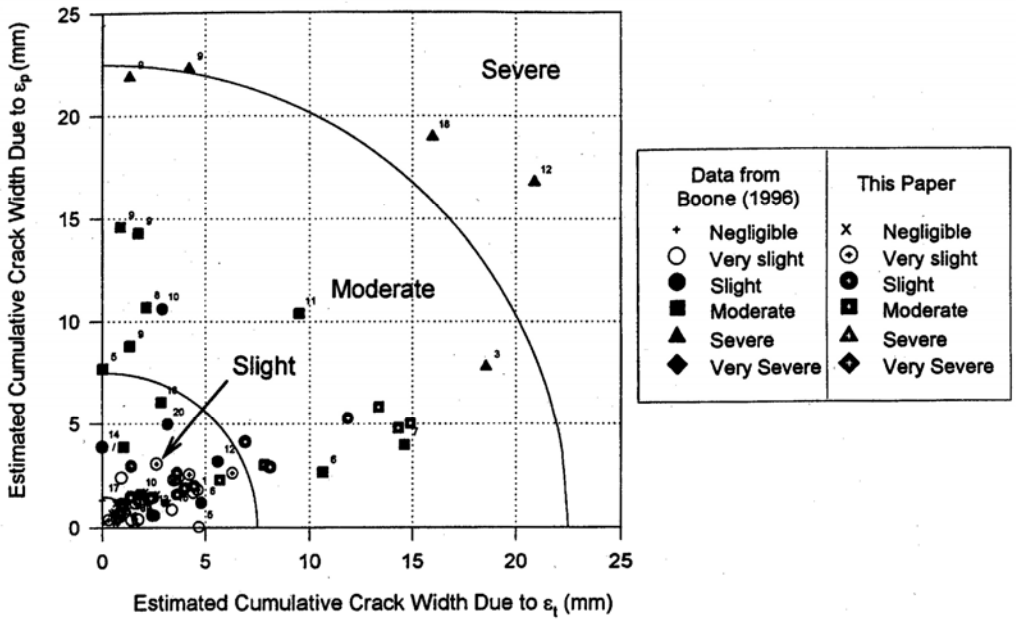

Figure 3.17 Building Damage Prediction Chart (Boone et al., 1999)

The method can be used in frame and load bearing wall structures. One case study at the Frances Xavier Warde School in Chicago was used to verify the method. The prediction was able to predict the onset of cracks in that school. Even though this method is more advanced, it is relatively complicated. It needs many parameters which are difficult to be obtained.

Several steps are required to use this method.

1. Predict a distribution of ground movements as shown in Figure 3.18.

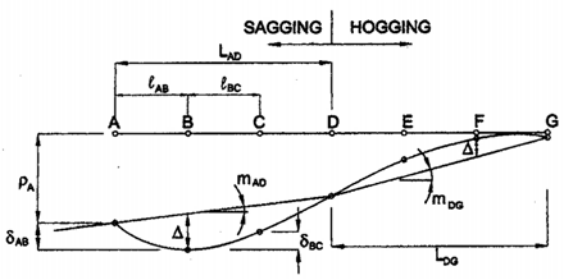

Figure 3.18 Distribution of Ground Movements (Finno et al., 2005)

Definitions:

ρ_i : settlement at any point i

δ_{ij} : differential settlement between point i and j

l_{ij} : distance between point i and j

δ_{ij}/l_{ij} : distortion between point i and j

L : length of a particular mode of deformation either sagging or hogging

m $= \delta_{ij}/L_{ij}$: average slope at particular mode of deformation

Δ : maximum deviation from the average slope at particular mode of deformation

Δ/L : deflection ratio

2. Locate the affected structure relative to the expected ground movements. If needed, divide the settlement profile at each wall line to be analyzed into sagging and hogging zones at inflection, tangent and end of structure points. Figure 3.19 shows the typical modes of deformation where m, ω, and γ_{add} are defined as slope, rigid body rotation, and additional shearing strain, respectively.

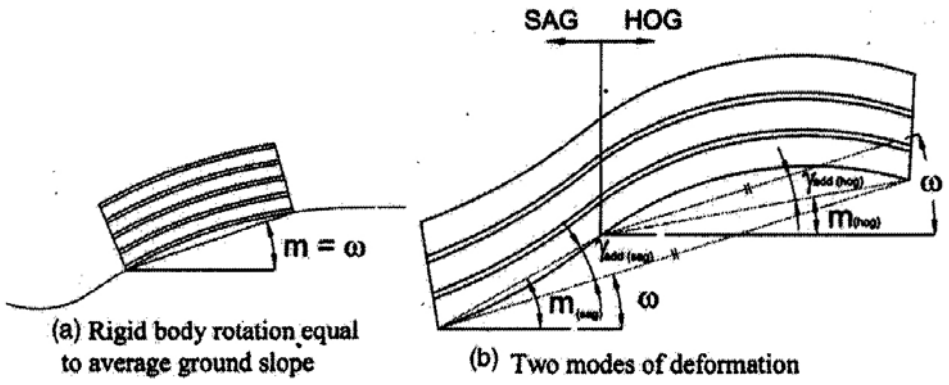

Figure 3.19 Typical Modes of Deformation (Finno et al., 2005)

3. Compute the slope ($m = \delta_{ij}/L_{ij}$) for each mode of deformation.
4. Estimate the rigid body rotation (ω) of the section being analyzed. For many practical cases, one can use the slope of the entire building from one extreme end to the other.
5. Compute the additional shearing strain in each mode of deformation by using $\gamma_{add} = m - \omega$
6. Define the geometry and structural properties of the pertinent section of building. Figure 3.20 shows a laminate beam model representing a structure.

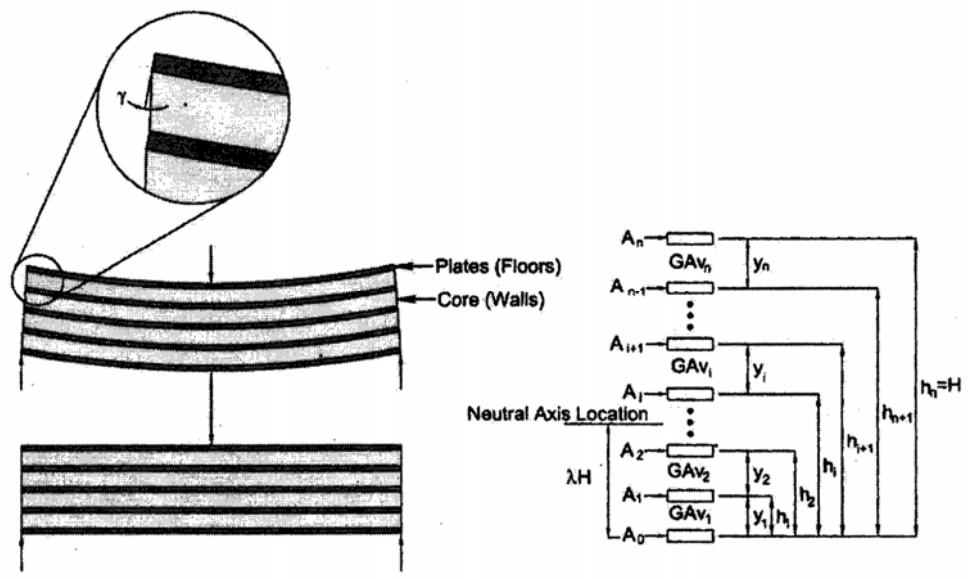

Figure 3.20 Laminate Beam Representation of Structure (Finno et al., 2005)

Definitions:

A_i : area of floor slab contributing to bending resistance

Av_i : shear area of wall i

a : percentage of open area in wall

E : Young's modulus of building component

E_c : Young's modulus of the column

I_c : moment of inertia of the column in the plane of wall

y_i : story height

G : shear modulus of building component

H : building height

h_i : distance from bottom of building to floor i

I : moment of inertia of laminate beam model

γ_i : shear strain in story i of laminate beam model

λ : distance from bottom of building to its neutral axis divided by H

V_i : shear in each story

V : total shear in the laminate beam

$$\lambda H = \frac{\sum_{i=0}^{n} A_i H_i}{\sum_{i=0}^{n} A_i} \tag{3.6}$$

$$I = \sum_{i=0}^{n} A_i \left(h_i - \lambda H\right)^2 \tag{3.7}$$

$$\frac{V_i}{V} = \frac{y_i}{I} \sum_{j=i}^{n} A_j \left(\lambda H - h_j\right) \tag{3.8}$$

$$\left(GA_v\right)_{column} = \frac{12 E_c I_c}{y_i^2} \tag{3.9}$$

$$\left(GA_v\right)_i = \Sigma\left[\left(GA_v\right)_{column} + \left(GA_v\right)_{wall}\left(1-a\right)\right] \tag{3.10}$$

$$\overline{GA_v} = \frac{1}{\sum_{i=1}^{n} \frac{y_i}{H} \frac{V_i}{V} \frac{1}{\left(GA_v\right)_i}} \tag{3.11}$$

7. Choose the appropriate critical strain for a given material and assumed failure mode from Boone (1996), ACI (1999, 2000), or other methods.
8. Use the bending stiffness and shear stiffness obtained by the laminate beam method and compute the value of limiting Δ/L that causes cracking for various failure modes from Equations 3.12 to 3.14. If the deflection ratios from the predicted settlements are greater than the limiting deflection ratios, cracking is likely. Parameters $\varepsilon_{b(top)}$ and $\varepsilon_{b(bottom)}$ are defined as maximum bending strain at the top and bottom of the laminated beam, respectively.

$$\frac{\Delta}{L} = \left(\frac{L}{12(1-\lambda)H} + \frac{EI}{\overline{GA_v} L(1-\lambda)H} \right) \varepsilon_{b(top)} \tag{3.12}$$

$$\frac{\Delta}{L} = \left(\frac{L}{12\lambda H} + \frac{EI}{\overline{GA_v} L\lambda H} \right) \varepsilon_{b(bottom)} \tag{3.13}$$

$$\frac{\Delta}{L} = \left(\frac{L^2 (GA_v)_i}{24EI \dfrac{V_i}{V}} + \frac{(GA_v)_i}{2\dfrac{V_i}{V}\overline{GA_v}} \right) \left(\gamma_{crict_i} - |m-\omega| \right) \tag{3.14}$$

3.7 Effect of Grade Beam on Horizontal Strain for Frame Structures

Boscardin (1980) did a series of finite element analysis to study the effect of grade beam on horizontal strain for frame structures. The soil is elastic with Young's modulus equal to 34.5 MPa and a Poisson's ratio of 0.3. The dimension of one frame is 7.3 m by 3.8 m. The spacing of each column is 7.3 m. The concrete stiffness for column and beam is 2.07×10^7 kPa. The frame structure consists of several stories and bays.

Figure 3.21 shows the effect of a number of stories on horizontal strain with and without grade beams. The GB value is the stiffness of grade beam relative to the stiffness of the first-story interior columns. It shows that the number of stories, whether the frame has grade beam or not, does not influence the horizontal strain. However, the effect of grade beams is very prominent. Without grade beam, the horizontal strain is about 1×10^{-3}. The presence of grade beam reduces the horizontal

strain to about $2.5x10^{-4}$. The higher the grade beam stiffness, the smaller is the horizontal strain. This is because a stiff grade beam will prevent the columns from separating. According to the building damage prediction chart by Boscardin and Cording (1989) as shown in Figure 3.16, this value is relatively very small. Therefore, it can be safely ignored.

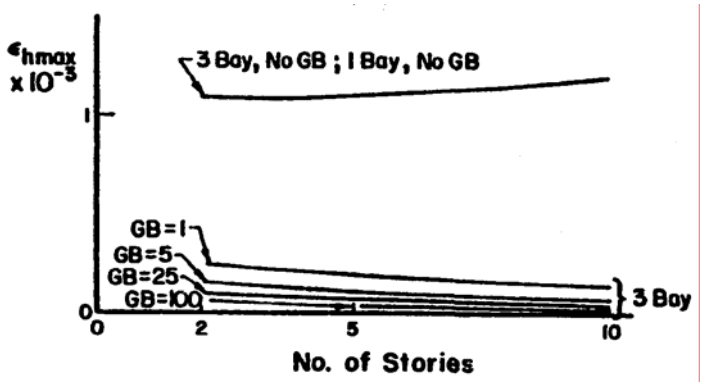

Figure 3.21 Effect of Number of Stories on Horizontal Strain (Boscardin, 1980)

Figure 3.22 shows the effect of number of bays on horizontal strain with and without grade beam. It shows that the number of bays does not affect the horizontal strain of the frame. The presence of grade beam highly influences the horizontal strain. In this case, with the grade beam stiffness equals to 5 times the column stiffness, the value of horizontal strain is only about $1.5x10^{-4}$ which can be regarded as negligible.

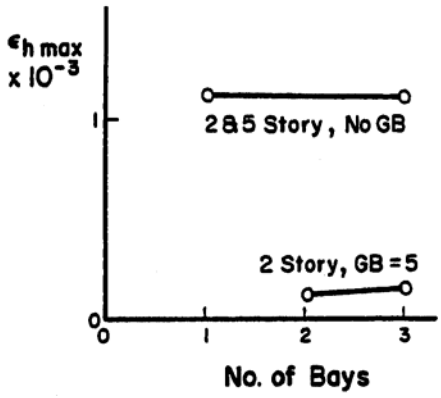

Figure 3.22 Effect of Number of Bays on Horizontal Strain (Boscardin, 1980)

Figure 3.23 shows the effect of grade beam stiffness on horizontal strain is negligible. The horizontal strains with grade beam stiffness equals to 1 or 100 are essentially same. It is also not affected by the number of stories. This result is very useful in practice for engineers who need to predict the damage of frames due to deep excavation. This study shows that horizontal strain is negligible as long as the grade beams are present. The exact dimensions of grade beam are not crucial.

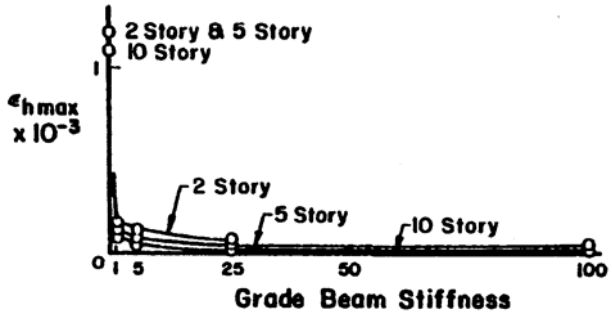

Figure 3.23 Effect of Grade Beam Stiffness on Horizontal Strain (Boscardin, 1980)

In modern structures, most of the buildings are well-reinforced laterally by stiff floor system. Therefore, it essentially eliminates lateral movements of the column due to lateral ground movements induced by deep excavation (Finno and Bryson, 2002). In other word, the effect of horizontal strain can be safely ignored except for some old historical buildings where grade beams do not exist.

3.8 Existing Procedure in Assessing Building Damage

Burland (1997) suggested three steps to assess the risk of building damage. They are preliminary assessment, second assessment, and detailed evaluation.

Step 1: Preliminary Assessment

The first step is to estimate or predict the greenfield settlement contours adjacent to an excavation or along the tunnel alignment. The maximum slope and maximum settlement at the location of each building are compared with the limiting values proposed by Rankin (1988). The limiting value for maximum slope, θ, is 1/500 and maximum settlement is 10 mm. If the maximum values are less than the limiting

values, the damage is likely to be negligible and the building is considered safe. For sensitive buildings, for example building with many glasses, smaller limiting values can be adopted.

Step 2: Second Assessment

All buildings exceeding the safe limits from first assessment are reassessed in this step. Any chart proposed by Burland and Wroth (1974), Boscardin and Cording (1989), Boone (1996), or method by Finno et al. (2005) can be used. The accuracy of the chart solution is highly dependent on the accuracy of greenfield prediction.

Frischmann, et al. (1994) reveals that the actual surface settlements with the presence of buildings on the site are radically different from those with greenfield settlement where no buildings were present. Burd et al. (2000) studied a numerical analysis for the construction of tunneling with a masonry building above it. It is interesting to note that the greenfield and building settlements are very different as shown in Figure 3.24.

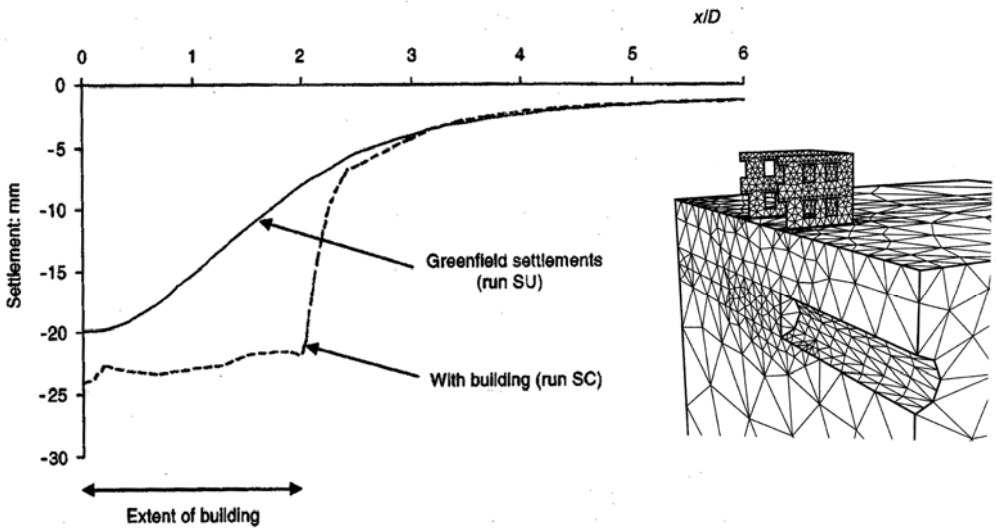

Figure 3.24 Comparison of Greenfield and Building Settlement (Burd et al., 2000)

Step 3: Detailed Evaluation

If Step 2 indicates that the damage category is moderate or greater, a detailed evaluation should be conducted for this particular building. Other factors, such as

structural joint, type of foundation, building position, structural stiffness, rate of loading, and previous deformation history should all be taken into consideration. Protective measures should be taken where necessary.

3.9 Protective Measures

Burland (1997) categorizes protective measures for buildings into six groups.

1. *Strengthening the ground* to increase the stiffness below foundation levels by grout injection or ground freezing.
2. *Strengthening of the building* to accommodate building deformations by using temporary or permanent propping or tie rods.
3. *Structural jacking to compensate settlement*, such as that used in Mansion house damage due to the extension work of Docklands Light Railway (Frischmann, et al., 1994).
4. *Underpinning* to minimizing differential movements. According to Cording et al. (1978), underpinning is not as useful in eliminating architectural damage for the following reasons:
    a. The disturbance of the structure due to underpinning can result in differential movements on the order of 6 to 19 mm which can result in cracking of the structure.
    b. Underpinning piles may be dragged down as the soil settles during excavation.
    c. Vertical underpinning piles will not prevent the lateral displacements that are typically of the same order as the settlements in a soil mass. It can cause architectural damage, particularly to a structure such as a brick bearing wall that is not laterally tied together.
5. *Installation of a physical barrier between the building foundation and the tunnel* to modify the shape of settlement trough and minimize ground displacements adjacent to and beneath the building.
6. *Compensation grouting* between the tunnel and building foundations by using controlled injection of grout to compensate for ground loss which was used successfully in Victory Arch and Waterloo and City Line tunnels (Harris et al., 1994).

Modifying the construction scheme rather than strengthening the building can also prevent damage. Chan and Yap (1992) reported a case of diaphragm wall construction which is very close to a masonry building. The 100 year old building is 4 stories high and is supported on shallow foundation. During the preliminary observations, it was indicated that the settlement of adjacent building arising from wall construction would be unacceptable. Therefore, special measures were adopted in the wall construction. It was found out that by raising the slurry level, limiting the panel length of diaphragm wall, rearranging the panel layout, and reducing the construction time could successfully prevent the development of any visible signs of cracking. The maximum building settlement was only 7.2 mm.

3.10 Effect of Wall Deflection on Foundation

Case studies from the MRT North East Line in Singapore provide a good opportunity to develop a correlation between wall movement and building settlement. The distance between the buildings and the excavation wall was about 8 m. Seven cases in Hong Kong during the construction of the mass rapid transit at the Argyle Station and the Wong Tai Sin Station (Morton et al., 1980) provide another set of valuable data. The distance between buildings and the nearest excavation wall was only 3.7 m. Burland and Hancock (1977) also provided data about building settlement due to excavation in London during the construction of the underground car park at the House of Commons in London. In that case, Westminster Hall, a 14th century building supported on shallow foundation, settled 22 mm due to 23 mm of wall deflection. The distance was about 5 m. All data were plotted in Figure 3.25 which shows the relationship between wall deflection and building settlement. The figure also shows that the amount of building settlement depends also on the foundation type. Buildings supported on piles experienced relatively small settlement. In most cases, the settlement is only 5 mm or less except for one case in Hong Kong where the settlement was 20 mm. The shop houses with unknown foundation support, settled up to 130 mm. They are likely to be supported on shallow foundation. The amount of settlement increases with increasing wall movement.

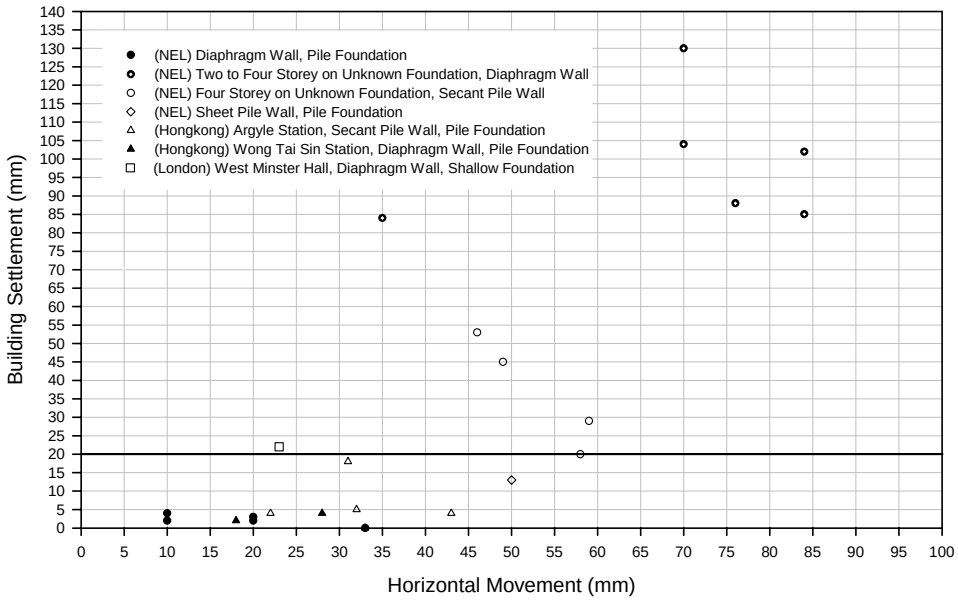

Figure 3.25 Relationship between Building Settlement and Wall Deflection

3.11 Summary

The ability to predict and ensure the safety of structures or utilities adjacent to the excavation or tunneling is very important. The simplest method is to use greenfield settlement to predict building damage. However, the limitation of this method is obvious. The building settlement can be very different from the greenfield settlement depending on the stiffness of the building. Burland and Wroth (1974) has laid down the basic understanding of building damage. This basic understanding has formed a framework for further research carried out by several researchers (Boscardin and Cording, 1989; Boone, 1996; and Finno et al., 2005). New charts and procedures have been proposed by these researchers. The assumptions and limitations of these methods have been discussed.

In assessing building damage, the effect of tilt and the presence of grade beams should be consider especially for buildings involving frame structure. It is unlikely that a frame structure will tilt as a single unit. The distortion will induce stresses and strains in the frames and they should be considered in the calculation. On the other hand, the presence of grade beams reduces horizontal strain to a minimum as shown by the finite element study by Boscardin (1980).

CHAPTER 4
ESTIMATION OF MOHR-COULOMB AND CAM CLAY PARAMETERS FOR EXCAVATION ANALYSIS

4.1 Introduction

The greenfield settlement has been used to assess building damage prior to commencement of excavation (Burland, 1997). The reliability of this assessment depends largely on how well the greenfield settlement can be predicted by the finite element method which in turn depends on the accuracy of soil model used and the corresponding soil parameters.

Mohr-Coulomb model is commonly used in practice in Singapore because of its simplicity. Unfortunately, poor understanding of its limitations has led to many failures in Singapore including the Nicoll Highway collapse in 2004. Theoretically, there are two ways to conduct an undrained analysis using Mohr-Coulomb model. The first option is to adopt the total stress approach using total stress parameters (c_u, ϕ_u, E_u, and $\nu = 0.495$). The second option is to conduct an effective stress analysis using effective stress parameters (c', ϕ', $E' = 0.9E_u$ and $\nu' = 0.33$). For undrained analysis involving soft clay, the first option can produce reliable results whereas the second option may produce erroneous results (Wong, 2003 & 2004).

Major shortcomings of Option 2 using the effective stress parameters in Mohr-Coulomb to model undrained condition in soft clay are illustrated in Figures 4.1 to 4.2. Figure 4.1 shows that the model will over-estimate the shear strength and under-predicts the excess pore pressure when p' equals to A. Other limitations are the nonlinear behaviour prior to failure and the stress dependency behaviour under drained behaviour are not captured as shown in Figure 4.2.

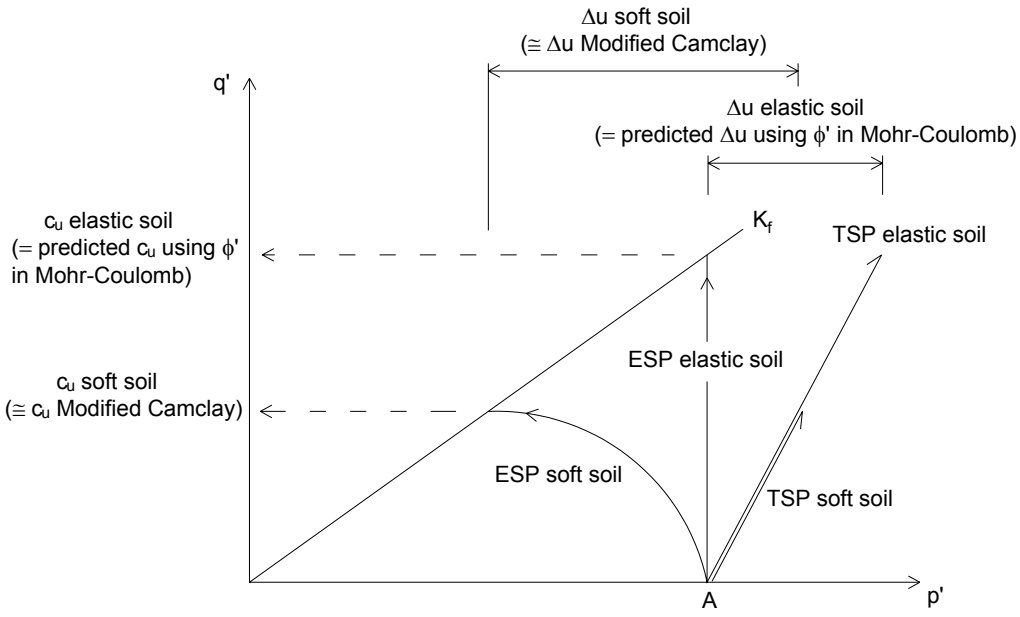

Figure 4.1 Modified Cam Clay and Mohr-Coulomb Model with Effective Stress Parameters

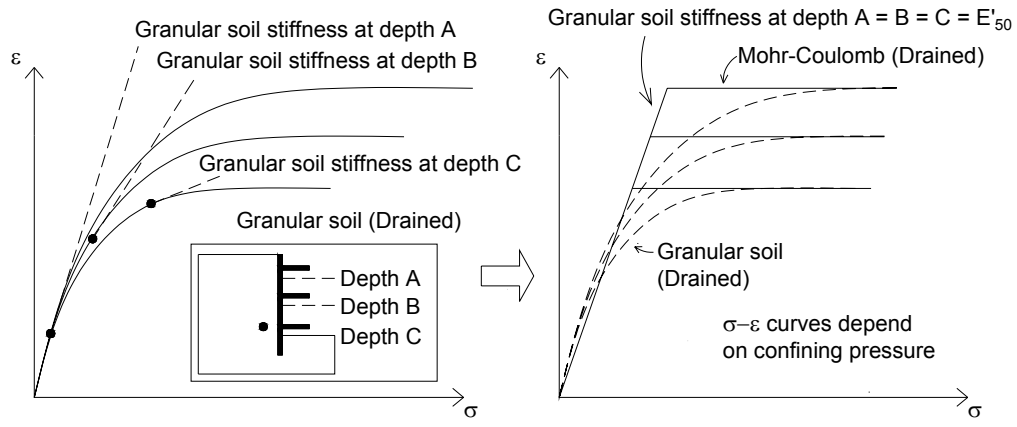

Figure 4.2 Soil Behaviour with Mohr-Coulomb Model under Drained Condition

Using the Mohr-Coulomb soil model with total stress parameters for undrained condition in soft soil can produce reasonable results. The input shear strength is directly used in the analysis which prevents over-prediction as shown in Figure 4.3. In terms of total stress, the soil stiffness is independent of confining pressure. Hence, stress discrepancy is not an issue. However, the pre-failure nonlinear behavior is still not properly modeled as shown in Figure 4.4.

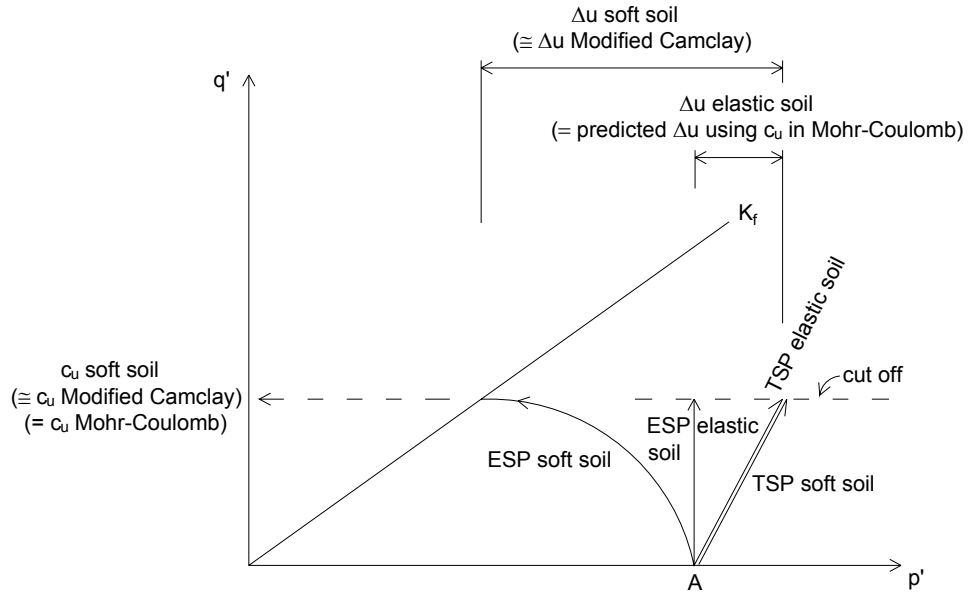

Figure 4.3 Mohr-Coulomb Model with Total Stress Parameters

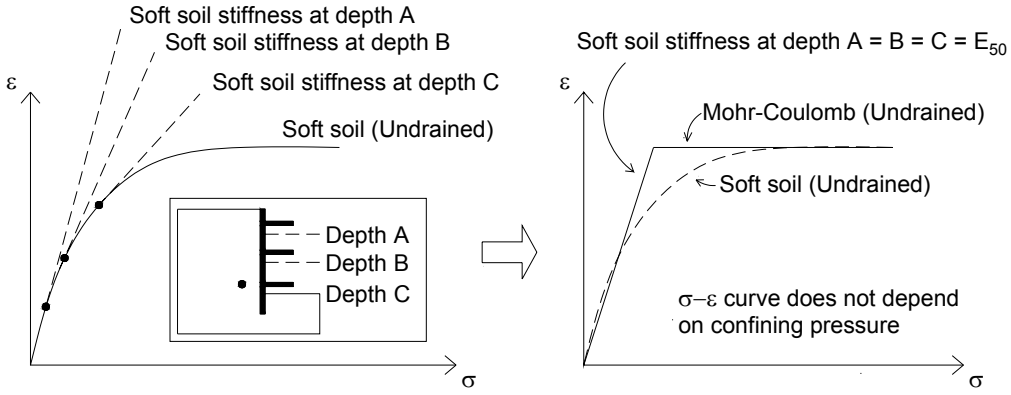

Figure 4.4 Soil Stiffness Behavior with Mohr-Coulomb Model in Undrained Condition

Mohr-Coulomb model although has many limitations, it is the most common model used in practiced. Another soil model which is better to model soft clay is Modified Cam Clay. The nonlinear behavior is properly captured. The model can also predict reasonable undrained shear strength and excess pore pressure as shown in Figures 4.1. It overcomes most of Mohr-Coulomb model shortcomings. However, Modified Cam Clay is not suitable for sand and heavily over-consolidated clay.

Both models, Mohr-Coulomb and Modified Cam Clay, do not include small strain non-linearity effect. Jardine et al. (1986) showed that in excavation, the small strain characteristics appear to have the greatest influence on the deflection profile around the loaded boundary. In the predicted ground settlement close to the wall, the soil with linear elastic model will heave more and the ground further away from the wall will also settle more as compared to the soil model with small strain non-linearity effect. In terms of wall deflection, the profiles are slightly different. This limitation should be acknowledged particularly in predicting ground settlement in order to avoid confusion between prediction and measurement.

There is a sophisticated model developed at MIT known as MIT-E3 constitutive model which is capable of simulating small strain nonlinearity, soil strength anisotropy, hysteretic and inelastic behaviour associated with reversal in load directions. The parameters involved are numerous and complex. For routine practical work, both Mohr-Coulomb and Modified Cam Clay models offer as attractive alternatives.

In this chapter, ten case records were back-analyzed using Modified Cam Clay for soft soil and Mohr-Coulomb for stiff soil. Six cases are from Singapore. They are Bugis MRT Station, Lavender MRT Station, MOE building, Syed Alwi project, Rochor complex, and the cut-and-cover tunnel between Farrer Park and Kandang Kerbau. Three cases are from Taipei. They are a 33-story office building, TNEC building, and the Formosa project. The last one is the Kotoku project in Japan. SAGE CRISP finite element was used for the back-analysis.

The purposes of the back-analysis are (1) to validate the application of Modified Cam Clay model in predicting soil movements in deep excavation and (2) to establish a frame work for evaluating soil parameters for the Modified Cam Clay and Mohr-Coulomb models.

4.2 Parameters of Modified Cam Clay Soil Model for Soft Clay

The basic soil parameters for the Modified Cam Clay model are as follows:

κ = slope of swelling and recompression line

λ = slope of normally consolidated line

e_Γ = void ratio on the critical state line at p' equals to 1 kPa

M = slope of critical state line projected to q versus p' plane

ν = Poisson's ratio

p'_c = maximum past pressure in terms of mean effective stress

Parameter M and p_c' can be calculated as follows:

$$M = \frac{6\sin\phi'_{cs}}{3-\sin\phi'_{cs}} \tag{4.1}$$

$$p'_c = \frac{\left(\frac{q_{\max}}{M}\right)^2}{p'_{\max}} + p'_{\max} \tag{4.2}$$

$$q_{\max} = (1-K_{nc})\left(\sigma'_v\sqrt{OCR}\right) \tag{4.3}$$

$$p'_{\max} = (2K_{nc}+1)\left(\frac{\sigma'_v\sqrt{OCR}}{3}\right) \tag{4.4}$$

where: ϕ'_{cs} = critical state friction angle

K_{nc} = coefficient of in-situ earth pressure at normally consolidated state

OCR = Over-Consolidation Ratio

σ'_v = vertical effective stress

Kulhawy and Mayne (1990) proposed a relationship between the slope of a normally consolidated line (C_c) and the slope of a swelling and recompression line (C_{ur}) to plasticity index (PI) as shown in Figure 4.5. The correlations are given in Equation 4.5 and 4.6.

$$\lambda = \frac{C_c}{\ln 10} = \frac{1}{\ln 10}\left(\frac{PI}{74}\right) = 0.00586PI \tag{4.5}$$

$$\kappa = \frac{C_{ur}}{\ln 10} = \frac{1}{\ln 10}\left(\frac{PI}{370}\right) = 0.00117PI \tag{4.6}$$

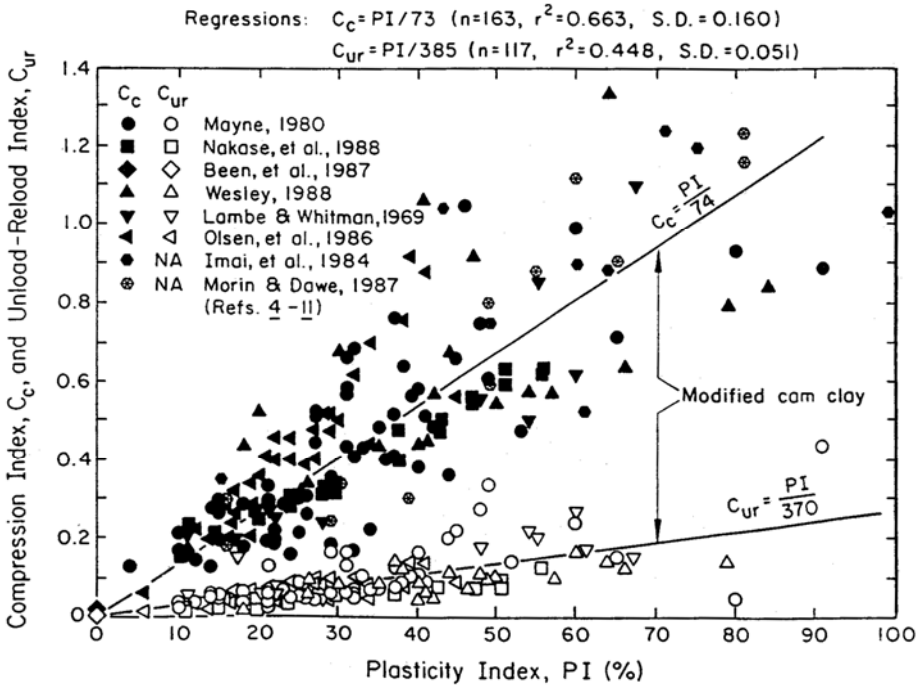

Figure 4.5 Plasticity Index versus Compression and Unload-Reload Index (Kulhawy and Mayne, 1990)

Mitchell (1976) proposed a chart to correlate the critical state friction angle and plasticity index as shown in Figure 4.6. The corresponding equation is given in Equation 4.7.

$$\sin \phi'_{cs} = 0.8 - 0.094 \ln PI \tag{4.7}$$

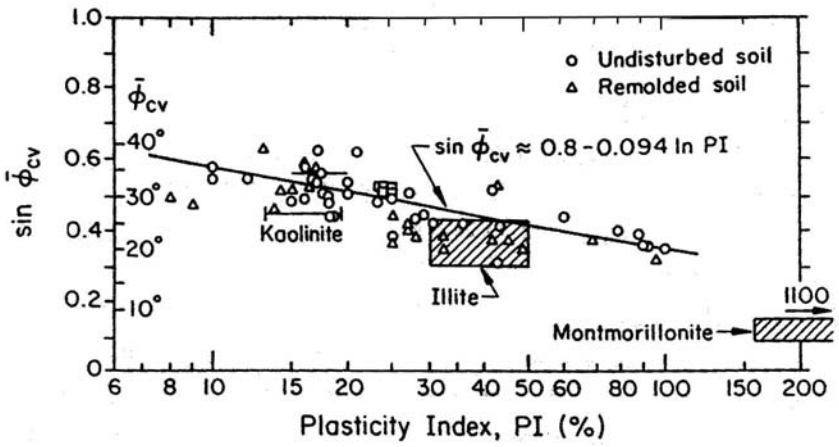

Figure 4.6 Critical State Friction Angle versus Plasticity Index (Mitchell, 1976)

Wood (1990) proposed an equation that relates e_Γ as a function of specific gravity (G_s), liquid limit LL (%), and plasticity index PI (%). The correlation is as follows:

$$e_\Gamma = G_s\left(LL + 0.3PI\right) \tag{4.8}$$

The OCR value can be approximated using Equation 4.9 (Jamiolkowski et al, 1985).

$$\left(\frac{c_u}{\sigma'_v}\right)_{over-consolidated} = \left(\frac{c_u}{\sigma'_v}\right)_{normally-consolidated} OCR^{0.8} \tag{4.9}$$

where: c_u = undrained shear strength

σ_v' = vertical effective stress

OCR = Over-Consolidation Ratio

$\left(\frac{c_u}{\sigma'_v}\right)_{normally-consolidated}$ = $0.23 \pm 0.04 \approx 0.22$ (commonly adopted)

4.3 Parameters of Mohr-Coulomb Soil Model for Clay

In order to predict elastic stiffness of clay and silt at 50% of the failure stress (E_{50}), Duncan and Buchigani (1976) has proposed a chart shown in Figure 4.7. Study done by Clough and Schmidt (1981) showed that it can give reasonable prediction of wall movement. Many researchers have also tried to correlate the undrained shear strength with the standard penetration blowcount N_{SPT} value. Stroud (1974) suggested that c_u is about 4 to 6 N_{SPT} in kPa (Eqn. 4.10). On the other hand, Kulhawy and Mayne (1990) suggested that it as 6 N_{SPT} in kPa (Eqn. 4.11). For Old Alluvium in Singapore, Li and Wong (2001) suggested c_u as 5.4 N_{SPT} kPa (Eqn. 4.12). In this study, c_u equals to 5 N_{SPT} is adopted.

$$c_u = 4 \sim 6N_{SPT} \tag{4.10}$$

$$c_u = 6N_{SPT} \tag{4.11}$$

$$c_u = 5.4N_{SPT} \tag{4.12}$$

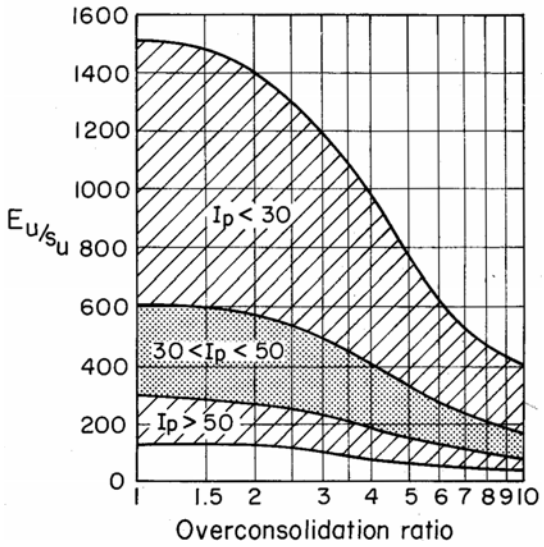

Figure 4.7 Over-Consolidation Ratio versus E_u/c_u (Duncan and Buchigani, 1976)

4.4 Parameters of Mohr-Coulomb Soil Model for Sand

Duncan and Chang (1970) shows that there is a relationship between tangent modulus (E'_i) and secant modulus (E'_s) based on the hyperbolic equation as expressed in Equation 4.13. Secant modulus (E'_s) is expressed as a function of failure ratio (R_f), stress level (S_L), modulus number (K), atmospheric pressure (P_a), and confining pressure (σ'_3). Based on the study by Duncan et al. (1974), a correlation between the modulus number (K) and relative density (D_r) was proposed in Equation 4.14. The n and R_f values are about 0.4 and 0.7, respectively. For E'_{50}, elastic stiffness of soil at 50% of the failure stress, the corresponding stress level (S_L) is 0.5. Parameter σ'_3 can also be expressed as a function of σ'_1 and OCR as shown in Equation 4.15. Therefore, by combining Equations 4.13 to 4.15, the secant modulus (E'_{50}) can be expressed as a function of D_r, σ'_1, ϕ', and OCR as shown in Equation 4.16.

$$E'_s = (1 - R_f S_L) E'_i = (1 - R_f S_L) \left[K P_a \left(\frac{\sigma'_3}{P_a} \right)^n \right] \tag{4.13}$$

$$K = 60 + 6D_r \tag{4.14}$$

$$\sigma_3' = \sigma_1'(1-\sin\phi')\sqrt{OCR} \tag{4.15}$$

$$\frac{E'_{50}}{P_a} = 0.65(60+6D_r)\left[(1-\sin\phi')\sqrt{OCR}\left(\frac{\sigma'_1}{P_a}\right)\right]^{0.4} \tag{4.16}$$

The correlation between ϕ' and D_r proposed by Schmertmann (1978) is adopted in this study. For fine, medium, and coarse sand, whether it is uniform or well-graded, the relationship between D_r and ϕ' can be expressed as Equations 4.17 to 4.19.

(Uniform fine sand) $\phi' = 28^\circ + 0.14D_r$ (4.17)

(Uniform medium or well-graded fine sand) $\phi' = 31.5^\circ + 0.12D_r$ (4.18)

(Uniform coarse or well-graded medium sand) $\phi' = 35^\circ + 0.10D_r$ (4.19)

Gibbs and Holtz (1957) established a correlation between relative density, N_{SPT} and effective overburden pressure base on a study on fine and coarse sand. Liao and Whitman (1986) proposed a correction of N_{SPT} for overburden pressure (C_N) as shown on Equation 4.20. Application of this correction to the correlation from Gibbs and Holtz (1957) yields a single curve between N_{corr} and relative density as shown in Figure 4.8. This modified chart can also be expressed as Equation 4.21. This equation is only applicable to N_{corr} values from 3 to 50.

$$C_N = 9.78\left(\frac{1}{\sigma_v'}\right)^{0.5} \leq 2 \tag{4.20}$$

$$D_r = -21.93 + 31(\ln(N_{corr})) \tag{4.21}$$

By combining Equations 4.16 to 4.19 and 4.21, E'_{50} can be expressed as a function of N_{corr}. The results are plotted in Figures 4.9 to 4.11. By combining Equations 4.17 to 4.19 and 4.21, the relationship between N_{corr} and ϕ' can be developed as shown in Figure 4.12.

It should be remembered that all of these charts are not intended to replace laboratory test. It should be used as a guide to obtain parameters that may be unavailable during design.

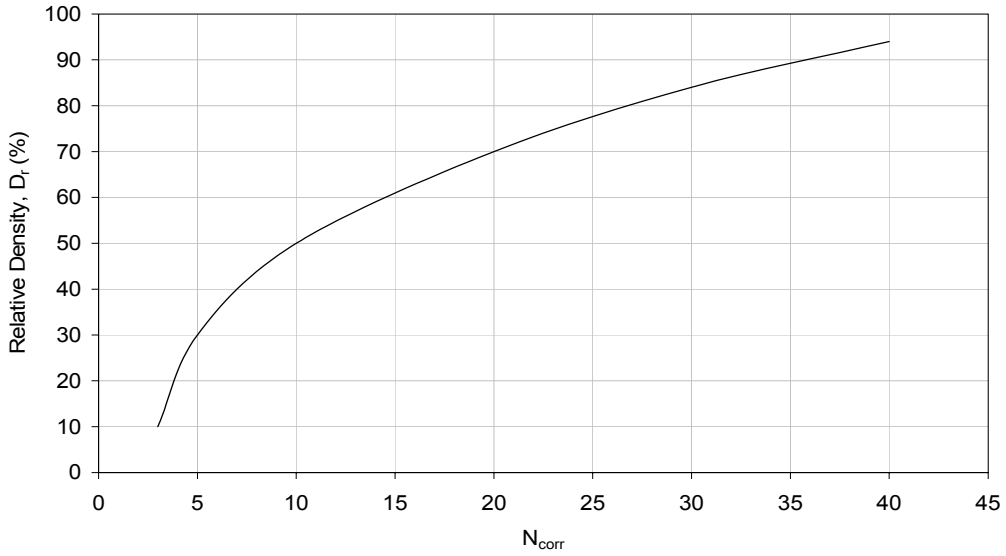

Figure 4.8 Correlation of D_r with N_{corr} for Fine to Coarse Sand
(Modified after Gibbs and Holtz, 1957)

4.5 Case Study

Empirical correlations of soil parameters for both Modified Cam Clay and Mohr-Coulomb models have been presented. In order to assess the reliability of these correlations, validation against case records were carried out. The eight cases from Singapore are cut-and-cover tunnel between Farrer Park and Kandang Kerbau, Bugis MRT Station, Lavender MRT Station, Syed Alwi project, MOE building, Rochor complex, Oxley Rise development, and development near River Valley road. Three cases are from Taipei which includes a 33-story office building, TNEC building, and the Formosa project. The last one is the Kotoku project in Japan.

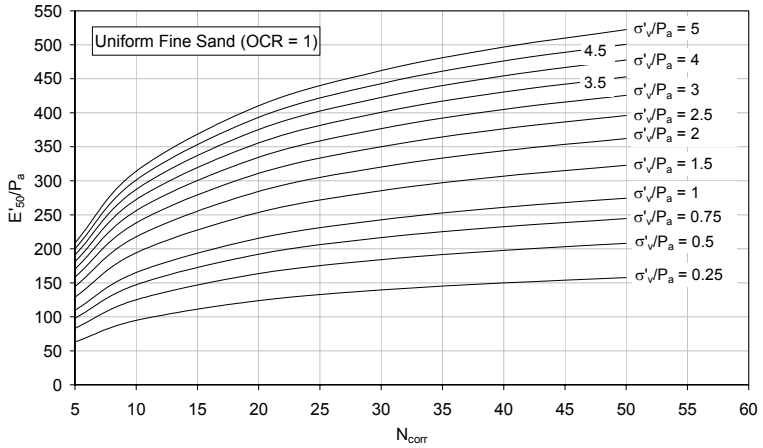

(a) Uniform Fine Sand (OCR = 1)

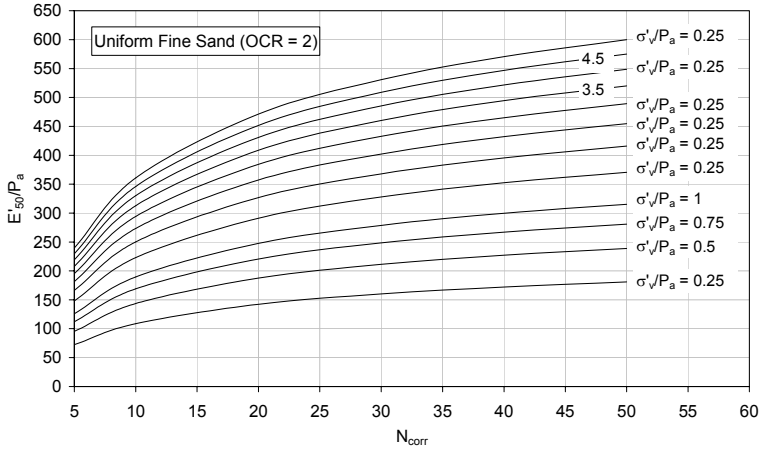

(b) Uniform Fine Sand (OCR = 2)

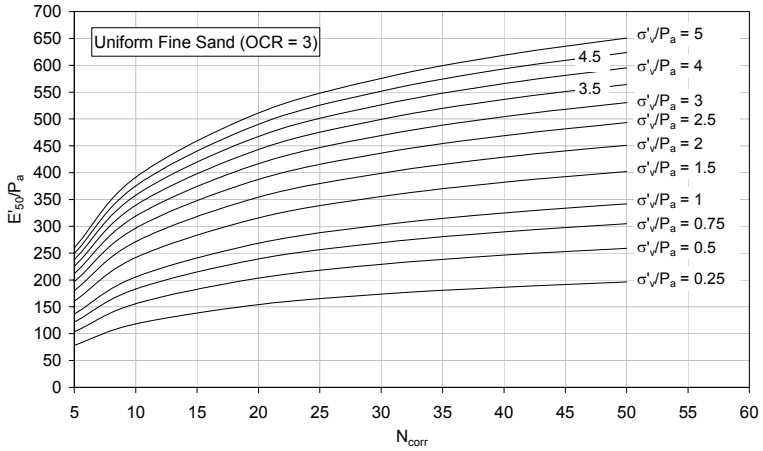

(c) Uniform Fine Sand (OCR = 3)

Figure 4.9 Proposed Chart to Roughly Estimate E'_{50} from N_{corr} in Uniform Fine Sand

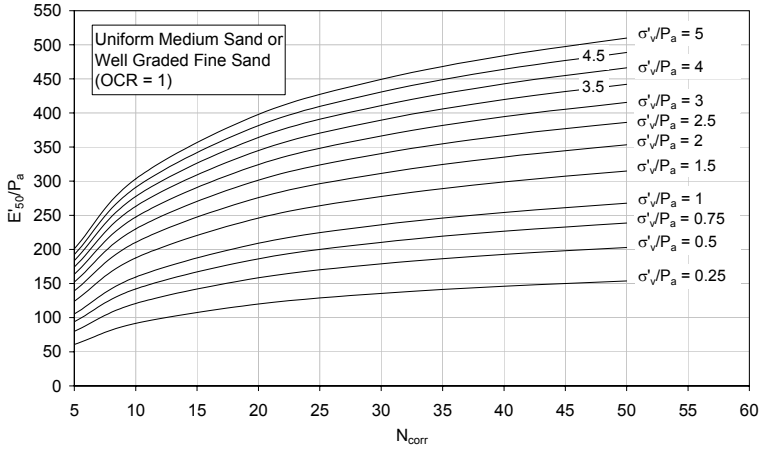

(a) Uniform Medium Sand or Well Graded Fine Sand (OCR = 1)

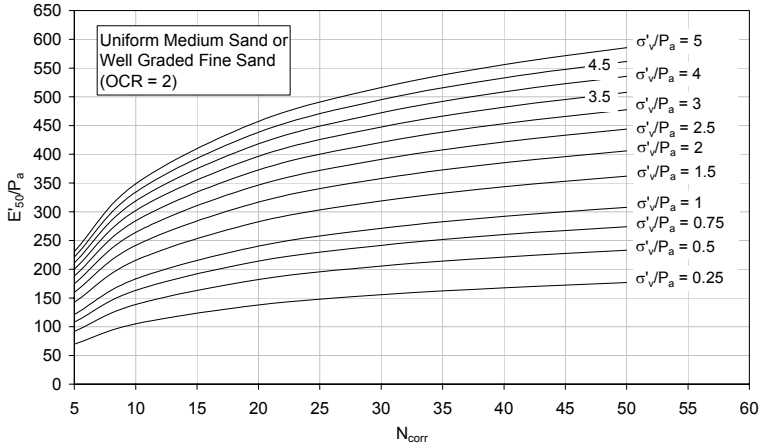

(b) Uniform Medium Sand or Well Graded Fine Sand (OCR = 2)

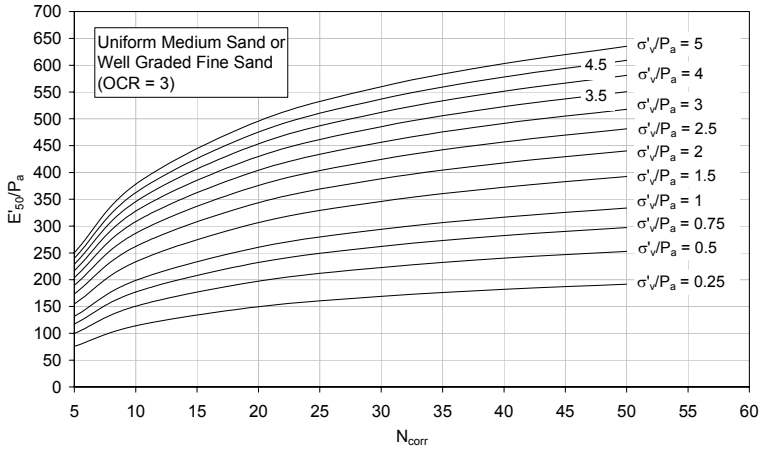

(c) Uniform Medium Sand or Well Graded Fine Sand (OCR = 3)

Figure 4.10 Proposed Chart to Roughly Estimate E'_{50} from N_{corr} in Uniform Medium Sand or Well Graded Fine Sand

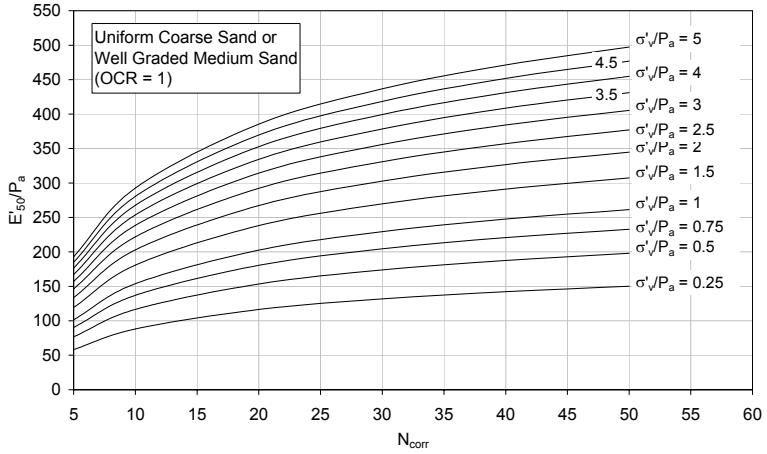

(a) Uniform Coarse Sand or Well Graded Medium Sand (OCR = 1)

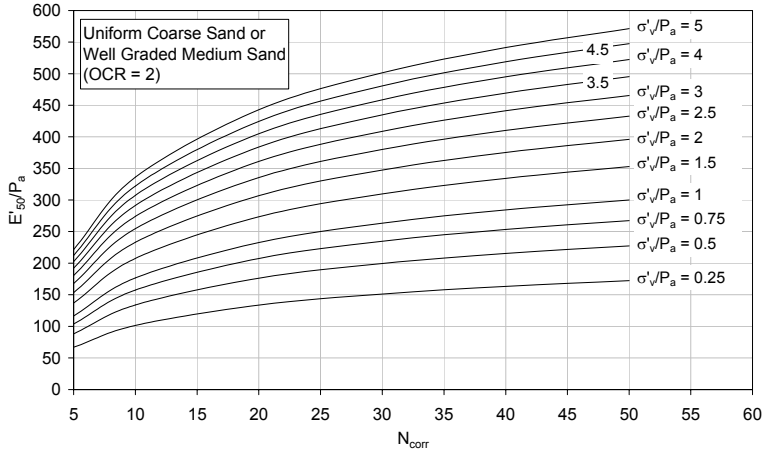

(b) Uniform Coarse Sand or Well Graded Medium Sand (OCR = 2)

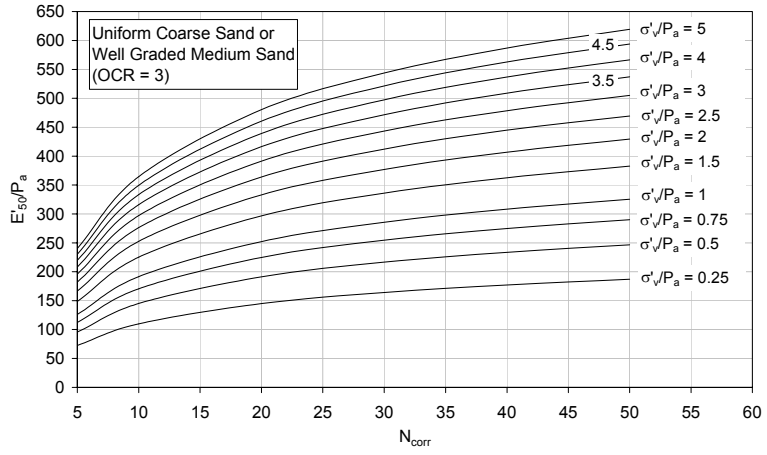

(c) Uniform Coarse Sand or Well Graded Medium Sand (OCR = 3)

Figure 4.11 Proposed Chart to Roughly Estimate E'_{50} from N_{corr} in Uniform Coarse Sand or Well Graded Medium Sand

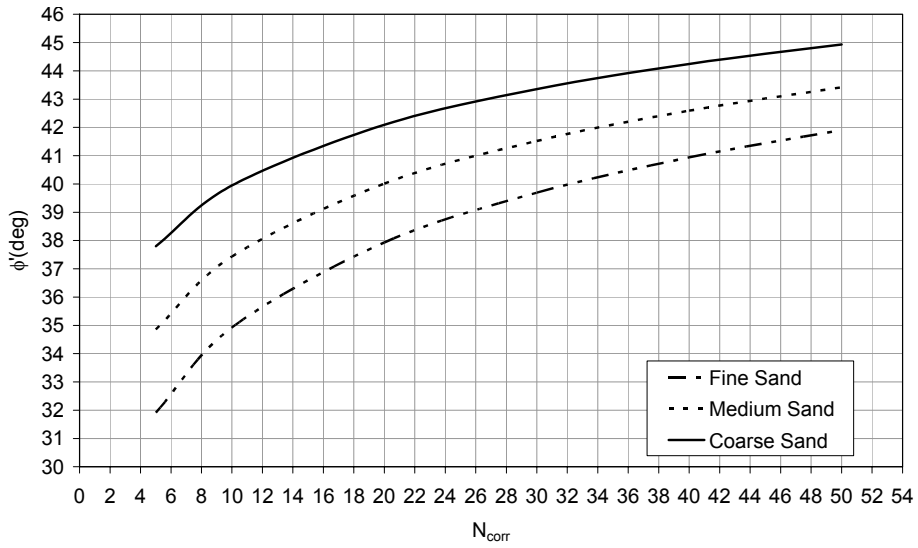

Figure 4.12 Estimation of Friction Angle of Sand, ϕ', from N_{corr}

The computer program SAGE CRISP is used in the back-analysis. Both Modified Cam Clay and Mohr-Coulomb models can be used. The soil is modeled using either 8 nodes of quadrilateral element or 6 nodes of triangular element. The retaining wall is modeled with either 8 nodes of rectangular element or 3 nodes of beam element. The strut is modeled with a 2-node of truss element. The Poisson's ratio for clay material is taken as 0.33. This is the recommended value given in a manual for undrained analysis to make sure that the water is sufficiently stiff with respect to the soil skeleton.

4.5.1 Case 1: Farrer Park – Kandang Kerbau (CH 31+895)

This cut-and-cover tunnel was part of the MRT North East Line construction in Singapore. The sectional view and finite element mesh are shown in Figure 4.13 and 4.14, respectively. The 800 mm thick diaphragm wall was constructed to a depth of 26 to 28.4 m. The excavation width was 21 m. It was done with bottom-up method. The original ground water level was about 1 m below surface. The soil parameters adopted in the analysis are shown in Tables 4.1 and 4.2. Preloading is not included due to missing record. The structural properties and excavation sequence are shown in Table 4.3 and 4.4, respectively. The computed and measured wall deflection profiles are shown in Figure 4.15.

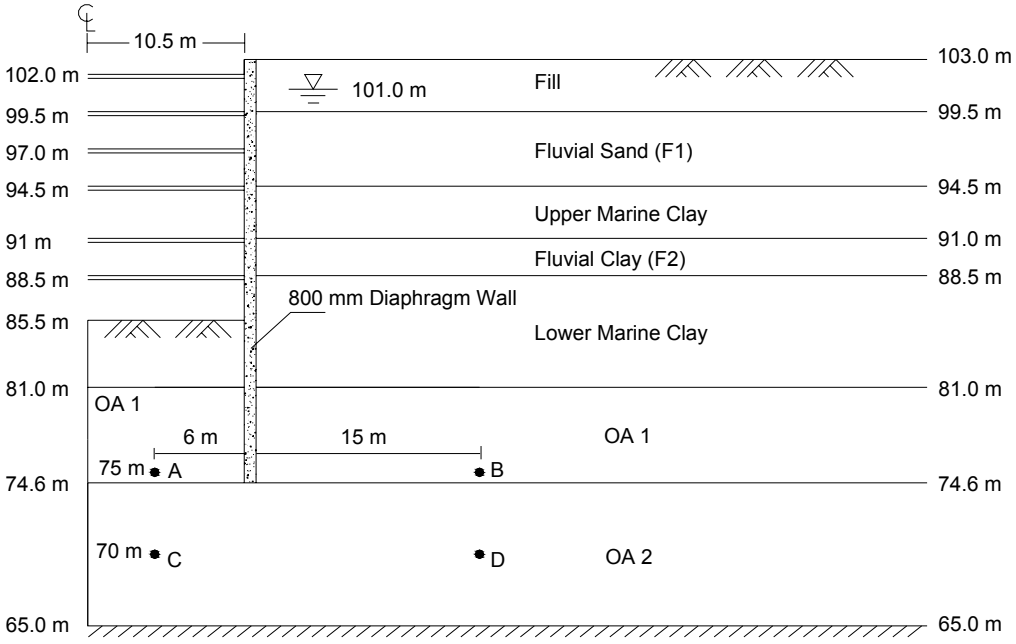

Figure 4.13 Cross-Section of Excavation at Farrer Park – Kandang Kerbau (CH 31+895) (Li, 2001)

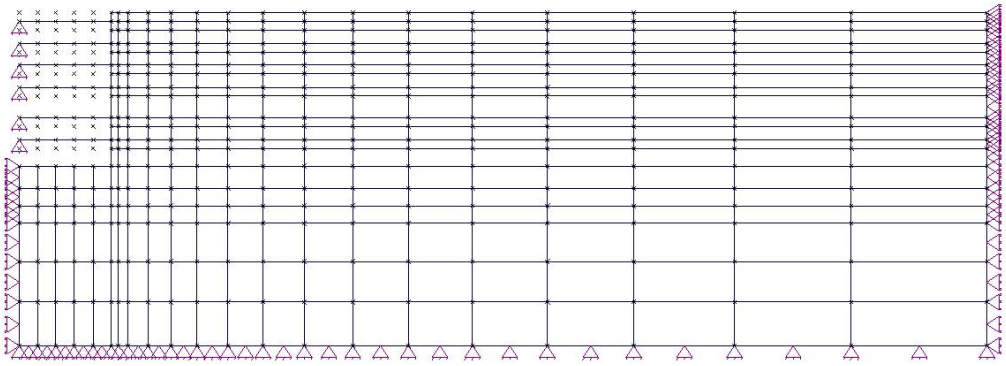

Figure 4.14 Finite Element Mesh for Excavation at Farrer Park – Kandang Kerbau (CH 31+895)

Table 4.1 Soil Properties of Upper and Lower Marine Clay at Farrer Park – Kandang Kerbau (CH 31+895)

Soil Type	γ_{sat}	PI	w_L	G_s	κ	λ	e_Γ	ϕ_{cs}	M	ν	k
	(kN/m^3)	(%)	(%)					(^{o})			(m/s)
UMC	16	55	85	2.65	0.0644	0.3223	2.69	25.0	0.984	0.33	$1x10^{-9}$
LMC	16	45	75	2.65	0.0527	0.2637	2.34	26.2	1.04	0.33	$1x10^{-9}$

Table 4.2 Soil Properties for Other Soils at Farrer Park – Kandang Kerbau (CH 31+895)

Soil Type	γ_{sat} (kN/m^3)	ν	E_{50} (kPa)	E_{ur} (kPa)	c (kPa)	ϕ (^{o})	k (m/s)
Fill (Sandy Soil, N = 6)	19	0.33	11000	-	0	38	$1x10^{-4}$
Fluvial Sand (F1) (N = 15)	19	0.33	20000	-	0	39	$1x10^{-5}$
Fluvial Clay (F2) (N = 5, PI = 30)	17	0.33	15000	-	25	0	$1x10^{-8}$
OA 1 (N = 30, PI = 20)	20	0.33	112500	337500	150	0	$1x10^{-9}$
OA 2 (N = 100, PI = 20)	20	0.33	375000	1125000	500	0	$1x10^{-9}$

Table 4.3 Structural Properties of Excavation at Farrer Park – Kandang Kerbau (CH 31+895)

Structural Members	E (kN/m^2)	A (m^2/m)	Preload (kN/m)
Strut (at RL 102 m)	2.07×10^8	0.019	Missing record
Strut (at RL 99.5 m)	2.07×10^8	0.0228	Missing record
Strut (at RL 97 m)	2.07×10^8	0.0258	Missing record
Strut (at RL 94.5 m)	2.07×10^8	0.0396	Missing record
Strut (at RL 91 m)	2.07×10^8	0.0396	Missing record
Strut (at RL 88.5 m)	2.07×10^8	0.0258	Missing record
Diaphragm wall (quadrilateral element)	2.8×10^7	-	-

Table 4.4 Excavation Sequence of Excavation at Farrer Park – Kandang Kerbau (CH 31+895)

Stage	Excavation Sequence
1	Excavate to RL 101 m
2	Install first level of strut at RL 102 m
3	Excavate to RL 98.5 m
4	Install second level of strut at RL 99.5 m
5	Excavate to RL 96 m
6	Install third level of strut at RL 97 m
7	Excavate to RL 93.5 m
8	Install fourth level of strut at RL 94.5 m
9	Excavate to RL 90 m
10	Install fifth levef of strut at RL 91 m
11	Excavate to RL 87.5 m
12	Install sixth level of strut at RL 88.5 m
13	Excavate to formation level at RL 85.5 m

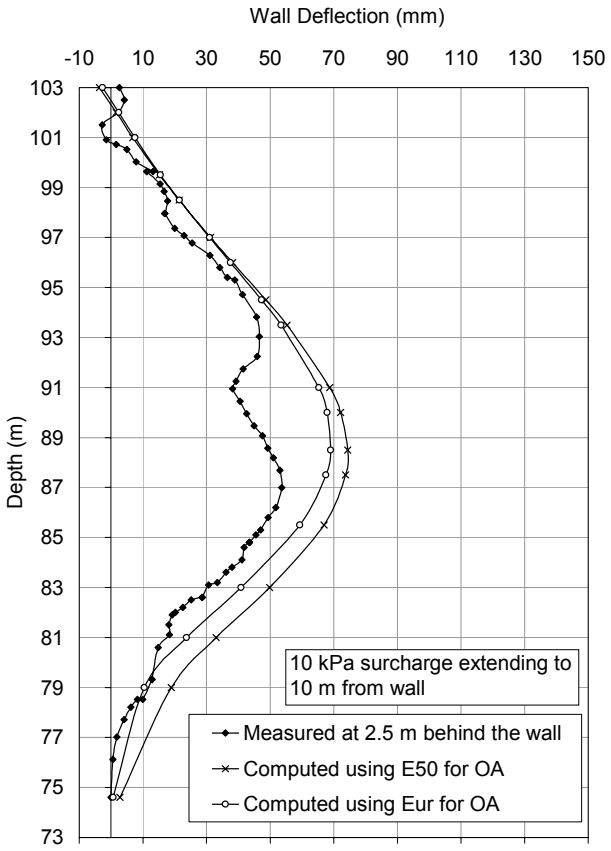

Figure 4.15 Wall Deflection at Farrer Park – Kandang Kerbau (CH 31+895)

Analyzes with two different stiffnesses for Old Alluvium (OA) were conducted. Figure 4.15 shows that using E_{ur} rather than E_{50} for OA seems to yield better agreement with measurements. At the base of excavation, the stress paths at Elements A and C are predominantly unloading as shown in Figure 4.16. Hence, E_{ur} is more appropriate. At a location behind the wall at Elements B and D, primary loading took place as shown in Figure 4.17. For simplicity, E_{ur} was used for both Old Alluvium strata. E_{ur} is assumed to be 3 times E_{50}. E_{50} was taken as 750 c_u based on Figure 4.7. The analysis using E_{ur} yielded slightly better agreement with the measured deflection especially in areas close to the bottom of wall. The measured maximum deflection is 55 mm. The computed values using E_{ur} and E_{50} for the OA strata are 69 and 74 mm, respectively. The differences are about +25% and +35%, respectively.

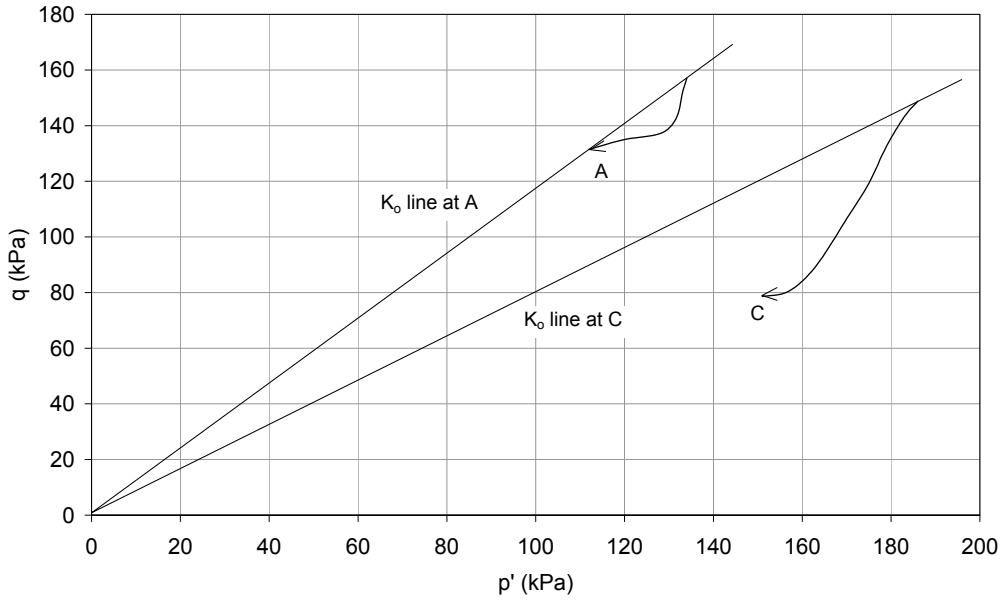

Figure 4.16 Stress Paths at Elements A and C

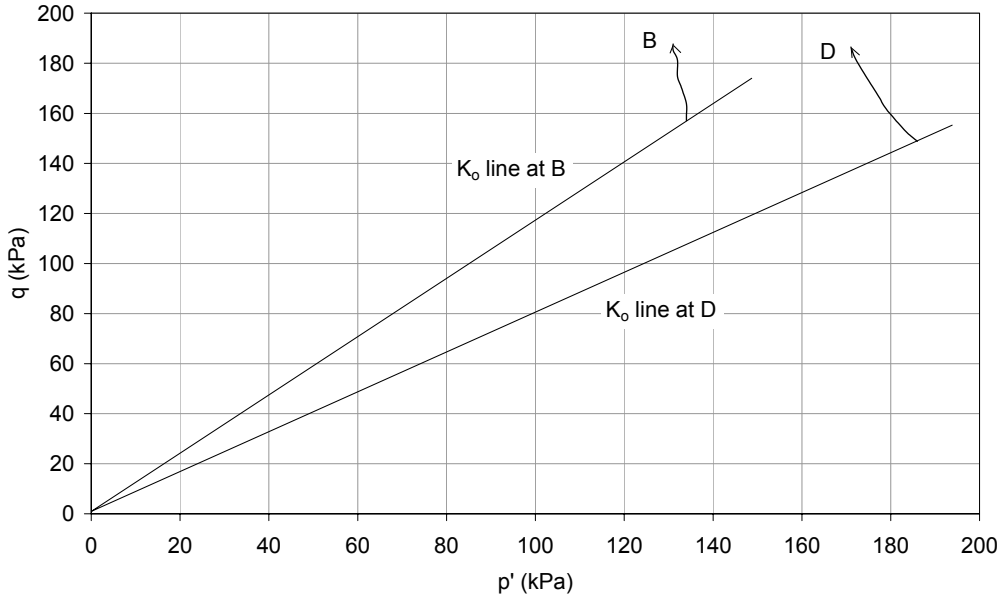

Figure 4.17 Stress Paths at Elements B and D

4.5.2 Case 2: Bugis MRT Station

Figure 4.18 shows the layout of the Bugis MRT station and the inclinometer locations. The cross-section and finite element mesh adopted in the analysis are shown in Figure 4.19 and 4.20, respectively. The soil parameters are shown in

Tables 4.5 and 4.6. The excavation had seven levels of struts. No preloads were used in the analysis due to missing record. The ground water table was 1.5 m below the ground surface. It was done with bottom-up method. The excavation sequence and structural properties are shown in Table 4.7 and 4.8, respectively. The result in Figure 4.21 shows that the maximum measured and predicted wall deflections are about 135 mm. However, using E_{ur} for fluvial sandy clay and OA, improves the agreement especially around the wall base. However, the maximum measured and predicted ground settlements are about the same at 140 mm regardless whether E_{50} or E_{ur} was used as shown in Figure 4.22. Due to the limitation of the soil model which cannot model the small strain non-linearity effect, the deflection shape is more difficult to match. It is easier to match the maximum ground settlement.

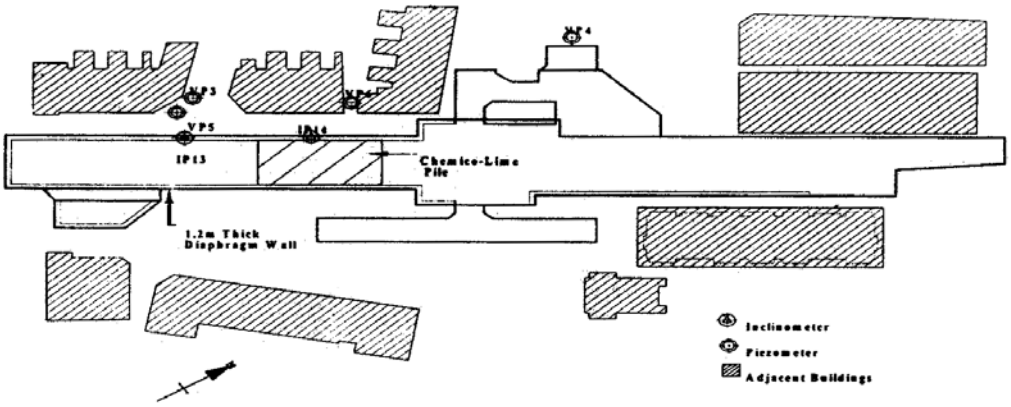

Figure 4.18 Layout of Bugis MRT Station (Shirlaw and Wen, 1999)

Table 4.5 Soil Properties of Upper and Lower Marine Clay at Bugis MRT Station

Soil Type	γ_{sat}	PI	LL	G_s	κ	λ	e_Γ	ϕ_{cs}	M	ν	k
	(kN/m^3)	(%)	(%)					(^{o})			(m/s)
UMC	16	50	70	2.65	0.0585	0.2930	2.25	25.0	0.98	0.33	1x10^{-10}
LMC	16	40	60	2.65	0.0468	0.2344	1.9	27.0	1.07	0.33	1x10^{-10}

Table 4.6 Soil Properties of Other Soils at Bugis MRT Station

Soil Type	γ_{sat}	ν	E_{50}	E_{ur}	c	ϕ	k
	(kN/m^3)		(kPa)	(kPa)	(kPa)	(^{o})	(m/s)
Fill (N = 5)	18	0.33	8000	-	26	0	1x10^{-5}
Fluvial Clay (PI = 30)	18	0.33	48000	-	80	0	1x10^{-10}
Fluvial Clayey Sand (N = 80)	19	0.33	50000	150000	0	40	1x10^{-8}
OA (N = 130)	20	0.33	55000	165000	10	37	1x10^{-8}
OA (N > 130)	20	0.33	65000	195000	20	37	1x10^{-8}

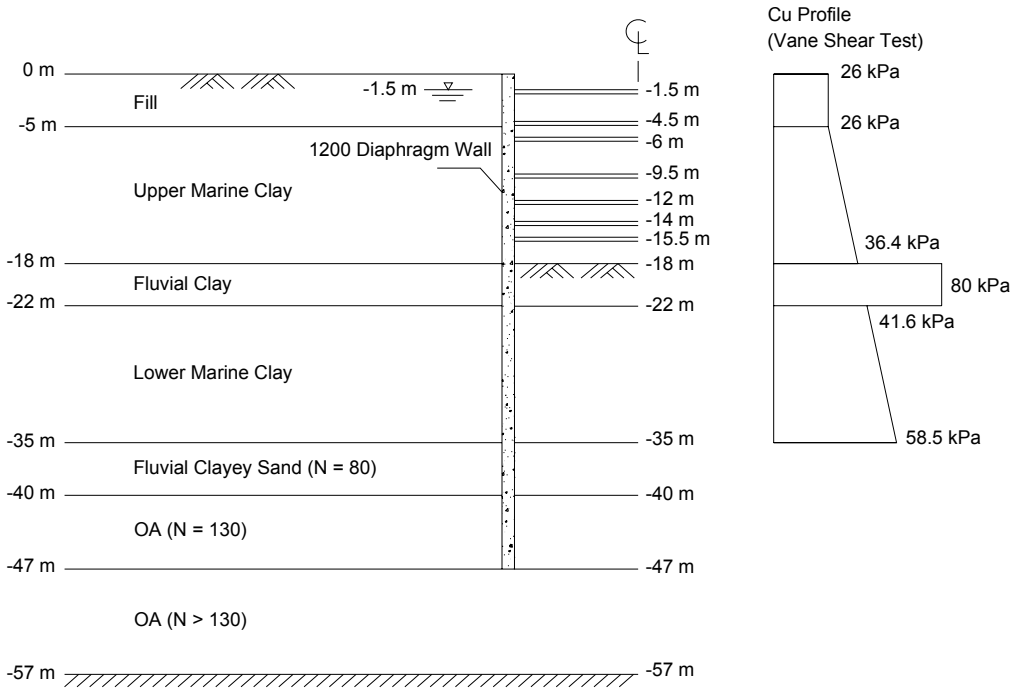

Figure 4.19 Cross-Section of Excavation at Bugis MRT Station

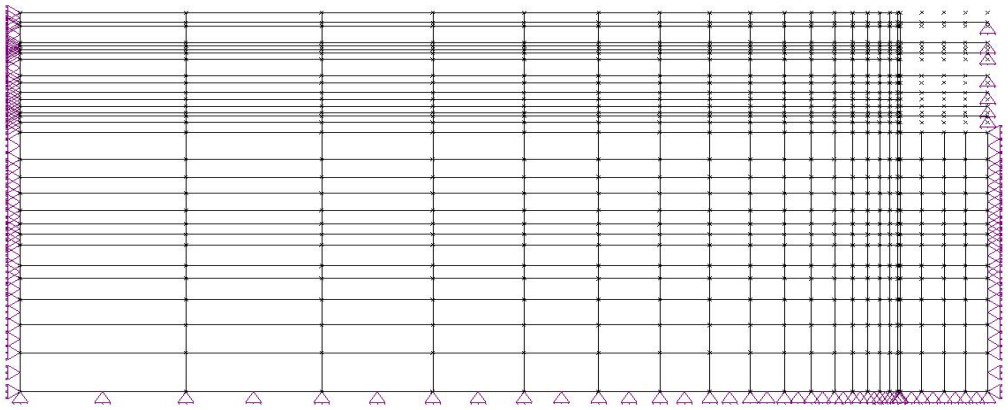

Figure 4.20 Finite Element Mesh for Bugis MRT Station

Table 4.7 Structural Properties of Excavation at Bugis MRT Station

Structural Members	E (kN/m^2)	A (m^2/m)	Preload (kN/m)
Strut (at -1.5 m)	2.07×10^8	0.00518	Missing record
Strut (at -4.5 m)	2.07×10^8	0.00518	Missing record
Strut (at -6 m)	2.07×10^8	0.00518	Missing record
Strut (at -9.5 m)	2.07×10^8	0.00518	Missing record
Strut (at -12 m)	2.07×10^8	0.00518	Missing record
Strut (at -14 m)	2.07×10^8	0.00518	Missing record
Diaphragm wall (quadrilateral element)	2.8×10^7	-	-

Table 4.8 Excavation Sequence at Bugis MRT Station

Stage	Excavation Sequence
1	Excavate to 2.5 m below a ground level (GL)
2	Install first level of strut at 1.5 m below GL
3	Excavate to 5.5 m below GL
4	Install second level of strut at 4.5 m below GL
5	Excavate to 6 m below GL
6	Install third level of strut at 6 m below GL
7	Excavate to 10.5 m below GL
8	Install fourth level of strut at 9.5 m below GL
9	Excavate to 13 m below GL
10	Install fifth level of strut at 12 m below GL
11	Excavate to 16.5 m below GL
12	Install sixth level of strut at 15.5 m below GL
13	Excavate to formation level at 18 m below GL

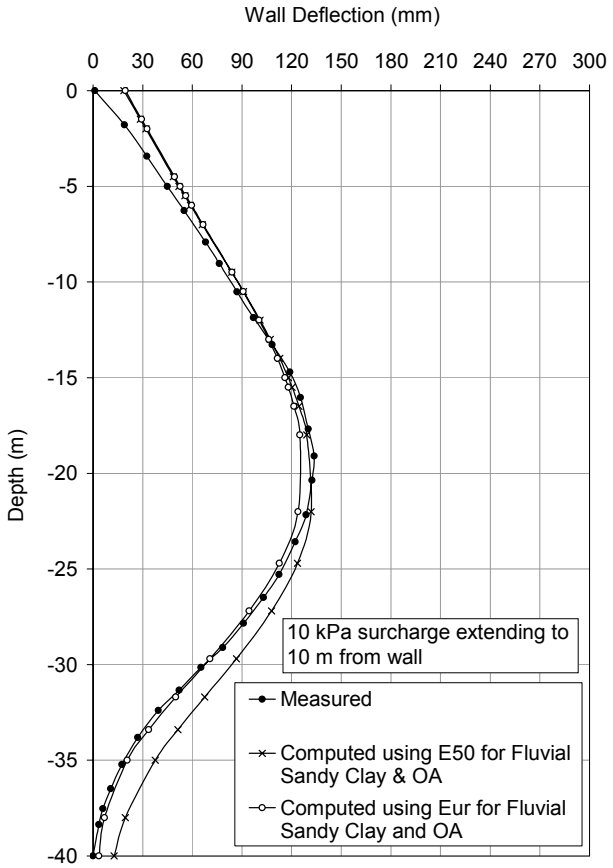

Figure 4.21 Wall Deflection of IP13 at Bugis MRT Station

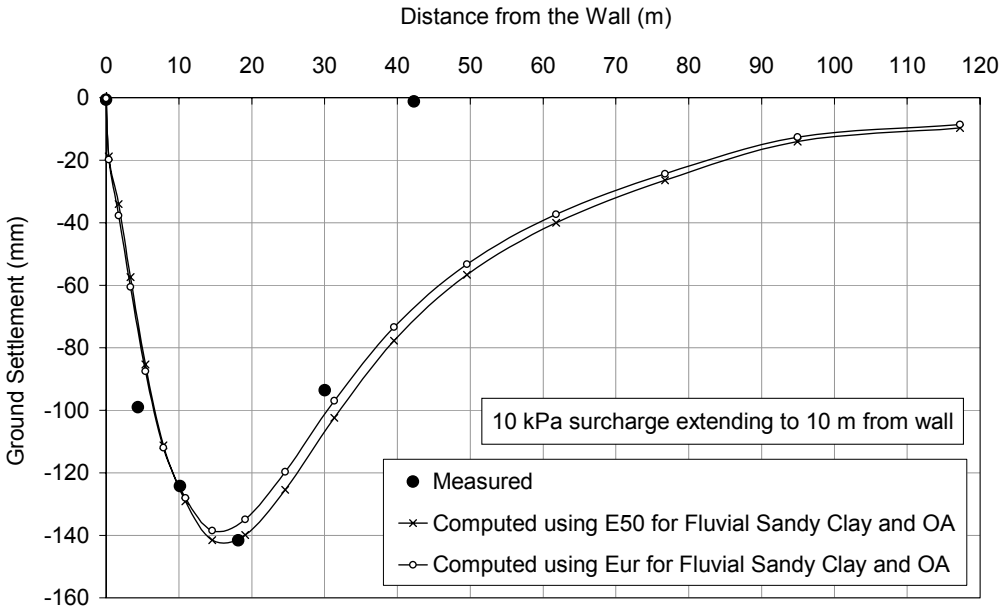

Figure 4.22 Ground Settlement at Bugis MRT Station

4.5.3 Case 3: Lavender MRT Station

Figure 4.23 and 4.24 show the sectional view of excavation and finite element mesh, respectively. It had six levels of struts and was supported by a 1000 mm thick diaphragm wall. The depth and width of excavation were 15.7 and 23 m, respectively. It was done with bottom-up method. The ground water table was about 1.5 m below surface. The soil parameters adopted in the analysis are shown in Tables 4.9 and 4.10. The preloads of struts from level 1 to 6 were 190, 390, 327, 260, 233, and 220 kN/m, respectively. The excavation sequence and structural properties are shown in Table 4.11 and 4.12, respectively. The computed and measured wall deflection profiles are shown in Figure 4.25. Using E_{50} for dense silty coarse sand and very dense clayey silt, it over-predicts the maximum wall deflection and the deflection at the wall base. However, if E_{ur} was used for these soil layers, it yield better agreement with measured values. In terms of wall deflection shape, however, it is not very good. The maximum measured and predicted wall deflections using E_{50} and E_{ur} are 38, 42, and 38, respectively. The analysis using E_{50} over-predicted the maximum deflection by about +10%.

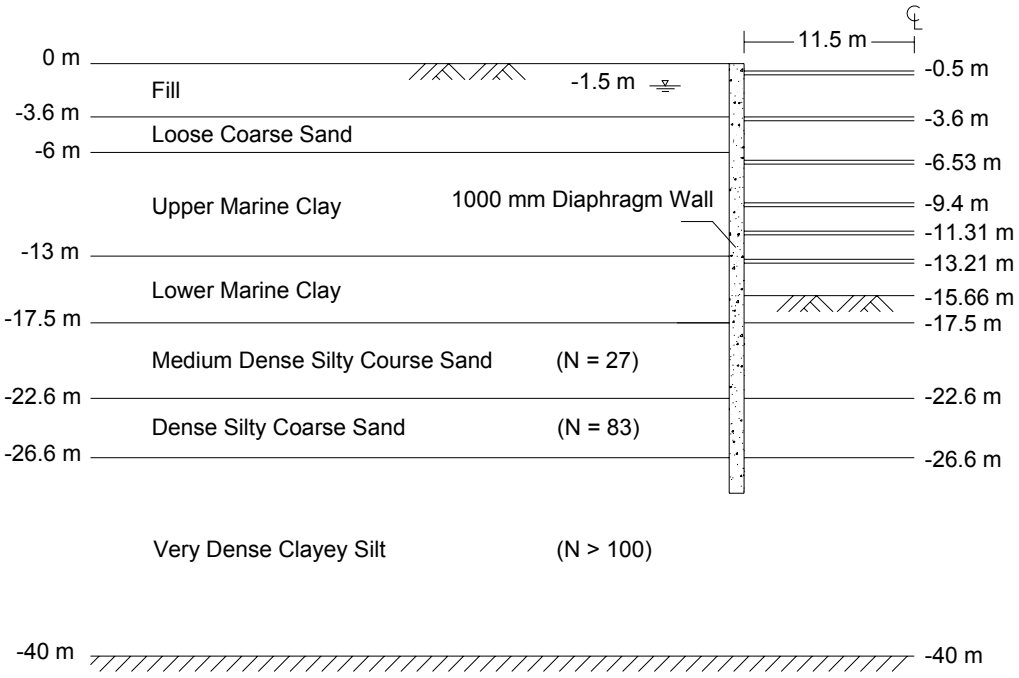

Figure 4.23 Cross-Section of Excavation at Lavender MRT Station

(Lim et al., 2003)

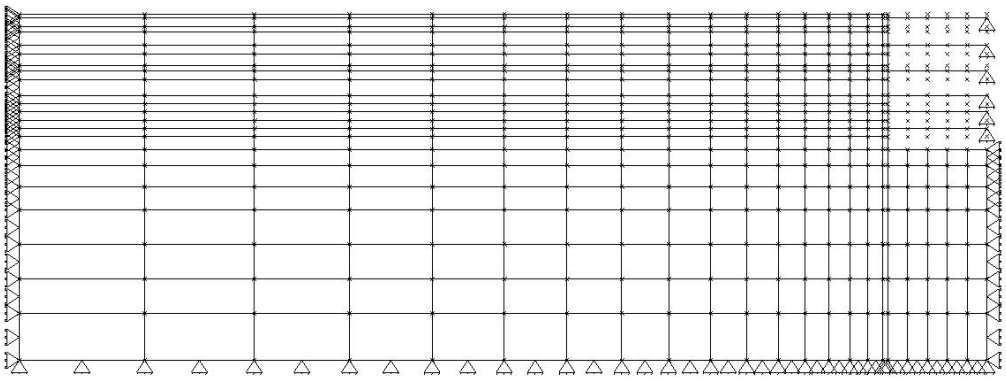

Figure 4.24 Finite Element Mesh for Lavender MRT Station

Table 4.9 Soil Properties of Upper and Lower Marine Clay at Lavender MRT

Soil Type	γ_{sat} (kN/m^3)	PI (%)	w_L (%)	G_s	κ	λ	e_Γ	ϕ_{cs} (^{o})	M	ν	k (m/s)
UMC	16	55	85	2.65	0.0644	0.3223	2.69	25.0	0.985	0.33	$1x10^{-10}$
LMC	16	45	75	2.65	0.0527	0.2637	2.34	26.2	1.04	0.33	$1x10^{-10}$

Table 4.10 Soil Properties of Other Soils at Lavender MRT

Soil Type	γ_{sat} (kN/m^3)	ν	E_{50} (kPa)	E_{ur} (kPa)	c (kPa)	ϕ (^{o})	k (m/s)
Fill	18	0.33	24000	-	80	0	$1x10^{-7}$
Loose coarse sand	20	0.33	10000	-	0	38	$1x10^{-4}$
Medium dense silty coarse sand (N = 27)	20	0.33	30000	-	0	40	$1x10^{-8}$
Dense silty coarse sand (N = 83)	20	0.33	43000	129000	0	45	$1x10^{-8}$
Very dense clayey silt	19	0.33	150000	450000	500	0	$1x10^{-10}$

Table 4.11 Excavation Sequence at Lavender MRT

Stage	Excavation Sequence
1	Excavate to 1.5 m below a ground level (GL)
2	Install first level of strut at 0.5 m below GL
3	Excavate to 7.5 m below GL
4	Install second level of strut at 6.5 m below GL
5	Excavate to 8 m below GL
6	Install third level of strut at 7 m below GL
7	Excavate to 12.5 m below GL
8	Install fourth level of strut at 11.5 m below GL
9	Excavate to 12.31 m below GL
10	Install fifth level of strut at 11.31 m below GL
11	Excavate to 14.21 m below GL
12	Install sixth level of strut at 13.21 m below GL
13	Excavate to formation level at 15.66 m below GL

Table 4.12 Structural Properties of Excavation at Lavender MRT Station

Structural Members	E (kN/m^2)	A (m^2/m)	Preload (kN/m)
Strut (at -0.5 m)	2.07×10^8	0.004	190
Strut (at -3.6 m)	2.07×10^8	0.0058	390
Strut (at -6.53 m)	2.07×10^8	0.0073	327
Strut (at -9.4 m)	2.07×10^8	0.0058	260
Strut (at -11.31 m)	2.07×10^8	0.0058	233
Strut (at -13.21 m)	2.07×10^8	0.0058	220
Diaphragm wall (quadrilateral element)	2.8×10^7	-	-

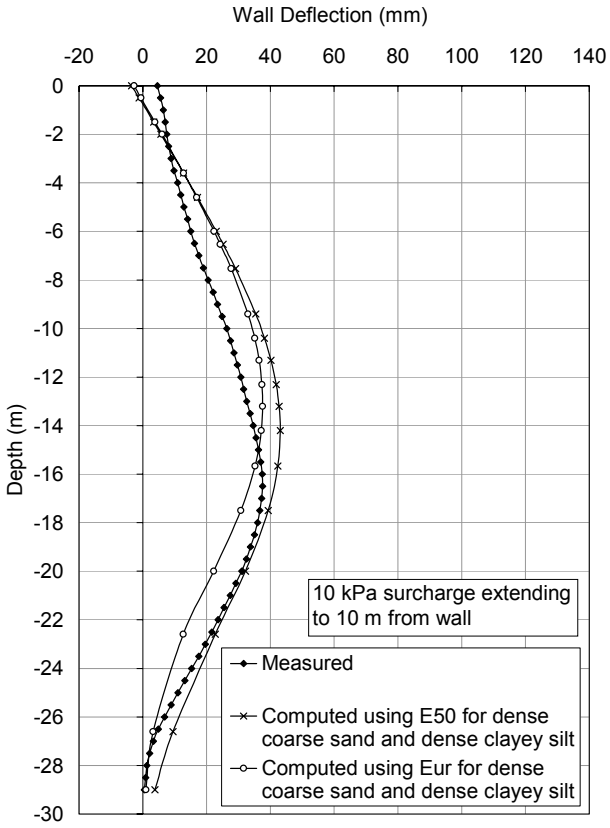

Figure 4.25 Wall Deflection at Lavender MRT station

4.5.4 Case 4: Syed Alwi Project

A typical cross-section and finite element mesh for this project are shown in Figure 4.26 and 4.27, respectively. The excavation width was about 28 m. There were only two levels of struts at 2 m and 5 m below ground surface. It was constructed with bottom-up method. The original ground water level was about 1.0 m below surface. The soil parameters adopted in the analysis are shown in Tables 4.13 and 4.14. The preloads of the top and bottom struts were 25 and 100 kN/m, respectively. The excavation sequence and structural properties are shown in Table 4.15 and 4.16, respectively. The computed and measured wall deflection profiles are as shown in Figure 4.28. Using E_{ur} rather than E_{50} on silty sand improves the prediction around the wall base and the maximum wall deflection. The maximum measured and predicted wall deflections using E_{ur} and E_{50} are 49, 54, and 59 mm, respectively. The difference using E_{ur} and E_{50} are about +10% and +20%, respectively.

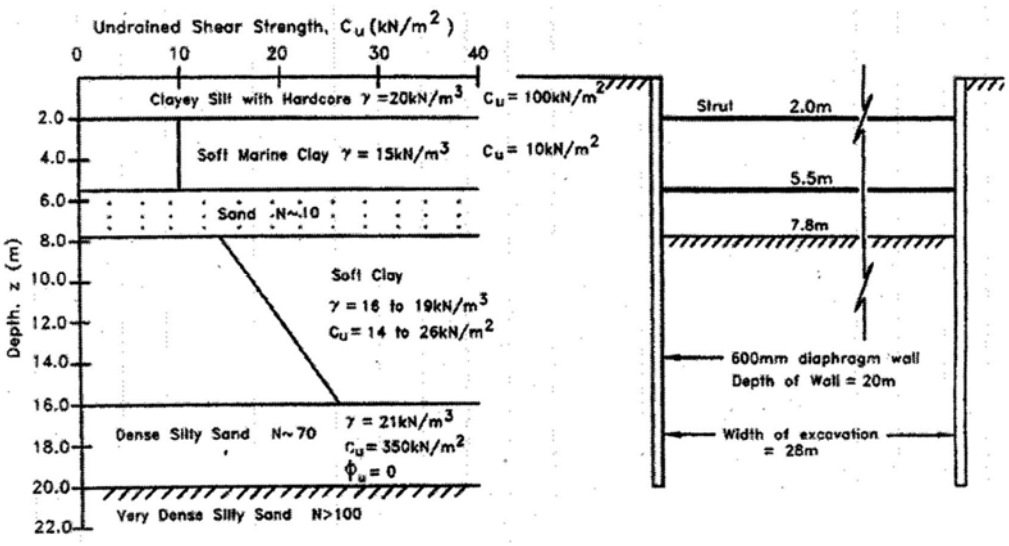

Figure 4.26 Cross-Section of Excavation at Syed Alwi Project (Lim et al., 2003)

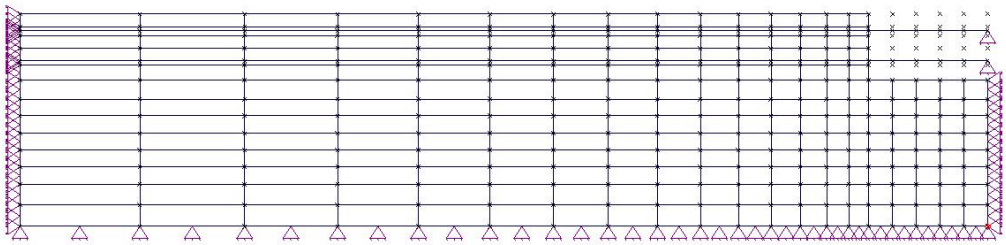

Figure 4.27 Finite Element Mesh for Syed Alwi Project

Table 4.13 Soil Properties of Soft Clay at Syed Alwi Project

Soil Type	γ_{sat} (kN/m^3)	PI (%)	w_L (%)	G_s	κ	λ	e_Γ	ϕ_{cs} (^{o})	M	ν	k (m/s)
Soft Marine Clay	15	55	85	2.65	0.0644	0.3223	2.69	25.0	0.985	0.33	$1x10^{-10}$
Soft Clay	17	45	75	2.65	0.0527	0.2637	2.34	26.2	1.04	0.33	$1x10^{-10}$

Table 4.14 Soil Properties of Other Soils at Syed Alwi Project

Soil Type	γ_{sat} (kN/m^3)	ν	E_{50} (kPa)	E_{ur} (kPa)	c (kPa)	ϕ (^{o})	k (m/s)
Clay Silt with Hardcore (PI = 30)	20	0.33	60000	-	100	0	$1x10^{-7}$
Sand	20	0.33	14000	-	0	38	$1x10^{-4}$
Dense Silty Sand (PI = 20)	21	0.33	262500	787500	350	0	$1x10^{-8}$
Very Dense Silty Sand (PI = 20)	21	0.33	375000	1125000	500	0	$1x10^{-9}$

Table 4.15 Excavation Sequence at Syed Alwi Project

Stage	Excavation Sequence
1	Excavate to 2.5 m below a ground level (GL)
2	Install first level of strut at 2 m below GL and preload to 25 kN/m
3	Excavate to 6 m below GL
4	Install second level of strut at 5.5 m below GL and preload to 100 kN/m
5	Excavate to formation level at 7.8 m below GL

Table 4.16 Structural Properties of Excavation at Syed Alwi Project

Structural Members	E (kN/m^2)	A (m^2/m)	I (m^4/m)	Preload (kN/m)
Strut (at -2 m)	2.07×10^8	0.004125	-	25
Strut (at -5.5 m)	2.07×10^8	0.004125	-	100
Diaphragm wall (beam element)	2.8×10^7	0.6	0.018	-

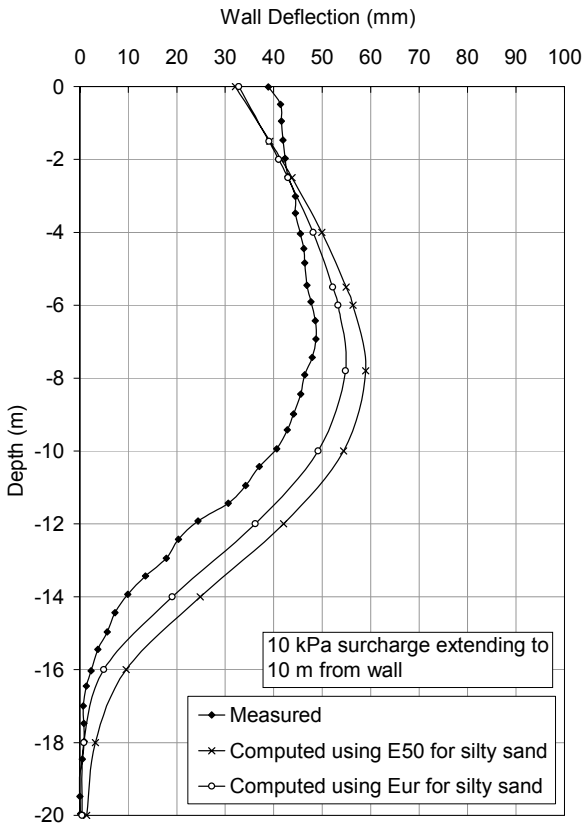

Figure 4.28 Wall Deflection at Syed Alwi

4.5.5 Case 5: Rochor Complex

Figure 4.29 and 4.30 show a typical cross-section and finite element mesh, respectively, of this project. The width of excavation was about 95 m. It was supported by 24 m long FSPIIIA sheet pile braced at three levels. It was constructed with bottom-up method. The original ground water table was about 1.5 m below surface. The soil parameters adopted in the finite element analysis are shown in Tables 4.17 and 4.18. The preloads of strut from top to bottom were 28, 104.3 and 175.1 kN/m, respectively. The excavation sequence and structural properties are shown in Table 4.19 and 4.20, respectively. The computed and measured wall deflection profiles are shown in Figure 4.31. The result shows that using E_{ur} for the firm clay and very stiff silty clay improves the prediction. The shape of measured wall deflection near the base revealed the possibility of translational displacement at wall toe. That means the actual wall deflection is likely to be larger than 150 mm. The computed maximum and wall deflections using E_{ur} and E_{50} are about 188 mm. The difference between the computed and measured values is about +25%.

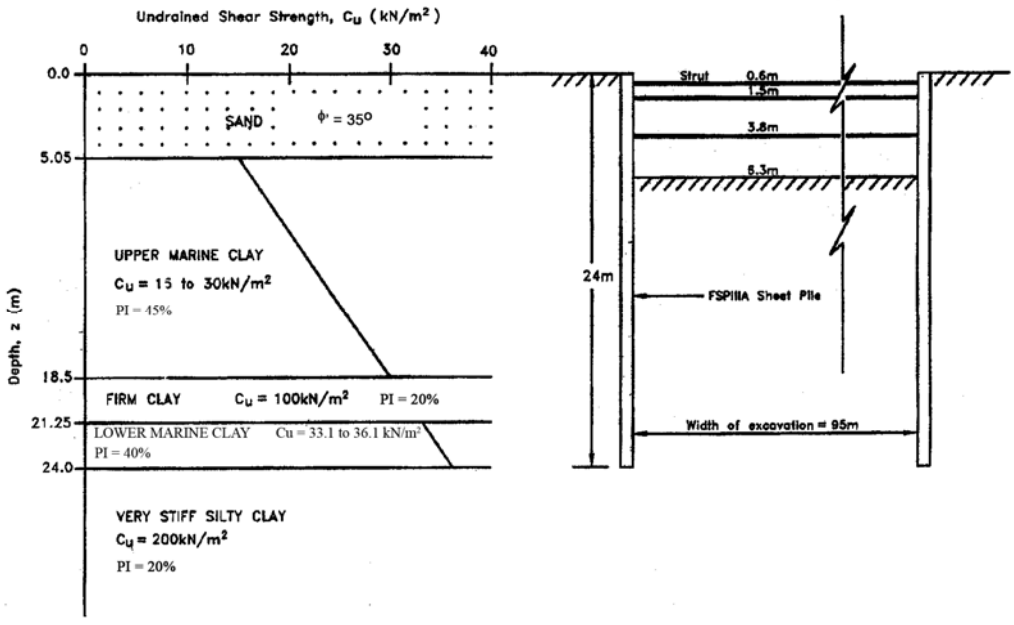

Figure 4.29 Cross-Section of Excavation at Rochor Complex (Lim et al., 2003)

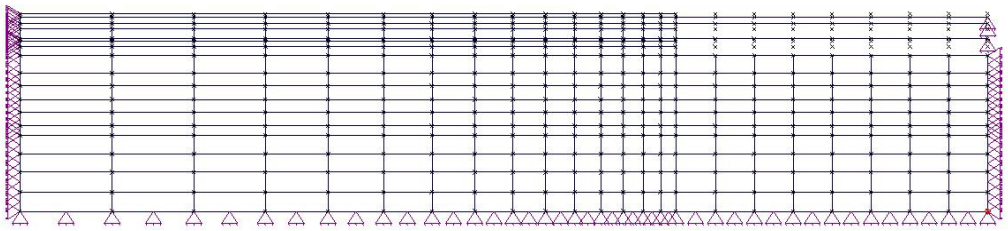

Figure 4.30 Finite Element Mesh for Rochor Complex

Table 4.17 Soil Properties of Upper and Lower Marine Clay at Rochor Complex

Soil Type	γ_{sat}	PI	w_L	G_s	κ	λ	e_Γ	ϕ_{cs}	M	ν	k
	(kN/m^3)	(%)	(%)					(^{o})			(m/s)
UMC	16	45	75	2.65	0.0527	0.2637	2.34	26.2	1.04	0.33	$1x10^{-10}$
LMC	16	40	70	2.65	0.0468	0.2344	2.173	27.0	1.07	0.33	$1x10^{-10}$

Table 4.18 Soil Properties for Other Soils at Rochor Complex

Soil Type	γ_{sat}	ν	E_{50}	E_{ur}	c	ϕ	k
	(kN/m^3)		(kPa)	(kPa)	(kPa)	(^{o})	(m/s)
Sand	20	0.33	15000	-	0	35	$1x10^{-4}$
Firm Clay	17	0.33	75000	-	100	0	$1x10^{-9}$
Very Stiff Silty Clay	18	0.33	150000	450000	200	0	$1x10^{-10}$

Table 4.19 Excavation Sequence at Rochor Complex

Stage	Excavation Sequence
1	Excavate to 1.5 m below a ground level (GL)
2	Install first level of strut at 0.6 m below GL and preload to 28 kN/m
3	Excavate to 2.4 m below GL
4	Install second level of strut at 1.5 m below GL and preload to 104.3 kN/m
5	Excavate to 4.2 m below GL
6	Install third level of strut at 3.8 m below GL and preload to 175.1 kN/m
7	Excavate to formation level at 6.3 m below GL

Table 4.20 Structural Properties of Excavation at Rochor Complex

Structural Members	E (kN/m^2)	A (m^2/m)	I (m^4/m)	Preload (kN/m)
Strut (at -0.6 m)	2.07×10^8	0.004	-	28
Strut (at -1.5 m)	2.07×10^8	0.008	-	104.3
Strut (at -3.8 m)	2.07×10^8	0.008		175.1
FSP IIIA Sheetpile (beam element)	2.07×10^8	0.0186	0.000228	-

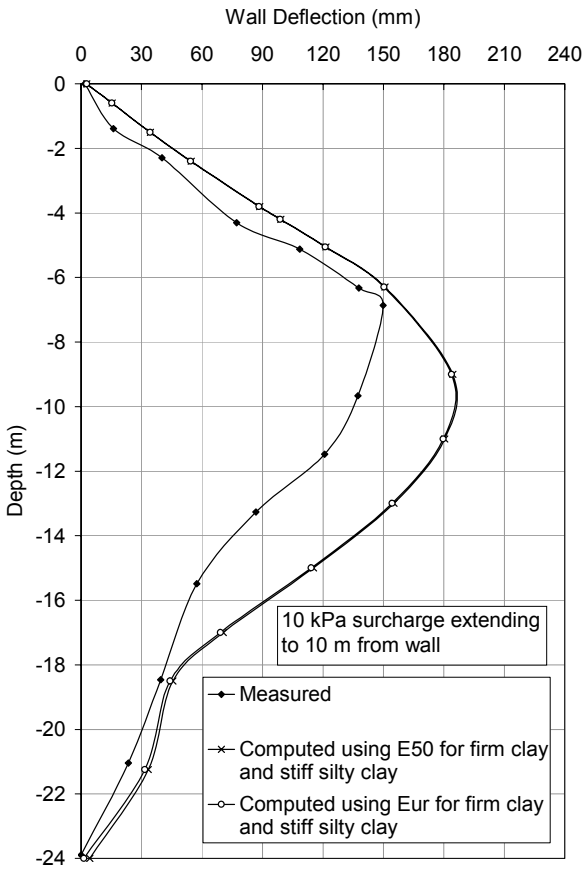

Figure 4.31 Wall Deflection at Rochor Complex (Lim et al., 2003)

4.5.6 Case 6: Ministry of Environment (MOE) Building

Figure 4.32 shows the cross-section and soil properties of this deep excavation. On the other hand, Figure 4.33 shows the finite element mesh used in the analysis. The excavation width was 70 m which was supported by YSPIV sheet piles penetrated to a depth of 24 m. It was done with bottom-up method. The original ground water table was about 0.5 m below surface. The soil parameters adopted in the analysis are shown in Tables 4.21 and 4.22. The preloads for all struts were 66.2 kN/m. The excavation sequence and structural properties are shown in Table 4.23 and 4.24, respectively. The computed and measured wall deflection profiles are shown in Figure 4.34. Using E_{ur} for dense silt improves the wall prediction especially at the wall base. The maximum measured and predicted wall deflections are about the same at 310 mm.

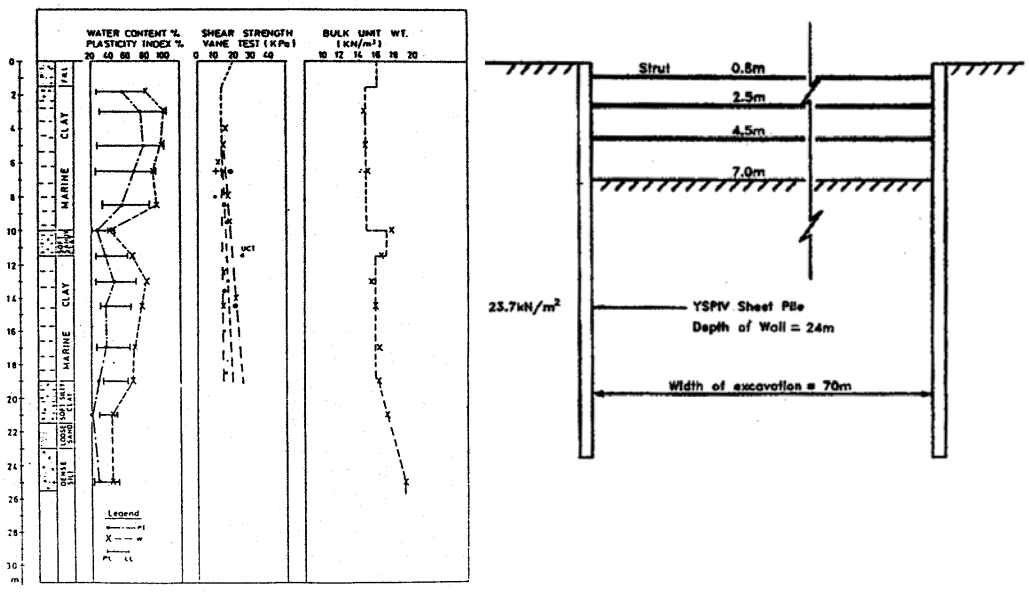

Figure 4.32 Cross-Section of Excavation at MOE Project (Kok, 1985)

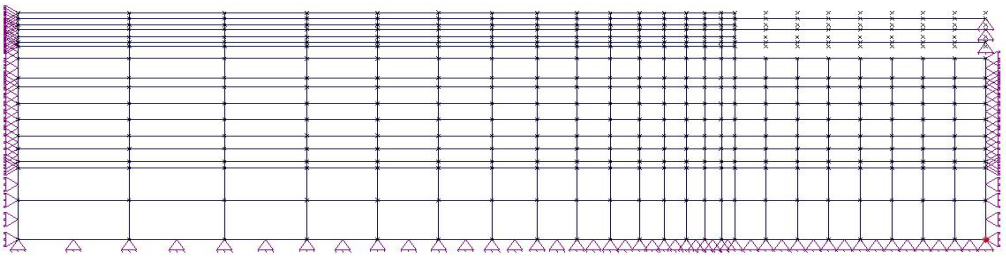

Figure 4.33 Finite Element Mesh for MOE Project

Table 4.21 Soil Properties of Upper and Lower Marine Clay at MOE Project

Soil Type	γ_{sat} (kN/m^3)	PI (%)	w_L (%)	G_s	κ	λ	e_Γ	ϕ_{cs} (^{o})	M	ν	k (m/s)
UMC	15	65	93	2.65	0.0761	0.3809	2.98	24.1	0.943	0.33	$1x10^{-9}$
LMC	16	50	68	2.65	0.0585	0.2930	2.19	25.6	1.01	0.33	$1x10^{-9}$
Soft Silty Clay	17	40	60	2.65	0.0468	0.2344	1.9	27.0	1.07	0.33	$1x10^{-9}$

Table 4.22 Soil Properties of Other Soils at MOE Project

Soil Type	γ_{sat} (kN/m^3)	ν	E_{50} (kPa)	E_{ur} (kPa)	c (kPa)	ϕ (^{o})	k (m/s)
Fill (Silty Clay) (PI = 40)	16	0.33	7200	-	18	0	$1x10^{-8}$
Sandy Clay (PI = 20)	17	0.33	9000	-	15	0	$1x10^{-7}$
Loose Sand (N = 6)	19	0.33	14000	-	0	35	$1x10^{-4}$
Dense Silt (N = 30)	19	0.33	90000	270000	150	0	$1x10^{-8}$

Table 4.23 Excavation Sequence at MOE Project

Stage	Excavation Sequence
1	Excavate to 1.8 m below a ground level (GL)
2	Install first level of strut at 0.8 m below GL and preload to 66.2 kN/m
3	Excavate to 3.7 m below GL
4	Install second level of strut at 2.5 m below GL and preload to 66.2 kN/m
5	Excavate to 5.1 m below GL
6	Install third level of strut at 4.5 m below GL and preload to 66.2 kN/m
7	Excavate to formation level at 7 m below GL

Table 4.24 Structural Properties of Excavation at MOE Project

Structural Members	E (kN/m^2)	A (m^2/m)	I (m^4/m)	Preload (kN/m)
Strut (at -0.8 m)	2.07×10^8	0.0058	-	66.2
Strut (at -2.5 m)	2.07×10^8	0.0058	-	66.2
Strut (at -4.5 m)	2.07×10^8	0.0058	-	66.2
YSP IV Sheetpile (beam element)	2.07×10^8	0.0186	0.000319	-

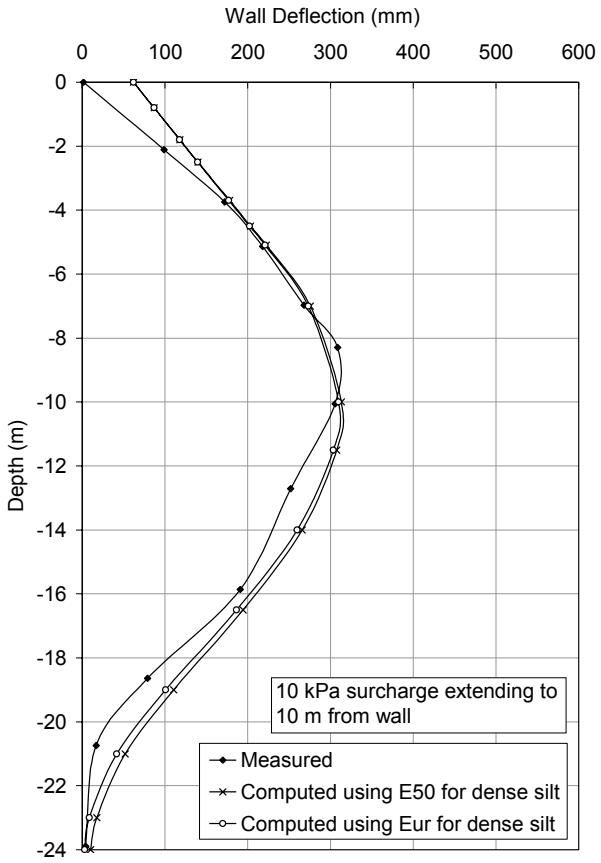

Figure 4.34 Wall Deflection at MOE Building

4.5.7 Case 7: Taipei Basin

Fang (1987) reported a 14.1 m deep excavation in the eastern part of Taipei Basin. The site plan is shown in Figure 4.35. The excavation width was about 68 m. The 700 mm thick diaphragm wall penetrated into the intermediate clay layer where the N_{SPT} was about 20. The wall length was 29.8 m. The excavation was constructed with bottom-up method. The cross-section and soil profile are shown in Figure 4.36. On the other hand, the finite element mesh is shown on Figure 4.37. The ground water table was about 2 m below surface. The preloading of struts was not included in the analysis due to unavailable information. The soil parameters adopted in the analysis are shown in Tables 4.25 and 4.26. For the intermediate clay layer, the average N_{SPT} of 20 yielded c_u =100 kPa. Since the water content of this clay is close to the plastic limit, the clay is stiff and over-consolidated. The excavation sequence and structural properties are shown in Table 4.27 and 4.28, respectively. The computed and measured wall deflection profiles are shown in Figure 4.38. Using E_{ur} in the intermediate clay and sand shows better agreement for both maximum wall deflection and deflection around the wall base. The maximum measured and predicted wall deflections using E_{ur} and E_{50} are 178, 180, and 190 mm, respectively. The corresponding differences are between +1% to +7%.

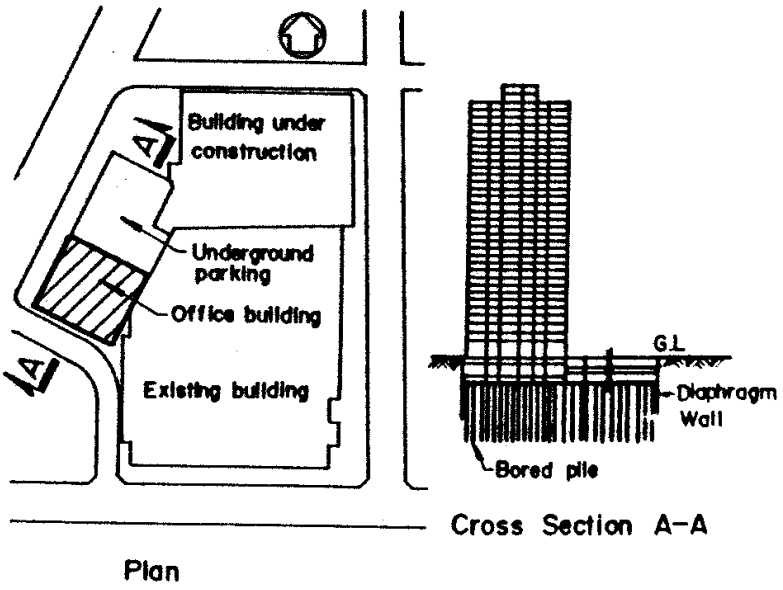

Figure 4.35 Location of deep excavation in Taipei Basin (Fang, 1987)

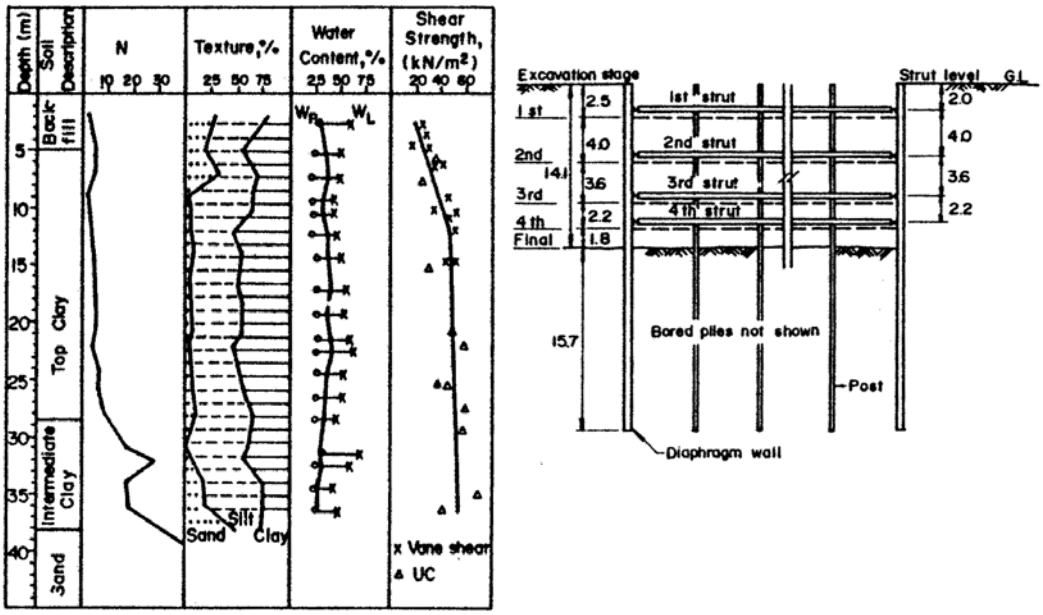

Figure 4.36 Typical Cross-Section of Deep Excavation and Soil Profile at Taipei Basin (Fang, 1987)

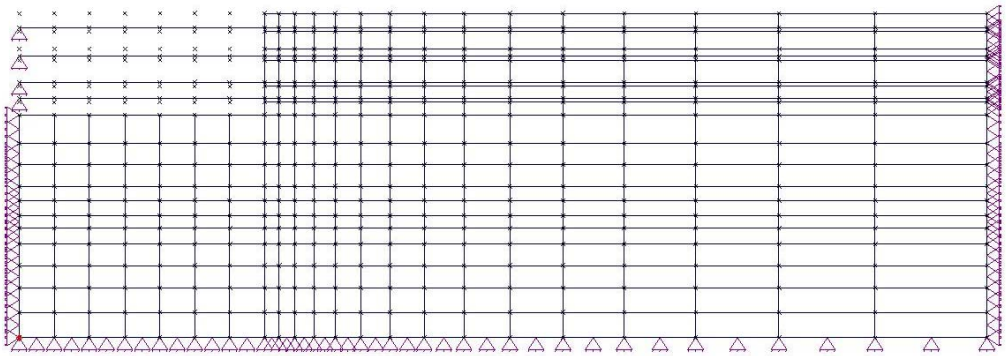

Figure 4.37 Finite Element Mesh for Taipei Basin Project

Table 4.25 Soil Properties of Clay at the 33-Storey Building in Taipei Basin

Soil Type	γ_{sat}	PI	w_L	G_s	κ	λ	e_Γ	ϕ_{cs}	M	ν	k
	(kN/m^3)	(%)	(%)					(^{o})			(m/s)
Top Clay	16.5	30	50	2.65	0.0350	0.1758	1.56	28.7	1.14	0.33	1x10^{-9}

Table 4.26 Soil Properties for Other Soils at the 33-Storey Building in Taipei Basin

Soil Type	γ_{sat}	ν	E_{50}	E_{ur}	c	ϕ	k
	(kN/m^3)		(kPa)	(kPa)	(kPa)	(^{o})	(m/s)
Back Fill (Sandy Clay) (PI = 40)	17	0.33	11250	-	25	0	1x10^{-6}
Intermediate Clay (PI = 25)	17	0.33	67500	202500	100	0	1x10^{-9}
Sand (N > 40)	20	0.33	45000	135000	0	42	1x10^{-5}

Table 4.27 Excavation Sequence at Taipei Basin Project

Stage	Excavation Sequence
1	Excavate to 2.5 m below a ground level (GL)
2	Install first level of strut at 2 m below GL
3	Excavate to 6.5 m below GL
4	Install second level of strut at 6 m below GL
5	Excavate to 10.1 m below GL
6	Install third level of strut at 9.6 m below GL
7	Excavate to 12.3 m below GL
8	Install fourth level of strut at 11.8 m below GL
9	Excavate to formation level at 14.1 below GL

Table 4.28 Structural Properties of Excavation at Taipei Basin Project

Structural Members	E (kN/m^2)	A (m^2/m)	I (m^4/m)	Preload (kN/m)
Strut (at -2 m)	2.07×10^8	0.0023	-	No information
Strut (at -6 m)	2.07×10^8	0.0028	-	No information
Strut (at -9.6 m)	2.07×10^8	0.0046	-	No information
Strut (at -11.8 m)	2.07×10^8	0.0046	-	No information
Diaphragm wall 700 mm (beam element)	2.8×10^7	0.7	0.02858	-

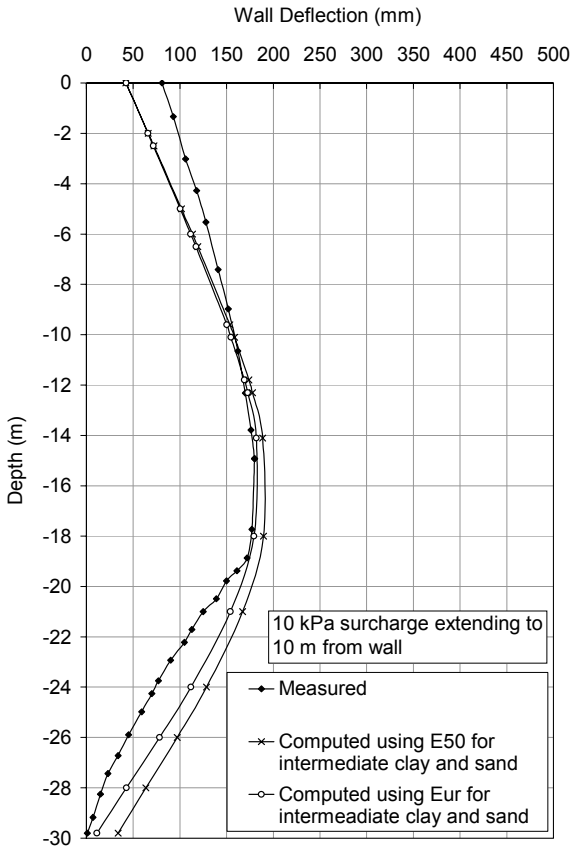

Figure 4.38 Wall Deflection at the 33-Storey Building in Taipei Basin

4.5.8 Case 8: TNEC Building

This study case was reported by Ou et al. (1998). It used the top-down construction method. A typical cross-section and the finite element mesh are shown in Figure 4.39 and 4.40, respectively. The depth and width of excavation were 19.7 and 43 m, respectively. The preloading for the first and second level of strut was 98.1 and 392 kN/m, respectively. The ground water table was 1.5 m below ground surface. The soil parameters adopted in the analysis are shown in Tables 4.29 and 4.30. The excavation sequence and structural properties are shown in Table 4.31 and 4.32, respectively. The computed and measured wall deflections are shown in Figure 4.41. The maximum measured and computed wall deflections using E_{ur} and E_{50} are 108, 129, and 132 mm, respectively. The corresponding differences are about 20%. The analysis using E_{ur} for the stiff silty clay and dense silty sand yielded better results for both maximum ground settlement and wall deflection. The computed and measured ground settlements are shown in Figure 4.42. The computed maximum ground settlement is about 78 mm. The shape of settlement troughs showed similar trend even though using E_{ur} yielded slightly better agreement. However, it should be noted that due to the limitation of soil model which cannot model the small strain non-linearity effect, the deflection shape is more difficult to match as compared to that of maximum ground settlement.

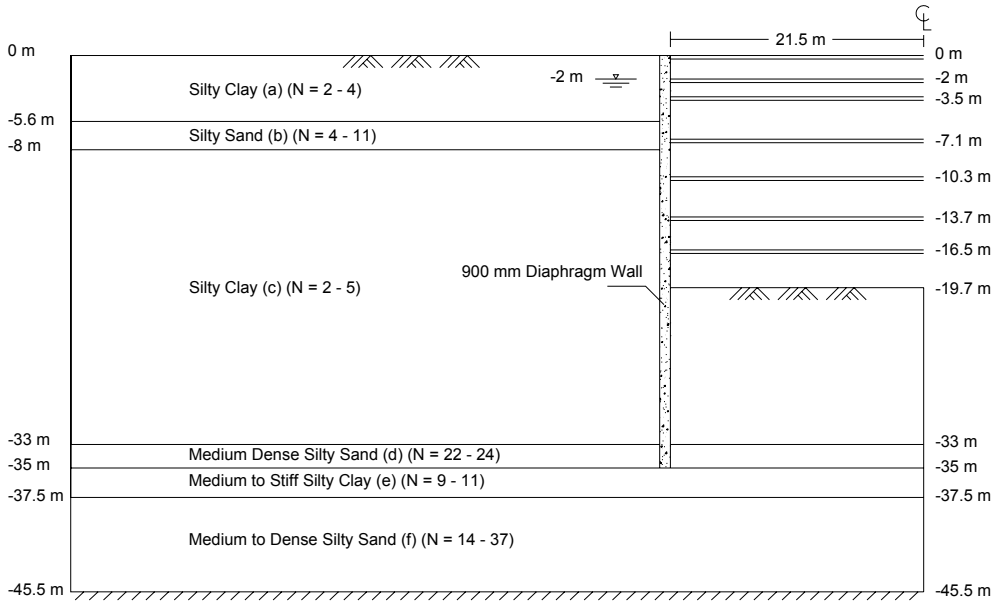

Figure 4.39 Cross-section of Deep Excavation at TNEC Building

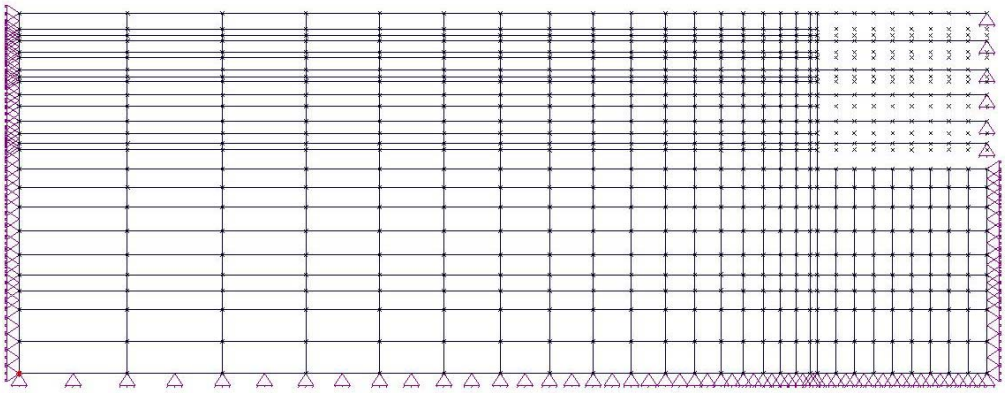

Figure 4.40 Finite Element Mesh for TNEC Building

Table 4.29 Soil Properties of Soft Silty Clay at TNEC Building

Soil Type	γ_{sat} (kN/m^3)	PI (%)	LL (%)	G_s	κ	λ	e_{Γ}	ϕ_{cs} (^{o})	M	ν	k (m/s)
Silty Clay (c) (N = 2-5)	19	15	40	2.7	0.0176	0.0879	1.2	33.0	1.333	0.33	$1x10^{-9}$

Table 4.30 Soil Properties of Silty Soils at TNEC Building

Soil Type	γ_{sat} (kN/m^3)	ν	E_{50} (kPa)	E_{ur} (kPa)	c (kPa)	ϕ (^{o})	k (m/s)
Silty Clay (a) (PI = 25, N = 2-4)	19	0.33	6750 to 27000	-	10 to 40	0	$1x10^{-9}$
Silty Sand (b) (N = 4 -11)	20	0.30	15000	-	0	35	$1x10^{-8}$
Silty Sand (d) (N = 22-24)	20	0.30	30000	90000	0	36	$1x10^{-8}$
Silty Clay (e) (PI = 25, N = 9-11)	19	0.33	202500	607500	300	0	$1x10^{-9}$
Silty Sand (f) (N = 14-37)	20	0.30	40000	120000	0	38	$1x10^{-8}$

Table 4.31 Excavation Sequence at TNEC Building

Stage	Excavation Sequence
1	Excavate to 2.8 m below a ground level (GL)
2	Install first level of strut (H300x300x10x15) at 2 m below GL and preload to 98.1 kN/m
3	Excavate to 4.9 m below GL
4	Cast floor slab at elevation of 3.5 m below GL
5	Demolish first level of strut and cast ground level of slab
6	Excavate to 8.6 m below GL
7	Cast floor slab at elevation of 7.1 m below GL
8	Excavate to 11.8 m below GL
9	Cast floor slab at elevation of 10.3 m below GL
10	Excavate to 15.2 m below GL
11	Cast floor slab at elevation of 13.7 m below GL
12	Excavate to 17.3 m below GL
13	Install second level of strut (H400x400x13x21) at 16.5 m below GL and preload to 392 kN/m
14	Excavate to formation level at 19.7 m below GL

Table 4.32 Structural Properties of Excavation at TNEC Building

Structural Members	E (kN/m^2)	A (m^2/m)	Preload (kN/m)
Strut (at 0 m)	2.8×10^7	0.6	-
Strut (at -2 m)	2.07×10^8	0.0015	98.1
Strut (at -3.5 m)	2.8×10^7	0.6	-
Strut (at -7.1 m)	2.8×10^7	0.6	-
Strut (at -10.3 m)	2.8×10^7	0.6	-
Strut (at -13.7 m)	2.8×10^7	0.6	-
Strut (at -16.5 m)	2.07×10^8	0.0073	392
Diaphragm wall 900 mm (quadrilateral element)	2.8×10^7	-	-

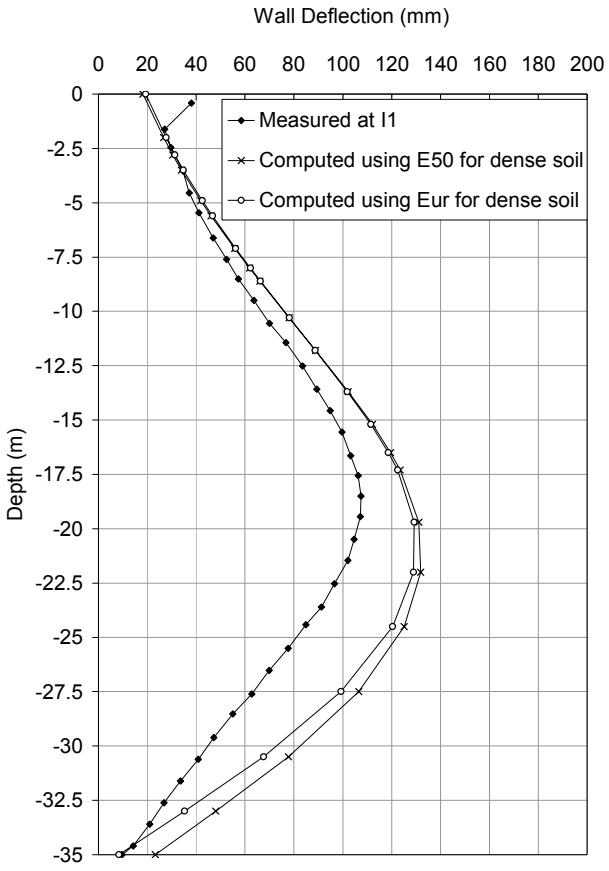

Figure 4.41 Wall Deflection of Deep Excavation Project at TNEC Building

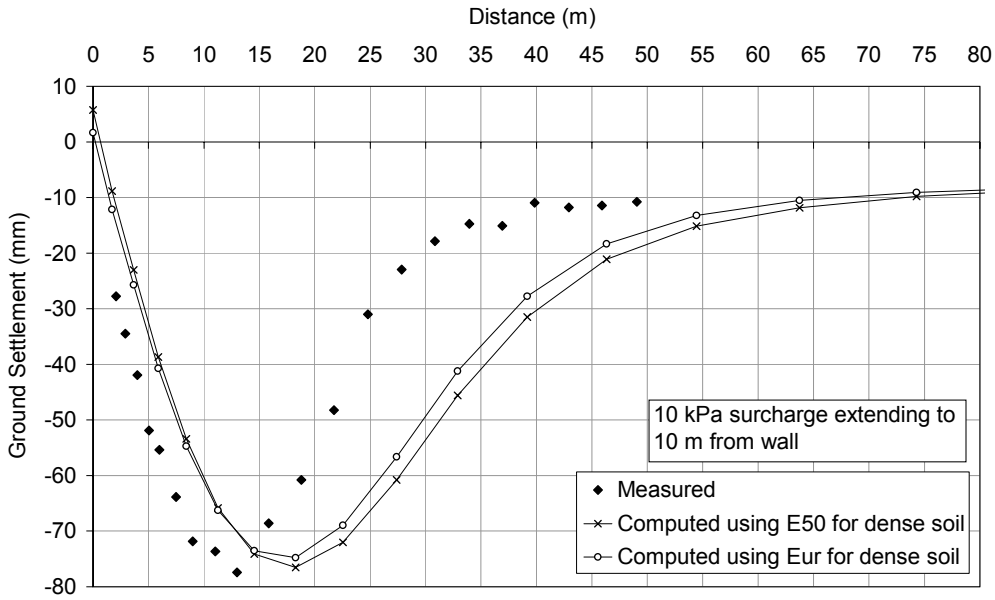

Figure 4.42 Ground Settlement of Deep Excavation Project at TNEC Building

4.5.9 Case 9: Formosa Project in Taiwan

This case was reported by Ou et al. (1993) and Hsieh and Ou (1998). The cross-section and finite element mesh are shown in Figure 4.43 and 4.44, respectively. The excavation width was about 35 m. It consisted of six levels of struts. Preloading was not included in the analysis due to unavailable information. The excavation was done with bottom-up method. The ground water level was about 2 m below surface. The soil parameters adopted in the analysis are shown in Tables 4.33 and 4.34. The excavation sequence and structural properties are shown in Table 4.35 and 4.36, respectively. The measured and predicted ground settlements are in good agreement as shown in Figure 4.45. However, it should be noted that due to the limitation of the soil model which cannot model the small strain non-linearity effect, the deflection shape is more difficult to match as compared to that of maximum ground settlement although the settlement troughs show similar trend. Using E_{ur} for gravel yielded slightly better results. The measured and computed wall deflections are shown in Figure 4.46. The results also show that using E_{ur} for gravel yields better result for the deflection around the wall base. The maximum measured and

predicted wall deflections are 62 and 75 mm, respective. The difference is about +21% regardless of the modulus used (E_{50} or E_{ur}).

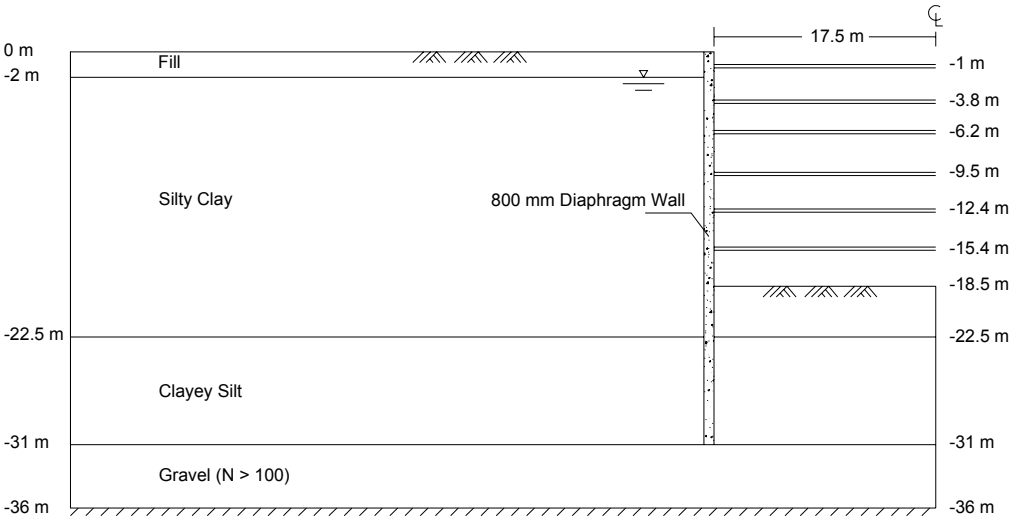

Figure 4.43 Cross-section of Deep Excavation in Formosa Project

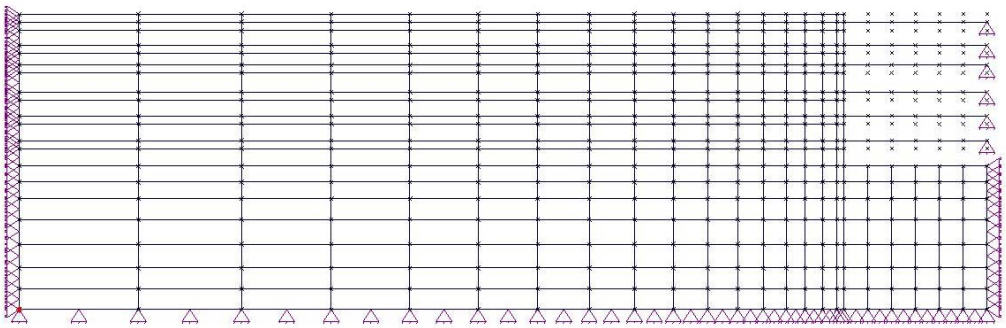

Figure 4.44 Finite Element Mesh for Formosa Project

Table 4.33 Soil Properties of Silty Clay at Formosa Project

Soil Type	γ_{sat}	PI	LL	G_s	κ	λ	e_Γ	ϕ_{cs}	M	ν	k
	(kN/m^3)	(%)	(%)					(^{o})			(m/s)
Silty Clay	19	10	30	2.7	0.0117	0.0586	0.89	32.0	1.287	0.33	1x10^{-9}

Table 4.34 Soil Properties of Other Soils at Formosa Project

Soil Type	γ_{sat}	ν	E_{50}	E_{ur}	c	ϕ	k
	(kN/m^3)		(kPa)	(kPa)	(kPa)	(^{o})	(m/s)
Fill	19	0.30	27000	-	40	0	1x10^{-6}
Clayey Silt (N = 11-17)	19	0.33	67500	-	100	0	1x10^{-8}
Gravel (N > 100)	20	0.25	60000	180000	0	44	1x10^{-4}

Table 4.35 Excavation Sequence at Formosa Project

Stage	Excavation Sequence
1	Excavate to 2 m below a ground level (GL)
2	Install first level of strut at 1 m below GL
3	Excavate to 4.8 m below GL
4	Install second level of strut at 3.8 m below GL
5	Excavate to 7.2 m below GL
6	Install third level of strut at 6.2 m below GL
7	Excavate to 10.5 m below GL
8	Install fourth level of strut at 9.5 m below GL
9	Excavate to 13.4 below GL
10	Install fifth level of strut at 12.4 m below GL
11	Excavate to 16.4 below GL
12	Install sixth level of strut at 15.4 m below GL
13	Excavate to formation level at 18.5 m below GL

Table 4.36 Structural Properties of Excavation at Formosa Project

Structural Members	E (kN/m^2)	A (m^2/m)	Preload (kN/m)
Strut (at -1 m)	2.07 x 10^8	0.0028	No information
Strut (at -3.8 m)	2.07 x 10^8	0.0028	No information
Strut (at -6.2 m)	2.07 x 10^8	0.0028	No information
Strut (at -9.5 m)	2.07 x 10^8	0.0028	No information
Strut (at -12.4 m)	2.07 x 10^8	0.0046	No information
Strut (at -15.4 m)	2.07 x 10^8	0.0046	No information
Diaphragm wall 800 mm (quadrilateral element)	2.8 x 10^7	-	-

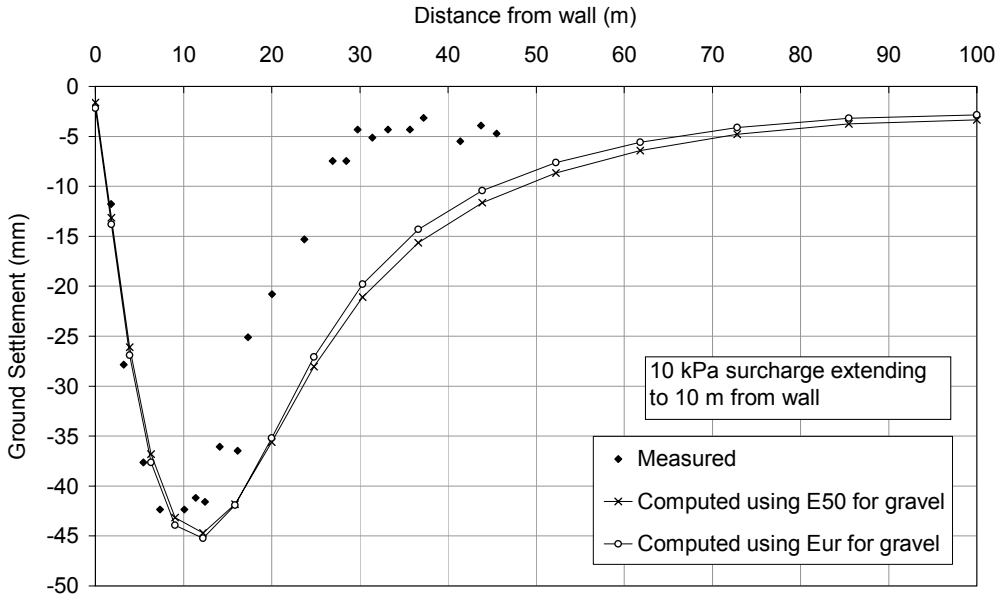

Figure 4.45 Ground Settlement of Deep Excavation at Formosa Project

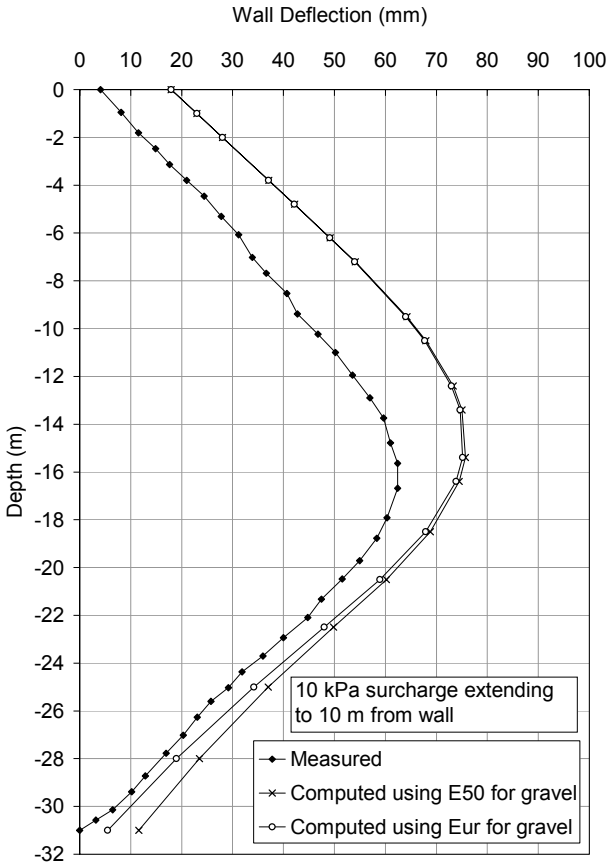

Figure 4.46 Wall Deflection of Deep Excavation at Formosa Project

4.5.10 Case 10: Kotoku Project

This project was reported by Miyoshi (1977). It was a deep excavation for subway construction in Tokyo. A typical cross-section and finite element mesh are shown in Figure 4.47 and 4.48. It had six levels of struts and was supported by 400 mm thick diaphragm wall combined with H piles. The excavation was constructed with bottom-up method. No preloads were applied in the analysis due to unavailable information. The ground water level was about 2 m below surface. The soil properties are shown in Tables 4.37 and 4.38. The excavation sequence and structural properties are shown in Table 4.39 and 4.40, respectively. The computed and measured ground settlements are shown in Figure 4.49. It shows that the predicted settlement trough matches reasonable well with measurement. However, the predicted ground settlements are smaller than those measured which are 136 and

150 mm, respectively. The difference is about -9%. The measured and computed wall deflections are shown in Figure 4.50. The maximum measured and computed wall deflections are 170 and 210 mm, respectively. The difference is about +23% regardless of the modulus used (E_{ur} or E_{50}). Results from the analysis using E_{ur} yielded a slightly better agreement with the measured ground settlement and wall deflection.

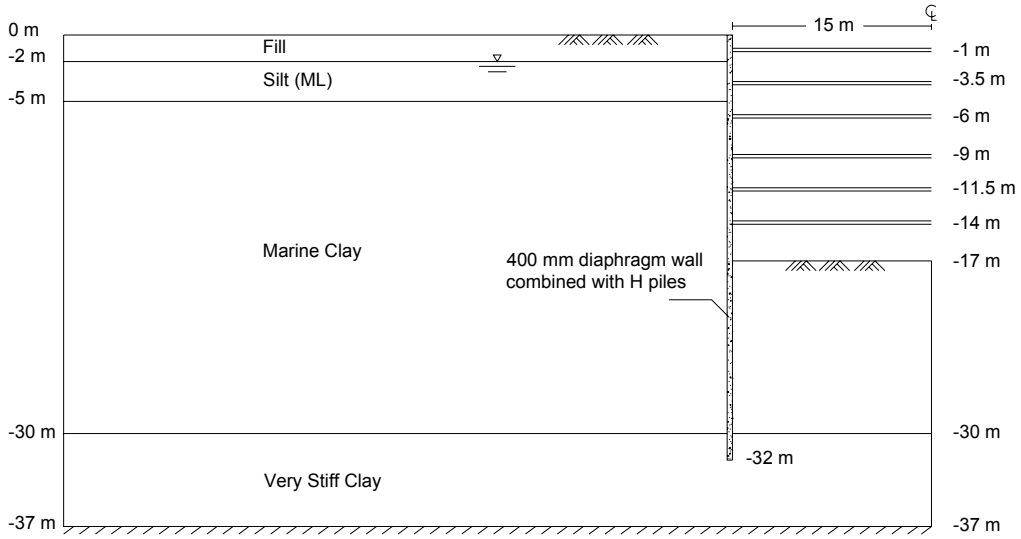

Figure 4.47 Cross-Section of Deep Excavation at Kotoku Project in Tokyo

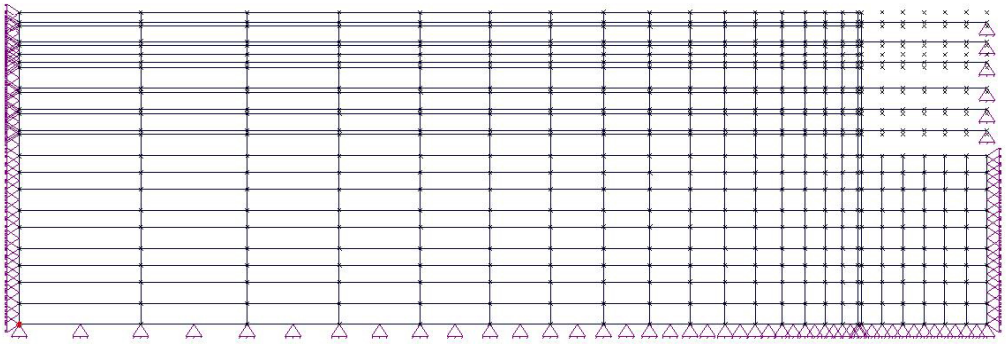

Figure 4.48 Finite Element Mesh for Kotoku Project

Table 4.37 Soil Properties of Marine Clay at Kotoku Project

Soil Type	γ_{sat} (kN/m^3)	PI (%)	LL (%)	G_s	κ	λ	e_Γ	ϕ_{cs} (^{o})	M	ν'	k (m/s)
Marine Clay	16	25	60	2.6	0.0293	0.1465	1.8	28.0	1.113	0.33	$1x10^{-9}$

Table 4.38 Soil Properties of Other Soils at Kotoku Project

Soil Type	γ_{sat} (kN/m^3)	ν	E_{50} (kPa)	E_{ur} (kPa)	c (kPa)	ϕ (^{o})	k (m/s)
Fill	19	0.30	30000	-	50	0	$1x10^{-7}$
Silt (ML)	16	0.33	30000	-	50	0	$1x10^{-8}$
Very Stiff Clay	16	0.33	96000	288000	160	0	$1x10^{-9}$

Table 4.39 Excavation Sequence at Kotoku Project

Stage	Excavation Sequence
1	Excavate to 1.5 m below a ground level (GL)
2	Install first level of strut at 1 m below GL
3	Excavate to 4 m below GL
4	Install second level of strut at 3.5 m below GL
5	Excavate to 6.5 m below GL
6	Install third level of strut at 6 m below GL
7	Excavate to 9.5 m below GL
8	Install fourth level of strut at 9 m below GL
9	Excavate to 12 below GL
10	Install fifth level of strut at 11.5 m below GL
11	Excavate to 14.5 below GL
12	Install sixth level of strut at 14 m below GL
13	Excavate to formation level at 17 m below GL

Table 4.40 Structural Properties of Excavation at Kotoku Project

Structural Members	E (kN/m^2)	A (m^2/m)	Preload (kN/m)
Strut (at -1 m)	2.07×10^8	0.0028	No information
Strut (at -3.5 m)	2.07×10^8	0.0028	No information
Strut (at -6 m)	2.07×10^8	0.0028	No information
Strut (at -9 m)	2.07×10^8	0.0074	No information
Strut (at -11.5 m)	2.07×10^8	0.0074	No information
Strut (at -14 m)	2.07×10^8	0.0074	No information
Diaphragm wall 800 mm (quadrilateral element)	2.8×10^7	-	-

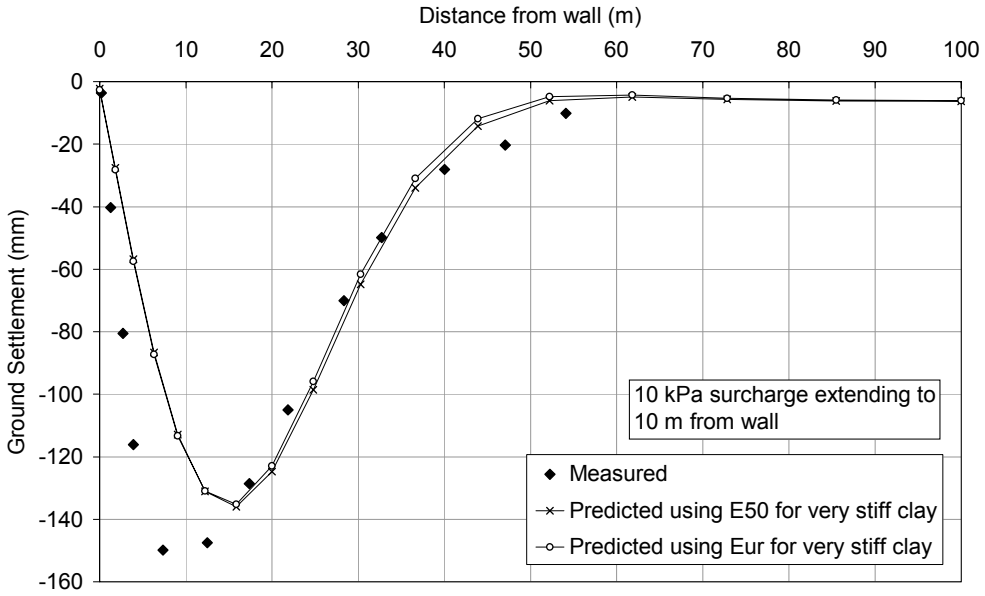

Figure 4.49 Ground Settlements at Kotoku Project

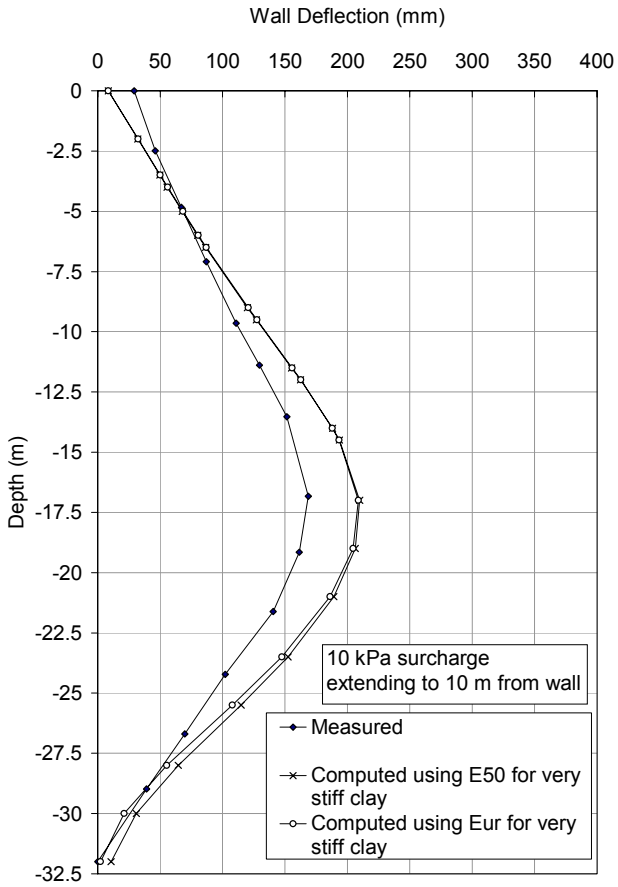

Figure 4.50 Wall Deflections at Kotoku Project

4.5.11 Case 11: Oxley Rise Development

This project was reported by Poh et al. (1997). The excavation was conducted in stiff soil. A typical cross-section and finite element mesh are shown in Figure 4.51 and 4.52. It consisted of three levels of struts and was supported by 600 mm thick diaphragm wall. The ground water level was about 4 m below surface. The excavation was approximately 50 m long, 33 m wide and 11.1 m deep. It was constructed with bottom-up method. The struts were not preloaded. The soil properties are shown in Table 4.41. The excavation sequence and structural properties are shown in Table 4.42 and 4.43, respectively. The computed and measured wall deflections are shown in Figure 4.53. The maximum measured and predicted values using E_{ur} and E_{50} are 10, 8.5 and 10.5 mm, respectively. Using E_{50} for moderately weak to strong sandstone yields better prediction for the maximum wall deflection. However, using E_{ur} for that soil layer improves the prediction around the wall toe. The differences in maximum wall deflection are about +15% and -5% using E_{ur} and E_{50}, respectively.

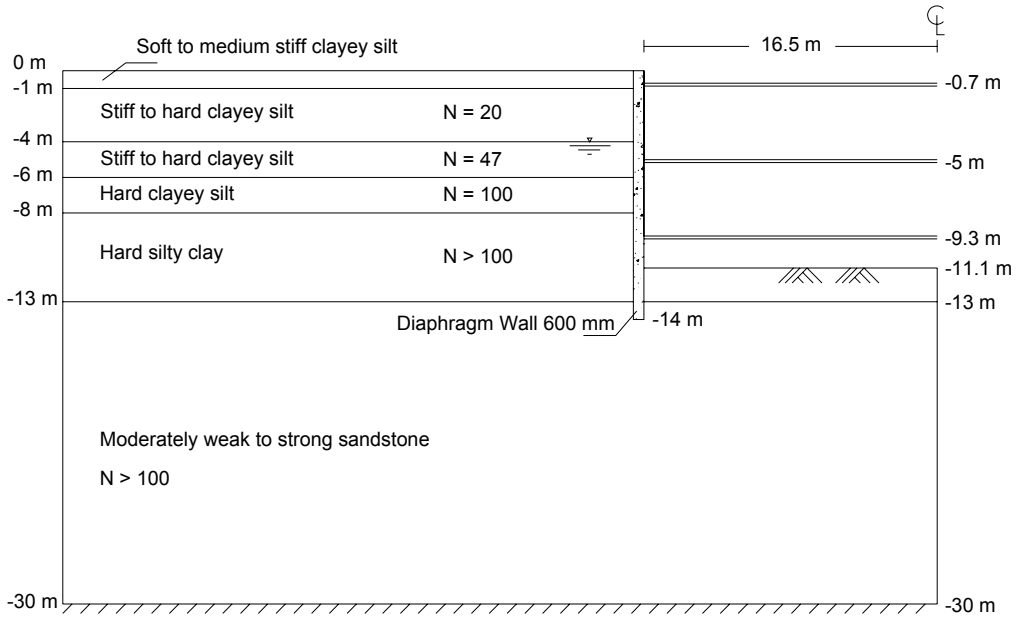

Figure 4.51 Cross-Section of Deep Excavation at Oxley Rise Development

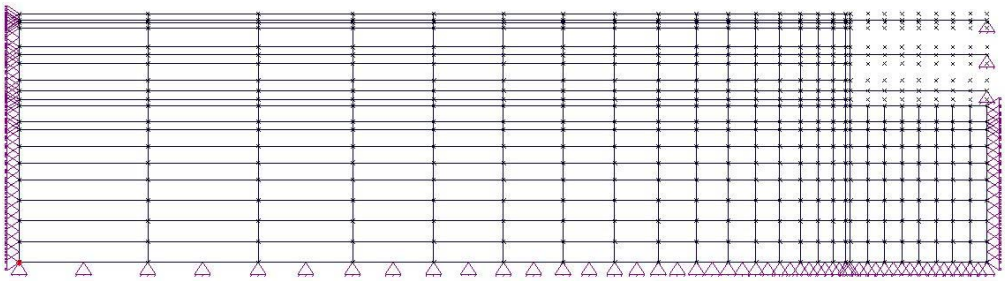

4.52 Finite Element Mesh for Oxley Rise Development

Table 4.41 Soil Properties at Oxley Rise Development

Soil Type	γ_{sat} (kN/m^3)	ν	E_{50} (kPa)	E_{ur} (kPa)	c (kPa)	ϕ (^{o})	k (m/s)
Soft to medium stiff clayey silt	19	0.33	6000	-	20	0	$1x10^{-7}$
Stiff to hard clayey silt (N = 20)	19.5	0.33	40000	-	100	0	$1x10^{-8}$
Stiff to hard clayey silt (N = 47)	20	0.33	94000	-	235	0	$1x10^{-8}$
Hard clayey silt (N = 100)	22	0.33	200000	-	500	0	$1x10^{-8}$
Hard silty clay (N > 100)	22	0.33	320000	-	800	0	$1x10^{-8}$
Moderately weak to strong sandstone (N > 100)	22	0.33	400000	1200000	1000	0	$1x10^{-8}$

Table 4.42 Excavation Sequence at Oxley Rise Development

Stage	Excavation Sequence
1	Excavate to 1.7 m below a ground level (GL)
2	Install first level of strut at 0.7 m below GL
3	Excavate to 6 m below GL
4	Install second level of strut at 5 m below GL
5	Excavate to 10.3 m below GL
6	Install third level of strut at 9.3 m below GL
7	Excavate to formation level at 11.1 m below GL

Table 4.43 Structural Properties of Excavation at Oxley Rise Development

Structural Members	E (kN/m^2)	A (m^2/m)	Preload (kN/m)
Strut (at -1 m)	2.07×10^8	0.0026	No preloading
Strut (at -3.5 m)	2.07×10^8	0.0074	No preloading
Strut (at -6 m)	2.07×10^8	0.0026	No preloading
Diaphragm wall 600 mm (quadrilateral element)	2.8×10^7	-	-

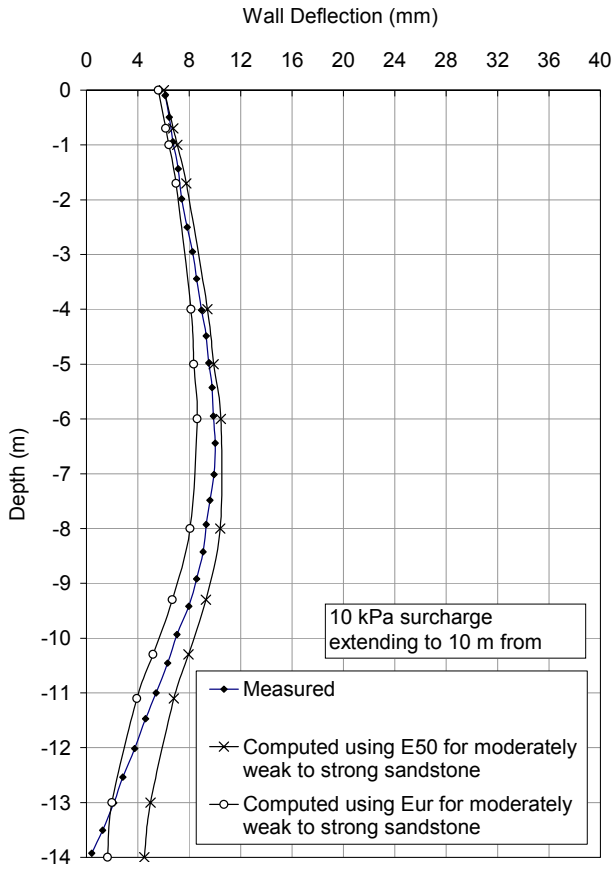

Figure 4.53 Wall Deflection Profiles at Oxley Rise Development

4.5.12 Case 12: Development near River Valley Road

This project was reported by Poh et al. (1997). This is a second case for excavation in stiff soil. The project is a 10-storey mixed commercial and residential development with two levels of basement as car park. The basement excavation was about 75 m long, 45 m wide and 10.5 m deep. The soil was retained by a 15.5 m long and 600 mm thick diaphragm wall. There was only one level of strut. The excavation was done with bottom-up method. The struts were not preloaded. A typical cross-section and finite element mesh are shown in Figure 4.54 and 4.55, respectively. The excavation sequence and structural properties are shown in Table 4.44 and 4.45, respectively. The soil properties are shown in Table 4.46. The measured and computed wall deflections are shown in Figure 4.56. Results of the analyses show that using E_{50} for very stiff sandy clayey silt and hard clayey sand is

not stiff enough especially the deflection around the wall bottom. The prediction was improved by using E_{ur}. The maximum measured and computed wall deflection using E_{ur} and E_{50} are 30, 28, and 34 mm, respectively. The corresponding differences are between +7% to +13 %.

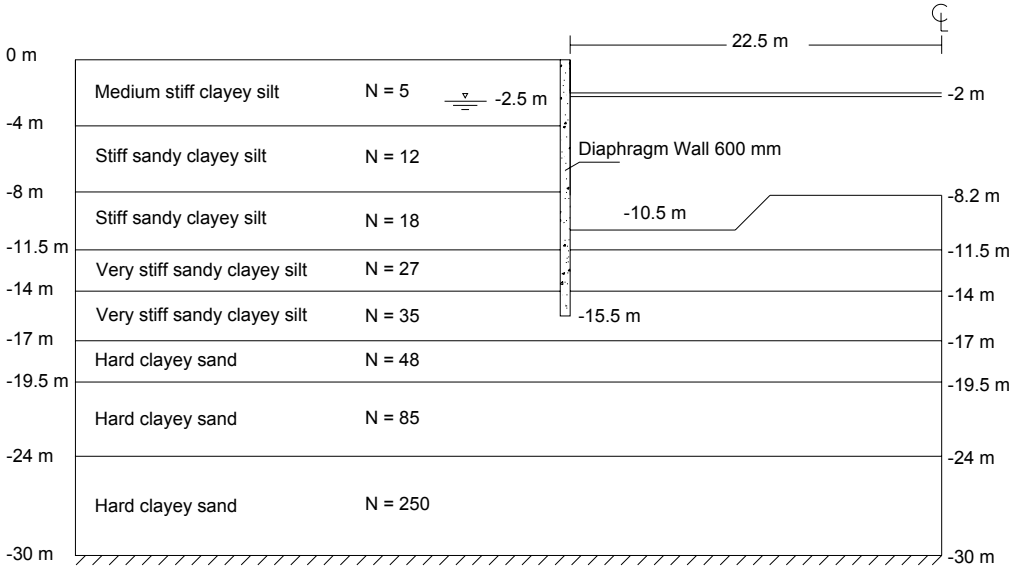

Figure 4.54 Cross-Section of Deep Excavation at River Valley Road Project

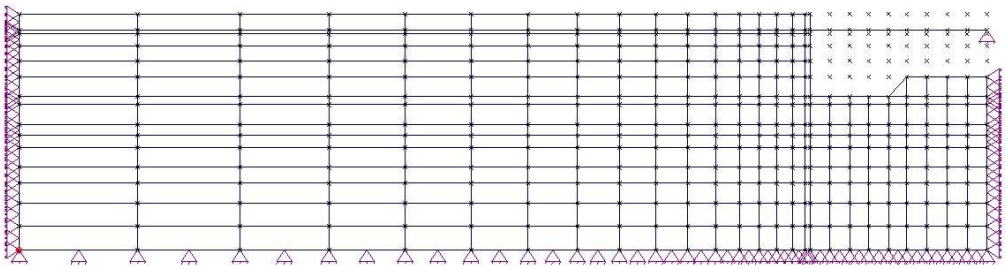

Figure 4.55 Finite Element Mesh for River Valley Road Project

Table 4.44 Excavation Sequence at River Valley Road Project

Stage	Excavation Sequence
1	Excavate to 2.5 m below a ground level (GL)
2	Install first level of strut at 2 m below GL
3	Excavate to formation level at 10.5 m below GL

Table 4.45 Structural Properties of Excavation at River Valley Road Project

Structural Members	E (kN/m^2)	A (m^2/m)	Preload (kN/m)
Strut (at -2 m)	2.07×10^8	0.0038	No preloading
Diaphragm wall 600 mm (quadrilateral element)	2.8×10^7	-	-

Table 4.46 Soil Properties at River Valley Road Project

Soil Type	γ_{sat} (kN/m^3)	ν	E_{50} (kPa)	E_{ur} (kPa)	c (kPa)	ϕ (^{o})	k (m/s)
Medium stiff clayey silt (N = 5)	18.5	0.33	7500	-	25	0	$1x10^{-7}$
Stiff sandy clayey silt (N = 12)	18.5	0.33	24000	-	60	0	$1x10^{-8}$
Stiff sandy clayey silt (N = 18)	19	0.33	36000	-	90	0	$1x10^{-8}$
Very stiff sandy clayey silt (N = 27)	19.5	0.33	54000	-	135	0	$1x10^{-8}$
Very stiff sandy clayey silt (N = 35)	20	0.33	70000	210000	175	0	$1x10^{-8}$
Hard Clayey Sand (N = 48)	20.5	0.33	96000	288000	240	0	$1x10^{-8}$
Hard Clayey Sand (N = 85)	21.5	0.33	170000	510000	425	0	$1x10^{-8}$
Hard Clayey Sand (N = 250)	22	0.33	500000	1500000	1250	0	$1x10^{-7}$

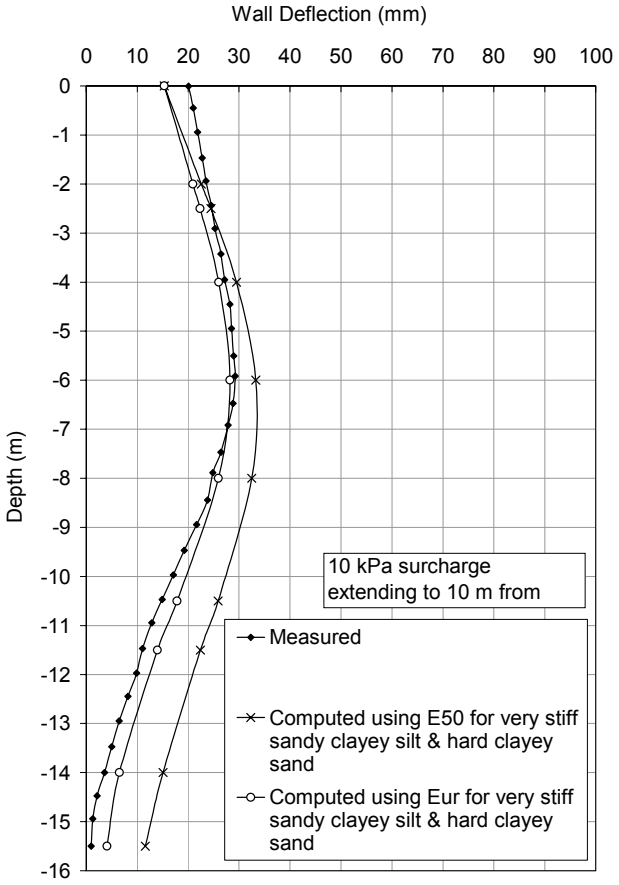

Figure 4.56 Wall Deflection at River Valley Road Project

4.6 Summary and Conclusion

A number of empirical charts and correlations have been adopted for the determination of soil parameters for the modified Cam Clay and Mohr-Coulomb models. In order to investigate their reliability, twelve cases involving soft and stiff soil have been back-analyzed with the aid of the computer program Sage Crisp. In all analyzes, the modified Cam Clay model was used for soft clay. The parameters were determined based largely on the Atterberg limits. The Mohr-Coulomb model was used for stiff clay and sand. The parameters for these soils were determined based on the SPT blow counts.

Ground settlement predictions were studied with four cases. The maximum settlements between prediction and measurement are in agreement within ±10%. The settlement troughs show similar trend. The presence of roads, buildings, and complex soil profile in the field may have contributed to differences between the predicted and measured values. Moreover, due to the limitation of the soil model which cannot model the small strain non-linearity effect, it also contributes to the differences in ground settlement profiles.

The computed maximum wall deflections fall within ±25% of the measured values for all except one case. Ten cases over-predicted the maximum wall deflection. Two cases yielded essentially the same deflection. Using E_{ur} compared to E_{50} improves the prediction especially around the bottom of wall.

All of these back-analyses show that the finite element analysis is a powerful method to predict soil movements around deep excavation even though it is not perfect. Some soil parameters which are not available can be estimated using published and proposed charts. They should be used with care since only twelve cases were used in the validation exercise. The new charts are not intended to replace field or laboratory tests. If soil properties from high quality tests are available, they should be used in the determination of soil parameters.

CHAPTER 5
NEW CHART FOR PREDICTING FRAME STRUCTURE DAMAGE

5.1 Introduction

Previous works regarding allowable building settlement up to 1974 are mainly based on empirical approach from measured settlements and the associated building damages. Terzaghi and Peck (1943) related differential settlements with building damage. Based on their observations, 20 mm of differential settlement is the safe limit. Skempton and MacDonald (1956) related angular distortion with building damage. They find out that an angular distortion of 1/300 is the safe limit. However, all of these values are not related with building dimension, such as the length and height of a building. Papers published by Polshin and Tokar (1957) showed that the safe limit of building settlement is affected by building dimension.

Burland and Wroth (1974) carried out an in depth study regarding the mechanism of building cracks. The simple theoretical study has provided a good understanding of the mechanism. Charts were developed relating cracking potential with building dimension and relative deflection. Boscardin and Cording (1989) also developed a similar chart to predict building damage. The importance of horizontal strain is highlighted in their chart.

Boone (1996) proposed another chart which considers the ground movement profile, location of building, building dimension, bending and shear stiffness of building and slippage between ground and foundation. The latest method is from Finno et al. (2005). It does not use chart to predict building damage. They extended the equations from Burland and Wroth (1974) to allow explicit input of Young's modulus (E) and shear modulus (G). The structure is modeled as a laminated beam. They used the computed deflection ratio as the damage criterion.

Burland and Wroth's (1974) chart categorizes building damage into severe, moderate and negligible. Boscardin and Cording chart assumed the L/H ratio to be one. It ignored the importance of building dimension as highlighted by Polshin and Tokar (1957). Boone (1996) assumed the horizontal strain in building to be the same as that of ground which may not be true in modern buildings. The method by Finno et al. (2005) requires manipulation of a series of equations which can be a tedious and difficult task.

In this paper, a chart for framed structures is proposed to predict building damages. Data from literatures and construction of MRT North East Line in Singapore showed that this practical chart works well in predicting building damage.

5.2 Deformation of Frame Structures

In a frame structure, cracks are usually caused by differential settlements and not by bending. According to Burland and Wroth (1974), it is shear strain rather than bending strain that causes cracking. The crack is usually a diagonal crack rather than vertical crack. Data from Fjeld (1963) confirms this type of damage for frame structures as shown in Figure 5.1. The situation becomes worse in the case of deep excavation or mining where the horizontal movement can be significant (Boscardin and Cording, 1989). The differential column settlement which causes diagonal cracks is illustrated in Figure 5.2.

In a frame structure, cracks in the infill wall are caused by differential settlement between columns. Therefore, it is logical to measure the dimension of building for a particular frame rather than the whole building as illustrated in Figure 5.3. Frame U is affected by dimension H1 and L1 and differential settlement between columns C1 and C2. It is not affected by the differential settlement between C2 and C3. Therefore, the damage analysis of infill wall for frame structures should be analyzed frame by frame rather than as a whole structure.

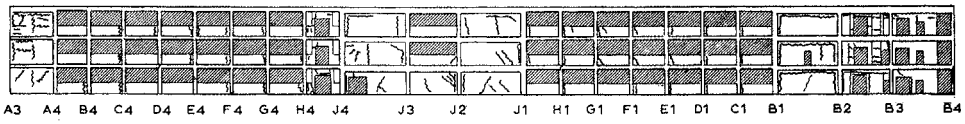

Figure 5.1 Differential Settlement at Each Column of Building (Fjeld, 1963)

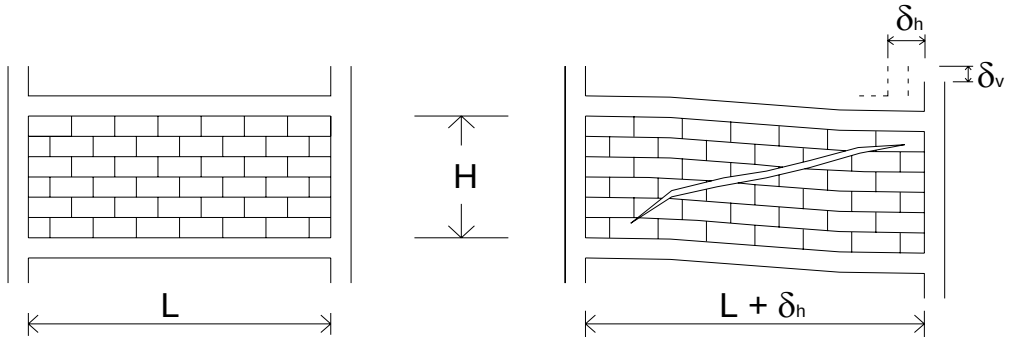

Figure 5.2 Differential Column Settlement Causing Diagonal Crack

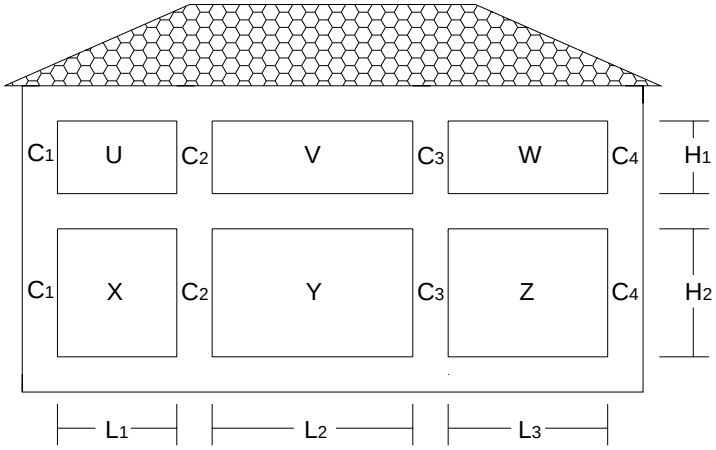

Figure 5.3 Frame Structures

Burland and Wroth (1974) reported that visible cracking is likely to occur at an average diagonal tensile strain between 0.00081 and 0.00137 with a mean value of 0.00115 which is very small. Therefore, it is almost impossible to prevent cracking in infilled frames. This type of frame movements and the inability of the infilled brick to prevent diagonal cracks can be used to derive an equation to predict the performance of frame structures due to ground movements as illustrated in Figure 5.4.

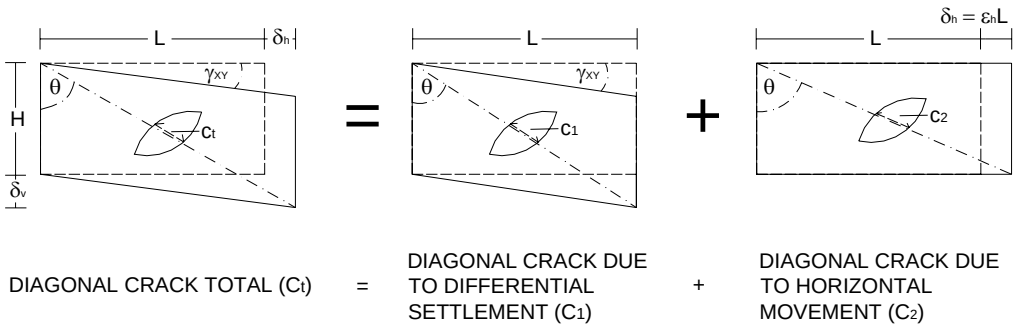

Figure 5.4 Diagonal Crack due to Differential Settlement and Horizontal Movement

Horizontal movement alone may not cause diagonal strain as shown in Figure 5.4. However, it can happen once the crack has occurred due to differential settlement. Once the crack occurs, it will become the weakest point. Any horizontal movements will enlarge this crack. Therefore, horizontal movement can increase the diagonal strain when it is combined with differential settlement.

The increase of diagonal strain due to differential settlement and horizontal movement can be expressed by Equation 5.1 from Gere and Timoshenko (1997). Using strain as a root equation to determine building damage is better than using stress equation. This is because ground settlement and building dimension can be readily measured. These measurements can be used to predict crack width or crack strain. Burland and Wroth (1974), Boscardin and Cording (1989), Boone (1996), and Finno et al. (2005) used stress equation to derive their methods. The difficulty is to select the appropriate stiffness to convert stress to strain components. This stiffness is difficult to estimate. Since what is measured and computed is displacement, using strain in the root equation can prevent this uncertainty.

$$\varepsilon_d = \varepsilon_{d1} + \varepsilon_{d2} = \gamma_{xy} \sin\theta \cos\theta + \varepsilon_h \sin^2\theta \qquad (5.1)$$

It was assumed that the crack width is directly proportional to the diagonal strain. Therefore, Equation 5.1 can be further expanded into Equations 5.2 to 5.4.

$$\varepsilon_d = \frac{c_t}{\sqrt{L^2 + H^2}} \tag{5.2}$$

$$\varepsilon_{d1} = \gamma_{xy} \sin\theta \cos\theta \Leftrightarrow \frac{c_1}{\sqrt{L^2 + H^2}} = \frac{\delta_v}{L}\left(\frac{L}{\sqrt{L^2 + H^2}}\right)\left(\frac{H}{\sqrt{L^2 + H^2}}\right) = \frac{\delta_v H}{L^2 + H^2} \tag{5.3}$$

$$\varepsilon_{d2} = \varepsilon_h \sin^2\theta \Leftrightarrow \frac{c_2 \sin\theta}{L}\left(\frac{L}{\sqrt{L^2 + H^2}}\right)^2 = \frac{c_2 L^2}{\left(L^2 + H^2\right)\sqrt{L^2 + H^2}} \tag{5.4}$$

The combination of Equations 5.2 to 5.4 can be used to predict the total width of diagonal crack as shown in Equation 5.5.

$$\frac{c_t}{\sqrt{L^2 + H^2}} = \frac{\delta_v H}{L^2 + H^2} + \frac{c_2 L^2}{\left(L^2 + H^2\right)\sqrt{L^2 + H^2}} = \frac{\delta_v H}{L^2 + H^2} + \frac{\left(kc_t\right)L^2}{\left(L^2 + H^2\right)\sqrt{L^2 + H^2}} \tag{5.5}$$

The factor k relates the horizontal strain to crack width. A value of zero means no horizontal strain. A value of 1 means the total crack is entirely due to horizontal movement. Furthermore, Equation 5.5 can be rearranged into Equation 5.6. The parameter θ is equal to $\tan^{-1}$(L/H) in degree.

$$\delta_v = c_t\left[\left(1 - k\right)\tan\theta \sin\theta + \cos\theta\right] \tag{5.6}$$

Parameter k can be determined from Equation 5.7. Parameter c_1 can be determined by rearranging Equation 5.3 as shown in Equation 5.8. Parameter c_2 can be determined from Figure 5.4 and is presented in Equation 5.9. Parameter c_t can be determined from Equation 5.10.

$$c_t = c_1 + c_2 \tag{5.7}$$

$$c_1 = \frac{\delta_v H}{\sqrt{L^2 + H^2}} \tag{5.8}$$

$$c_2 = \frac{\delta_h}{\sin\theta} = \frac{\varepsilon_h L}{\sin\theta} \tag{5.9}$$

$$c_t = \frac{c_2}{k} = \frac{\left(\frac{\varepsilon_h L}{\sin\theta}\right)}{k} = \frac{\varepsilon_h L}{k \sin\theta} \tag{5.10}$$

Equation 5.10 can be expanded into Equation 5.11.

$$c_t = c_1 + c_2 \Leftrightarrow \frac{\varepsilon_h L}{k \sin\theta} = \frac{\delta_v H}{\sqrt{L^2 + H^2}} + \frac{\varepsilon_h L}{\sin\theta} \tag{5.11}$$

Equation 5.11 can be rearranged into Equation 5.12.

$$k = \frac{\varepsilon_h \sqrt{L^2 + H^2}}{\delta_v \cot\theta \sin\theta + \varepsilon_h \sqrt{L^2 + H^2}} \tag{5.12}$$

When the horizontal strain (ε_h) is zero, k is equal to 0 which means cracking is only caused by differential settlement (δ_v) between two columns. When δ_v equals to zero, k is equal to 1. In this case, cracking is solely due to the horizontal strain.

Equations 5.6 and 5.12 can be used to predict building damage. Equation 5.6 shows the relationship between frame dimension (L and H), total crack width (c_t), and the corresponding allowable differential settlement (δ_v). On the other hand, the factor k in Equation 5.12 determines the contributions from differential settlement and horizontal strain. Both equations can be plotted into 3-D graphs with several c_t values. It is illustrated in Figure 5.5 for c_t equals to 25 mm. In order to observe the effect of horizontal strain more clearly, Figure 5.6 is plotted for certain k value. It is a projection of the 3-D graph onto the δ_v - θ plane.

Two major conclusions can be obtained from Figures 5.5 and 5.6. When L/H increases, the tolerable settlement between columns also increases. It shows that if L increases or H decreases, the frame structure is more tolerable to differential settlement. This observation is similar to that reported by Burland and Wroth (1974). On the other hand, Figure 5.6 shows that when the horizontal strain

increases (increasing in k value), the building is less tolerable with differential settlement. This is also similar to the observation by Boscardin and Cording (1989).

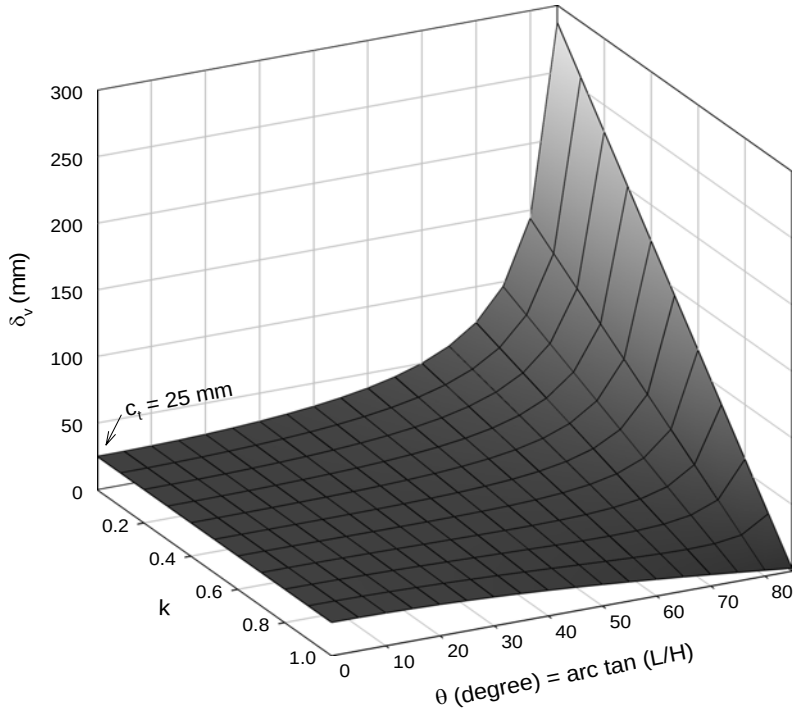

Figure 5.5 A 3-D Plot of Equations 5.6 and 5.12 with c_t = 25 mm

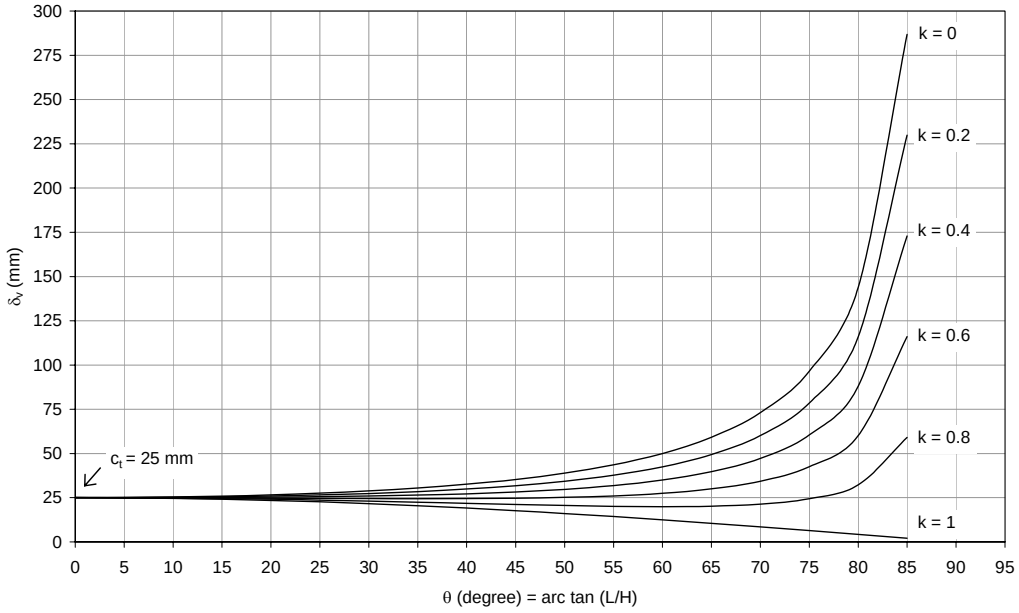

Figure 5.6 2-D Plot of Equations 5.6 and 5.12 with c_t = 25 mm

The proposed method considers only the differential settlement between columns, horizontal strain, and building dimension. In reality, other factors may also affect the crack width. Recent research by Dowding and McKenna (2005) has shown that the crack width is also influenced by the environmental changes such as temperature and humidity. This factor is not considered in the proposed method.

5.3 A New Chart to Predict Frame Damage

Burland and Wroth (1974) proposed several categories of building damage from negligible to very severe. The approximate crack width for each category is given as a guide to classify the damage as shown in Table 5.1. In a frame structure, this width is the total crack (c_t). Therefore, by inputting this value into Equation 5.6, several equations can be obtained to separate each class of damage. With the parameter c_t being known, it is necessary to assess the parameter k which describes the effect of horizontal strain.

Table 5.1 Classification of Visible Damage (Adapted from Burland, 1997)

No	Class of Damage	Approximate Width of Crack (mm)
0	Negligible	0.1
I	Very Slight	1
II	Slight	5
III	Moderate	< 15
IV	Severe	< 25
V	Very Severe	> 25

Boscardin (1980) did a series of finite element analysis to study how the effects of grade beam on the integrity of a frame structure are. It was found out that the presence of grade beam prevents any significant horizontal strains to develop in the building. Finno and Bryson (2002) also reported similar findings. Therefore, damage due to horizontal strain is unlikely except for some old historical buildings where grade beams are absent. This issue can be modeled by setting parameter k equals to zero as an input in Equation 5.6.

The differential settlement between two columns consists of two components as illustrated in Figure 5.7. Simple experiments by Leonard (1975) showed that for a

frame structure, it is unlikely that the columns on each footing will rotate through the same angle as the overall structure. Therefore, tilting can also induce stresses and strains to the building and hence cracking. Burland et al. (1977) also stated that it might not appropriate to remove tilting in frame buildings supported on separate footings.

On the other hand, Boscardin and Cording (1989) and Boone (1996) assumed that tilting in a frame structure would not cause damage. Tilting would only cause the frame structure to rotate as a rigid body.

Both views can be valid. It depends largely on the rigidity of the structure. If a structure is very rigid, tilting will not cause any significant damage. For a relatively flexible structure, tilting can damage the building. Another issue is related to mix foundations where some part of the building is supported on piles and another part on footings. In this case, each frame may tilt differently. Therefore, settlement due to tilting can cause damage.

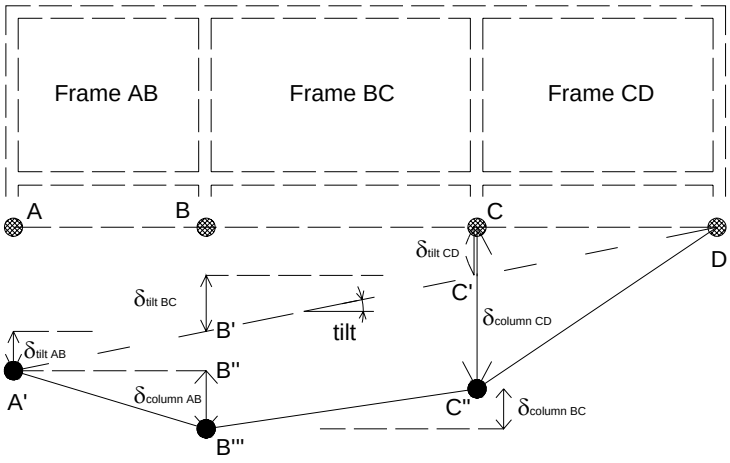

Figure 5.7 Settlement of Frame Columns

Figure 5.7 shows the settlement of a framed structure. Damage in Frame CD depends on settlement between Columns C and D. If Frame CD is very rigid, $\delta_{tilt,CD}$ will not cause damage. In this case, damage is caused by ($\delta_{column,CD}$ - $\delta_{tilt,CD}$). However, if Frame CD is not rigid, then $\delta_{column,CD}$ should be used. On the other

hand, for Frame AB, regardless of its rigidity, using $\delta_{column\ AB} + \delta_{tilt\ AB}$ as a source of damage would be more appropriate.

In order to solve this discrepancy, the differential settlement (δ_v) in Equation 5.6 can be expressed in terms of $\delta_v = \delta_{column} \pm \delta_{tilt}$. Equation 5.6 combined with crack width in Table 5.1 can then be expanded into Equations 5.13 to 5.17 where parameter δ is in mm. Results are plotted in Figure 5.8.

$$\delta_{column} \pm \delta_{tilt} = 0.1(\tan\theta \sin\theta + \cos\theta) \quad (5.13)$$

$$\delta_{column} \pm \delta_{tilt} = 1(\tan\theta \sin\theta + \cos\theta) \quad (5.14)$$

$$\delta_{column} \pm \delta_{tilt} = 5(\tan\theta \sin\theta + \cos\theta) \quad (5.15)$$

$$\delta_{column} \pm \delta_{tilt} = 15(\tan\theta \sin\theta + \cos\theta) \quad (5.16)$$

$$\delta_{column} \pm \delta_{tilt} = 25(\tan\theta \sin\theta + \cos\theta) \quad (5.17)$$

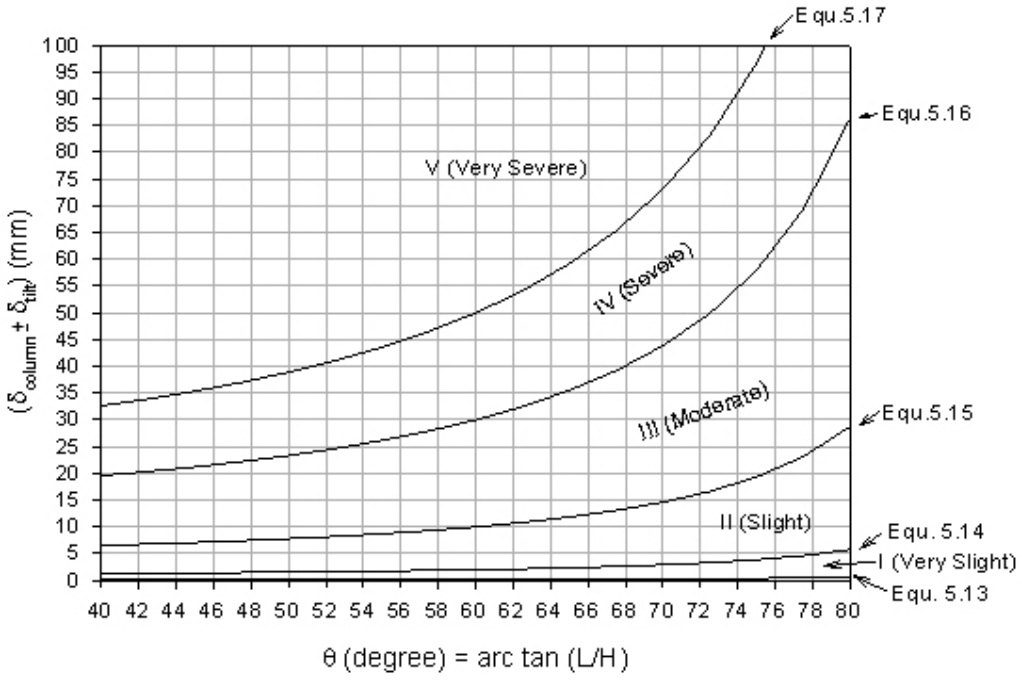

Figure 5.8 Damage Categories from Equation 5.13 to 5.17

Published data as well as data collected from the construction of MRT North East Line (NEL) in Singapore are used to validate this chart. This validation is given in Section 5.6 after the description of the MRT NEL construction.

5.4 MRT North East Line Project in Singapore

Back in 1986, the North East Line (NEL) was already planned as an extension to the existing East West and North South MRT lines. The project started in 1997 and the train started operation in June 2003. With a length of about 18 km, the alignment of NEL crosses hundreds of buildings which are mainly frame structures. It provides a good opportunity to study the effect of ground movements and building responses. The responses of several shop houses due to ground movements from these projects will be used to verify the proposed chart for assessment of building damage. In addition, data from published papers will also be used.

5.4.1 Shop Houses at Block C706A

These shop houses have two stories and consists of 14 frame structures as shown in Figure 5.9. The ground settlement contours from March 1999 to February 2001 are shown in Figure 5.10. Shop houses a, b, c, and d are old frame structures compared to others. The damage level for these frames can be categorized into class 3 (moderate) or higher. Protection works were in place to protect the arches in front of these shop houses (a – d) as shown in Figure 5.11. The damage level at other parts of shop houses, d – n, can be categorized as class 2. Cracks which occurred in these shop houses were easily filled. There was no brickwork to be replaced except some repainting of external brickworks as shown in Figure 5.12 in front of shop houses C706 a-m facing Race Course Road.

Figure 5.9 Typical Shop Houses C706A

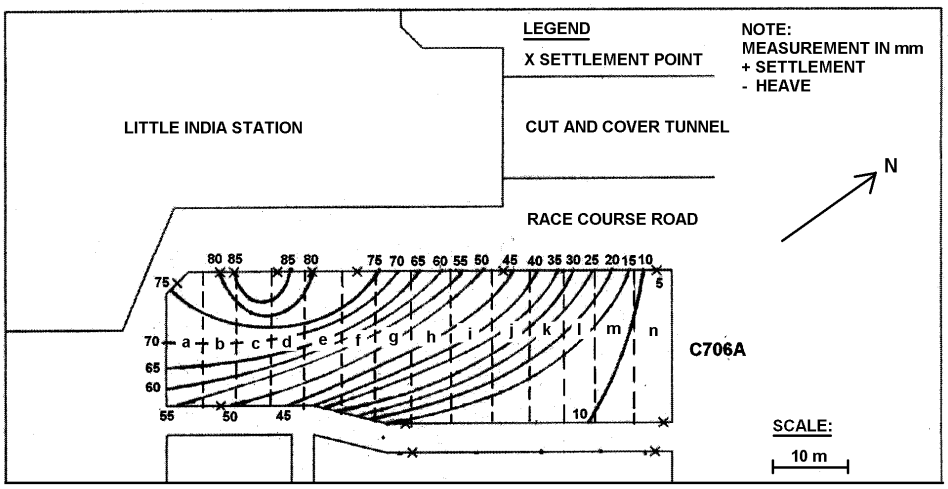

Figure 5.10 Ground Settlement Contours between March 1999 and February 2001

Figure 5.11 Protection of Arch

Figure 5.12 Repairing on the Infill Frame Structures at C706 e-n Shop Houses

5.4.2 Shop Houses at Block C706C

The shop houses consist of three stories as shown in Figure 5.13. The building settlement contours of these shop houses are shown in Figure 5.14. Some cracks occurred in these shop houses. Based on the ease of repair, the damage can be categorized as 2. The cracks are shown in Figures 5.15 and 5.16. Unfortunately, the foundation type is unknown. Judging from the settlement contours, it is likely that these shop houses are supported on raft foundation.

Figure 5.13 Shop Houses C706C

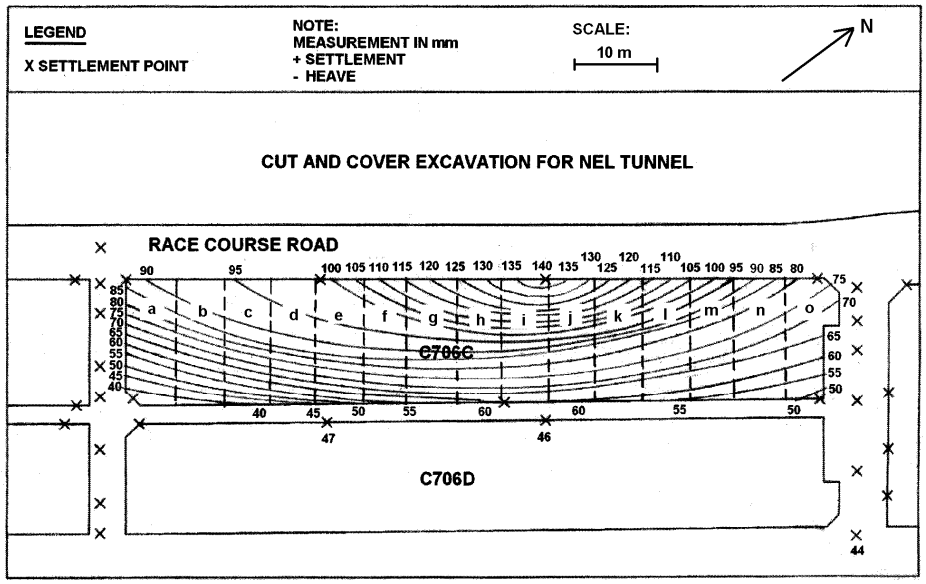

Figure 5.14 Building Settlement Contours between March 1999 and February 2001

Figure 5.15 Cracks at C706C-a (Sendal Bar)

5.16 Typical Cracks Occurred behind Shop Houses C706C

5.4.3 Shop Houses at Block C706E

The shop houses consist of two to four stories frame structures as shown in Figure 5.17. The settlement contours of these shop houses are shown in Figure 5.18. From the settlement contour plot between March 1999 and February 2001, it can be seen that large differential settlements had developed. The maximum settlement was 115 mm and the minimum settlement was 45 mm. This large differential settlement had caused a lot of cracking in these shop houses. The damage can be categorized as 2. Unfortunately, the types of foundation support are also unknown.

Figure 5.17 Shop Houses C706E

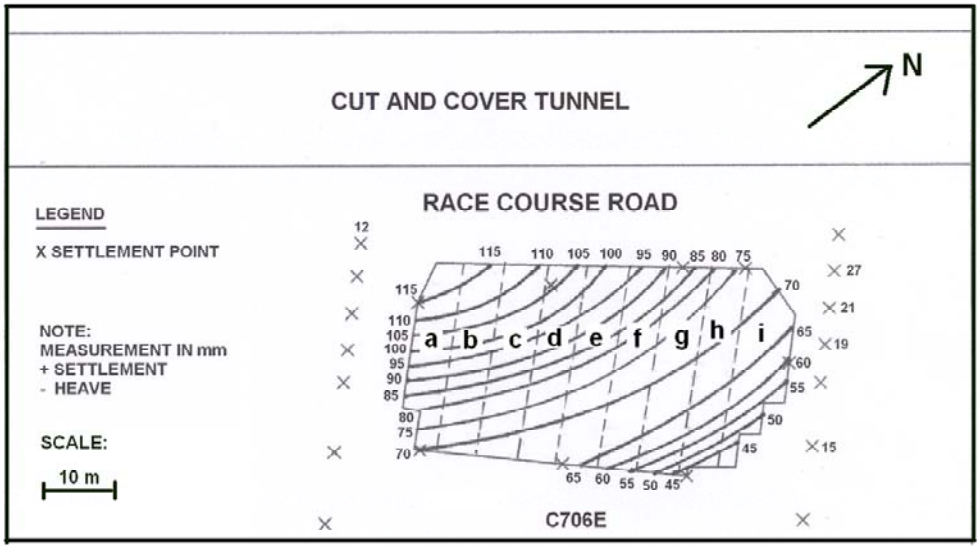

Figure 5.18 Building Settlement Contours at Shop Houses C706E

5.4.4 Shop Houses at Block C708A

The settlement contours are shown in Figure 5.19. The shop houses consist of 5 to 6 storey. At these shop houses, cracks developed due to differential settlement at Satchi Club are shown in Figure 5.20. The damages are categorized as 2. The distance between this building and the excavation wall is about 28 m. Even though the distance is far away, a differential settlement of about 15 mm can still occur in these terrace shops. Unfortunately, the foundation type is not known.

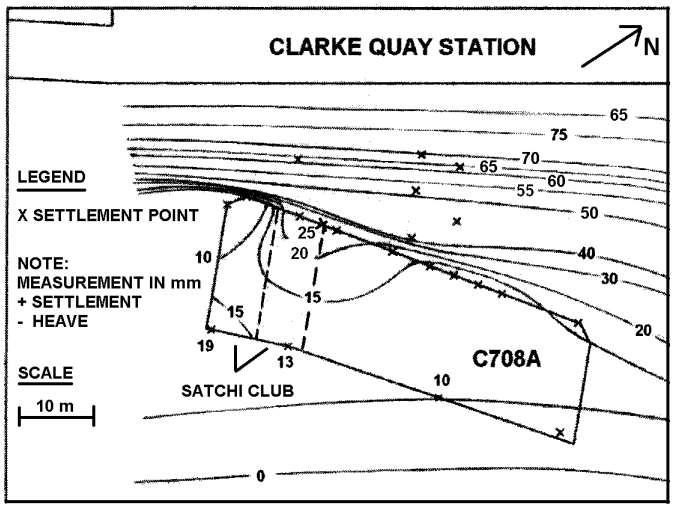

Figure 5.19 Shop Houses C708A at Clarke Quay Station

Figure 5.20 Diagonal and Vertical Cracks at Satchi Club

5.5 Summary of Frame Damage Data

All the data from published papers and the construction of MRT NEL are summarized in Table 5.2. The values of δ_{tilt} from cases 8 and 9 are not calculated because they are not known. For cases 70 to 78, the δ_{tilt} values are also not calculated. The buildings associated with these two cases are shown in Figure 5.17 and 5.20, respectively. These frame structures are not structurally connected. Therefore, it is unlikely that they would rotate together as a rigid body. The damages were likely due to δ_{column}. After obtaining δ_{column} and δ_{tilt} for each frame, the values of (δ_{column}+δ_{tilt}) or (δ_{column}-δ_{tilt}) is then calculated based on the settlement profile. For the damage criteria, they are judged from the reported damage or field observation.

5.6 Verification of Proposed Chart

Figure 5.21 shows the proposed damage criteria together with the data from Table 5.2. The number besides the symbol refers to the case number. There are four "moderate damage" points plotted in the "slightly damage" zone. These points are located quite close to the line separating slight and moderate damage category. There is one "severe damage" point plotted in the "severe damage" zone. Again, this point is located quite close to the line separating severe and very severe damage. Despite the minor discrepancies, the proposed chart is capable of predicting damage to frame structures reasonable well. It should also be noted that the reliability of this method depends largely on the accuracy of the predicted ground movements.

The advantage of proposed chart is that it is easy to obtain the parameters. The differential settlement between columns (δ_{column}), the tilt settlement (δ_{tilt}), and frame dimensions (L and H) are not difficult to measure. However, it will be a challenge to be able to predict them accurately. The chart can also predict the building damage in several categories. The major shortcoming of this chart is that it cannot predict frame damage if horizontal strain occurs. Fortunately, modern frame structures

Table 5.2 Summary of Measured Data from Published Papers and MRT North East Line in Singapore

Summarized Data										
No	Reference	Case	L	H	θ = arc tan(L/H)	δ_{column}	δ_{tilt}	$\delta_{column} \pm \delta_{tilt}$	Damage Category	Reported Damage
			m	m	degree	mm	mm	mm		
1	Brand/Luang (1975)	Infill wall A6-A5	10	3.75	69.44	60	18	42	4	Cracking which widened rapidly, frequent repairs, loss of weather-tightness
2	Brand/Luang (1975)	Infill wall A6-B6	10	3.75	69.44	10	0	10	2	Cracks
3	Finno et al. (2005)	Infill wall section A-A' North Segment	8	3.96	63.66	2	5.5	7.5	2	Slight damage
4	Finno et al. (2005)	Infill wall section A-A' South Segment	8	3.96	63.66	11	4	7	2	Slight damage
5	Finno et al. (2005)	Infill wall section B-B' Column A-B	7.3	3.96	61.52	21	8	13	3	Moderate damage
6	Finno et al. (2005)	Infill wall section B-B' Column C-D	6.9	3.96	60.15	5	8	3	2	Slight damage
7	Finno et al. (2005)	Infill wall section B-B' Column D-E	13.8	3.96	73.99	3	16	13	2	Slight damage
8	Fjeld (1964)	Infill wall A3-A4 (1st floor)	6.5	5.5	49.76	37.5	-	37.5	4	Serious cracks
9	Fjeld (1964)	Infill wall A3-A4 (2nd & 3rd floor)	6.5	4	58.39	37.5	-	37.5	4	Serious cracks
10	Fjeld (1964)	Infill wall B4-C4 (1st floor)	4.88	5.5	41.58	10	5	5	2	Cracks
11	Fjeld (1964)	Infill wall B4-C4 (2nd & 3rd floor)	4.88	4	50.66	10	5	5	2	Cracks
12	Fjeld (1964)	Infill wall C4-D4 (1st floor)	4.88	5.5	41.58	11	5	6	2	Cracks
13	Fjeld (1964)	Infill wall C4-D4 (2nd & 3rd floor)	4.88	4	50.66	11	5	6	2	Cracks
14	Fjeld (1964)	Infill wall E4-F4 (1st floor)	4.88	5.5	41.58	1	5	4	2	Cracks
15	Fjeld (1964)	Infill wall E4-F4 (2nd & 3rd floor)	4.88	4	50.66	1	5	4	2	Cracks
16	Fjeld (1964)	Infill wall F4-G4 (1st floor)	4.88	5.5	41.58	7	5	2	2	Cracks
17	Fjeld (1964)	Infill wall F4-G4 (2nd & 3rd floor)	4.88	4	50.66	7	5	2	2	Cracks
18	Fjeld (1964)	Infill wall H4-J4 (1st floor)	4.88	5.5	41.58	6	5	11	2	Cracks
19	Fjeld (1964)	Infill wall H4-J4 (2nd & 3rd floor)	4.88	4	50.66	6	5	11	2	Cracks
20	Fjeld (1964)	Infill wall J1-J2 (1st floor)	9	5.5	58.57	52	35	17	3	Large cracks in a corner
21	Fjeld (1964)	Infill wall J1-J2 (2nd & 3rd floor)	9	4	66.04	52	35	17	3	Large cracks in a corner
22	Fjeld (1964)	Infill wall J3-J4 (1st floor)	9	5.5	58.57	19	35	16	3	Large cracks in a corner
23	Fjeld (1964)	Infill wall J3-J4 (2nd & 3rd floor)	9	4	66.04	19	35	16	3	Large cracks in a corner
24	Fjeld (1964)	Infill wall J1-H1 (1st floor)	4.88	5.5	41.58	6	5	1	2	Cracks
25	Fjeld (1964)	Infill wall J1-H1 (2nd & 3rd floor)	4.88	4	50.66	6	5	1	2	Cracks

Table 5.2 Summary of Measured Data from Published Papers and MRT North East Line in Singapore *(Continued)*

Summarized Data										
No	Reference	Case	L	H	θ = arc tan(L/H)	δ_{column}	δ_{tilt}	$\delta_{column} \pm \delta_{tilt}$	Damage Category	Reported Damage
			m	m	degree	mm	mm	mm		
26	Fjeld (1964)	Infill wall H1-G1 (1st floor)	4.88	5.5	41.58	6	5	2	2	Cracks
27	Fjeld (1964)	Infill wall H1-G1 (2nd & 3rd floor)	4.88	4	50.66	6	5	2	2	Cracks
28	Fjeld (1964)	Infill wall G1-F1 (1st floor)	4.88	5.5	41.58	10	5	11	2	Cracks
29	Fjeld (1964)	Infill wall G1-F1 (2nd & 3rd floor)	4.88	4	50.66	10	5	11	2	Cracks
30	Fjeld (1964)	Infill wall F1-E1 (1st floor)	4.88	5.5	41.58	9	5	4	2	Cracks
31	Fjeld (1964)	Infill wall F1-E1 (2nd & 3rd floor)	4.88	4	50.66	9	5	4	2	Cracks
32	Fjeld (1964)	Infill wall E1-D1 (1st floor)	4.88	5.5	41.58	16	5	11	2	Cracks
33	Fjeld (1964)	Infill wall E1-D1 (2nd & 3rd floor)	4.88	4	50.66	16	5	11	2	Cracks
34	Fjeld (1964)	Infill wall D1-C1 (1st floor)	4.88	5.5	41.58	8	5	3	2	Cracks
35	Fjeld (1964)	Infill wall D1-C1 (2nd & 3rd floor)	4.88	4	50.66	8	5	3	2	Cracks
36	Fjeld (1964)	Infill wall C1-B1 (1st floor)	4.88	5.5	41.58	6	5	1	2	Cracks
37	Fjeld (1964)	Infill wall C1-B1 (2nd & 3rd floor)	4.88	4	50.66	6	5	1	2	Cracks
38	Fjeld (1964)	Infill wall B1-B2 (1st floor)	9	5.5	58.57	70	40	30	4	Large cracks, door jammed, difficulty in using lift
39	Fjeld (1964)	Infill wall B1-B2 (2nd & 3rd floor)	9	4	66.04	70	40	30	4	Large cracks, door jammed, difficulty in using lift
40	Fjeld (1964)	Infill wall B2-B3 (1st floor)	7	5.5	51.84	50	40	10	3	Serious cracks
41	Fjeld (1964)	Infill wall B2-B3 (2nd & 3rd floor)	7	4	60.26	50	40	10	3	Serious cracks
42	NEL project C706	C706A - a - Infill wall facing Race Course Rd	5	2.7	61.63	2	5	7	2	Cracks easily be filled
43	NEL project C706	C706A - b - Infill wall facing Race Course Rd	5	2.7	61.63	7	5	12	2	Cracks easily be filled
44	NEL project C706	C706A - c - Infill wall facing Race Course Rd	5	2.7	61.63	3	5	8	2	Cracks easily be filled
45	NEL project C706	C706A - d - Infill wall facing Race Course Rd	5	2.7	61.63	5	5	10	2	Cracks easily be filled
46	NEL project C706	C706A - e - Infill wall facing Race Course Rd	5	3	59.04	6	5	1	2	Cracks easily be filled
47	NEL project C706	C706A - f - Infill wall facing Race Course Rd	5	3	59.04	3	5	2	2	Cracks easily be filled
48	NEL project C706	C706A - g - Infill wall facing Race Course Rd	5	3	59.04	10	5	5	2	Cracks easily be filled
49	NEL project C706	C706A -h - Infill wall facing Race Course Rd	5	3	59.04	8	5	3	2	Cracks easily be filled
50	NEL project C706	C706A - i - Infill wall facing Race Course Rd	5	3	59.04	8	5	3	2	Cracks easily be filled

Table 5.2 Summary of Measured Data from Published Papers and MRT North East Line in Singapore *(Continued)*

Summarized Data										
No	Reference	Case	L	H	θ = arc tan(L/H)	δ_{column}	δ_{tilt}	$\delta_{column} \pm \delta_{tilt}$	Damage Category	Reported Damage
			m	m	degree	mm	mm	mm		
51	NEL project C706	C706A - j - Infill wall facing Race Course Rd	5	3	59.04	7	5	2	2	Cracks easily be filled
52	NEL project C706	C706A - k - Infill wall facing Race Course Rd	5	3	59.04	8	5	3	2	Cracks easily be filled
53	NEL project C706	C706A - l - Infill wall facing Race Course Rd	5	3	59.04	9	5	4	2	Cracks easily be filled
54	NEL project C706	C706A - m - Infill wall facing Race Course Rd	5	3	59.04	10	5	5	2	Cracks easily be filled
55	NEL project C706	C706C - a - Infill wall facing Race Course Rd	6	3	63.43	7	1	8	2	Cracks easily be filled
56	NEL project C706	C706C - b - Infill wall facing Race Course Rd	6	3	63.43	3	1	4	2	Cracks easily be filled
57	NEL project C706	C706C - c - Infill wall facing Race Course Rd	6	3	63.43	3	1	4	2	Cracks easily be filled
58	NEL project C706	C706C - d - Infill wall facing Race Course Rd	6	3	63.43	2	1	3	2	Cracks easily be filled
59	NEL project C706	C706C - e - Infill wall facing Race Course Rd	6	3	63.43	6	1	7	2	Cracks easily be filled
60	NEL project C706	C706C - f - Infill wall facing Race Course Rd	6	3	63.43	10	1	11	2	Cracks easily be filled
61	NEL project C706	C706C - g - Infill wall facing Race Course Rd	6	3	63.43	9	1	10	2	Cracks easily be filled
62	NEL project C706	C706C - h - Infill wall facing Race Course Rd	6	3	63.43	9	1	10	2	Cracks easily be filled
63	NEL project C706	C706C - i - Infill wall facing Race Course Rd	6	3	63.43	7	1	8	2	Cracks easily be filled
64	NEL project C706	C706C - j - Infill wall facing Race Course Rd	6	3	63.43	11	1	10	2	Cracks easily be filled
65	NEL project C706	C706C - k - Infill wall facing Race Course Rd	6	3	63.43	13	1	12	2	Cracks easily be filled
66	NEL project C706	C706C - l - Infill wall facing Race Course Rd	6	3	63.43	11	1	10	2	Cracks easily be filled
67	NEL project C706	C706C - m - Infill wall facing Race Course Rd	6	3	63.43	10	1	9	2	Cracks easily be filled
68	NEL project C706	C706C - n - Infill wall facing Race Course Rd	6	3	63.43	12	1	11	2	Cracks easily be filled
69	NEL project C706	C706C - o - Infill wall facing Race Course Rd	6	3	63.43	8	1	7	2	Cracks easily be filled
70	NEL project C706	C706E - a - infill wall facing Race Course Rd	5.6	3	61.82	4.5	-	4.5	2	Cracks easily be filled
71	NEL project C706	C706E - b - infill wall facing Race Course Rd	5.6	3	61.82	4.5	-	4.5	2	Cracks easily be filled
72	NEL project C706	C706E - c - infill wall facing Race Course Rd	5.6	3	61.82	5	-	5	2	Cracks easily be filled
73	NEL project C706	C706E - d - infill wall facing Race Course Rd	5.6	3	61.82	7	-	7	2	Cracks easily be filled
74	NEL project C706	C706E - e - infill wall facing Race Course Rd	5.6	3	61.82	7	-	7	2	Cracks easily be filled
75	NEL project C706	C706E - f - infill wall facing Race Course Rd	5.6	3	61.82	10	-	10	2	Cracks easily be filled
76	NEL project C706	C706E - g - infill wall facing Race Course Rd	5.6	3	61.82	5	-	5	2	Cracks easily be filled
77	NEL project C708	C708A (Satchi Club) - facing New Bridge Rd	6	2.5	67.38	8	-	8	2	Cracks easily be filled
78	NEL project C708	C708A (Satchi Club) - facing New Bridge Rd	6	2.5	67.38	10	-	10	2	Cracks easily be filled

usually have grade beams or stiff floor system which prohibits the development of horizontal strain.

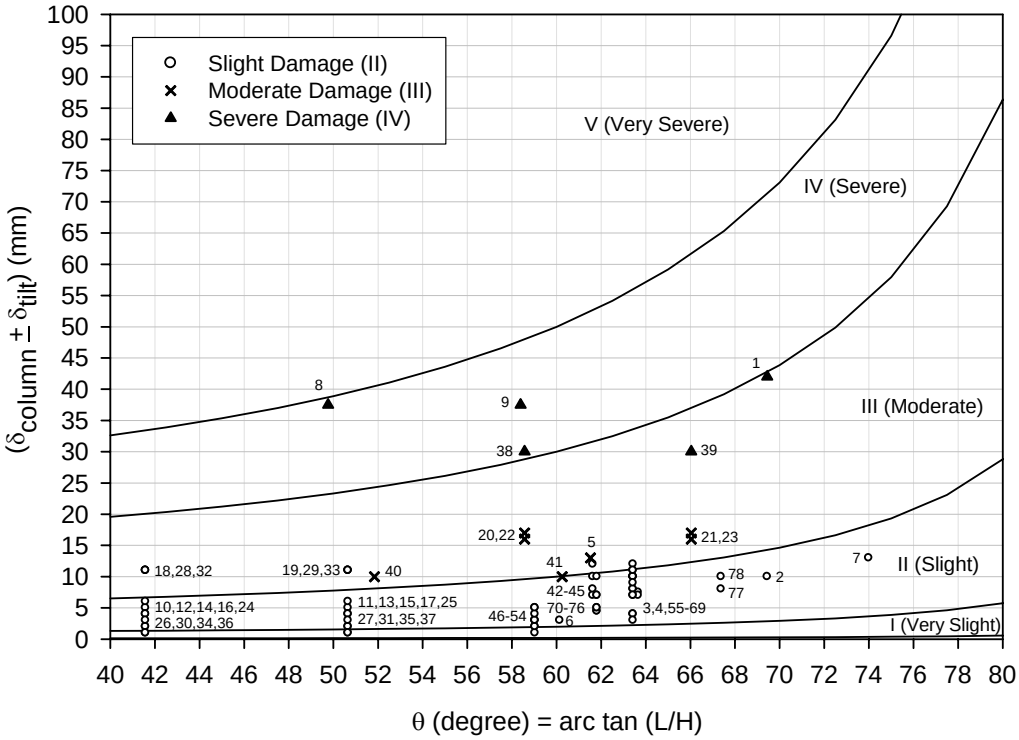

Figure 5.21 Proposed Chart to Predict Frame Damage

5.7 Comparison of Proposed Chart with Boscardin and Cording (1989)

The data in Table 5.2 are also plotted in the chart by Boscardin and Cording (1989) as shown in Figure 5.22. The parameter $(\delta_{column} \pm \delta_{tilt})/L$ is equivalence to β (angular distortion) where L is the distance between two columns. The horizontal strain is assumed to be zero because of the presence of grade beams in the frame structures.

The comparison shows that many data points do not agree with the proposed criteria. Moderate damage is predicted as very slight and slight damage. Several data points that belong to slight damage fall into the very slight damage zone. The main reason of these discrepancies is probably because the building dimension is not taken into consideration. They assumed the ratio of L/H equals to 1. However, none of data in Table 5.2 has that ratio.

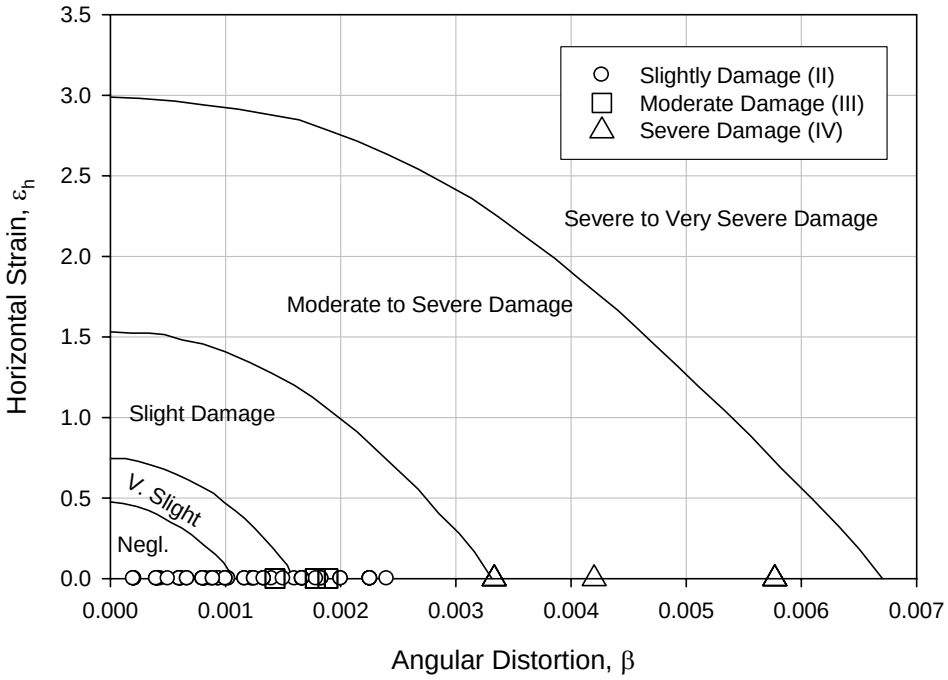

Figure 5.22 Damage Assessment by Boscardin and Cording Chart (1989)

5.8 Summary

Predicting building damage involves many uncertainties. Therefore, empirical approach was preferred in the past. Burland and Wroth (1974) has made an important contribution to understand the crack mechanism even tough the model is very simple. Following a similar frame work, a simple chart for assessing damage potential of frame structure has been proposed. Four parameters are needed. They are differential settlement between each column (δ_{column}), settlement due to tilt (δ_{tilt}), and frame dimensions (L and H). Condition of frame structures, such as its rigidity, should be investigated to judge whether δ_{tilt} should be included or not.

The proposed chart has been validated against field data. Nonetheless, there are limitations in this chart. It is only applicable to situations where the horizontal strain is negligible. It is not applicable to old historical frame structures where there are no grade beams tying the columns. Moreover, it can only be used for frame structure instead of load bearing wall where cracks is mainly due to bending. For many modern frame structures where grade beam is common, this chart is applicable.

CHAPTER 6
METHOD TO TRANSFORM GREENFIELD SETTLEMENT OF DEEP EXCAVATION FROM 2-D INTO 3-D FINITE ELEMENT ANALYSIS

6.1 Introduction

Soil movements induced by deep excavations can cause damage to surrounding buildings. These movements can be estimated using numerical analysis such as the finite element method. At this moment, the method for predicting building damage is largely based on greenfield settlement because of simplicity and convenience.

Burland and Wroth (1974) proposed charts to predict the building damage based on greenfield settlement. During the construction of Jubilee Line Extension in London, the building damage prediction in that area was based on greenfield settlement (Burland, 2001). The construction was successfully completed. None of historical buildings were seriously damaged.

The best method to predict the greenfield settlement is based on 3-D finite element analysis. Unfortunately, it is not an easy task and is also time consuming. At present, routine designs are based on 2-D analysis. The objective of this chapter is to establish a method to estimate 3-D greenfield settlement from 2-D analysis. In the proposed method, the chosen shape of excavation is rectangular. The wall extends all the way to the hard stratum. The ground settlement profile is concave.

In this chapter, the method to transform greenfield settlement from 2-D to 3-D is presented. Several hypothetical cases are then back-analyzed using the proposed method. Two case studies during the construction of underground car park at the House of Commons in London and construction of Taipei National Enterprise Center (TNEC) in Taiwan are used to validate the proposed method. Lastly, a set of

equations are proposed to produce the ground settlement profile following similar ideas by Clough and O'Rourke (1990) and Hsieh and Ou (1998).

6.2 Proposed Ground Settlement Equations

The curve fitting approach is adopted to obtain the ground settlement profile. It consists of two parts which can be generated by Equations 6.1 and 6.2 as shown in Figure 6.1.

$$y = ax^2 + bx + c \tag{6.1}$$

$$y = \frac{1}{-1 + dx^3} \tag{6.2}$$

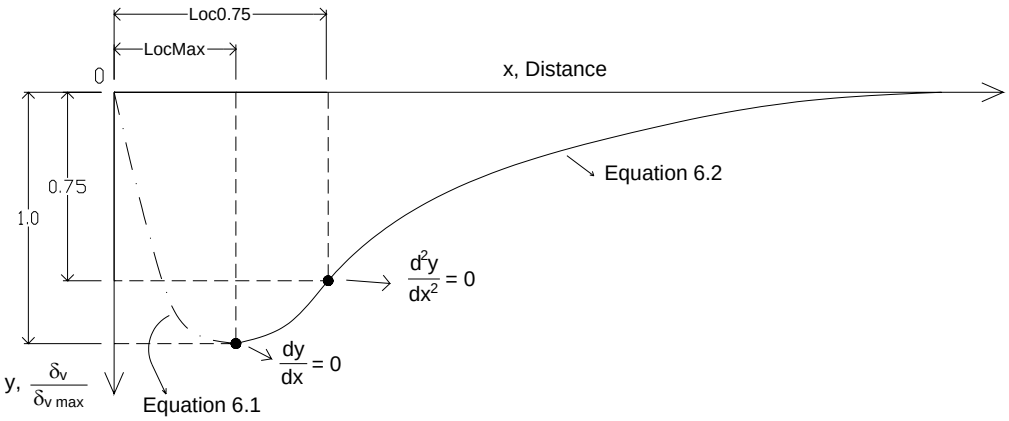

Figure 6.1 Equations for Fitting Ground Settlement Profile

Equation 6.1 has two boundary conditions. They are:

1. At x = 0, y is equal to zero.
2. At x = LocMax, the slope is zero (i.e. $\frac{dy}{dx} = 0$)

Assuming $y = \frac{\delta_v}{\delta_{v\max}}$, together with these boundary conditions, Equation 6.1 can be rewritten as Equation 6.3.

$$y = \frac{\delta_v}{\delta_{v\max}} = \frac{1}{LocMax^2}x^2 - \frac{2}{LocMax}x \tag{6.3}$$

In order for Equation 6.2 to fit nicely with the other part of ground settlement profile, it is important to know the location at point of infliction in the ground settlement profile. Mathematically, it can be presented as the location where $\frac{d^2y}{dx^2} = 0$. The differentiation of Equation 6.2 yields parameter *d* equals to $-\frac{1}{2x^3}$. After studying the results of all the finite element analyses, it was decide that this point should be located at $y = 0.75\left(\frac{\delta_v}{\delta_{v\max}}\right)$. The corresponding location along the x-axis is designated as Loc0.75. Therefore, Equation 6.2 can be expressed as follows:

$$y = \frac{1}{-1 - \frac{1}{2(Loc0.75)^3}x^3} \tag{6.4}$$

Further trial and error resulted in shifting the x location to $\left(x - \frac{LocMax}{2}\right)$. Moreover, it is also better to modify the exponent "3" on x as n value according to Figure 6.2. Therefore, Equation 6.4 can be modified to yield Equation 6.5.

$$y = \frac{\delta_v}{\delta_{v\max}} = \frac{1}{-1 - \frac{1}{2(Loc0.75)^3}\left(x - \frac{LocMax}{2}\right)^n} \tag{6.5}$$

For the corner, the n value is taken as 3.1 which is at zero distance from the excavation corner as shown in Figure 6.2.

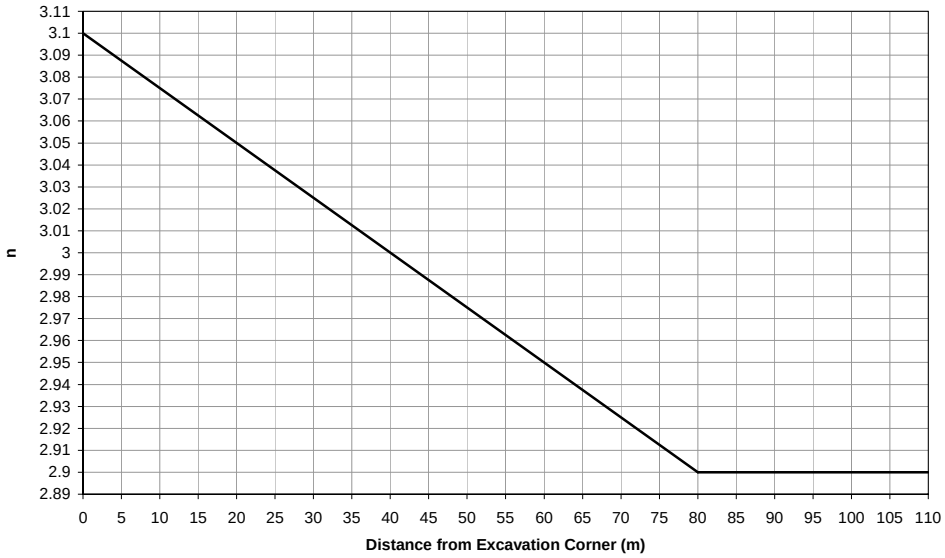

Figure 6.2 Parameter n in Equation 6.5

Both Equations 6.3 and 6.5 are used to generate greenfield settlement from 2-D to 3-D. They required 3 parameters which are $\delta_{v\,max}$, LocMax, and Loc0.75. Equation 6.3 generates the settlement profile up to the point of maximum settlement. Equation 6.5 generates the remaining profile beyond LocMax.

6.3 Proposed Charts

In order to set up the charts, several hypothetical studies with different excavation dimensions were modeled using the finite element software ABAQUS. The model extended laterally up to 150 m from the diaphragm wall to minimize the boundary effect on ground settlement (Ou and Shiau, 1998). Brick element with 20 nodes was used. The interface friction between wall and soil was not modeled. The depth of excavation was 10 m. The soil was excavated layer by layer. Excavation was carried out to 1 m below a strut level prior to the installation of strut. The 3-D model, the cross section, and the dimensions are shown in Figures 6.3, 6.4, and Table 6.1, respectively.

The soil profile consisted of two layers: fill and soft clay. The Modified Cam Clay model was used for both soils with parameters as shown in Table 6.2. The

diaphragm wall was modeled as an impermeable. The ground water table was at 1 m below the surface. The structural properties are shown in Table 6.3.

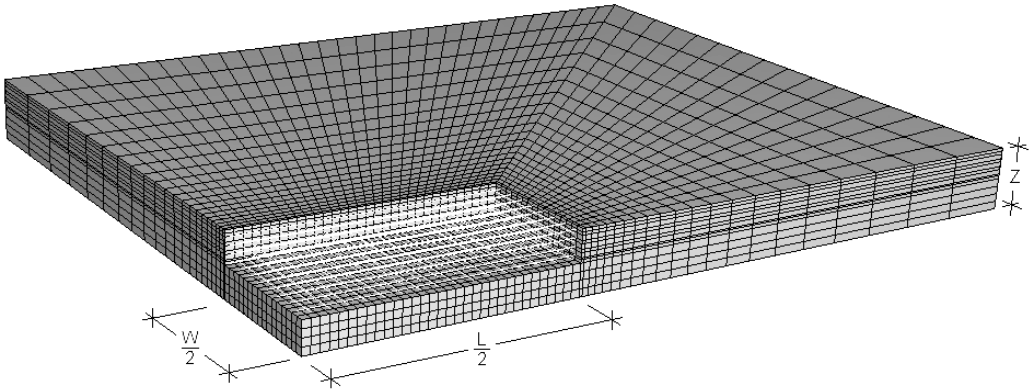

Figure 6.3 3-D Finite Element Model of a Deep Excavation

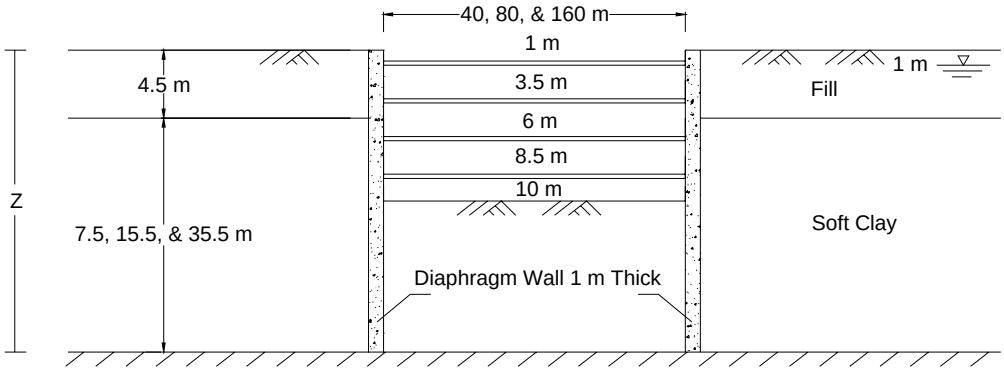

Figure 6.4 Cross-Section of the Model

Table 6.1 Analyzed Dimensions of Deep Excavation

Case	Width of Wall (W) (m)	Length of Wall (L) (m)	Thickness (Z) (m)
1	40	80	20
2	40	80	12
3	40	80	40
4	40	160	20
5	80	160	20
6	20	80	20
7	40	40	20
8	80	80	20

Table 6.2 Soil Parameters for Fill and Soft Clay

Soil Type	γ_{sat} (kN/m^3)	κ	λ	M	ν'	k (m/s)
Fill	19	0.02	0.1	1.244	0.33	$1x10^{-6}$
Soft Clay	16	0.0585	0.293	0.984	0.33	$1x10^{-8}$

Table 6.3 Structural Properties of Strut and Diaphragm Wall

Structural Members	E (kN/m^2)	A (m^2/m)	Preload (kN/m)
Strut at all level	2.07×10^8	0.02	No preloading
Diaphragm wall 1000 mm (brick element)	2.8×10^7	-	-

Results are used to develop Charts 1 to 9 as shown in Figure 6.5 to 6.13. Charts 1 to 3 can be used to predict the 3-D equivalents of LocMax, Loc0.75 and $\delta_{v,max}$ from 2-D. Charts 4 to 6 enable one to determine LocMax, Loc0.75, and $\delta_{v,max}$ at various locations along the excavation wall. Charts 7 to 9 enable one to determine the parameters around the corner area.

Charts 1 and 2 show that the conversion of LocMax and Loc0.75 from 2-D to 3-D is affected by the length of the wall. However, $\delta_{v,max}$ is also affected by the depth of soil as shown in Chart 3. Charts 4 and 5 show that the distributions of LocMax and Loc0.75 are essentially constant at 20 m or more from the corner. Chart 6 shows that the distribution of $\delta_{v,max}$ is also affected by the length of wall. Charts 7 and 8 show that the variations of LocMax and Loc0.75 around the corner are within 15%. However, the $\delta_{v,max}$ distribution varied widely at the corner as shown in Chart 9.

6.4 Procedure to Transform Greenfield Settlement from 2-D to 3-D

Two equations (Equations 6.3 and 6.5) and nine charts (Charts 1 to 9) have been proposed to transform greenfield settlement from 2-D to 3-D. The procedure is as follows:

1. Normalize the 2-D settlement profile relative to its maximum value, $\delta_{v,max}$.
2. Determine the value of LocMax, Loc0.75, and $\delta_{v,max}$ from Step 1.
3. Convert these parameters from 2-D to 3-D using Charts 1, 2, and 3.

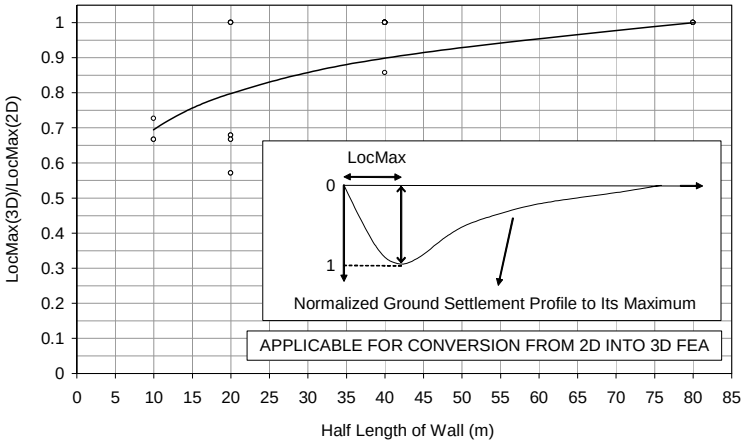

Figure 6.5 Chart 1: Conversion of LocMax from 2-D to 3-D

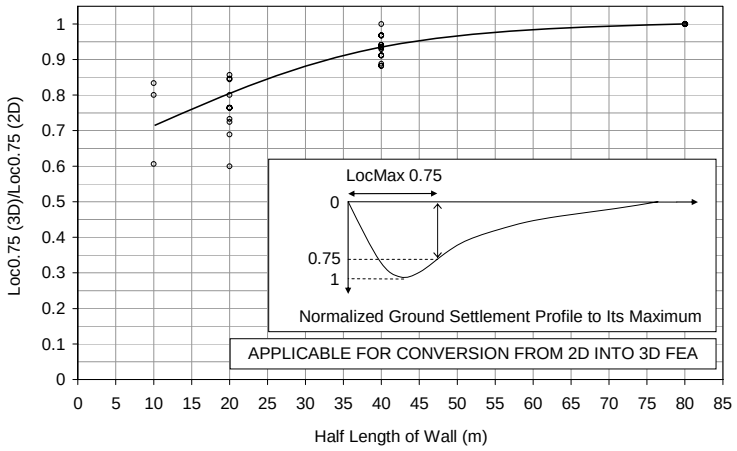

Figure 6.6 Chart 2: Conversion of Loc0.75 from 2-D to 3-D

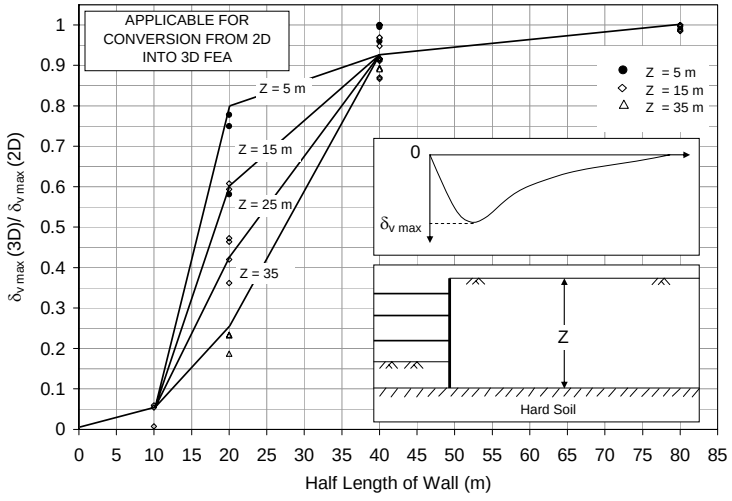

Figure 6.7 Chart 3: Conversion of $\delta_{v\,max}$ from 2-D to 3-D

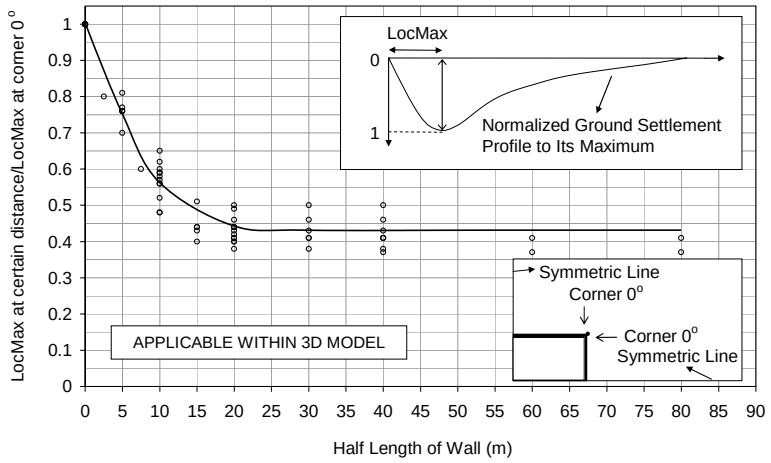

Figure 6.8 Chart 4: Distribution of LocMax along Excavation Wall

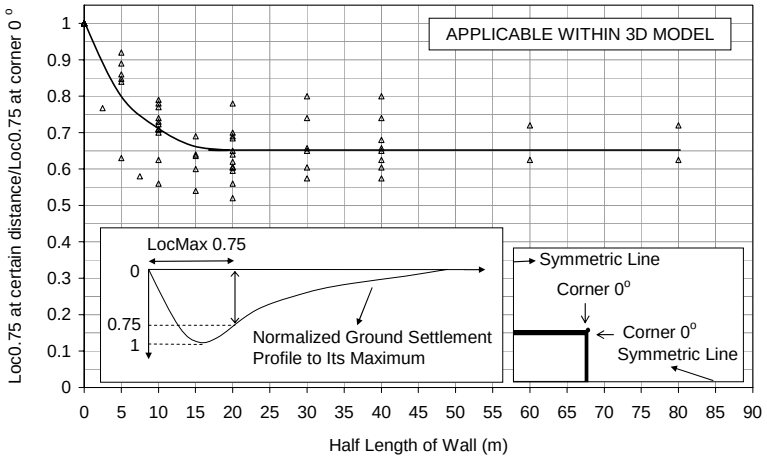

Figure 6.9 Chart 5: Distribution of Loc0.75 along Excavation Wall

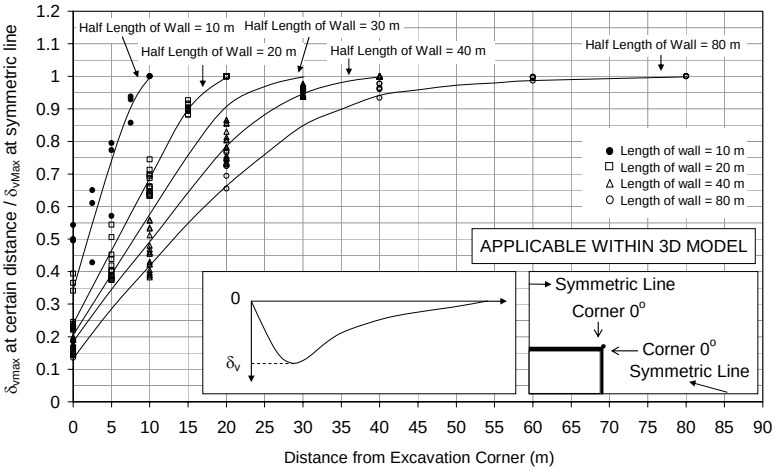

Figure 6.10 Chart 6: Distribution of $\delta_{v\,max}$ along Excavation Wall

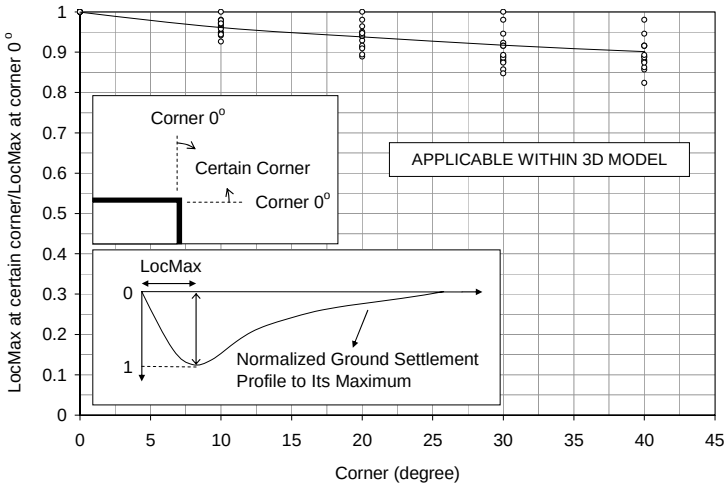

Figure 6.11 Chart 7: Distribution of LocMax along Excavation Corner

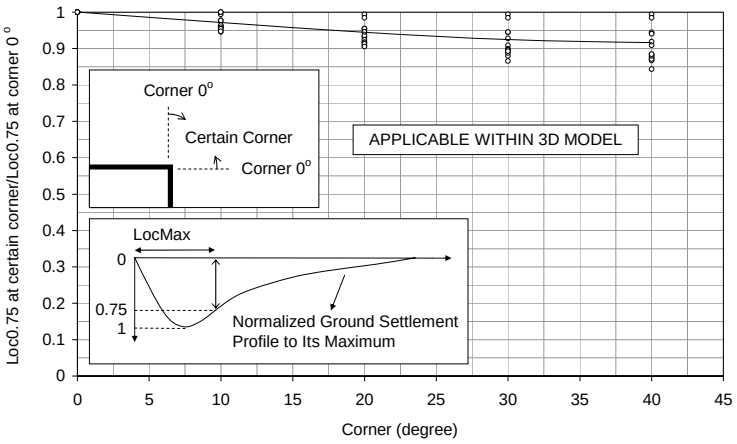

Figure 6.12 Chart 8: Distribution of Loc0.75 along Excavation Corner

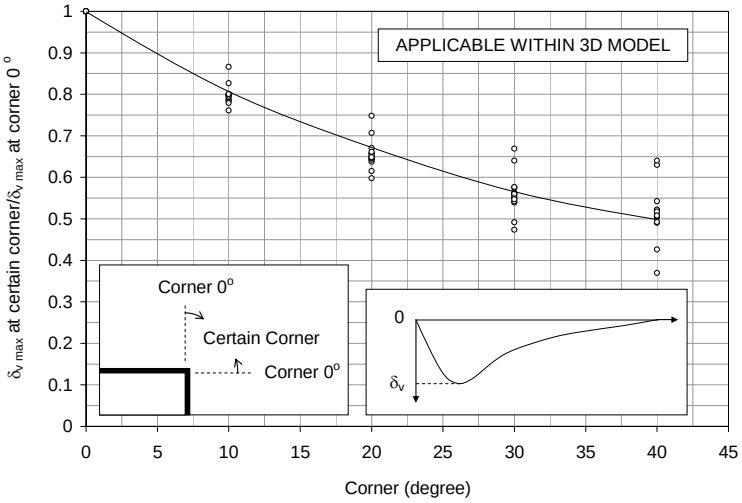

Figure 6.13 Chart 9: Distribution of $\delta_{v,max}$ along Excavation Corner

4. Calculate the distribution of LocMax, Loc0.75, and $\delta_{v\ max}$ along the retaining wall using Charts 4, 5, and 6, respectively.
5. Calculate the distribution of LocMax, Loc0.75, and $\delta_{v\ max}$ around the excavation corner using Charts 7, 8, and 9, respectively.
6. Establish the ground settlement equations at each location using Equations 6.3 and 6.5 with parameters from Steps 1 to 5.
7. Plot the results in terms of a contour or profiles at the different locations.

6.5 Example of Calculation

An example is used to illustrate the application of the proposed method. The dimension of the excavation is 40 m x 80 m. The depth of fill and soft clay is 4.5 m and 15.5 m, respectively. The plan view of this example is shown in Figure 6.14. Figures 6.15 and 6.16 show the 2-D ground settlement at cross-section A-A and its normalization to maximum ground settlement, respectively.

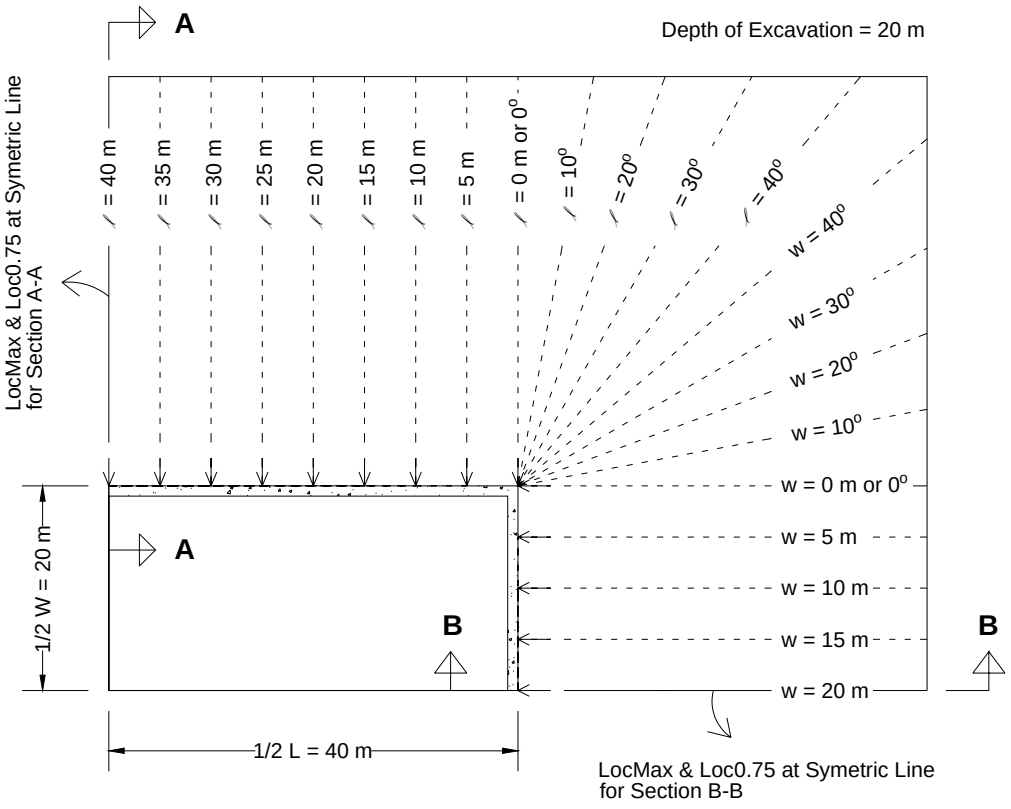

Figure 6.14 Top View of Excavation

This example only shows the calculations for cross-sections "/" since they are the same for sections "w". From / = 40 m to / = 40°, the 2-D parameters were determined based on Section A-A. From w = 20 m to w = 40° the parameters were based on Section B-B. For the corner section, it was assumed that the parameters from Section A-A is valid from / = 0° until / = 40° and those from Section B-B are valid from w = 0° until w = 40°.

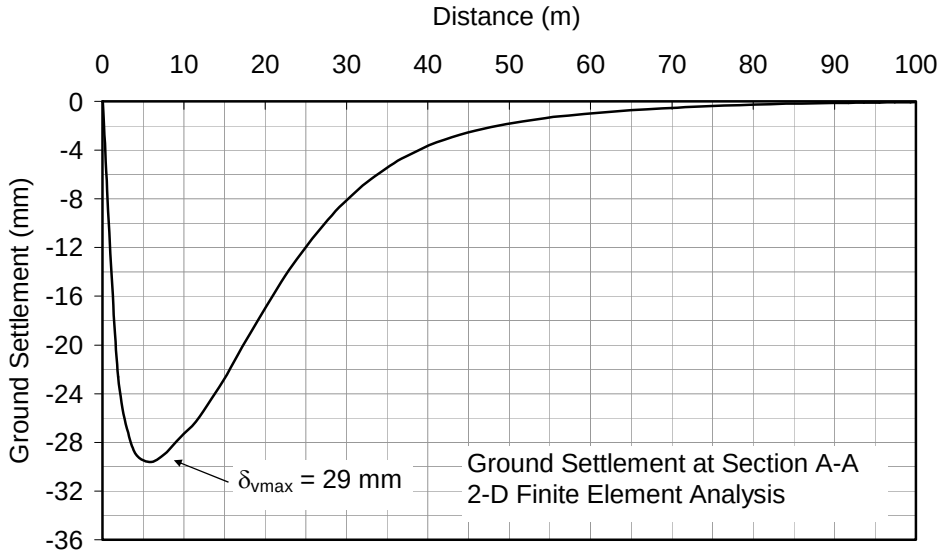

Figure 6.15 Ground Settlement at Section A-A from 2-D FEA

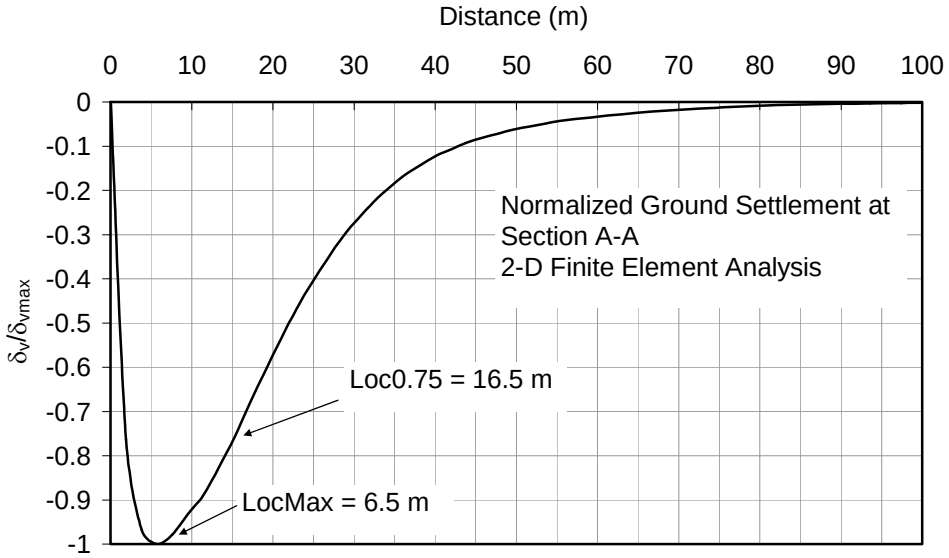

Figure 6.16 Normalized Ground Settlement at Section A-A from 2-D FEA

The calculation procedures for cross-sections l = 40 m until l = 40° are as follows:

(a) ½ L (half length of diaphragm wall) = 40 m.

(b) 2-D finite element result:

- LocMax at Symmetric Line (2-D) = $LocMax_{l=40m(2D)}$ = 5.5 m.
- Loc0.75 at Symmetric Line (2-D) = $Loc0.75_{l=40m(2D)}$ = 16.5 m.
- $\delta_{v\ max\ l=40m(2\text{-}D)}$ = 29 mm.

(c) Conversion from 2-D FEA to 3-D:

- $LocMax_{l=40m(3D)} = LocMax_{l=40m(2D)} \times Correction\ Factor\ (Chart\ 1)$

  $= 5.5 \times 0.9 = 4.95$ m.
- $Loc0.75_{l=40m(3D)} = Loc0.75_{l=40m(2D)} \times Correction\ Factor\ (Chart\ 2)$

  $= 16.5 \times 0.945 = 15.6$ m.
- $\delta_{v\max l=40m(3D)} = \delta_{v\max l=40m(2D)} \times Correction\ Factor\ (Chart\ 3)$

  $= 29 \times 0.925 = 26.83$ m.

(d) Determination of LocMax at selected locations from corner to L/2 (0 until 40 m) using Chart 4.

- l = 0 m $\Rightarrow \dfrac{LocMax_{l=40m(3D)}}{LocMax_{l=0(3D)}} = 0.425 \Rightarrow LocMax_{l=0m(3D)} = \dfrac{4.95}{0.425} = 11.65$ m.
- l = 5 m $\Rightarrow \dfrac{LocMax_{l=5m(3D)}}{LocMax_{l=0(3D)}} = 0.75$

  $\Rightarrow LocMax_{l=5m(3D)} = 0.75 \times 11.65 = 8.74$ m.
- l = 10 m $\Rightarrow \dfrac{LocMax_{l=10m(3D)}}{LocMax_{l=0(3D)}} = 0.56$

  $\Rightarrow LocMax_{l=10m(3D)} = 0.56 \times 11.65 = 6.52$ m.
- Results are summarized in Table 6.4.

Table 6.4 LocMax Values for Cross-Sections at l = 0 to 40 m

Cross Section l (m)	Correction Factor (Chart 4)	$LocMax_{(3D)}$ (m)
0	1	11.65
5	0.75	8.74
10	0.56	6.52
15	0.49	5.71
20	0.44	5.13
25	0.425	4.95
30	0.425	4.95
35	0.425	4.95
40	0.425	4.95

(e) Determination of LocMax around a corner of excavation wall with $l = 0^o$ to $l = 40^o$ using Chart 7.

- $l = 10^o \Rightarrow \dfrac{LocMax_{l=10^o(3D)}}{LocMax_{l=0^o(3D)}} = 0.96$

  $\Rightarrow LocMax_{l=10^o(3D)} = 11.65 \times 0.96 = 11.18$ m.

  Note: $LocMax_{l=0m(3\text{-}D)}$ equals to $LocMax_{l=0^o(3\text{-}D)}$

- $l = 20^o \Rightarrow \dfrac{LocMax_{l=20^o(3D)}}{LocMax_{l=0^o(3D)}} = 0.94$

  $\Rightarrow LocMax_{l=5m(3D)} = 11.65 \times 0.94 = 10.95$ m.

- Results are summarized in Table 6.5.

Table 6.5 LocMax Values for Cross-Sections at $l = 0^o$ to 40^o

Cross Section l (m)	Correction Factor (Chart 7)	$LocMax_{(3D)}$ (m)
0^o	1	11.65
10^o	0.96	11.18
20^o	0.94	10.95
30^o	0.92	10.72
40^o	0.9	10.49

(f) Determination of Loc0.75 at selected locations from corner to L/2 (l = 0 to 40 m) using Chart 5.

- $l = 0$ m $\Rightarrow \dfrac{Loc0.75_{l=40m(3D)}}{Loc0.75_{l=0(3D)}} = 0.65$

  $\Rightarrow Loc0.75_{l=0m(3D)} = \dfrac{15.6}{0.65} = 24$ m.

- $l = 5$ m $\Rightarrow \dfrac{Loc0.75_{l=5m(3D)}}{Loc0.75_{l=0(3D)}} = 0.8$

  $\Rightarrow Loc0.75_{l=5m(3D)} = 0.8 \times 24 = 19.2$ m.

- $l = 10$ m $\Rightarrow \dfrac{Loc0.75_{l=10m(3D)}}{Loc0.75_{l=0(3D)}} = 0.71$

  $\Rightarrow Loc0.75_{l=10m(3D)} = 0.71 \times 24 = 17.04$ m.

- Results are summarized in Table 6.6.

Table 6.6 Loc0.75 Values for Cross-Sections at $l = 0$ to 40 m

Cross Section l (m)	Correction Factor (Chart 5)	$Loc0.75_{(3D)}$ (m)
0	1	24
5	0.8	19.2
10	0.71	17.04
15	0.67	16.08
20	0.65	15.6
25	0.65	15.6
30	0.65	15.6
35	0.65	15.6
40	0.65	15.6

(g) Determination of Loc0.75 around the corner of excavation with $l = 0^o$ to 40^o using Chart 8.

- $l = 10^o \Rightarrow \dfrac{Loc0.75_{l=10^o(3D)}}{Loc0.75_{l=0^o(3D)}} = 0.97$

  $\Rightarrow Loc0.75_{l=10^o(3D)} = 24 \times 0.97 = 23.28$ m.

  Note: $Loc0.75_{l=0m(3-D)}$ equals to $Loc0.75_{l=0^o(3-D)}$

- $l = 20^o \Rightarrow \dfrac{Loc0.75_{l=20^o(3D)}}{Loc0.75_{l=0^o(3D)}} = 0.95$

  $\Rightarrow Loc0.75_{l=5m(3D)} = 24 \times 0.95 = 22.8$ m.

- Results are summarized in Table 6.7.

Table 6.7 Loc0.75 Values for Cross Section $l = 0^o$ to 40^o

Cross Section l	Correction Factor (Chart 8)	$Loc0.75_{(3D)}$ (m)
0^o	1	24
10^o	0.97	23.28
20^o	0.95	22.8
30^o	0.93	22.32
40^o	0.92	22.08

(h) Determination of $\delta_{v,max(3\text{-}D)}$ around the corner of excavation wall at $l = 0$ to 40 m using Chart 6.

- $l = 0$ m $\Rightarrow \dfrac{\delta_{v\max l=0m(3D)}}{\delta_{v\max l=40m(3D)}} = 0.18 \Rightarrow \delta_{v\max(3D),l=0} = 0.18 \times 29 = 5.22$ mm.

- $l = 5$ m $\Rightarrow \dfrac{\delta_{v\max(3D),l=5m}}{\delta_{v\max(3D),l=40m}} = 0.35 \Rightarrow \delta_{v\max(3D),l=0} = 0.35 \times 29 = 10.15$ mm.

- Results are summarized in Table 6.8.

Table 6.8 $\delta_{v,max(3\text{-}D)}$ Values for Cross Section $l = 0$ to 40 m

Cross Section l (m)	Correction Factor (Chart 6)	$\delta_{v\ max(3D)}$ (mm)
0	0.18	4.83
5	0.35	9.39
10	0.5	13.42
15	0.65	17.44
20	0.79	21.2
25	0.88	23.61
30	0.95	25.49
35	0.98	26.29
40	1	26.83

(i) Determination of $\delta_{v,max(3\text{-}D)}$ around the corner of an excavation with $l = 0^o$ to 40^o using Chart 9.

- $l = 10^o \Rightarrow \dfrac{\delta_{v\max l=10^o(3D)}}{\delta_{v\max l=0^o(3D)}} = 0.82$

$$\Rightarrow \delta_{v\max l=10^o(3D)} = 4.83 \times 0.82 = 3.96 \text{ mm.}$$

Note: $\delta_{v,max\ l=0^o(3\text{-}D)}$ *equals to* $\delta_{,max\ l=0m(3\text{-}D)}$

- $l = 20^o \Rightarrow \dfrac{\delta_{v\max l=20^o(3D)}}{\delta_{v\max l=0^o(3D)}} = 0.68$

  $\Rightarrow \delta_{v\max l=20^o(3D)} = 4.83 \times 0.68 = 3.28$ mm.

- Results are summarized in Table 6.9.

Table 6.9 $\delta_{v,max(3\text{-}D)}$ Values for Cross-Sections at $l = 0^o$ to 40^o

Cross Section l	Correction Factor (Chart 8)	$\delta_{v\ max(3D)}$ (mm)
0^o	1	4.83
10^o	0.82	3.96
20^o	0.68	3.28
30^o	0.57	2.75
40^o	0.5	2.42

(j) After obtaining all the required parameters, the ground settlement equations can be set up based on Equations 6.3 and 6.5. Parameter n is obtained from Figure 6.2. In the equations below, the parameter x and δ_v are in meters and millimeters, respectively. The equations are as follows:

- <u>$l = 0$ m</u>

  $\delta_{v1} = 4.83\left(0.007368x^2 - 0.1716738x\right)$

  $\delta_{v2} = 4.83\left[\dfrac{1}{-1-0.0000362\left(x-5.825\right)^{3.1}}\right]$

- <u>$l = 5$ m</u>

  $\delta_{v1} = 9.39\left(0.0130911x^2 - 0.228833x\right)$

  $\delta_{v2} = 9.39\left[\dfrac{1}{-1-0.0000706\left(x-4.37\right)^{3.0875}}\right]$

- <u>$l = 10$ m</u>

  $\delta_{v1} = 13.42\left(0.0235237x^2 - 0.3067485x\right)$

  $\delta_{v2} = 13.42\left[\dfrac{1}{-1-0.0001011\left(x-3.26\right)^{3.075}}\right]$

- <u>$l = 15$ m</u>

  $\delta_{v1} = 17.44\left(0.030671x^2 - 0.3502627x\right)$

$$\delta_{v2} = 17.44\left[\frac{1}{-1-0.0001203(x-2.855)^{3.0625}}\right]$$

- <u>l = 20 m</u>

$$\delta_{v1} = 21.2\left(0.0379984x^2 - 0.3898635x\right)$$

$$\delta_{v2} = 21.2\left[\frac{1}{-1-0.0001317(x-2.565)^{3.05}}\right]$$

- <u>l = 25 m</u>

$$\delta_{v1} = 23.61\left(0.0408122x^2 - 0.4040404x\right)$$

$$\delta_{v2} = 23.61\left[\frac{1}{-1-0.0001317(x-2.475)^{3.0375}}\right]$$

- <u>l = 30 m</u>

$$\delta_{v1} = 25.49\left(0.0408122x^2 - 0.4040404x\right)$$

$$\delta_{v2} = 25.49\left[\frac{1}{-1-0.0001317(x-2.475)^{3.025}}\right]$$

- <u>l = 35 m</u>

$$\delta_{v1} = 26.29\left(0.0408122x^2 - 0.4040404x\right)$$

$$\delta_{v2} = 26.29\left[\frac{1}{-1-0.0001317(x-2.475)^{3.0125}}\right]$$

- <u>l = 40 m</u>

$$\delta_{v1} = 26.83\left(0.0408122x^2 - 0.4040404x\right)$$

$$\delta_{v2} = 26.83\left[\frac{1}{-1-0.0001317(x-2.475)^{3}}\right]$$

- <u>l = 10°</u>

$$\delta_{v1} = 3.96\left(0.0080005x^2 - 0.1788909x\right)$$

$$\delta_{v2} = 3.96\left[\frac{1}{-1-0.00004(x-5.59)^{3.1}}\right]$$

- <u>l = 20°</u>

$$\delta_{v1} = 3.28\left(0.0083401x^2 - 0.1826484x\right)$$

$$\delta_{v2} = 3.28\left[\frac{1}{-1-0.000042(x-5.475)^{3.1}}\right]$$

- $\underline{/ = 30^{o}}$

$$\delta_{v1} = 2.75\left(0.0087018x^{2} - 0.1865672x\right)$$

$$\delta_{v2} = 2.75\left[\frac{1}{-1-0.000045(x-5.36)^{3.1}}\right]$$

- $\underline{/ = 40^{o}}$

$$\delta_{v1} = 2.42\left(0.0090876x^{2} - 0.1906578x\right)$$

$$\delta_{v2} = 2.42\left[\frac{1}{-1-0.000046(x-5.245)^{3.1}}\right]$$

(k) All of above equations can then be plotted using a spreadsheet such as Microsoft Excel. However, it should be noted that they are only for Sections $/ =$ 40 m to $/ = 40^{o}$.

(l) The calculation procedures for the Sections w = 20 m to $w = 40^{o}$ are not shown as they are similar to those of the $/$ sections.

(m) Results are shown in Figures 6.17 to 6.19. Figures 6.17 and 6.18 show the ground settlement contours from 3-D finite element analysis and those computed from 2-D, respectively. The agreements are favorable. On the other hand, Figure 6.19 shows the ground settlement profiles at selected locations.

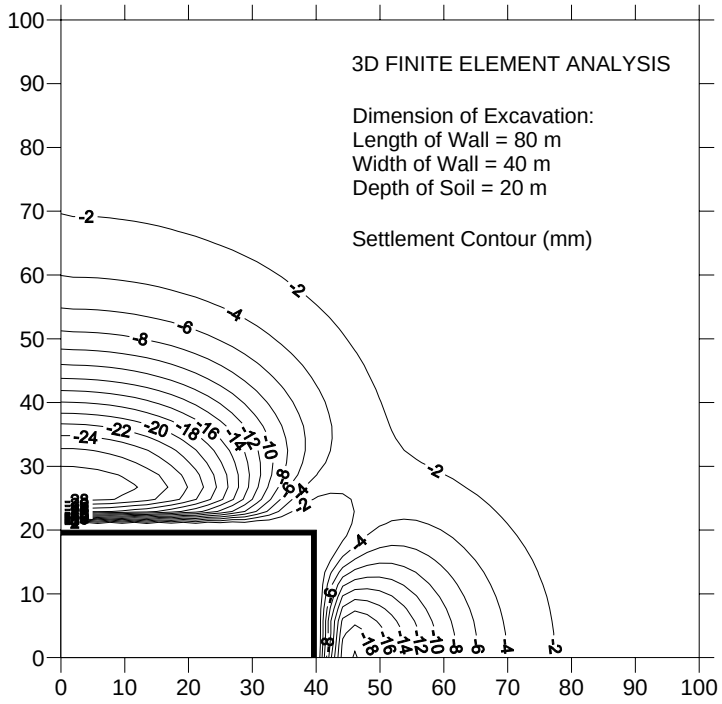

Figure 6.17 3-D FEA Ground Settlement Contour for Case 1: 80x40x20

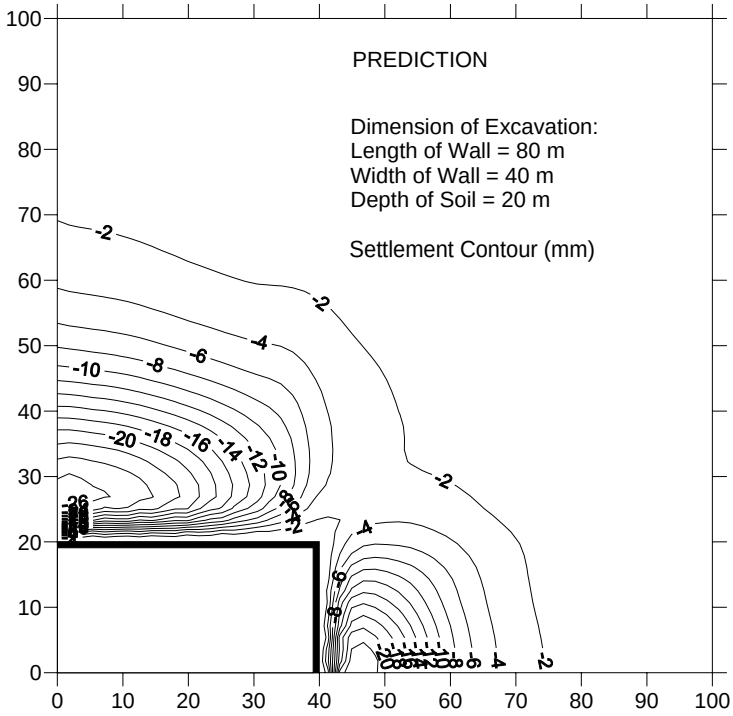

Figure 6.18 Predicted Ground Settlement Contour for Case 1: 80x40x20

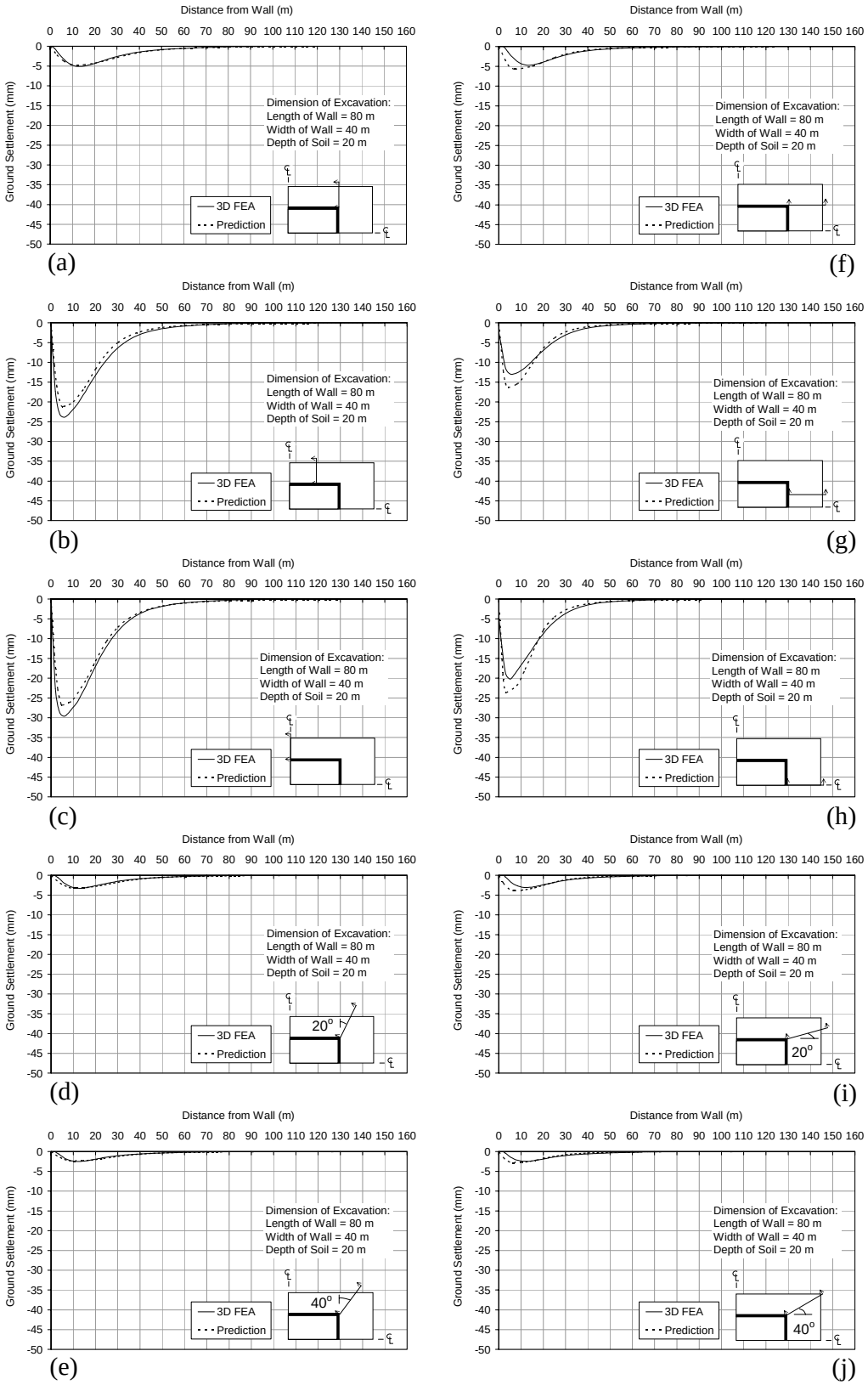

Figure 6.19 Settlement Profiles for Case 1:80x40x20

6.6 Back Analysis of Hypothetical Study

The proposed method was applied to Cases 2 to 8 from Table 6.1. The computed 3-D greenfield settlement contours and the settlement profiles at selected locations are compared with those determined from 3-D finite element analysis as shown in Figures 6.17 to 6.40 and Figure 6.42 to 6.47. The agreements are acceptable. Results are also summarized in Table 6.10.

Table 6.10 Excavation Dimension, Soil Depth, and List of Figures

No	Case	Length of Excavation (m)	Width of Excavation (m)	Depth of Soil (m)	Results in Figures
1	80x40x20	80	40	20	6.17 - 6.19
2	80x40x12	80	40	12	6.20 - 6.22
3	80x40x40	80	40	40	6.23 - 6.25
4	160x40x20	160	40	20	6.26 - 6.28
5	160x80x20	160	80	20	6.29 - 6.31
6	80x20x20	80	20	20	6.32 - 6.34
7	40x40x20	40	40	20	6.35 - 6.37
8	80x80x20	80	80	20	6.38 - 6.40
9	80x40x20 (Different Camclay Parameters)	80	40	20	6.42 - 6.44
10	80x40x40 (Mohr-Coulomb Parameters)	80	40	40	6.45 - 6.47

In addition to these 8 cases, two more cases were added. Case 9 utilizes the Modified Cam Clay model with parameters shown in Table 6.11. The geometry is shown in Figure 6.4. Case 10 deals with stiff clay using the Mohr-Coulomb model. The parameters and the cross-section are shown in Table 6.12 and Figure 6.41, respectively.

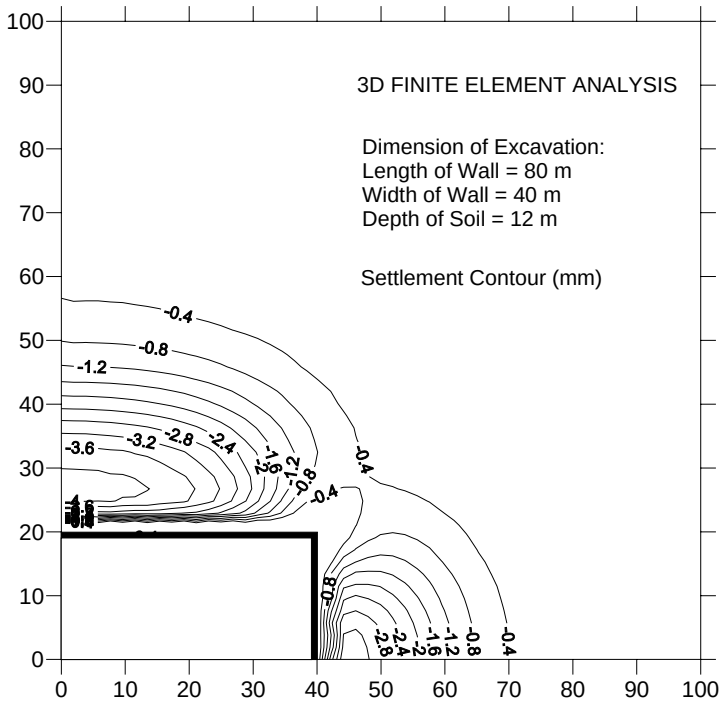

Figure 6.20 3-D FEA Ground Settlement Contour for Case 2: 80x40x12

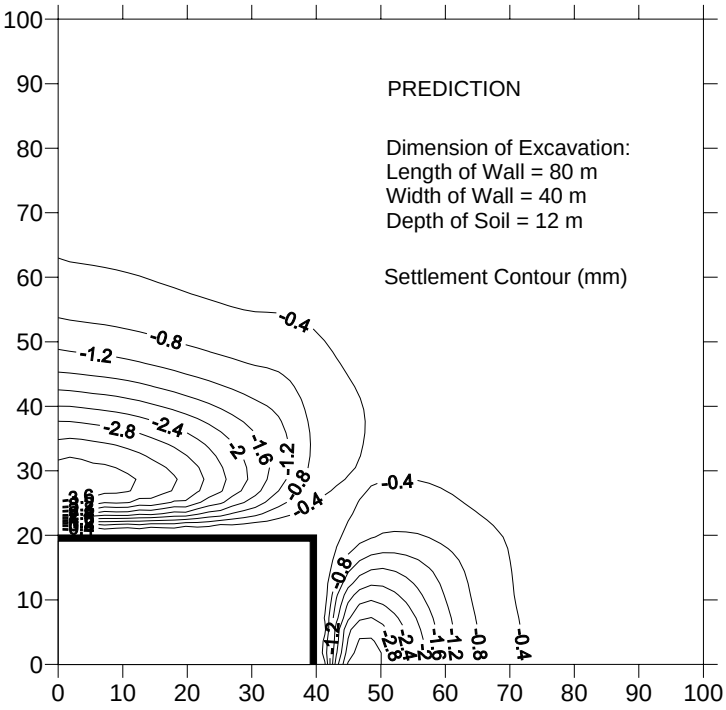

Figure 6.21 Predicted Ground Settlement Contour for Case 2: 80x40x12

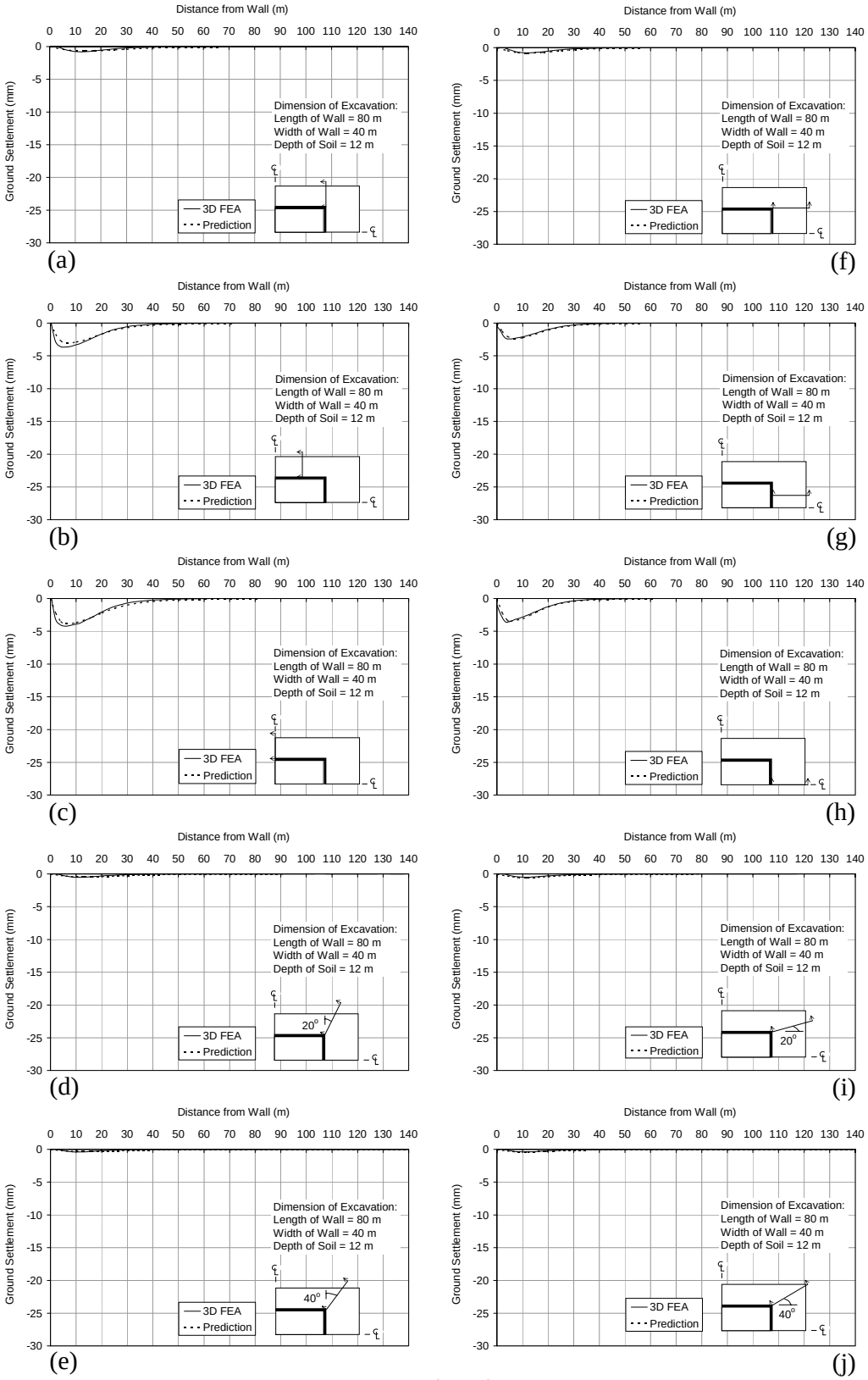

Figure 6.22 Settlement Profiles for Case 2: 80x40x12

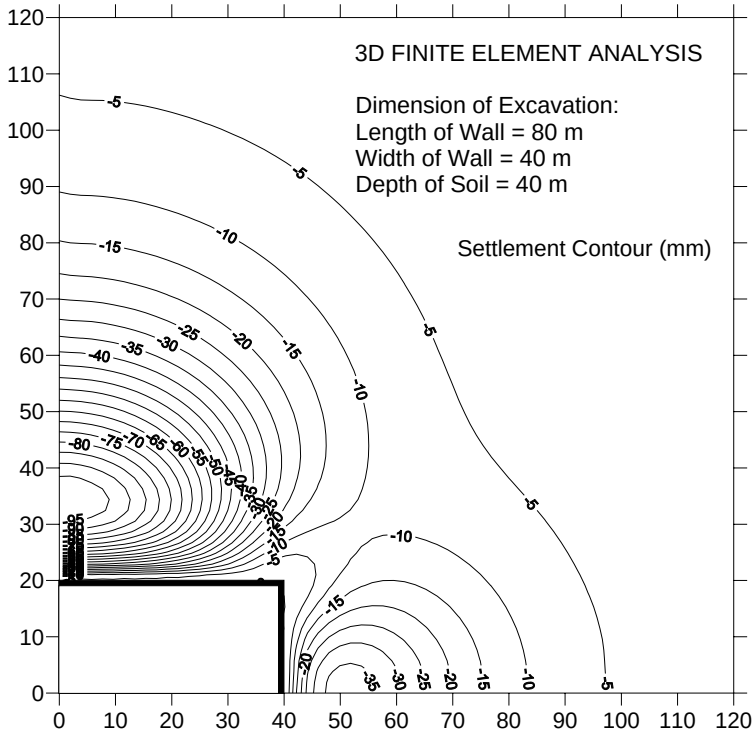

Figure 6.23 3-D FEA Ground Settlement Contour for Case 3: 80x40x40

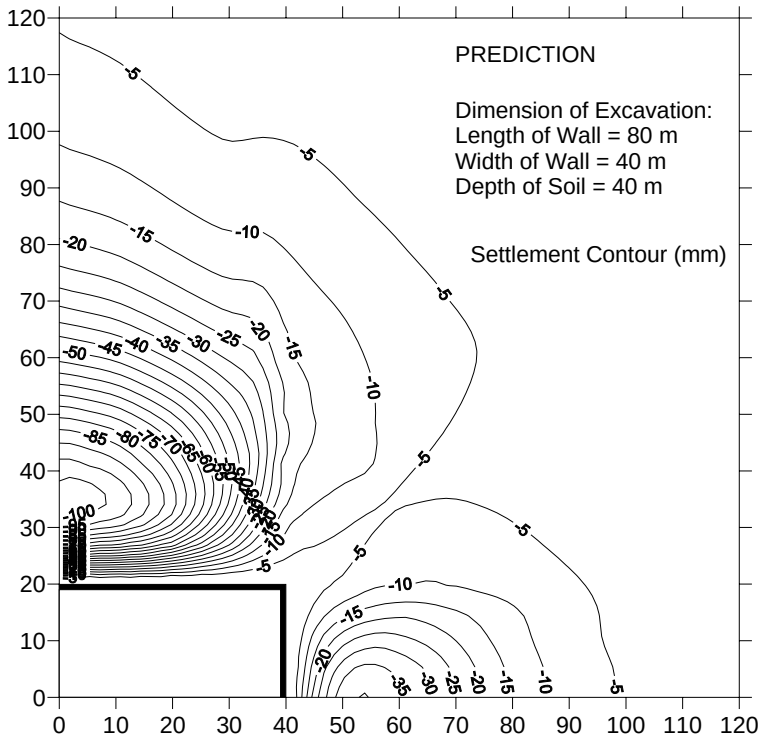

Figure 6.24 Predicted Ground Settlement Contour for Case 3:80x40x40

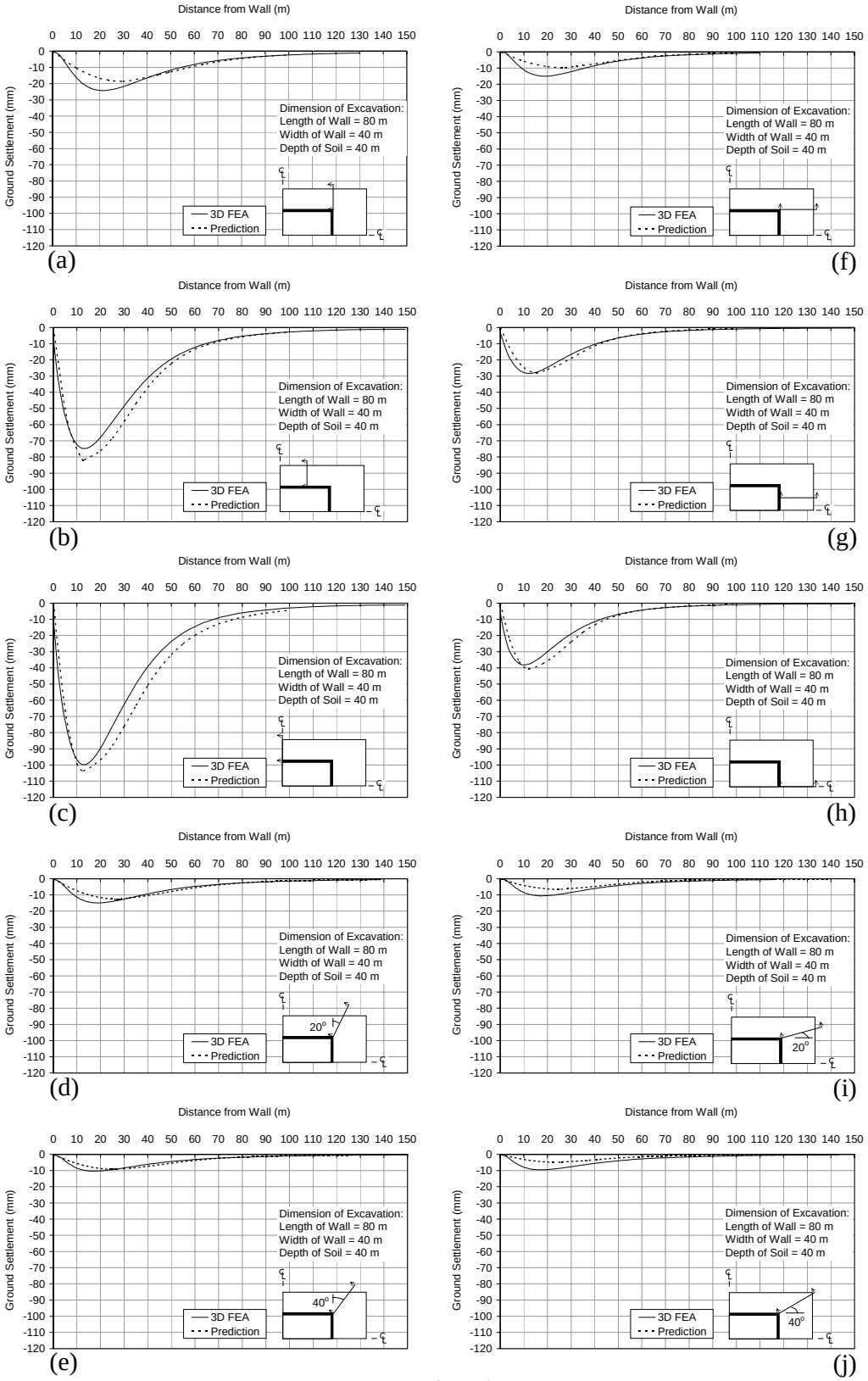

Figure 6.25 Settlement Profiles for Case 3: 80x40x40

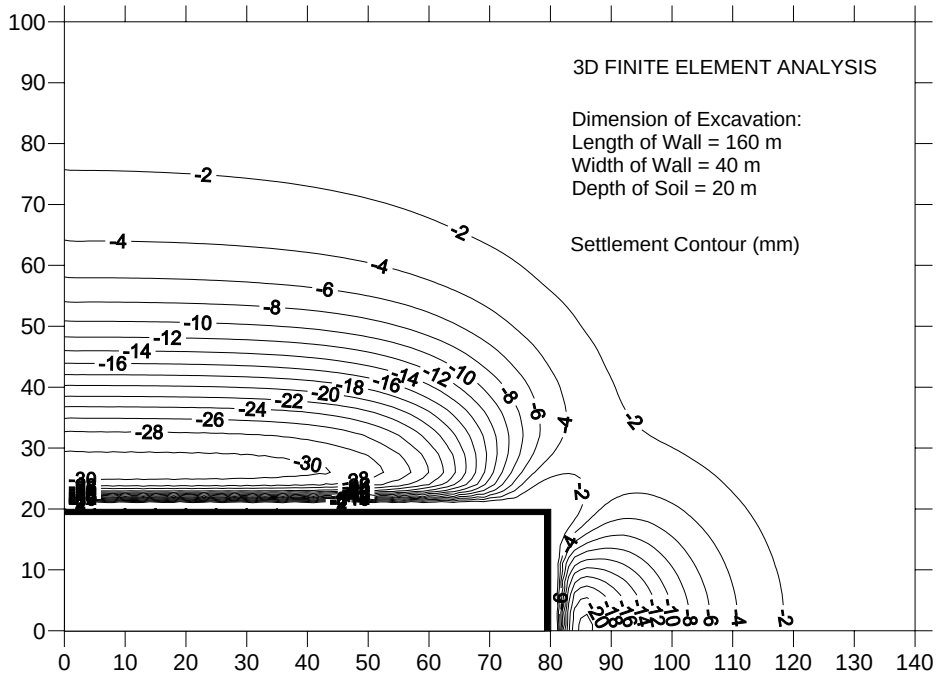

Figure 6.26 3-D FEA Ground Settlement Contour for Case 4: 160x40x20

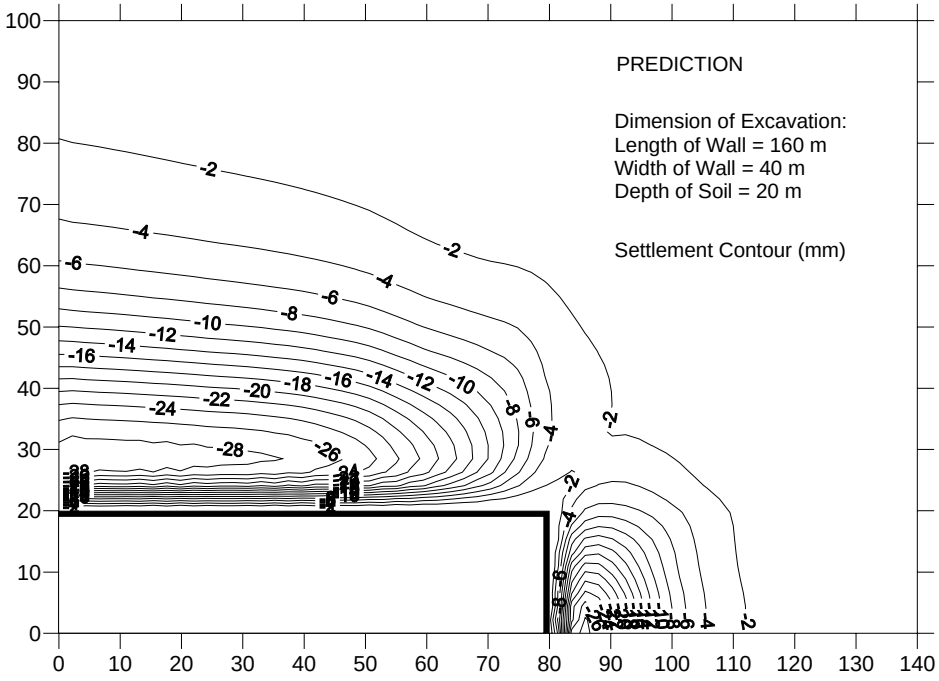

Figure 6.27 Predicted Ground Settlement Contour for Case 4: 160x40x20

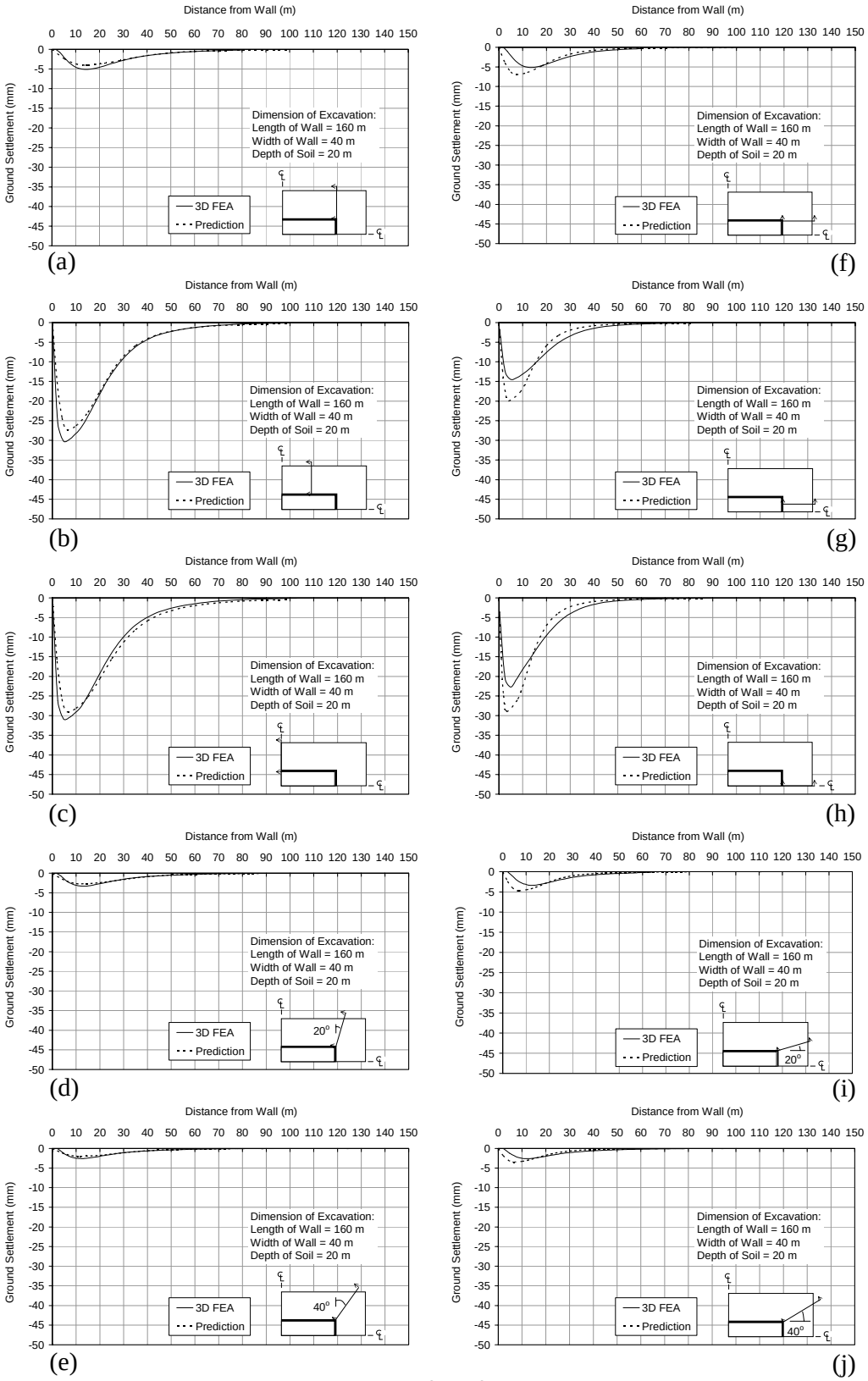

Figure 6.28 Settlement Profiles for Case 4: 160x40x20

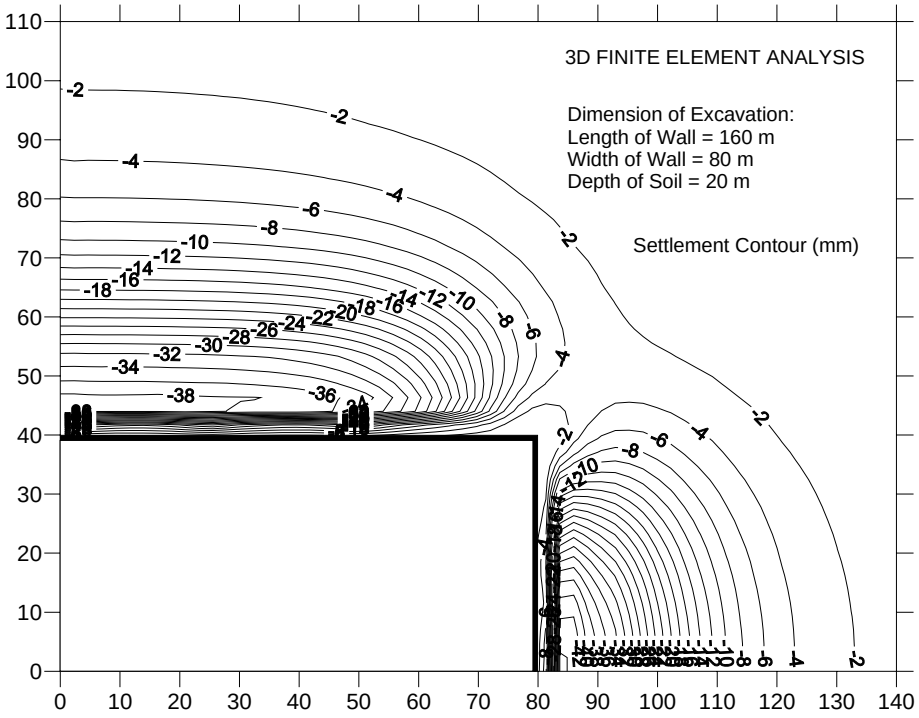

Figure 6.29 3-D FEA Ground Settlement Contour for Case 5: 160x80x20

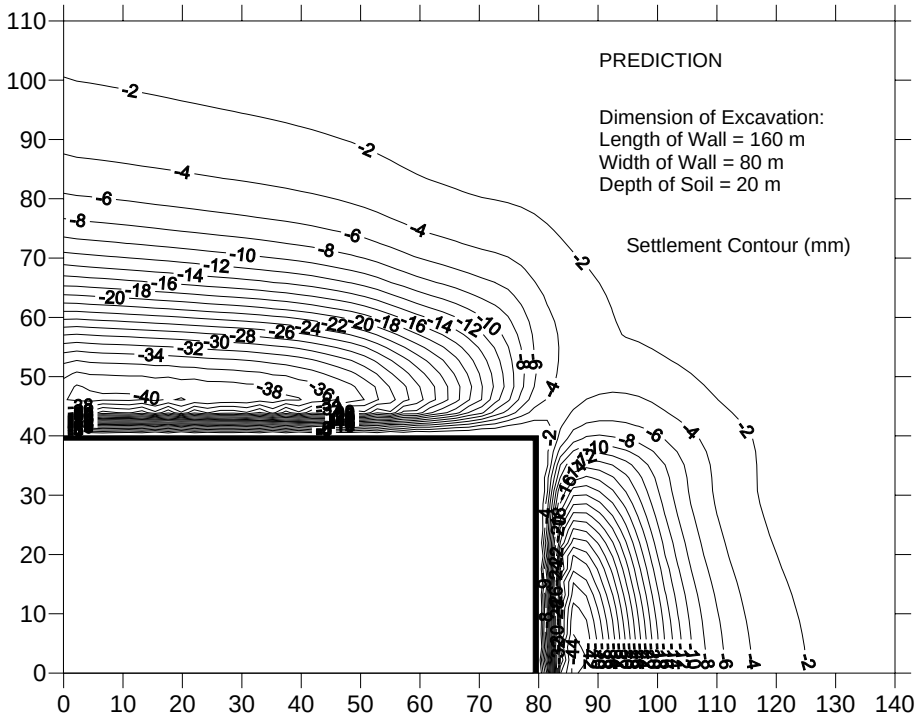

Figure 6.30 Predicted Ground Settlement Contour for Case 5: 160x80x20

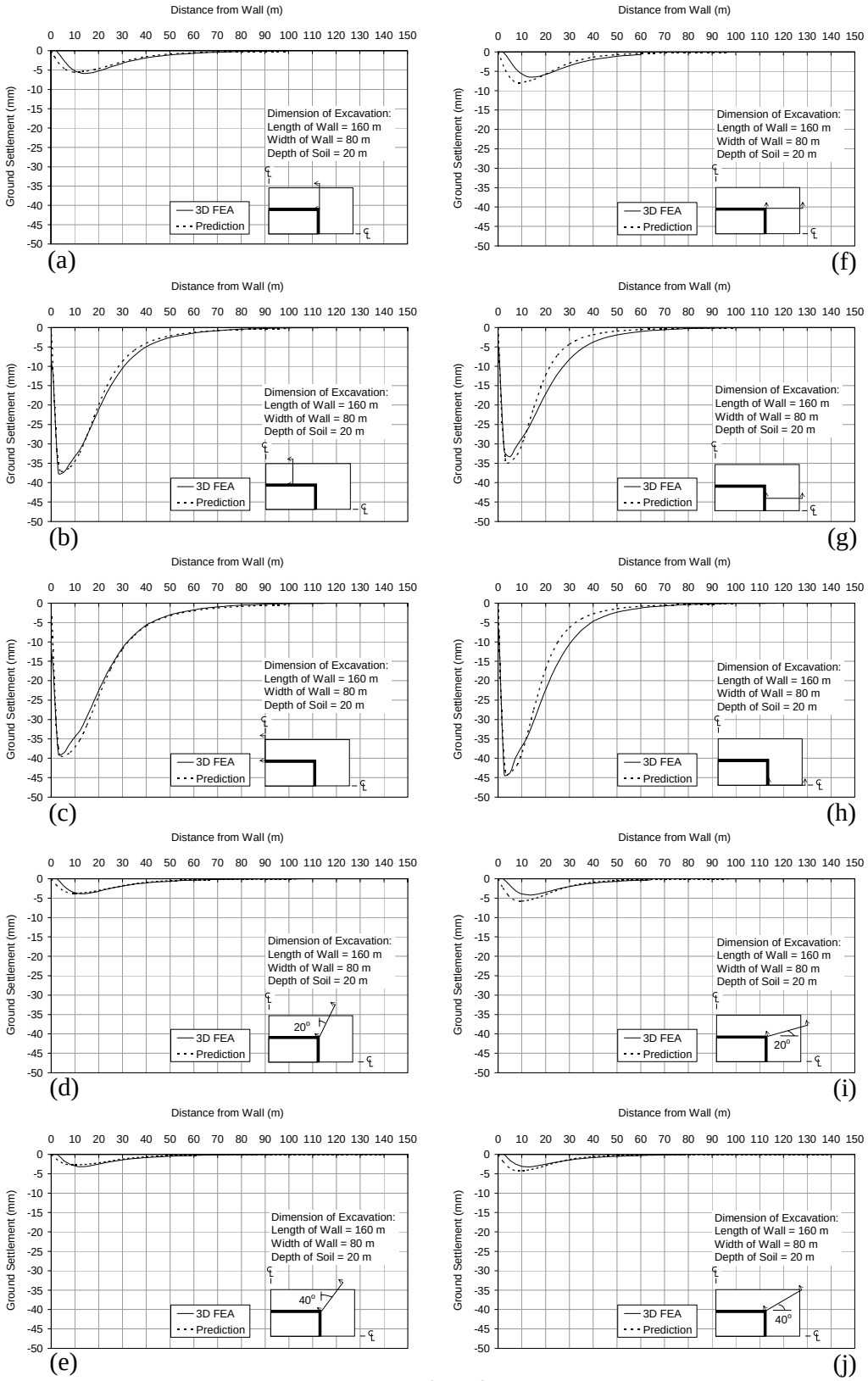

Figure 6.31 Settlement Profiles for Case 5: 160x80x20

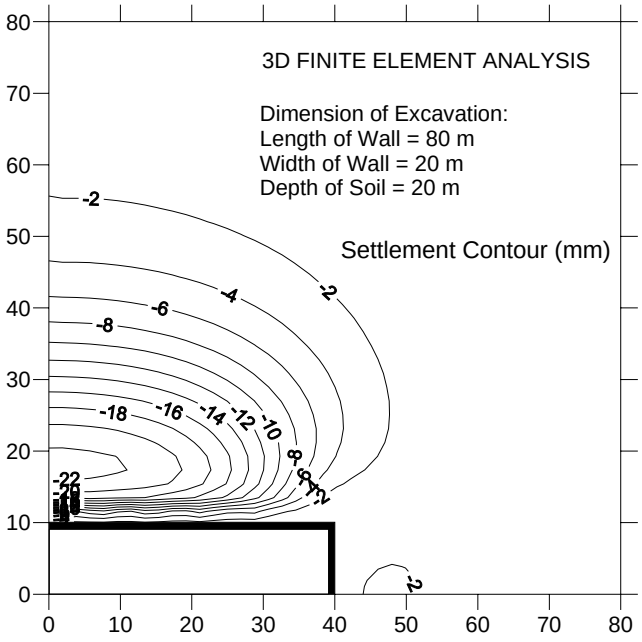

Figure 6.32 3-D FEA Ground Settlement Contour for Case 6: 80x20x20

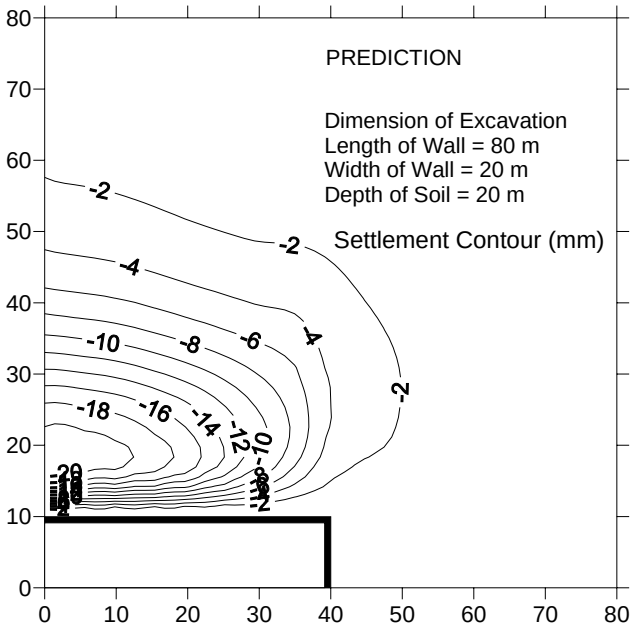

Figure 6.33 Predicted Ground Settlement Contour for Case 6: 80x20x20

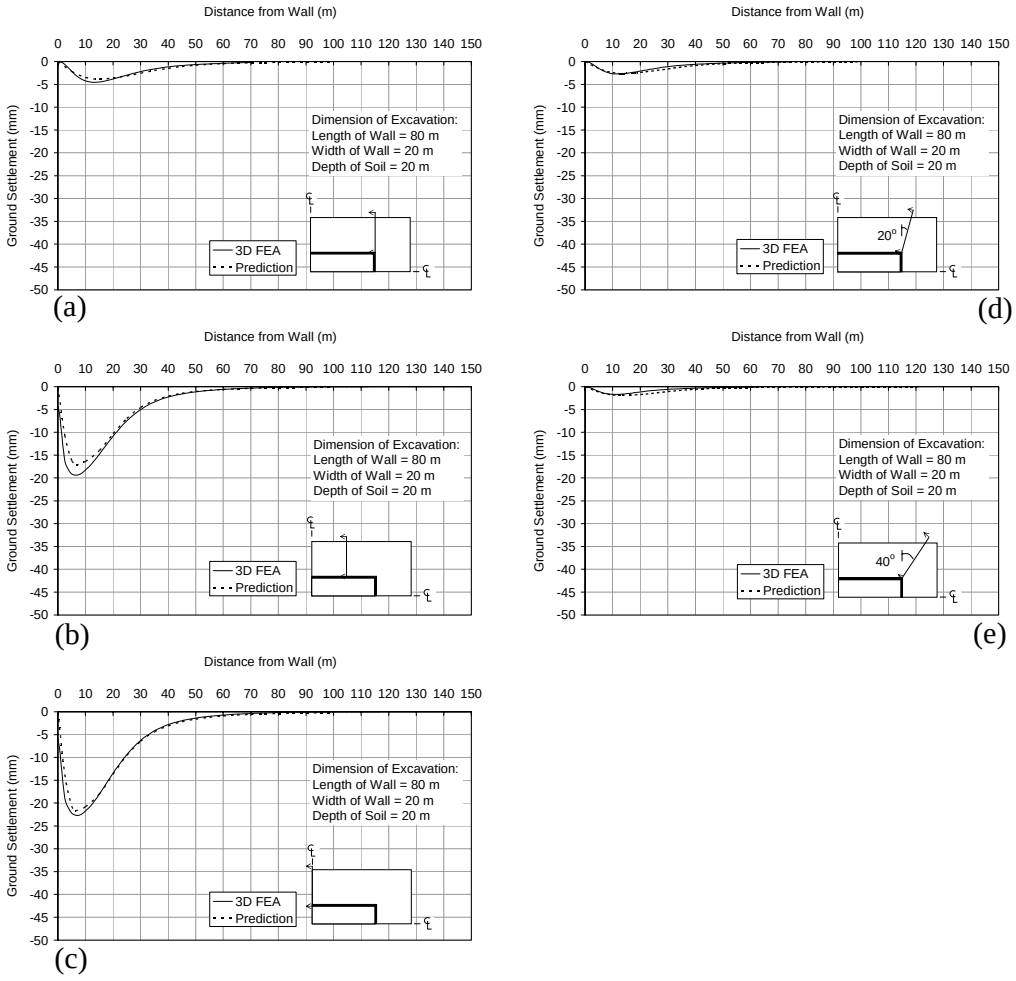

Figure 6.34 Settlement Profiles for Case 6: 80x20x20

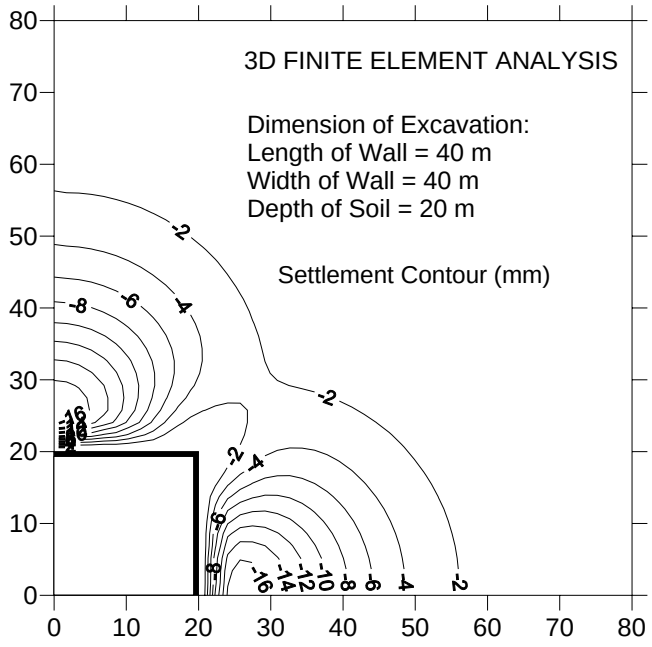

Figure 6.35 3-D FEA Ground Settlement Contour for Case 7: 40x40x20

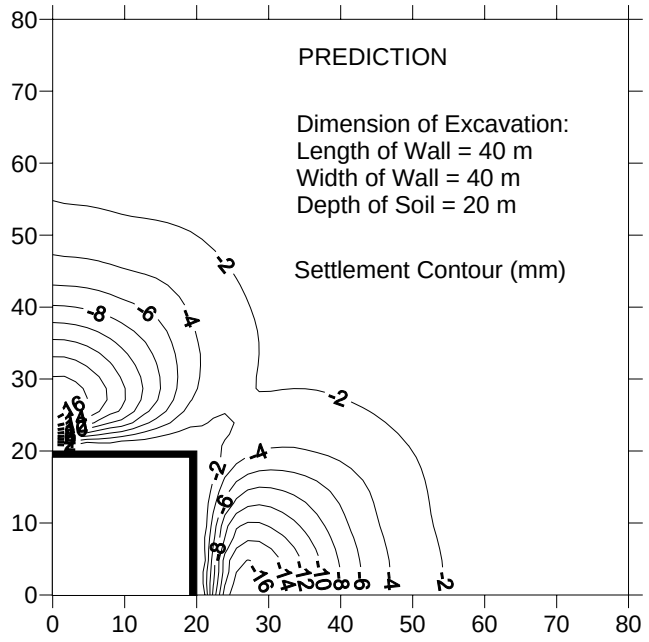

Figure 6.36 Predicted Ground Settlement Contour for Case 7: 40x40x20

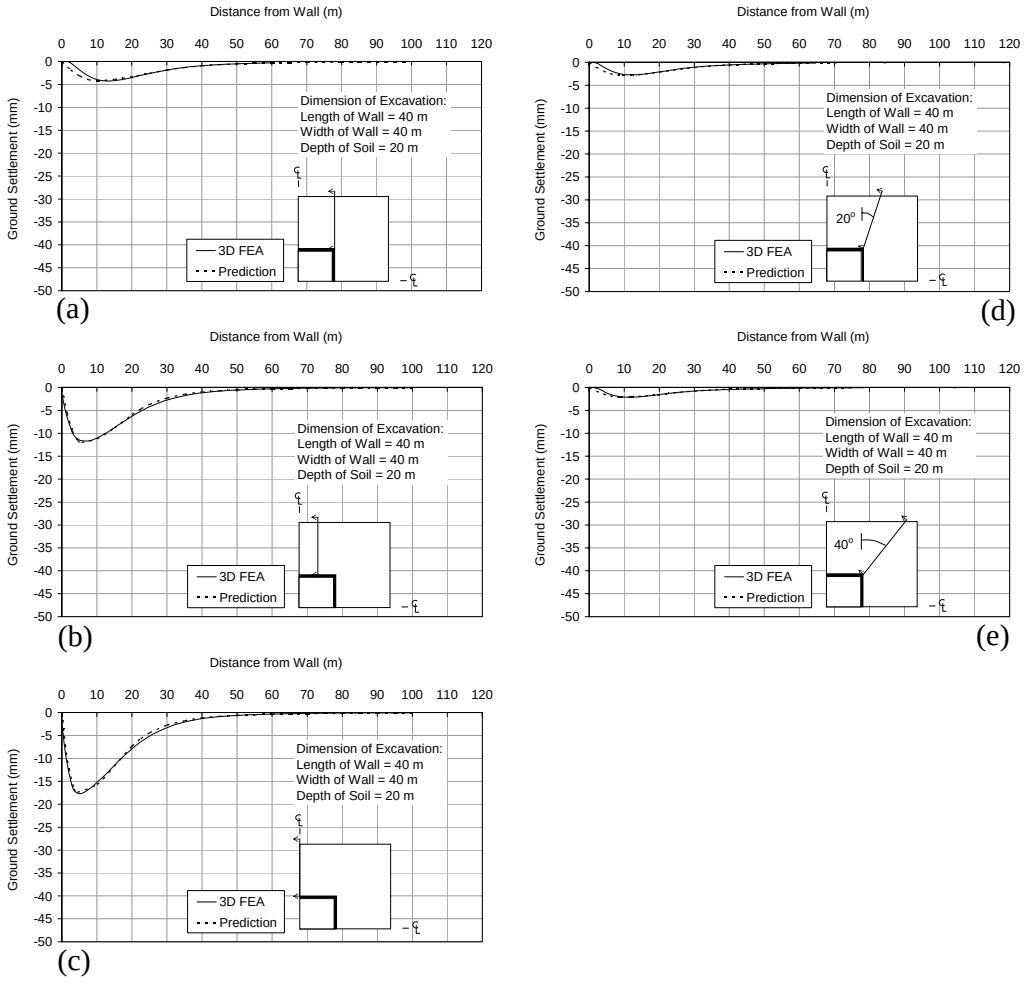

Figure 6.37 Settlement Profiles for Case 7: 40x40x20

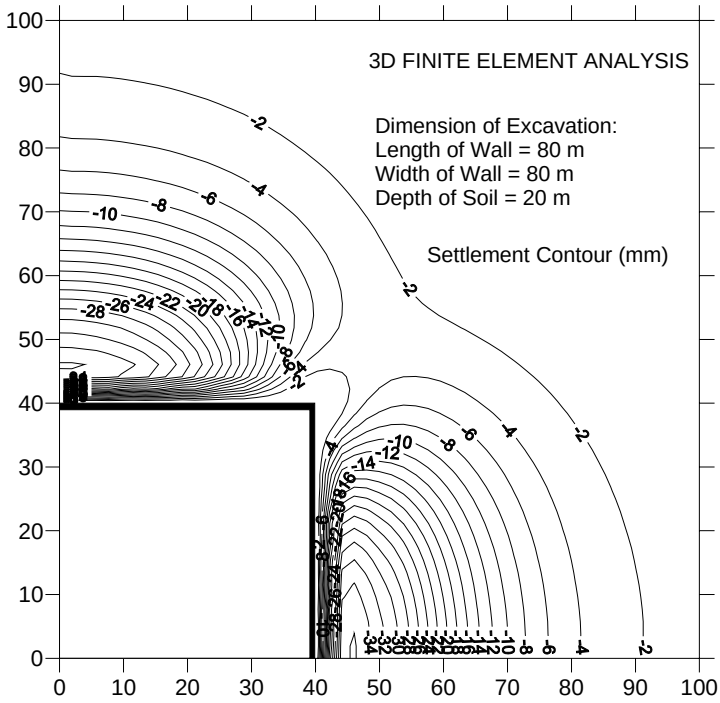

Figure 6.38 3-D FEA Ground Settlement Contour for Case 8: 80x80x20

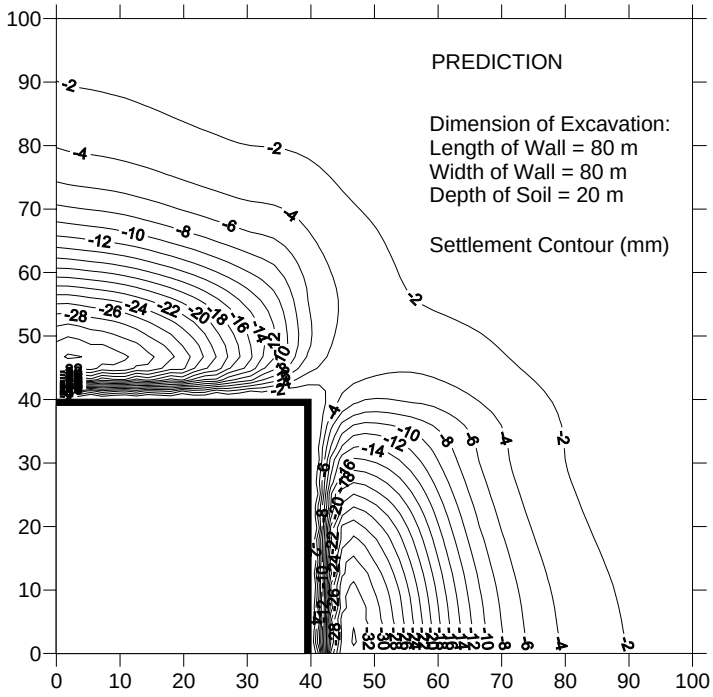

Figure 6.39 Predicted Ground Settlement Contour for Case 8: 80x80x20

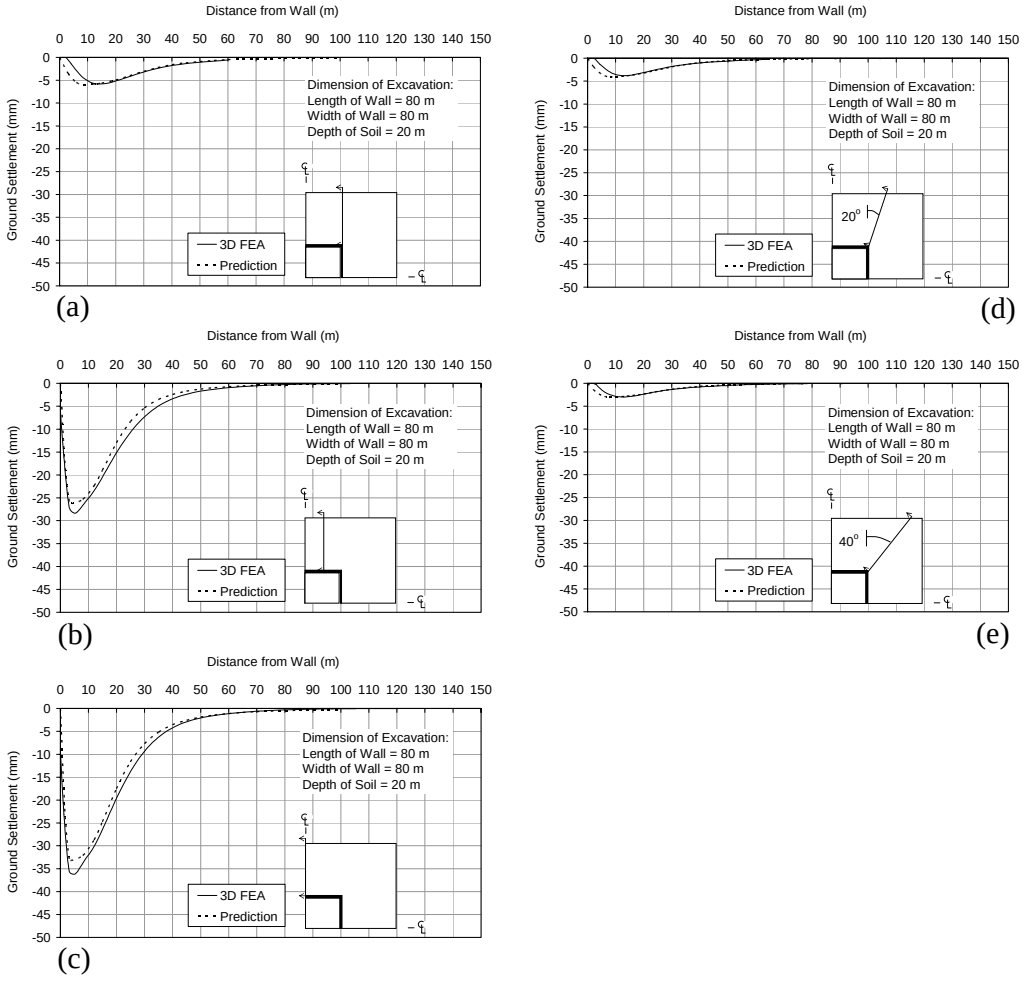

Figure 6.40 Settlement Profiles for Case 8: 80x80x20

Table 6.11 Soil Parameters for Fill and Soft Clay

Soil Type	γ_{sat} (kN/m^3)	κ	λ	M	ν'	k (m/s)
Fill	19	0.02	0.1	1.244	0.33	$1x10^{-6}$
Soft Clay	16	0.0293	0.1465	1.19	0.33	$1x10^{-8}$

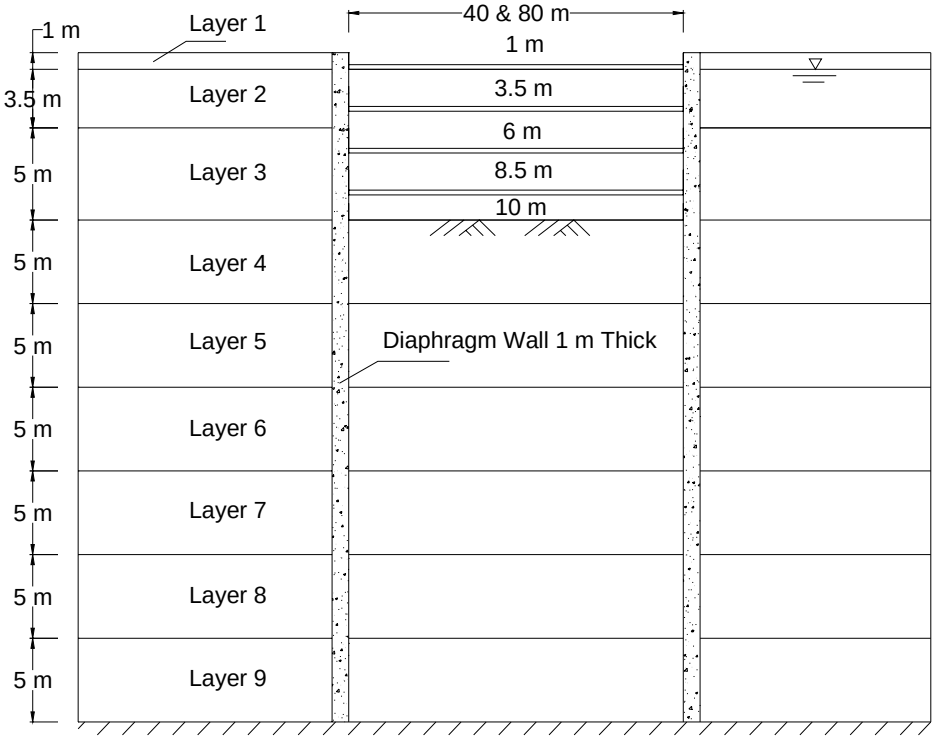

Figure 6.41 Cross-section of Excavation for Modified Cam Clay Model

Table 6.12 Soil Parameters for Layers 1 to 9

Soil	γ_{sat}	ν	E (kPa)	c (kPa)	ϕ (^{o})
Layer 1	19	0.33	3000	10	0
Layer 2	19	0.33	7500	25	0
Layer 3	19	0.33	10500	35	0
Layer 4	19	0.33	18000	60	0
Layer 5	19	0.33	24000	80	0
Layer 6	19	0.33	45000	150	0
Layer 7	19	0.33	60000	200	0
Layer 8	19	0.33	75000	250	0
Layer 9	19	0.33	90000	300	0

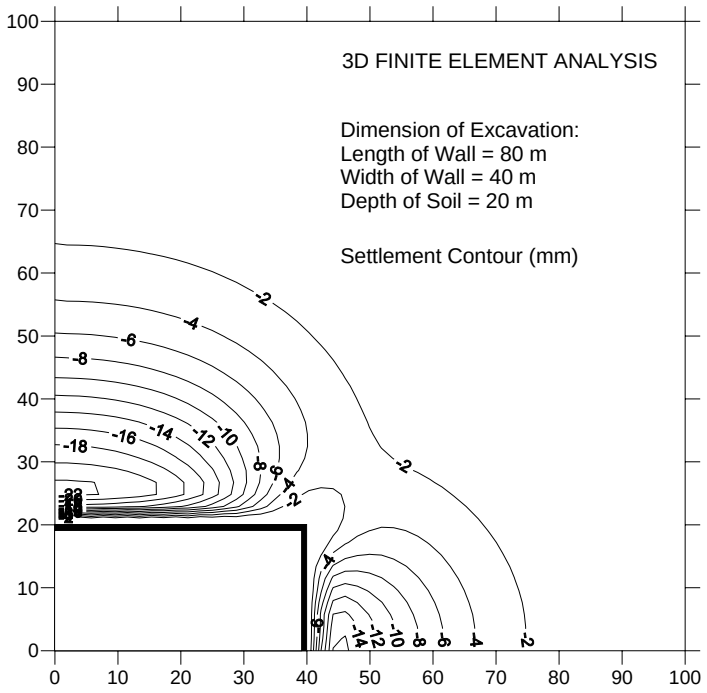

Figure 6.42 3-D FEA Ground Settlement Contour for Case 9: 80x40x20 (Modified Cam Clay Parameters)

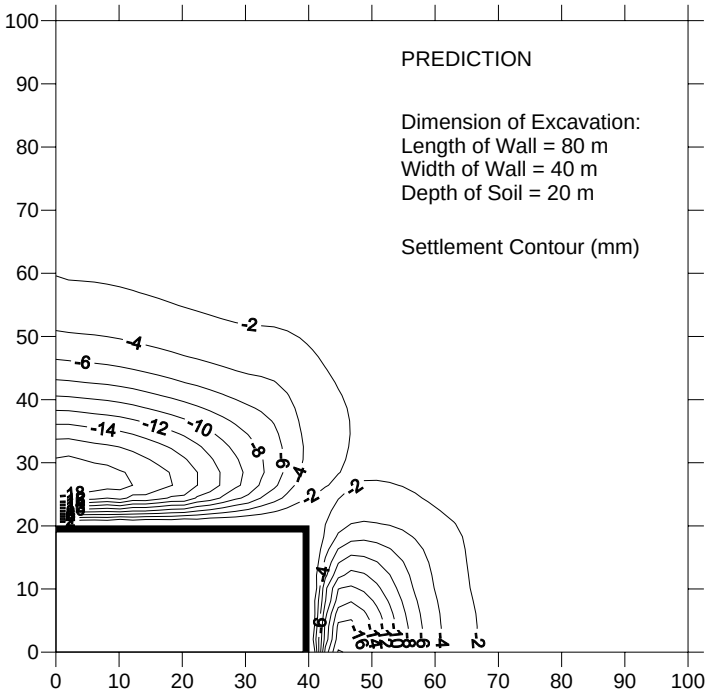

Figure 6.43 Predicted Ground Settlement Contour for Case 9: 80x40x20 (Modified Cam Clay Parameters)

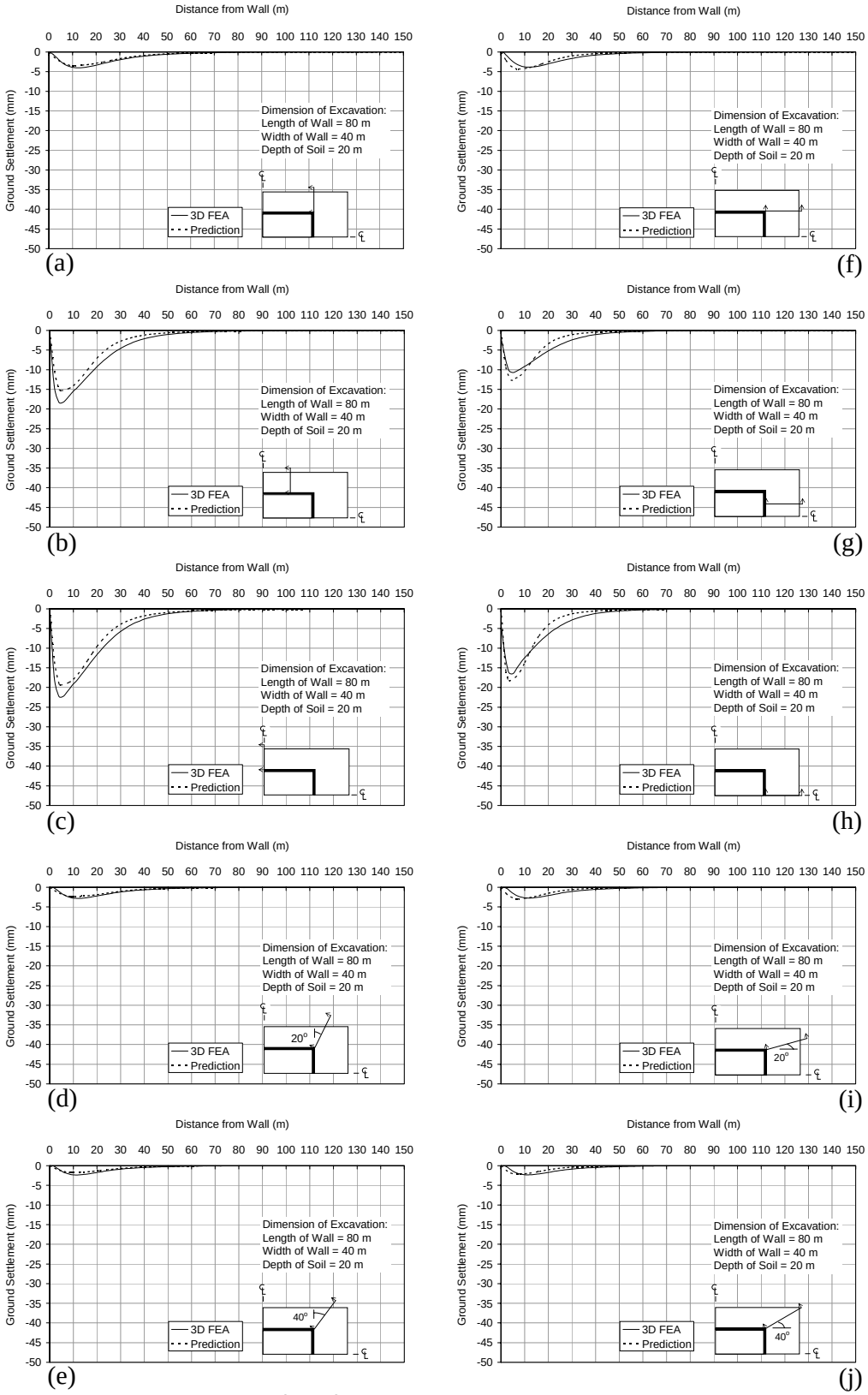

Figure 6.44 Settlement Profiles for Case 9: 80x40x20 (Mod. Cam Clay Parameters)

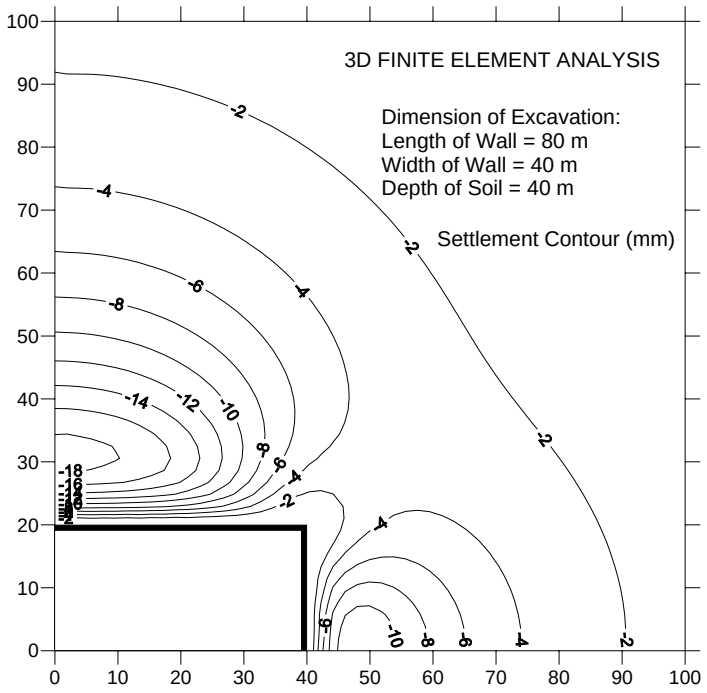

Figure 6.45 3-D FEA Ground Settlement Contour for Case 10: 80x40x20 (Mohr-Coulomb Parameters)

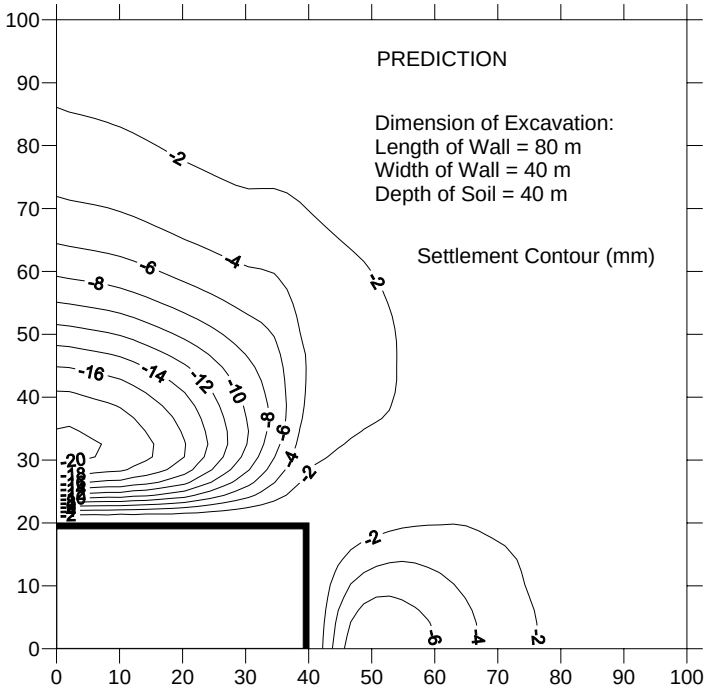

Figure 6.46 Predicted Ground Settlement Contour for Case 10: 80x40x20 (Mohr-Coulomb Parameters)

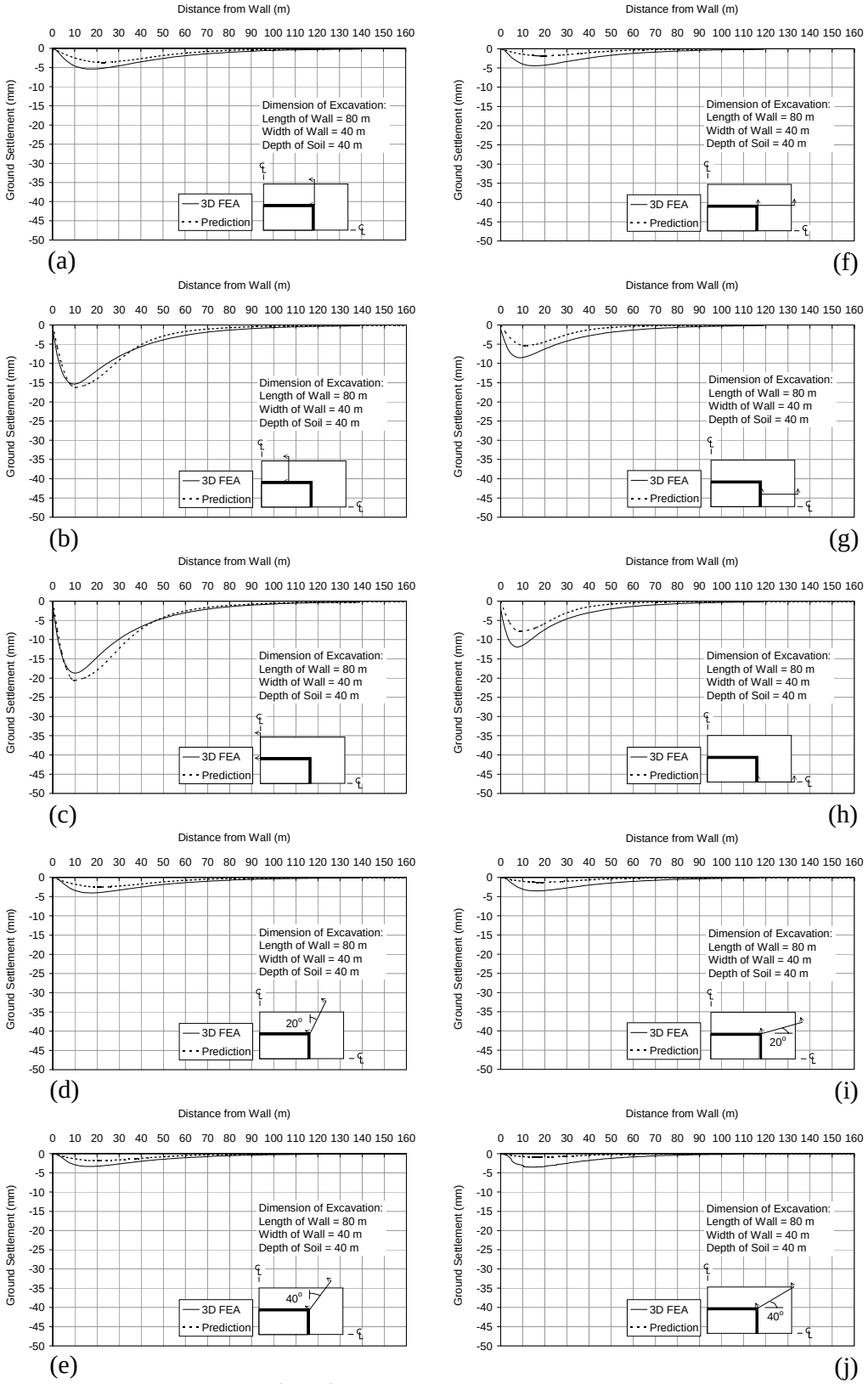

Figure 6.47 Settlement Profiles for Case 10: 80x40x40 (Mohr-Coulomb Parameters)

6.7 Errors in Using Proposed Method

All ten cases have been back-analyzed for validation purpose. The ground settlement contours and settlement profiles have been compared. Another way to check the reliability of the proposed method is to study the error in terms of magnitude and percentage. Sometimes the magnitude can be small, but the percentage is high or vice versa. Therefore, both types of errors are studied.

Three parameters are investigated which are LocMax, Loc0.75, and $\delta_{v,max}$. They are chosen because they are the key variables in Equations 6.3 and 6.5. Figures 6.48 and 6.49 show the error of $\delta_{v,max}$ along the long and narrow sides of wall, respectively. Positive sign means over-prediction and vice-versa when compared with the results from 3-D finite element analysis. Results show that in terms of magnitude, the error is within 5 mm, but in terms of percentage, the error can be as much as 20%. For the case with Mohr-Coulomb model, the maximum percentage error is about 70% as shown in Figure 6.49c. However, in terms of magnitude, that error is only 2 mm. Therefore, even though the percentage error is high, in terms of magnitude, it is still acceptable.

Figures 6.50 and 6.51 show the error of LocMax along the long and narrow sides of wall, respectively. In terms of magnitude, the error is about 5 mm. In terms of percentage, most cases show that the maximum error is about 40%. Case 1 (80x40x20) has a maximum error of 50% as shown in Figure 6.51c. In term of magnitude it is 6 m which may appear to be large. However, a comparison on the entire settlement profile (Figure 6.19c) provides a clearer perspective on the accuracy and reliability of this method. The agreement is still acceptable.

Figures 6.52 and 6.53 show the error of Loc0.75 along the long and narrow sides of wall, respectively. Most cases show that the maximum magnitude error is only about 5 m, but in terms of percentage, the error is about 20%. The maximum error occurs in Case 3 (80x40x40) with maximum error of 8 m and percentage error of 25%. In terms of magnitude, the discrepancy may be large. However, in terms of percentage, it is still acceptable.

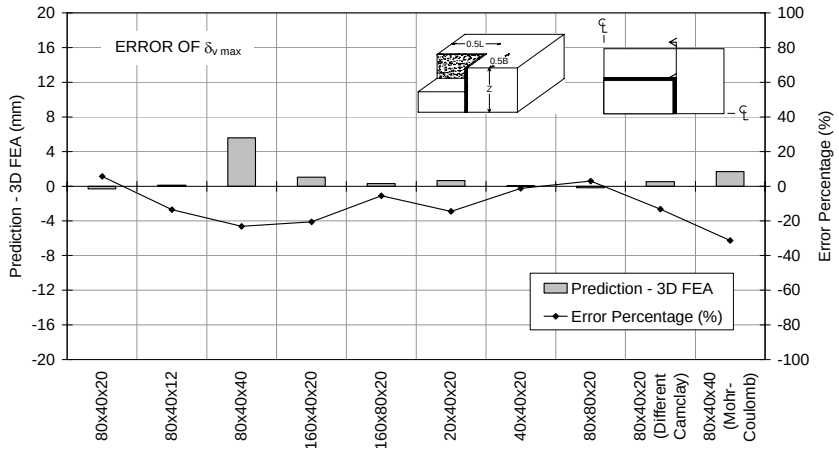

(a)

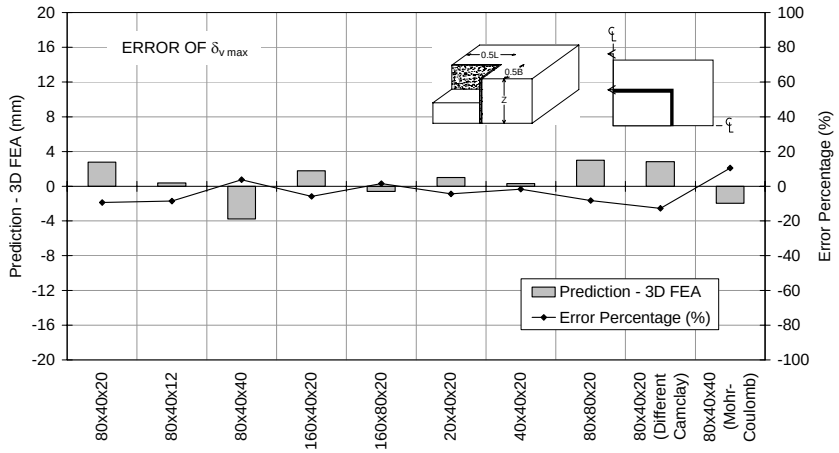

(b)

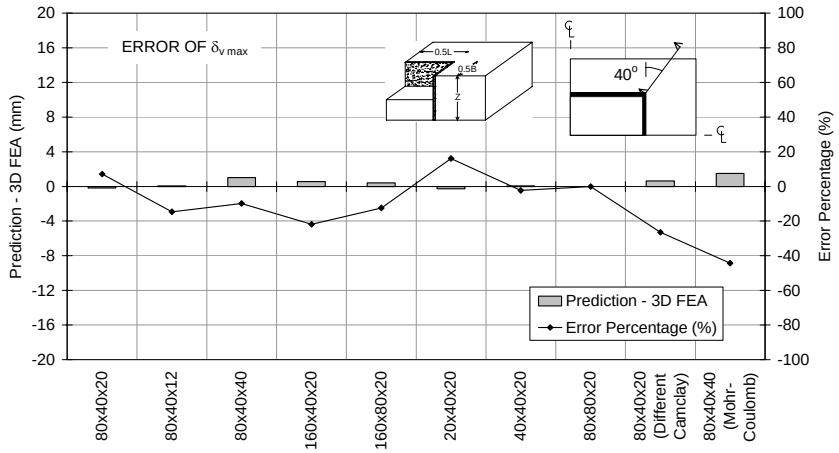

(c)

Figure 6.48 Error of $\delta_{v,max}$ in the Long Side of Wall

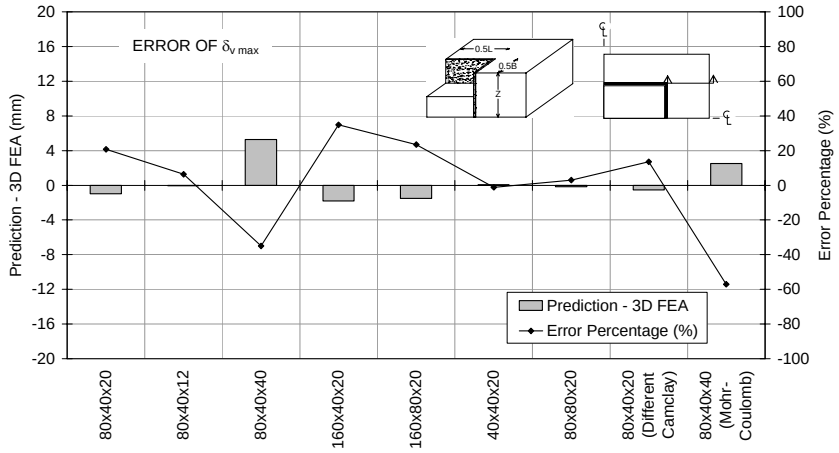

(a)

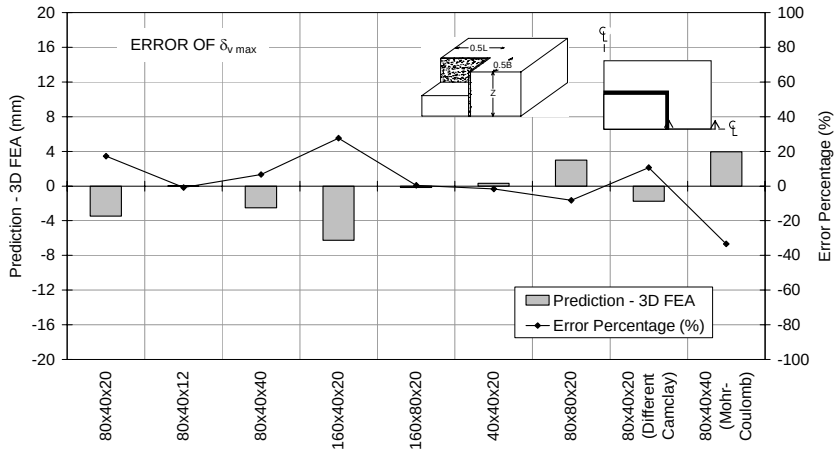

(b)

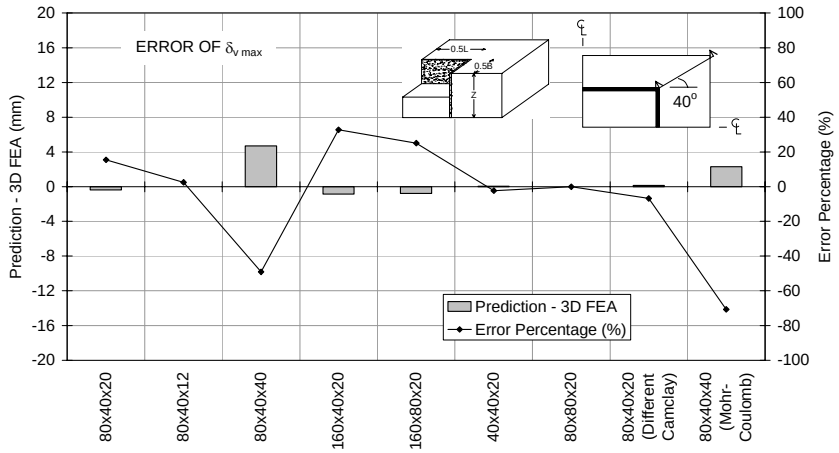

(c)

Figure 6.49 Error of $\delta_{v,max}$ in the Narrow Side of Wall

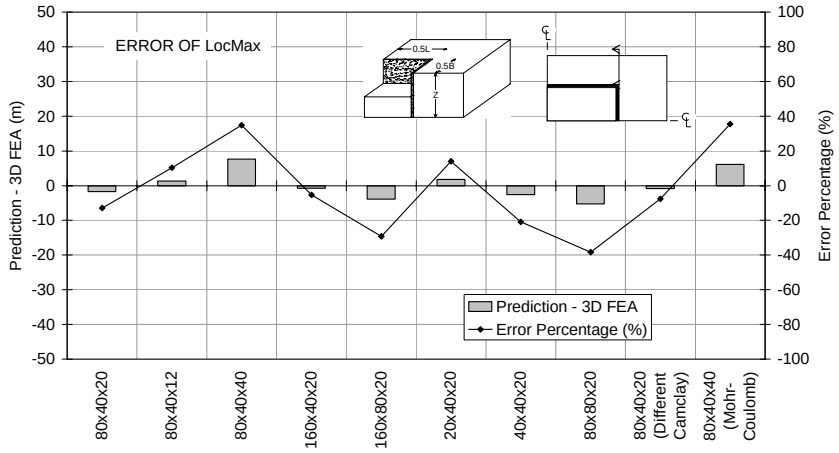

(a)

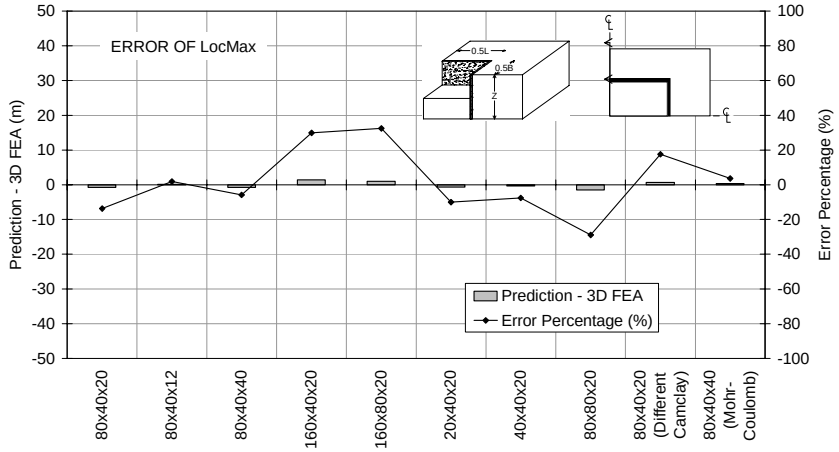

(b)

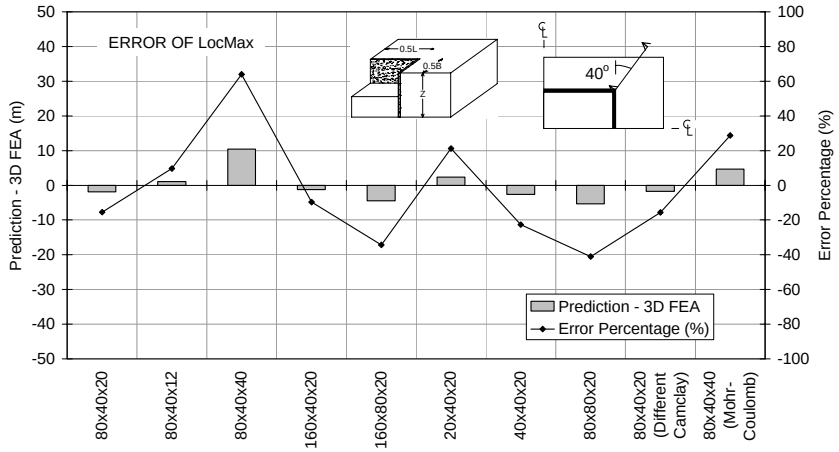

(c)

Figure 6.50 Error of LocMax in the Long Side of Wall

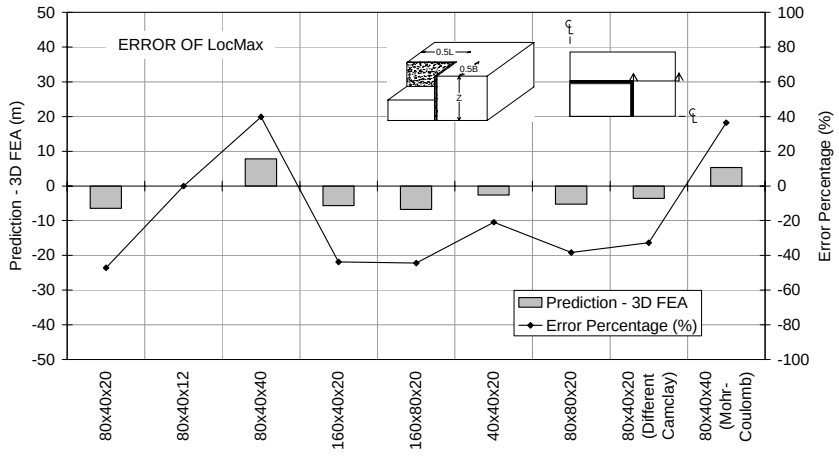

(a)

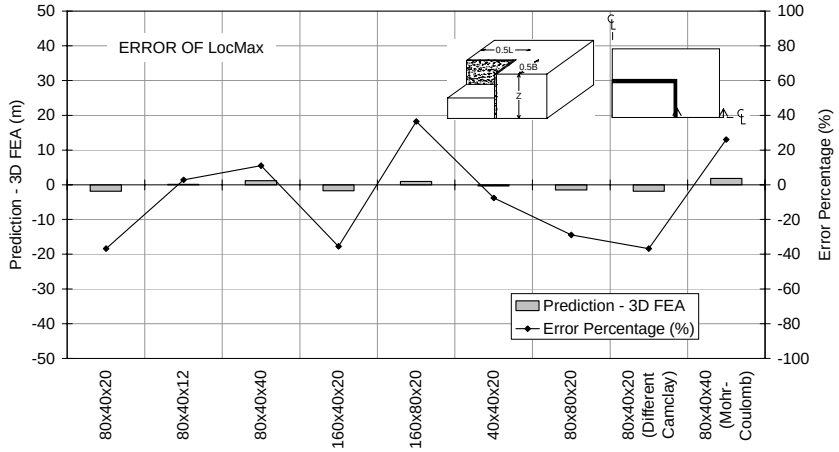

(b)

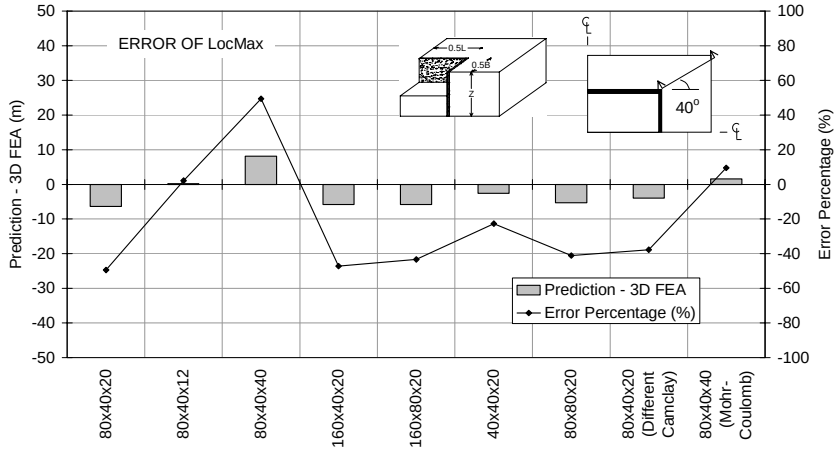

(c)

Figure 6.51 Error of LocMax in the Narrow Side of Wall

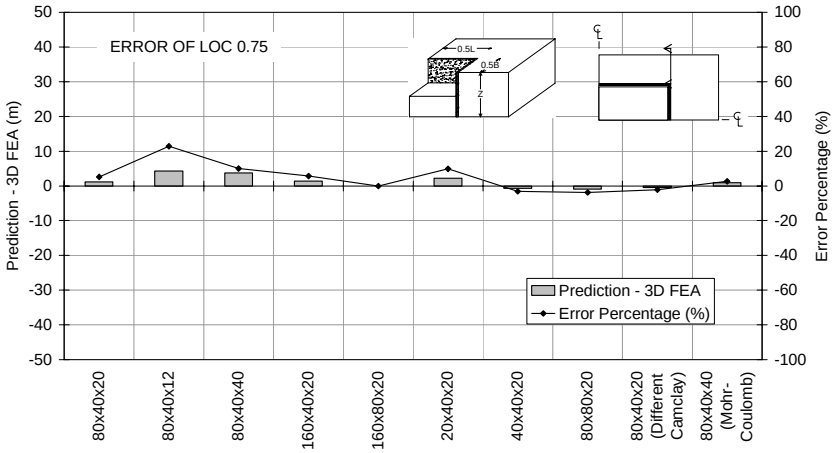

(a)

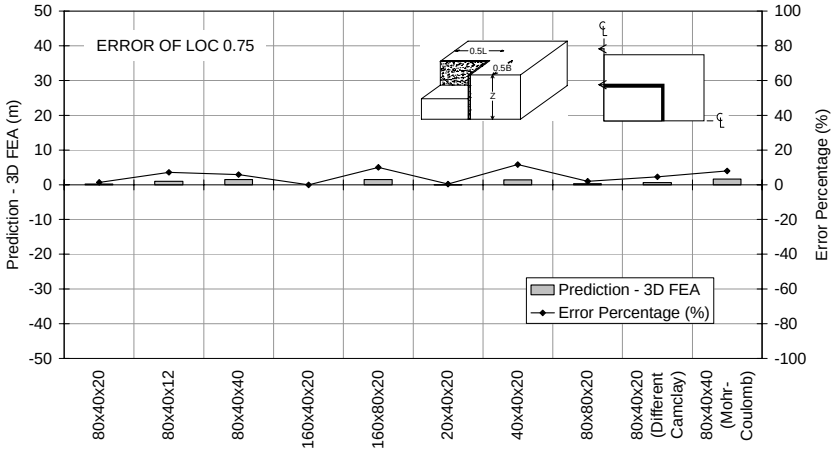

(b)

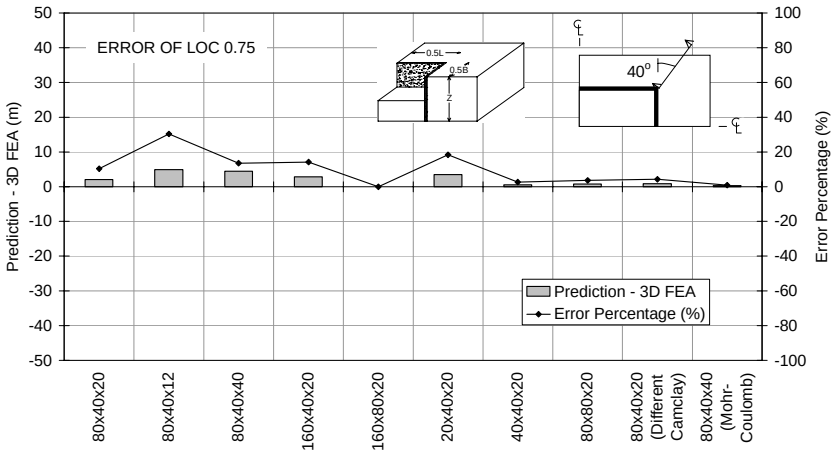

(c)

Figure 6.52 Error of Loc0.75 in the Long Side of Wall

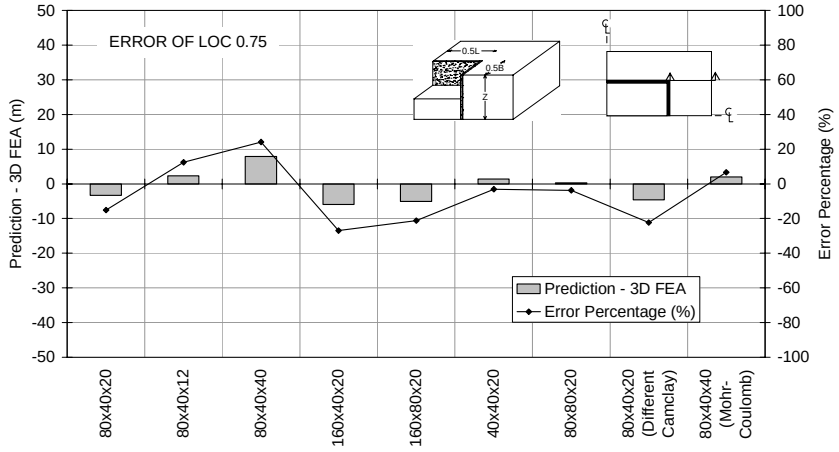

(a)

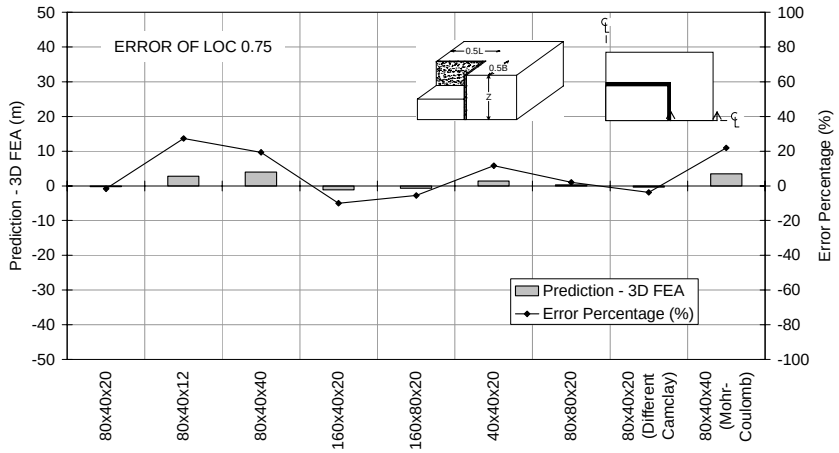

(b)

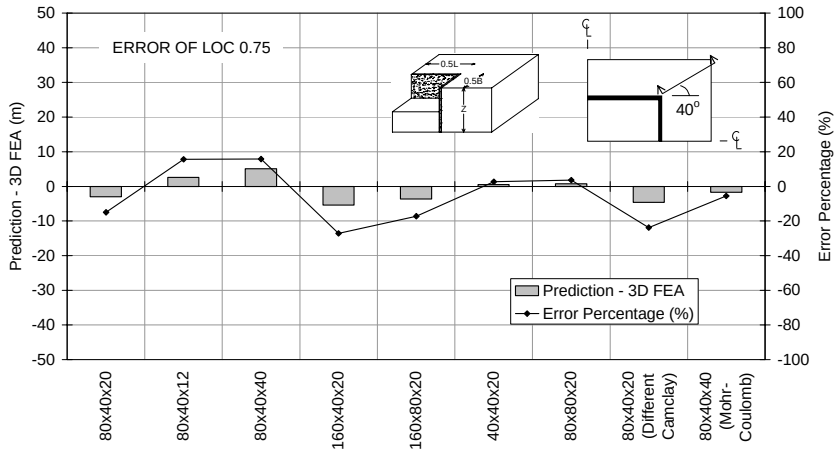

(c)

Figure 6.53 Error of Loc0.75 in the Narrow Side of Wall

6.8 Comparison of 2-D and 3-D Excavation in Finite Element Analysis

In order to have a better visualization about the difference of 2-D and 3-D excavation in the finite element analysis, wall deflections and ground settlements are plotted from the previous analysis. The chosen example is Case 3: 80x40x40. The wall deflections from both sides of walls are shown in Figure 6.54a and 6.54b. Figure 6.54a shows that the 2-D wall deflection is similar with 3-D line 'A'. The closer the distance to the corner, the smaller is the wall deflection. Similar behavior is also observed at Figure 6.54b. However, the difference is at a distance of 20 m from the wall corner, the plain-strain condition (2-D FEA) has not been achieved.

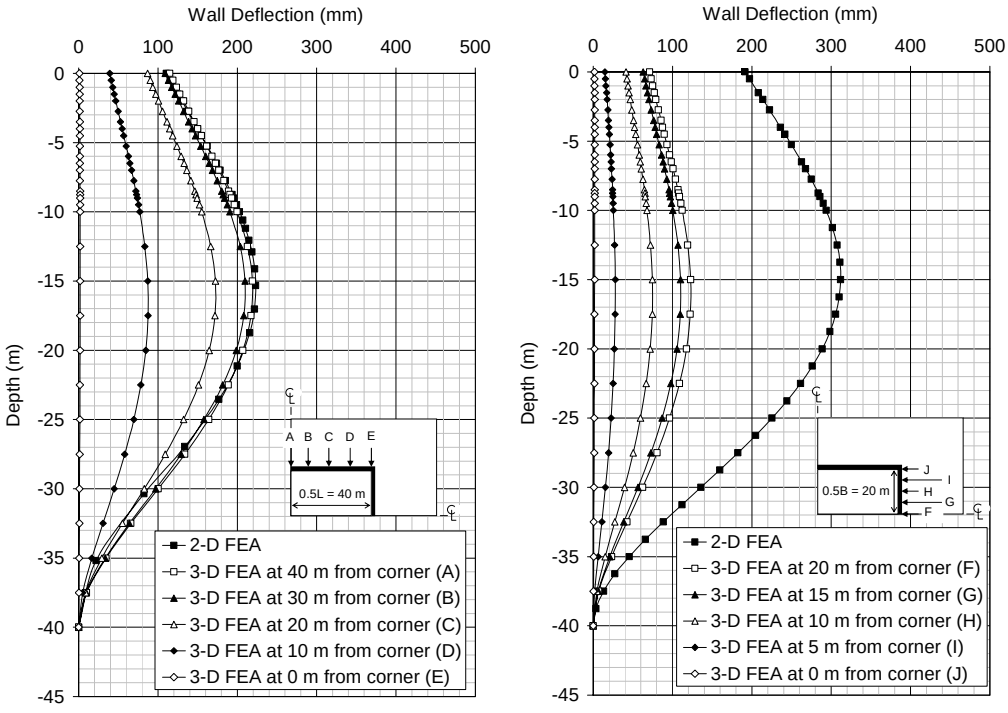

(a) Wall Deflection along 0.5L (b) Wall Deflection along 0.5B

Figure 6.54 Comparison of Wall Deflection between 2-D and 3-D FEA

The corresponding ground settlements are shown in Figure 6.55 and 6.56. Figure 6.55 shows that the ground settlement for line "K" is still smaller than the plain-strain condition (2-D FEA) although the wall deflection at that location has reached plain-strain condition. Both figures also show that the closer the distance to the corner, the smaller is the ground settlement. This behavior highlights the

importance of getting proper greenfield settlement in predicting building damage. Using 2-D greenfield settlement is not appropriate if the building location is close to the corner.

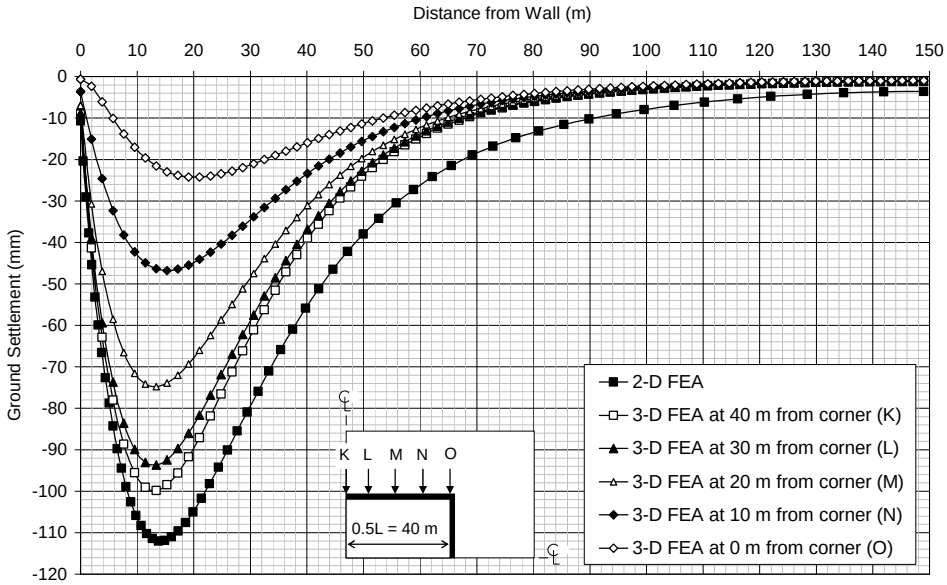

Figure 6.55 Comparison of Ground Settlement between 2-D and 3-D FEA at 0.5L = 40 m

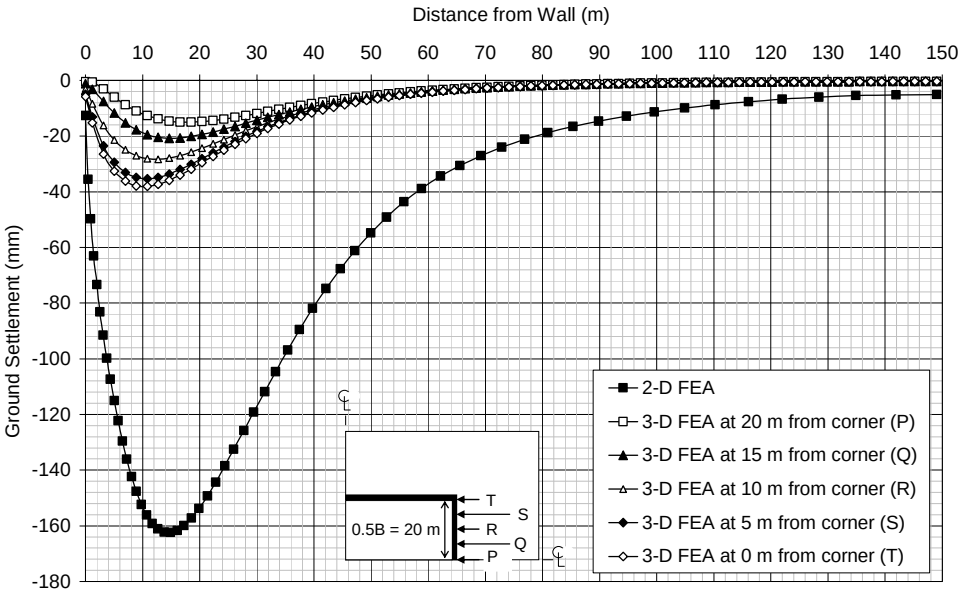

Figure 6.56 Comparison of Ground Settlement between 2-D and 3-D FEA at 0.5B = 20 m

6.9 Study Case 1: Underground Car Park at the House of Commons in London (Burland and Hancock, 1977)

Burland and Hancock (1977) reported measurements of ground settlement and wall deflection during the construction of underground car park at the House of Commons in London. The site plan is shown in Figure 6.57. The shape of the excavation is approximately square. The soil is a stiff material as shown in Figure 6.58. The excavation was done by constructing the floor successively from the top downwards. The cross section of the excavation is shown in Figure 6.59.

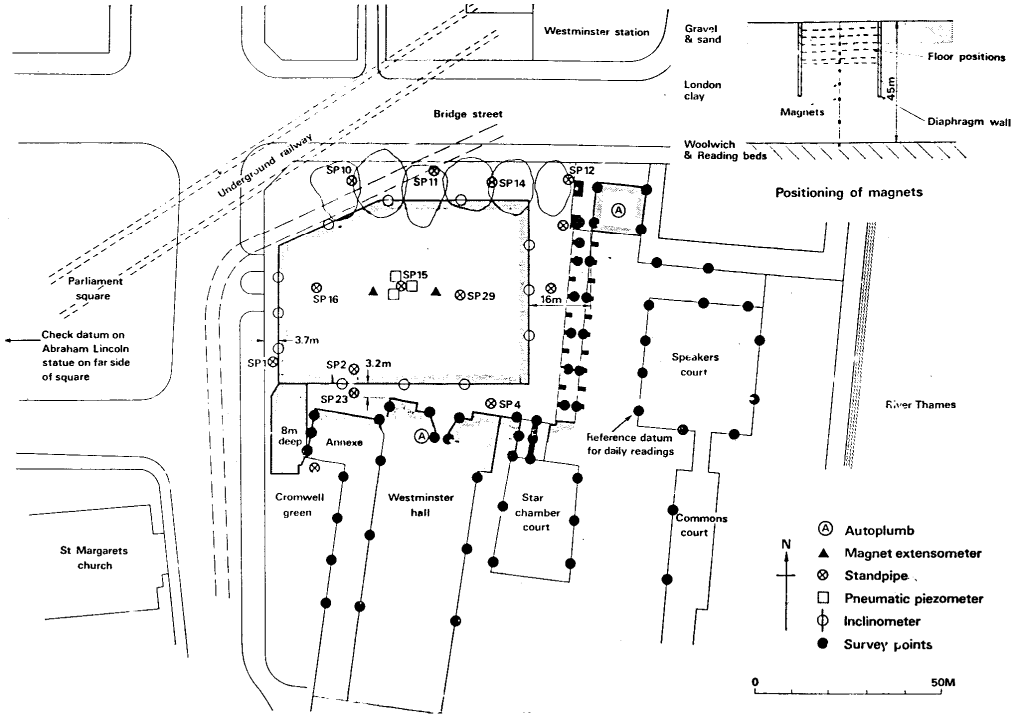

Figure 6.57 Location of Underground Car Park (Burland and Hancock, 1977)

Measurements from the survey points are shown in Figures 6.60 and 6.61. Figure 6.60 shows the settlement along cross-sections A-A and B-B. Parameters LocMax, Loc0.75, and $\delta_{v,max}$ are obtained directly from measurements (Figure 6.60). Therefore they reflect the 3-D field condition. Hence, it is not necessary to use Charts 1 to 3 for conversion from 2-D to 3-D. The equations of ground settlement can then be set up to generate the contour plot as shown in Figure 6.62.

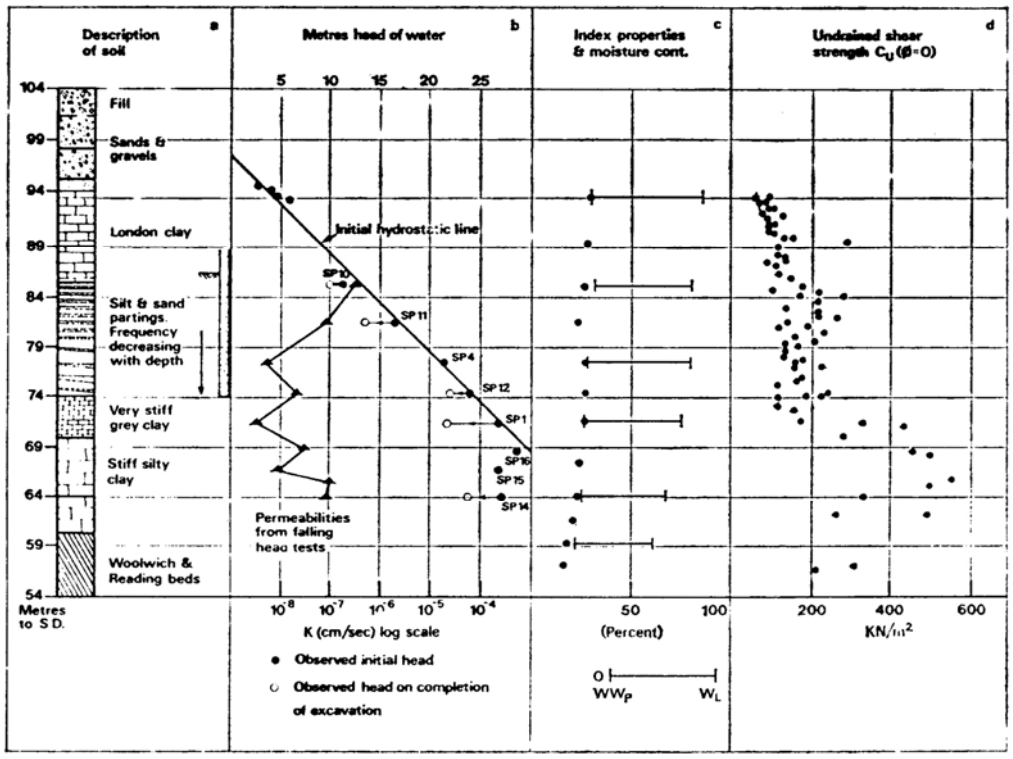

Figure 6.58 Soil Condition at Underground Car Park (Burland and Hancock, 1977)

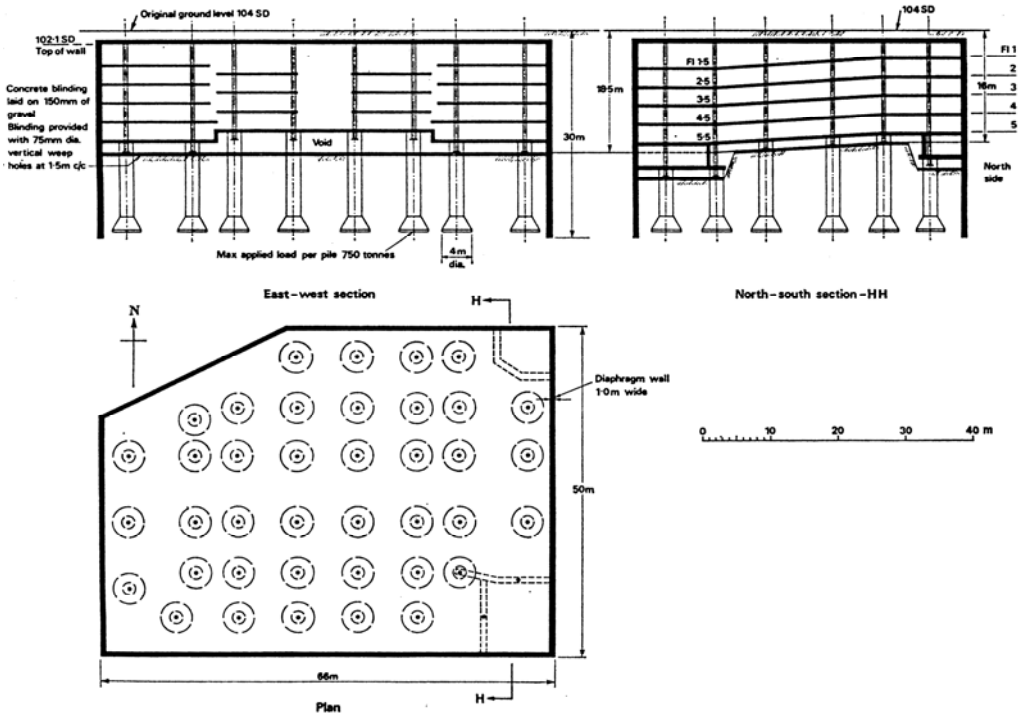

Figure 6.59 Cross Section at Underground Car Park (Burland and Hancock, 1977)

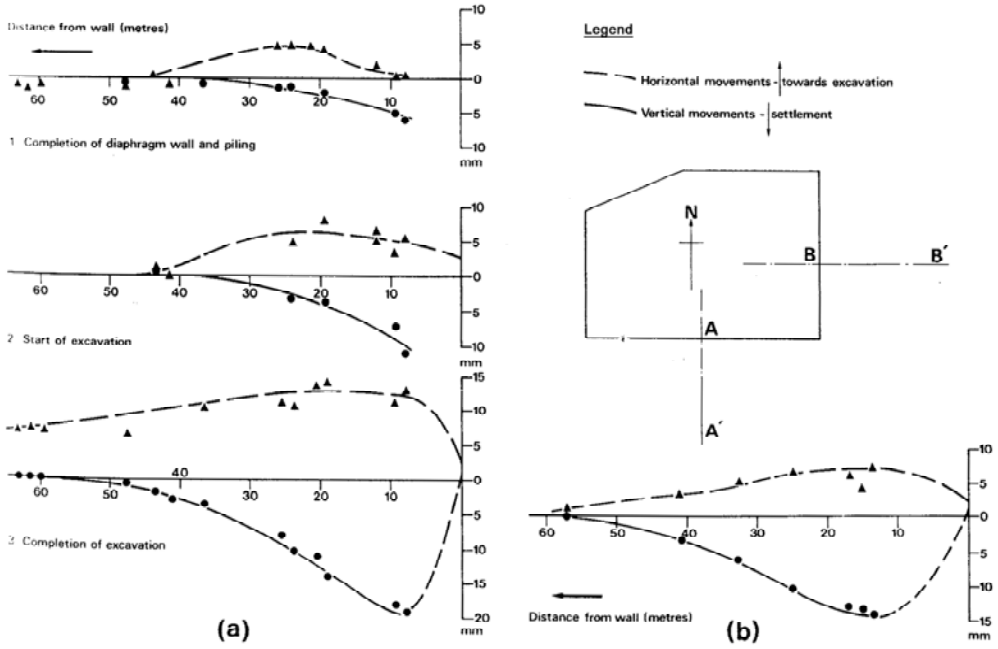

Figure 6.60 Observed horizontal and vertical movements at
(a) the South wall and (b) the East wall (Burland, et al., 1979)

Figure 6.61 shows the settlement contours constructed from survey points fixed on the buildings. The construction of these contours is very subjective. Instead of using these settlement contours to compare with predicted results, it is more meaningful to compare with survey points directly ash shown in Figure 6.62. The agreement is reasonable.

6.10 Study Case 2: Taipei National Enterprise Center (TNEC) (Ou, et al., 2000)

The TNEC is an 18-story building with five levels of basement. It is surrounded by 7 buildings as shown in Figure 6.63. Many ground settlement points were installed at the locations shown in Figure 6.64. The basement was constructed using the top-down construction method. The retaining wall in each excavation stage was supported by a concrete floor slab as shown in Figure 6.65. Figure 6.66 shows the soil profile involving soft soil. The ground water table was around 2 m below the ground surface. This case record provides a good opportunity to study the corner effect on ground settlement.

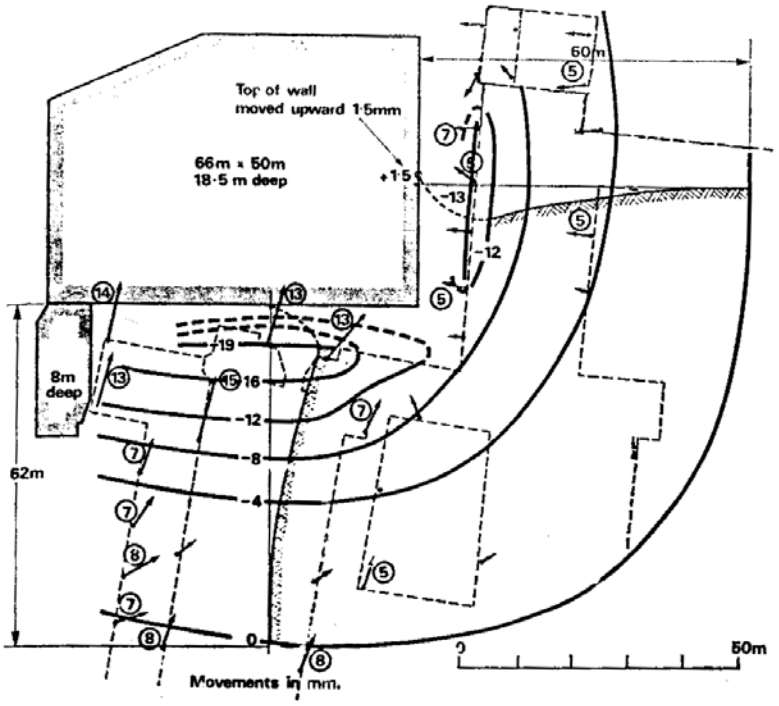

Figure 6.61 Observed Ground Settlement (Burland and Hancock, 1977)

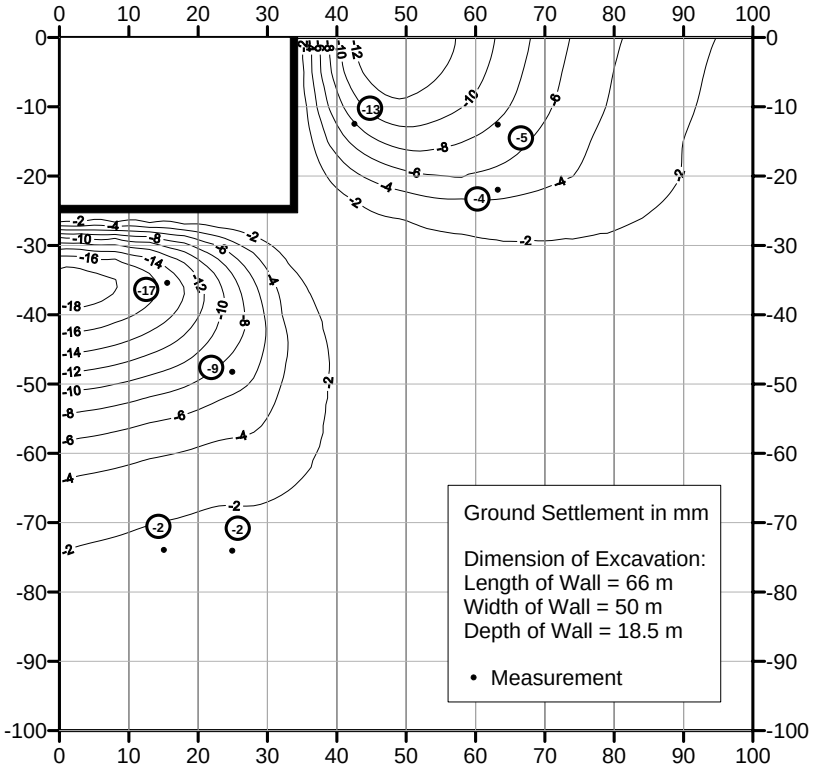

Figure 6.62 Predicted Ground Settlement Using the Proposed Method

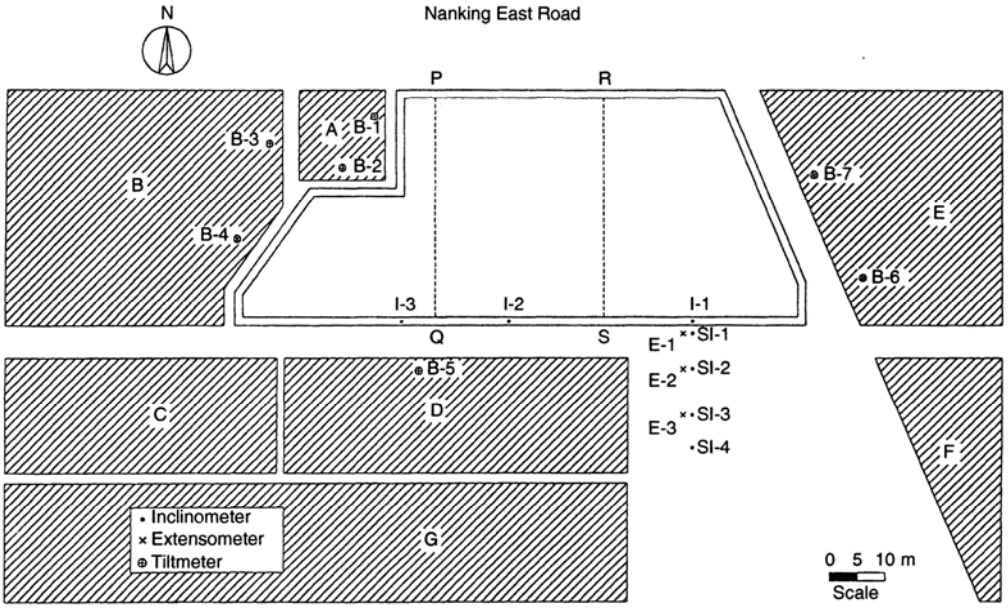

Figure 6.63 Location of TNEC Construction (Ou, et al., 2000)

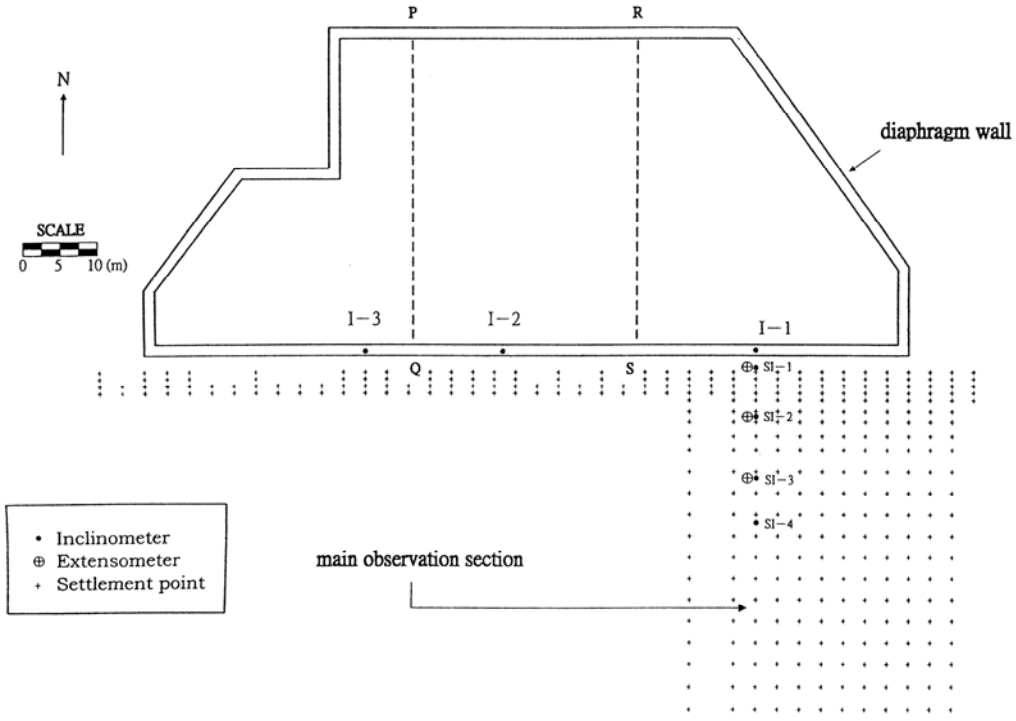

Figure 6.64 Instrumentation Monitoring at TNEC Construction (Ou, et al., 2000)

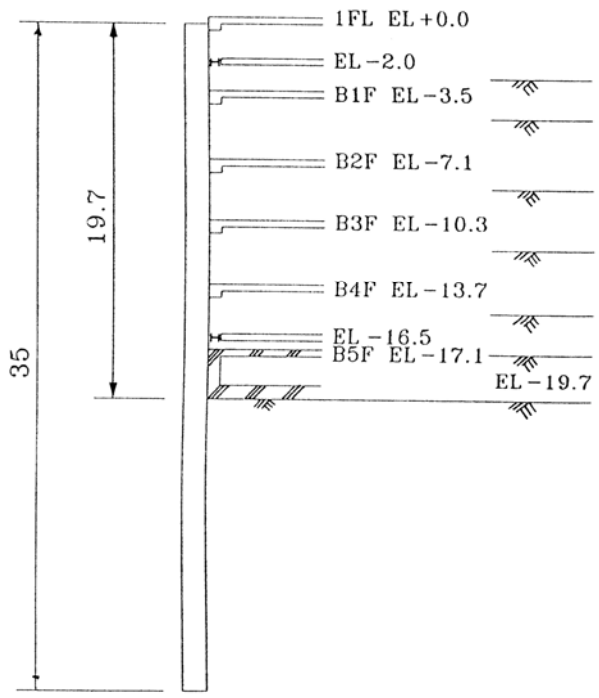

Figure 6.65 Construction Sequence at TNEC (Ou, et al., 2000)

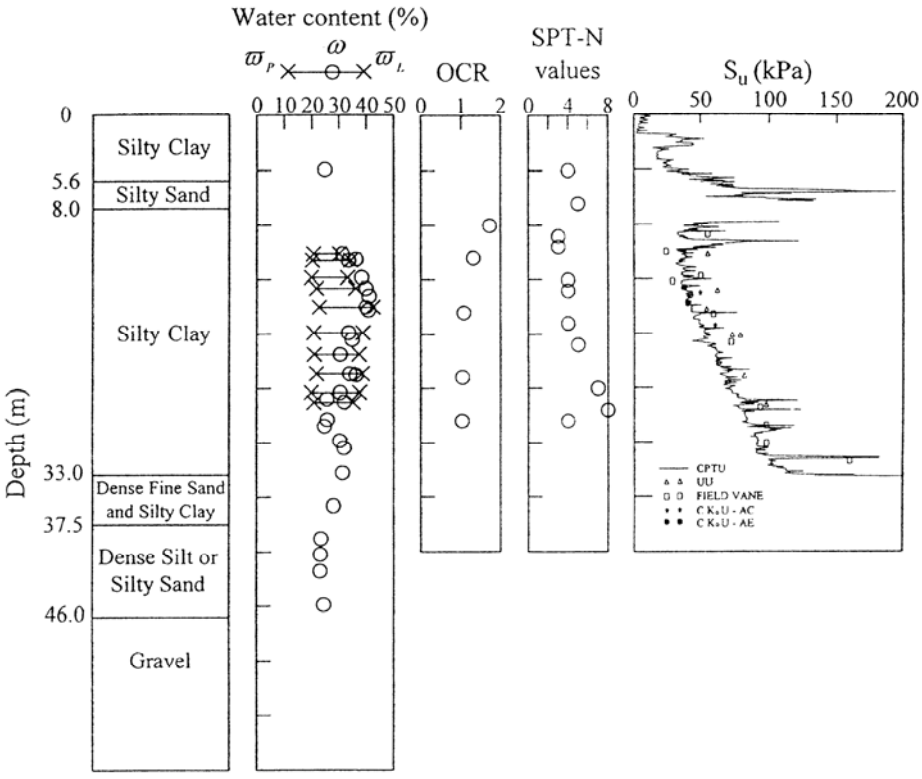

Figure 6.66 Soil Condition at TNEC (Ou, et al., 2000)

Although the excavation shape is not perfectly rectangular and the presence of many buildings precludes an ideal greenfield condition, it is still of practical interest to investigate whether the proposed method is still applicable or not.

The measured and predicted settlement contours are shown in Figure 6.67 and 6.68, respectively. Several cut sections at the southeast corner are also compared as shown in Figure 6.69. The agreements are quite favorable. The presence of surrounding buildings around the excavation zone might have contributed to the differences.

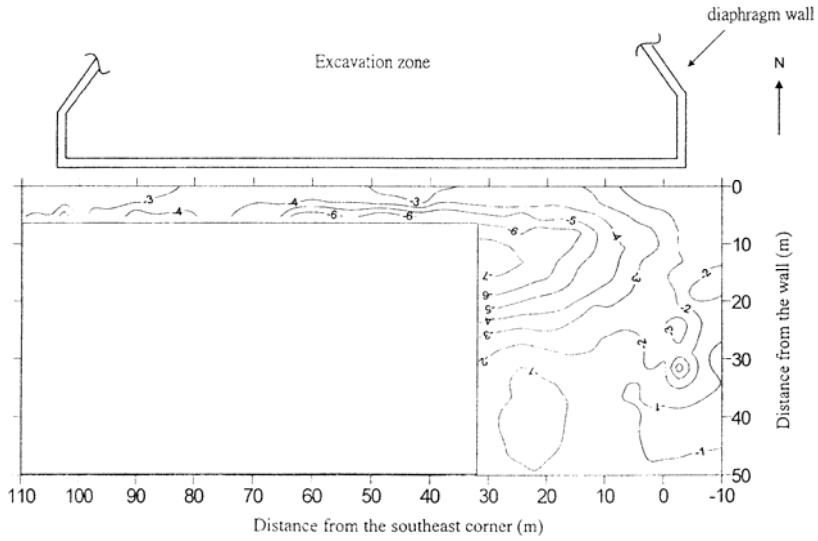

Figure 6.67 Measured Ground Settlement Contours at TNEC (Ou, et al., 2000)

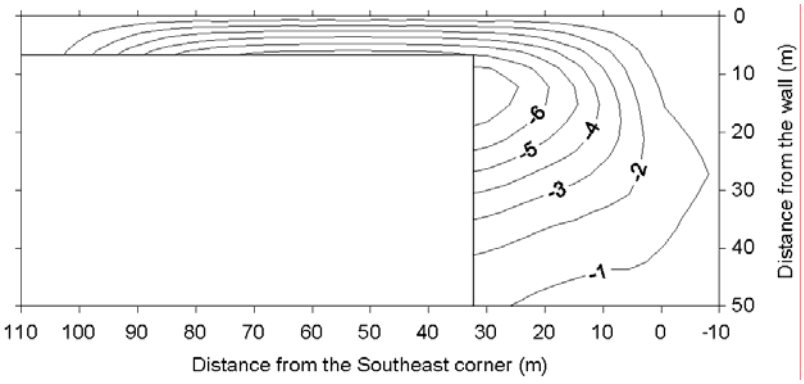

Figure 6.68 Predicted Ground Settlement Contours at TNEC

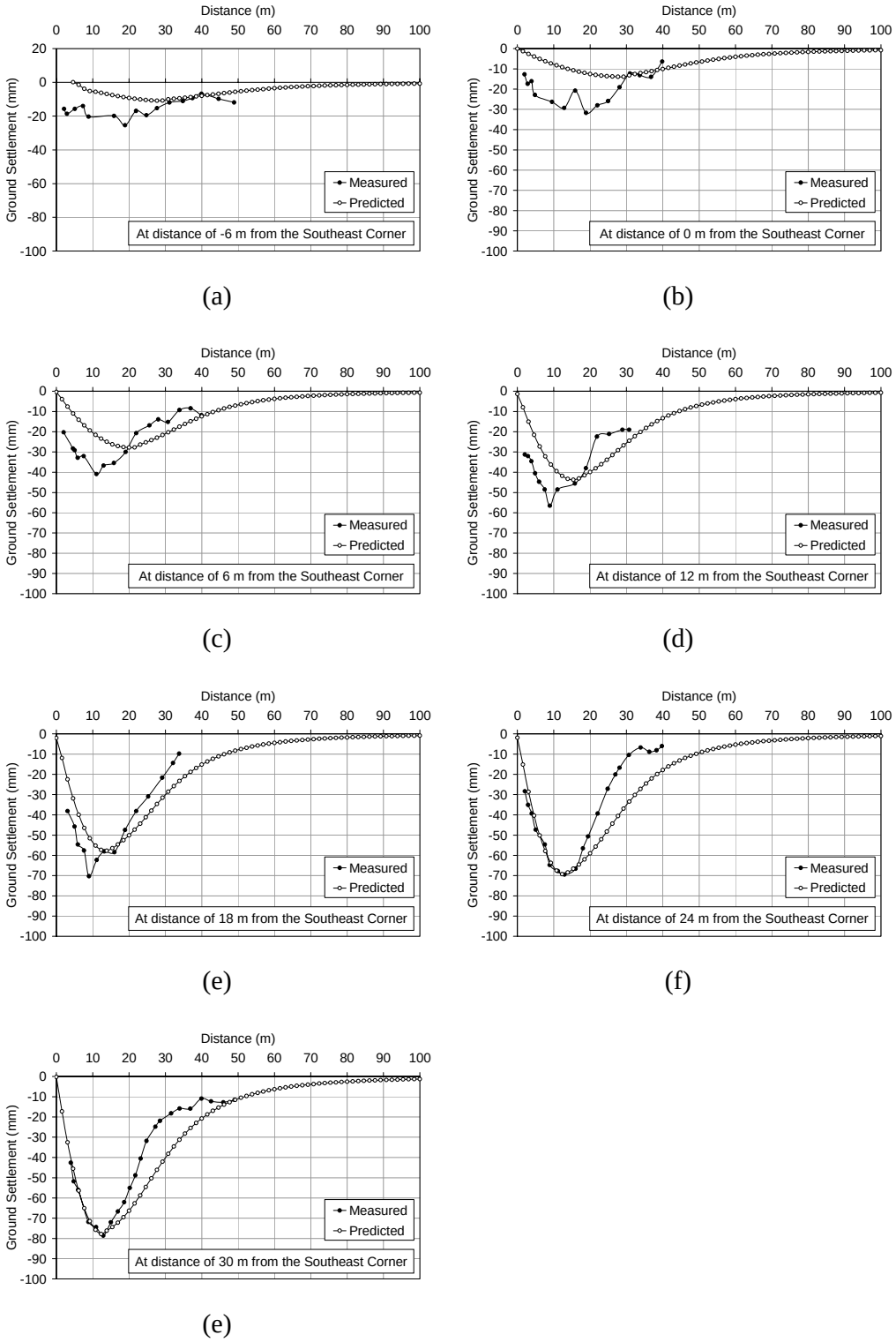

Figure 6.69 Comparison of Measured and Predicted Ground Settlement at TNEC

6.11 Modified Ground Settlement Equations

Clough and O'Rourke (1990) and Hsieh and Ou (1998) proposed a method to predict the ground settlement distribution. The prerequisite is that the maximum ground settlement and the depth of excavation must be known. Following similar approach, Equations 6.3 and 6.5 can be extended to predict the ground settlement distribution. Parameters LocMax and Loc0.75 can be modified as a function of excavation depth.

The locations of $\delta_v/\delta_{v,max}$ proposed by the two parties are different. Clough and O'Rourke (1990) suggested that the location of $\delta_v/\delta_{v,max}$ is scattered from 0 to 0.75 of excavation depth (H). On the other hand, Hsieh and Ou (1998) suggested 0.5 of excavation depth. This study adopted the suggestion by Hsieh and Ou (1998). Therefore, LocMax equals to 0.5H.

Parameter Loc0.75 can be taken as 1.5 LocMax or equals to 0.75 H. Parameter n of Equation 6.5 is taken as 3. These two parameters were established based on trial and error. With these substitutions, the ground settlement profile can be predicted once the depth of excavation and maximum ground settlement are known. They are shown in Equations 6.6 and 6.7.

$$\delta_v = \delta_{v\max}\left[\frac{4}{H}x\left(\frac{x}{H}-1\right)\right] \tag{6.6}$$

$$\delta_v = \delta_{v\max}\left[\frac{1}{-1-\frac{1.117}{H^3}\left(x-\frac{H}{4}\right)^3}\right] \tag{6.7}$$

The six case studies by Hsieh and Ou (1998) are used to verify the ability of both equations in predicting ground settlement profile. The comparisons are shown in Figures 6.70 to 6.75. Results from Equations 6.6 and 6.7 are quite similar to those by Hsieh and Ou's method. The main difference is the shape of profile generated by the proposed equations is more realistic as compared to a series of straight lines. It

should be noted that the ground settlement prediction is only a rough estimation since the settlement profile can be affected by many factors.

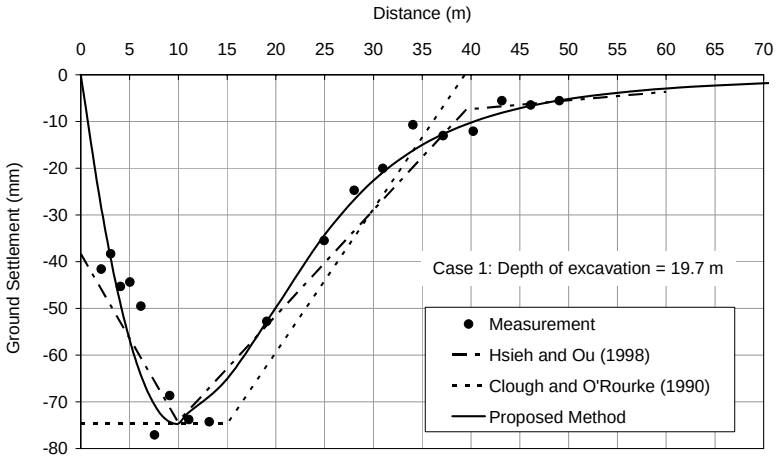

Figure 6.70 Case Study 1 with Excavation Depth at 19.7 m

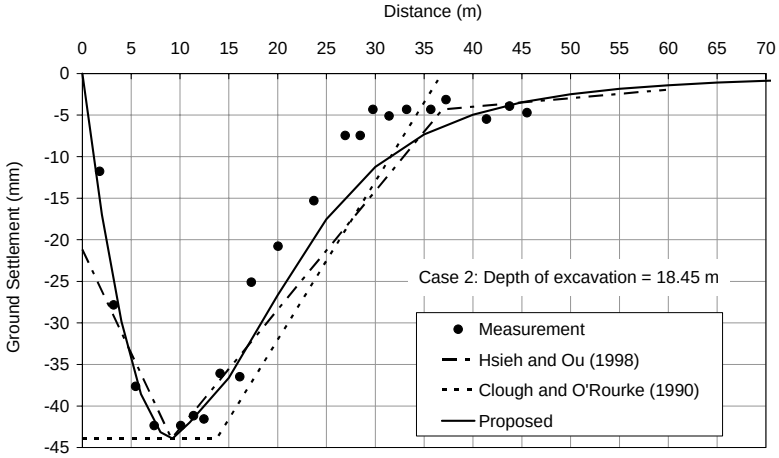

Figure 6.71 Case Study 2 with Excavation Depth at 18.45 m

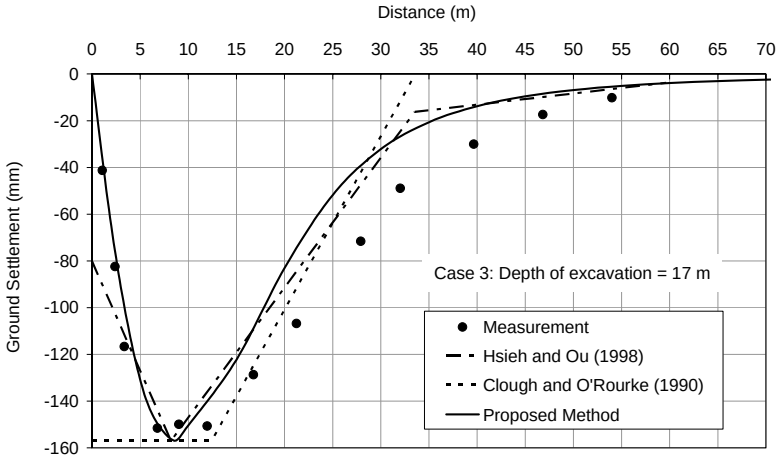

Figure 6.72 Case Study 3 with Excavation Depth at 17 m

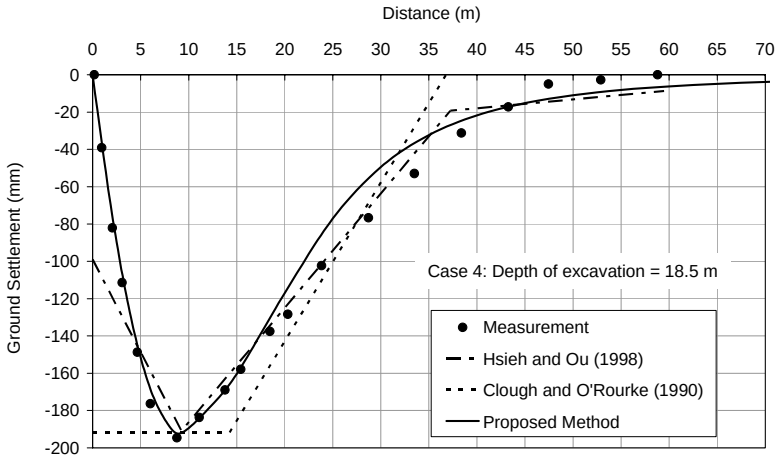

Figure 6.73 Case Study 4 with Excavation Depth at 18.5 m

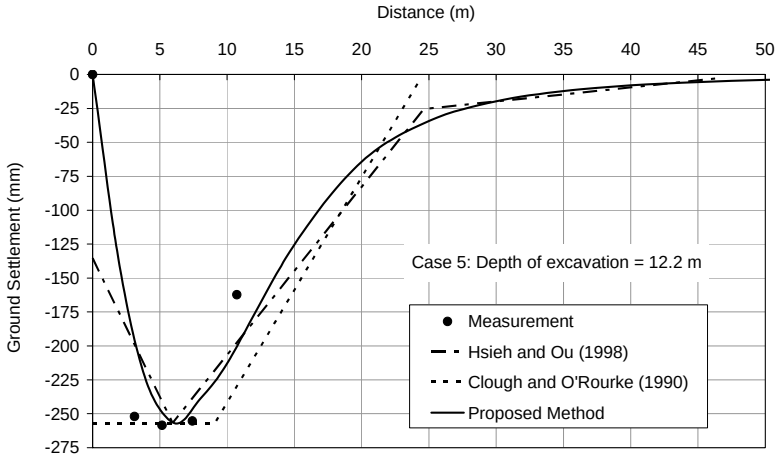

Figure 6.74 Case Study 5 with Excavation Depth at 12.2 m

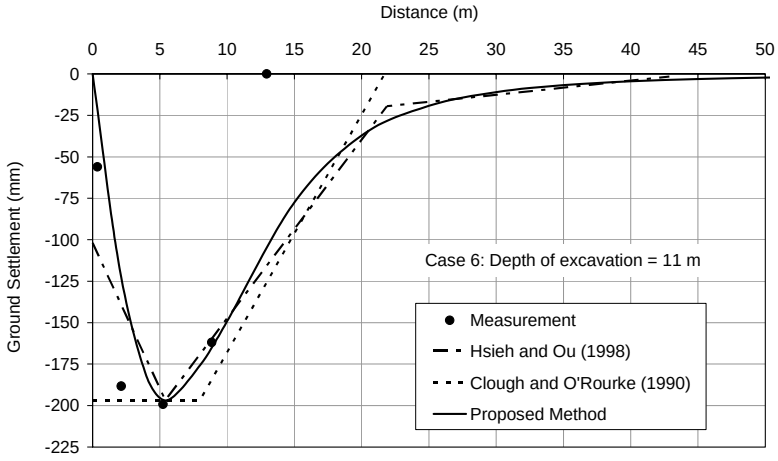

Figure 6.75 Case Study 6 with Excavation Depth at 11 m

6.12 Summary

A new method has been proposed to convert greenfield settlement from 2-D to 3-D. The limitation of the method is it is only applicable to the rectangular shape of the excavation with full penetration of wall all the way to hard stratum. The procedure requires the use of two equations (Eqn. 6.3 and 6.5) and nine charts (Charts 1 to 9). Several hypothetical studies and two study cases have been back-analyzed. In terms of error, it has been shown that in some cases the error is large in terms of magnitude but small in terms of percentage whereas in other cases, the magnitude is small but the percentage is larger. But on the whole, this method produces reasonable results.

Figure 6.49c shows the error of $\delta_{v,max.}$ The error in percentage is high which is about 70%. However, in terms of magnitude error, it is only 2 mm which is practically insignificant. As for Loc0.75, most cases show that the maximum magnitude error is only about 5 m, but in terms of percentage, the error is less than 20%. However, there are a few cases where the error is large in terms of both magnitude and percentage. Take Case 1 in Figure 6.51c, the percentage error of LocMax is 50% while the magnitude error is 6 m which is high in both counts. However, when the entire settlement profile (Figure 6.19j) is viewed in perspective, the agreement is still acceptable.

Two case studies have been back-analyzed to investigate the applicability of the proposed method. The agreements between predicted and measured results are reasonable. The corner effect on the ground settlement is well captured.

Equations 6.6 and 6.7 can be used to predict ground settlement distribution. They can be used if the maximum ground settlement and depth of excavation are known. These equations generate results similar to those proposed Clough and O'Rourke (1990) and Hsieh and Ou (1998). It should be noted that the equations only caters for rough estimation since ground settlement can be affected by many factors.

CHAPTER 7
PREDICTION OF RAFT SETTLEMENT DUE TO DEEP EXCAVATION

7.1 Introduction

In Chapter 6, a method was proposed to convert 2-D green field settlement into 3-D green field settlement. This settlement has been used to estimate building damage (Burland, 1995). This approach works well for buildings supported on flexible shallow foundation. However, it may not be applicable to relatively stiff foundation system, such as a raft with 3 m thickness.

This chapter proposes a method to predict raft settlement from 3-D green field settlement. The first step is to convert the green field settlement into nodal forces using appropriate spring stiffness. It is then followed by a raft analysis according to Winkler (1867) taking into consideration the raft stiffness. This method is applicable to stiff soil (N_{SPT} > 30) where the behavior is predominantly linear elastic. It is not applicable to soft soil because of soil yielding and non-linear behavior.

Six hypothetical examples were used to validate this method. All analyzes were done with the aid of the computer program ABAQUS. Different soil materials and geometries of the raft were also studied to investigate the range of application of this method. In a raft analysis, the main difficulty is in choosing the spring stiffness. Therefore, a range of spring stiffness was used to investigate the sensitivity of this parameter.

This chapter is organized as follows: Firstly, it explains the method and its limitations. Secondly, it illustrates how to use this method using two examples. Thirdly, more examples are used to illustrate its capability in handling different conditions. Finally, conclusions were drawn.

7.2 The Proposed Method

The first step is to establish the 3-D green field settlement either using the method proposed in Chapter 6 or by conducting a 3-D finite element analysis. Figure 7.1 shows contours of idealized green field settlement around an excavation. Next, the green field settlements at the building location are converted into forces using appropriate spring stiffness (Equation 7.1). Finally, these forces are used as part of the input in the raft analysis as shown in Figure 7.2. The raft stiffness is included in this analysis.

$$F = k\delta_v \tag{7.1}$$

where F = nodal force (kN);

k = spring stiffness (kN/m); and

δ_v = ground settlement (m)

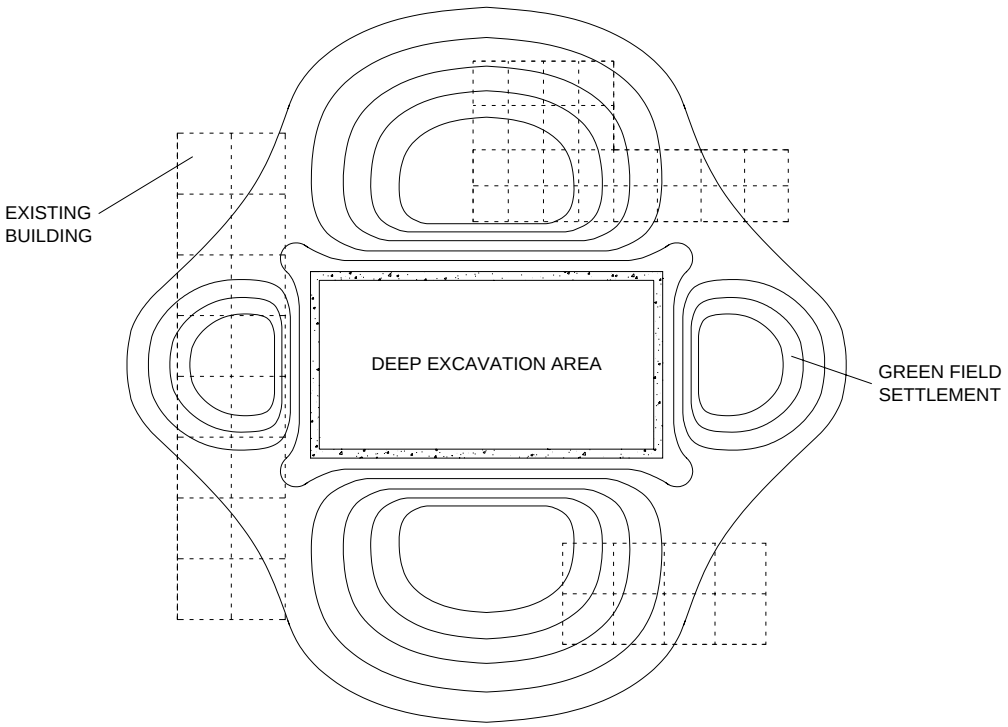

Figure 7.1 Greenfield Settlement Contours and Buildings Location

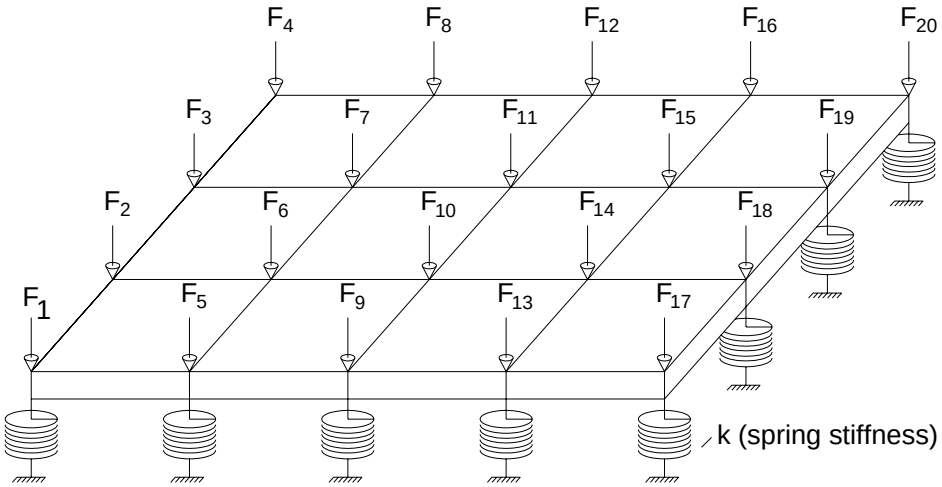

Figure 7.2 Raft Analysis

The spring stiffness in Equation 7.1 represents an elastic material. Therefore, it is applicable only for stiff soil which deforms within the elastic limit. The elastic spring stiffness can be estimated using the averaged soil stiffness. Assuming a spring with a length of 1 m supporting the load covering an area of 1 m^2, the spring stiffness can be estimated using the average soil stiffness, E_{ave}, as shown in Equation 7.2.

$$k = E_{ave}\left(\frac{A}{L}\right) \tag{7.2}$$

where k = stiffness of spring (kN/m);

E_{ave} = average stiffness of soil (kPa);

A = area of spring (m^2); and

L = length of spring (m)

One of the reasons why this method is not applicable to soft soil is because of non-linear yielding of the soil. For stiff soil, it is easier to handle because the system is predominantly linear elastic. Therefore, elastic springs can be used. For a given load increment ΔF, the amount of settlement will be the same regardless of the starting point at A or B ($\Delta\delta_{va} = \Delta\delta_{vb}$) as shown in Figure 7.3(a). However, this is not the case for a nonlinear spring which resembles soft soil as shown in Figure 7.3(b). The amount of settlement is highly dependent on the loading path.

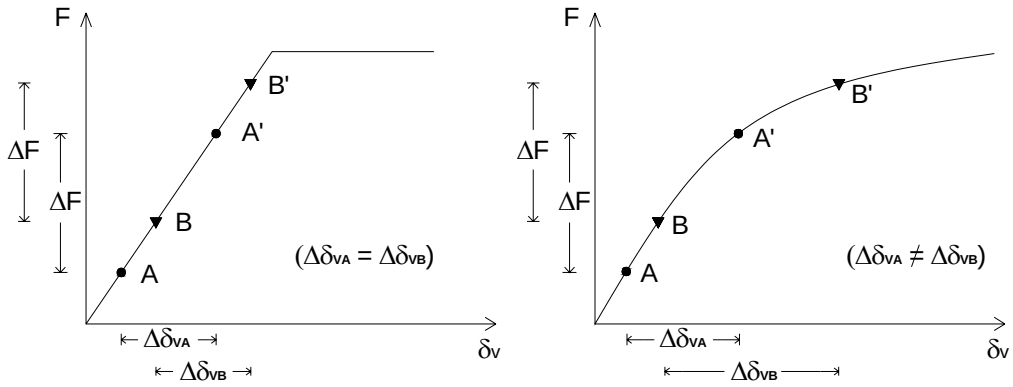

(a) Linear Spring for Stiff Soil (b) Non-Linear Spring for Soft Soil

Figure 7.3 Load Settlement Behavior for Linear and Non-Linear Spring

7.3 Two Illustrated Problems

Two examples are presented to illustrate how to use the proposed method and to highlight the limitations. The first one is a 2-D example and the second one is a 3-D example.

7.3.1 Example 1: 2-D Hypothetical Excavation

In the 2-D example, the applied pressure on the raft (20 m wide and 1 m thick) increases from 20 to 160 kPa to simulate different building loads. The purpose is to look into the limitation of the method once the soil reached plastic condition. The cross-section of excavation is shown in Figure 7.4. The soil and structural properties are summarized in Table 7.1 and 7.2, respectively.

The proposed method requires a series of four analyses. The first one is to determine the green field settlement due to excavation without the raft. The second one is to determine the raft settlement due to excavation under different building loads. In this analysis, the soil was fully consolidated under the building load prior to excavation. The third analysis is to determine the spring stiffnesses and the corresponding forces based on the results of first analysis. The last one is a raft analysis according to Wrinkler to obtain the raft settlement due to deep excavation. The raft stiffness is included in this analysis.

From Step 1, the computed green field settlements varied from -11.83 mm at the left end of the raft to a maximum of -13.18 mm near the centre and -9.97 mm at the right edge. The results are summarized in Table 7.3.

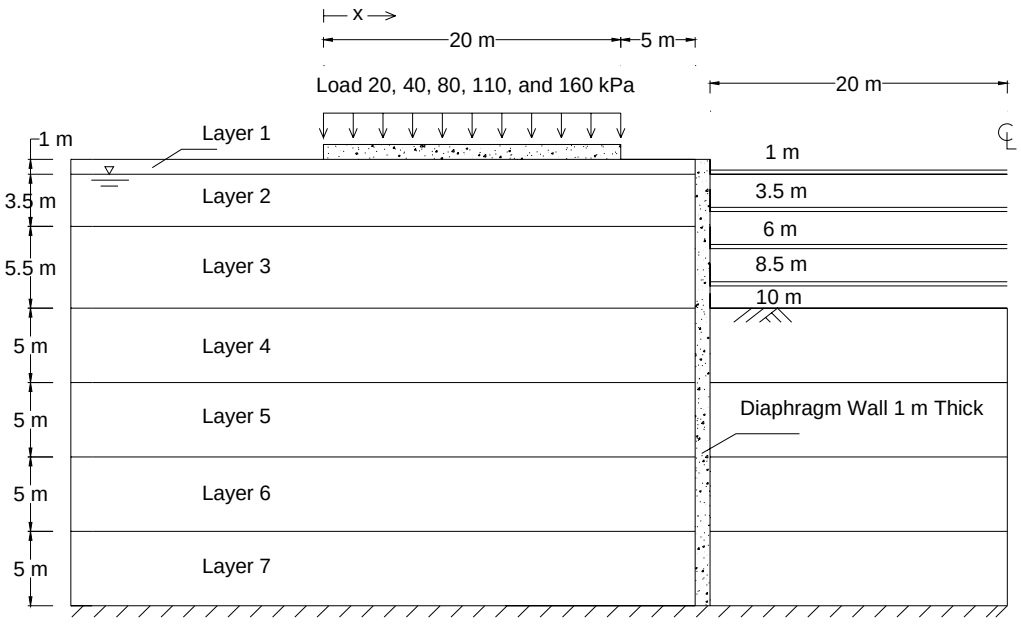

Figure 7.4 Cross-Section of Example 1: 2-D Hypothetical Excavation

Table 7.1 Soil Properties of Example 1: 2-D Hypothetical Excavation

Layer	γ_{sat} (kN/m3)	ν	ϕ (^{o})	c_u (kPa)	E (kPa)
1	19	0.33	0	20	6000
2	19	0.33	0	28	8400
3	19	0.33	0	60	18000
4	19	0.33	0	98	29400
5	19	0.33	0	134	40200
6	19	0.33	0	170	51000
7	19	0.33	0	200	60000

Table 7.2 Structural Properties of Example 1: 2-D Hypothetical Excavation

Structural Members	E (kN/m^2)	A (m^2/m)	Preload (kN/m)
Strut (all levels)	2.07×10^8	0.00518	No preloading
Diaphragm wall (quadrilateral element)	2.8×10^7	1	-

The spring stiffness is calculated based on the average soil stiffness, E_{ave}. The width of raft is 20 m. The influence zone beneath the raft is assumed to be equal to the raft width. Therefore, the weighed average E_{ave} is calculated as follows:

$$E_{ave} = \frac{1\times E_{Layer1} + 3.5\times E_{Layer2} + 5.5\times E_{Layer3} + 5\times E_{Layer4} + 5\times E_{Layer5}}{20}$$

$$= \frac{1\times 6000 + 3.5\times 8400 + 5.5\times 18000 + 5\times 29400 + 5\times 40200}{20} \approx 24000 \text{ kPa}$$

The spring stiffness is calculated based on Equation 7.2 by taking A and L of spring equals to 1 m^2 and 1 m, respectively. The calculation is as follows:

$$k = E_{ave}\left(\frac{A}{L}\right) = 24000\left(\frac{1}{1}\right) = 24000 \text{ kN/m}$$

The forces are computed according to Equation 7.1 as illustrated in Figure 7.5 and tabulated in Table 7.3. With the forces known, a 2-D raft analysis with appropriate raft stiffness was carried out to determine the raft settlement. The results are shown in Figure 7.6. The raft analysis generated almost identical results as those from the second analysis for building loads up to 40 kPa. This is because the induced soil stresses due to excavation are largely within the elastic limit. Hence, the raft settlement is independent of the building load up to 40 kPa. When the building load is greater than 40 kPa, the 2-D FEA produced larger settlement. This is because part of the soil mass had yielded and undergone plastic deformation. The non-linear behavior cannot be captured by the elastic springs. Hence, the proposed method is no longer applicable.

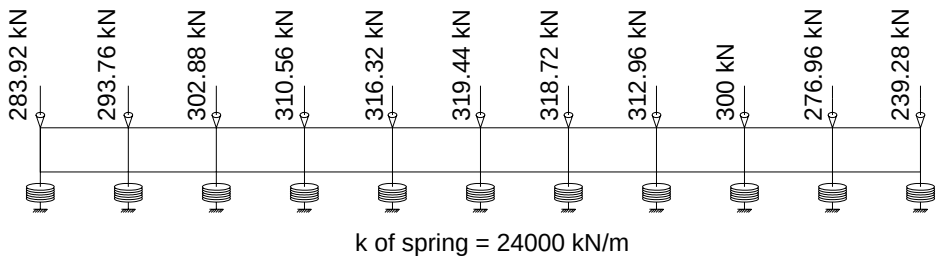

Figure 7.5 Illustrated Raft Analysis of Example 1

Table 7.3 Calculation Procedures for Example 1

X (m)	Greenfield (mm)	k (kN/m)	Force = k x Greenfield (kN)	Predicted Settlement from Raft Analysis (mm)
0	-11.83	24000	-283.92	-12.6
2	-12.24	24000	-293.76	-12.68
4	-12.62	24000	-302.88	-12.78
6	-12.94	24000	-310.56	-12.85
8	-13.18	24000	-316.32	-12.87
10	-13.31	24000	-319.44	-12.82
12	-13.28	24000	-318.72	-12.68
14	-13.04	24000	-312.96	-12.45
16	-12.5	24000	-300	-12.15
18	-11.54	24000	-276.96	-11.79
20	-9.97	24000	-239.28	-11.44

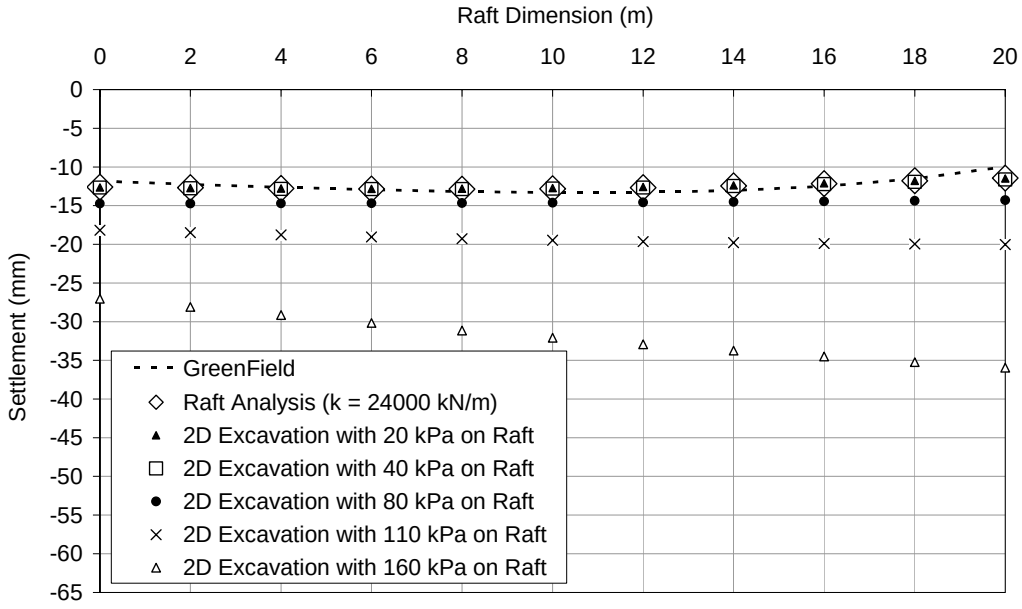

Figure 7.6 Results of Analysis of Example 1

7.3.2 Example 2: 3-D Hypothetical Excavation

In the 3-D example, the soil properties, structural properties, and cross-section of excavation are shown in Figure 7.7. The deformed mesh is shown in Figure 7.8. The raft has a dimension of 20 x 40 x 1 m resting on stiff soil. The applied load on raft is 50 kPa. The depth of excavation is 13 m.

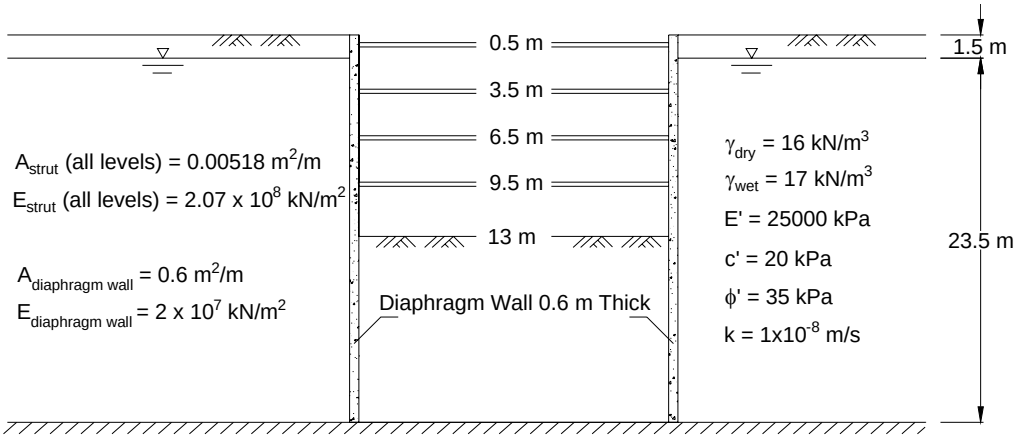

Figure 7.7 Cross-Section of Example 2: 3-D Hypothetical Excavation

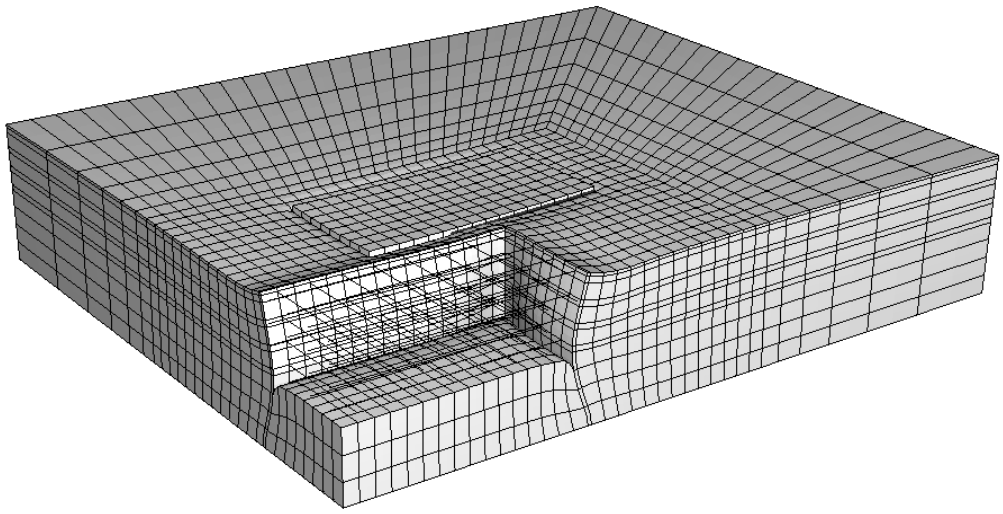

Figure 7.8 Example 2: Deformed Mesh and Location of Raft

In the first step of analysis, the raft was not included. Therefore, green field settlements were obtained as shown in Figure 7.9. The forces on the raft are then computed based on these settlements. Next, a raft analysis was conducted.

In this example, two different values of spring stiffness were used. The first one was 25000 kN/m as determined using Equation 7.2. The second one adopted an arbitrary value of 1000 kN/m. The purpose is to study the effect of stiffness on the raft settlement. The calculation procedure is tabulated in Table 7.4. The green field settlement contours are shown in Figure 7.9.

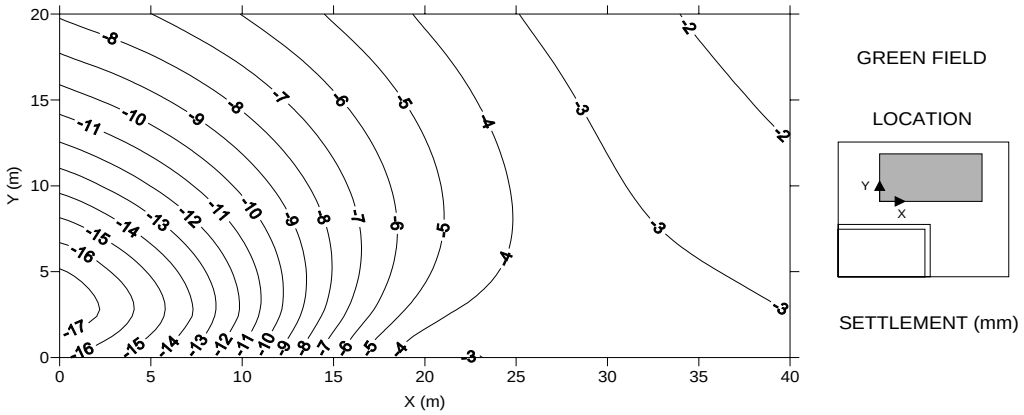

Figure 7.9 Green field Settlement Contours of Example 2 from 3-D Analysis

Table 7.4 Calculation Procedures for Example 2

X	Y	Green Field	Forces (kN) = Green Field x k	
(m)	(m)	(mm)	k = 1000 (kN/m)	k = 25000 (kN/m)
0	0	-16.035	-16.035	-400.875
2.5	0	-15.264	-15.264	-381.6
5	0	-14.148	-14.148	-353.7
7.5	0	-12.626	-12.626	-315.65
10	0	-10.68	-10.68	-267
12.5	0	-8.441	-8.441	-211.025
15	0	-6.165	-6.165	-154.125
17.5	0	-4.269	-4.269	-106.725
20	0	-3.139	-3.139	-78.475
22.5	0	-2.905	-2.905	-72.625
25	0	-3.206	-3.206	-80.15
27.5	0	-3.593	-3.593	-89.825
30	0	-3.848	-3.848	-96.2
32.5	0	-3.923	-3.923	-98.075
35	0	-3.844	-3.844	-96.1
37.5	0	-3.656	-3.656	-91.4
40	0	-3.402	-3.402	-85.05
0	2.5	-17.869	-17.869	-446.725
2.5	2.5	-16.895	-16.895	-422.375
5	2.5	-15.573	-15.573	-389.325
⋮	⋮	⋮	⋮	⋮
40	20	-1.571	-1.571	-39.275

An additional 3-D analysis was carried out, so that these results can be used to compare with those obtained from the raft analysis. The settlement contours of the raft from the 3-D analysis are shown in Figure 7.10. The comparisons are made using 6 cross-sections as shown in Figures 7.11 to 7.16.

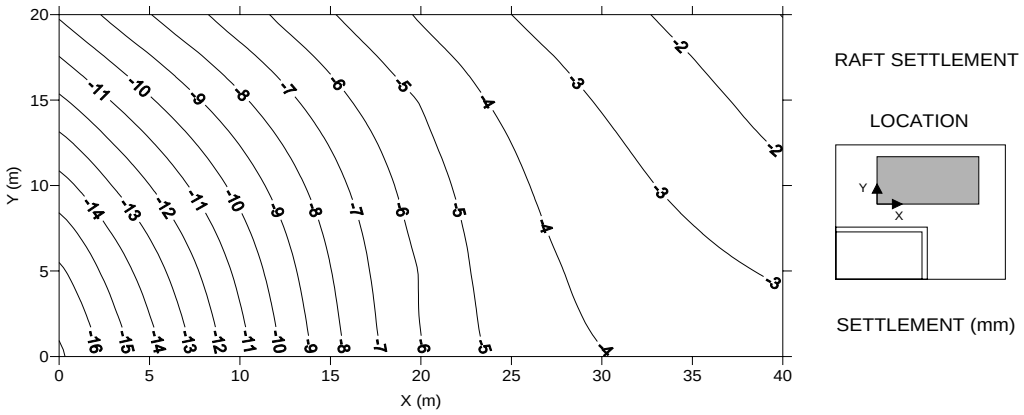

Figure 7.10 Raft Settlement from 3-D Analysis of Example 2

From Figures 7.11 to 7.16, it can be seen that the raft settlement is not always close to the green field settlement. This is especially true if the raft is stiff. On the other hand, the effect of spring stiffness is not very significant. This is an advantage since predicting spring stiffness is not an easy task.

The two hypothetical examples show that the raft settlement in stiff soil due to deep excavation can be determined following the proposed method using green field settlement. Further validation of this method was carried out using 4 hypothetical examples with different raft geometries and thicknesses.

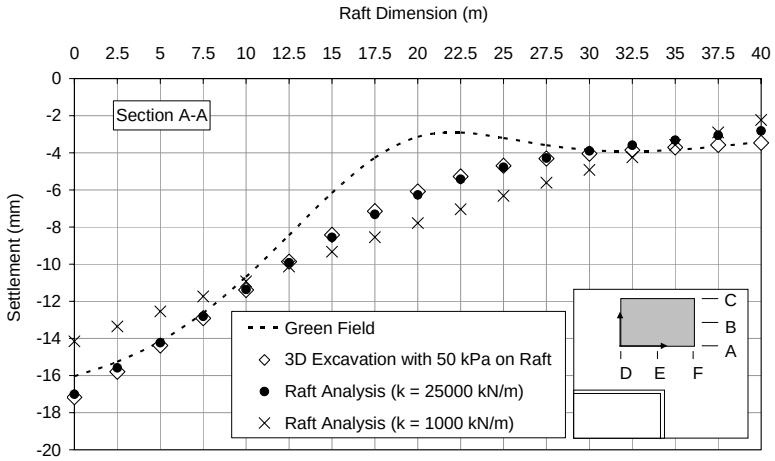

Figure 7.11 Example 2: Comparison of Raft 20x40x1 m Settlement at Section A-A

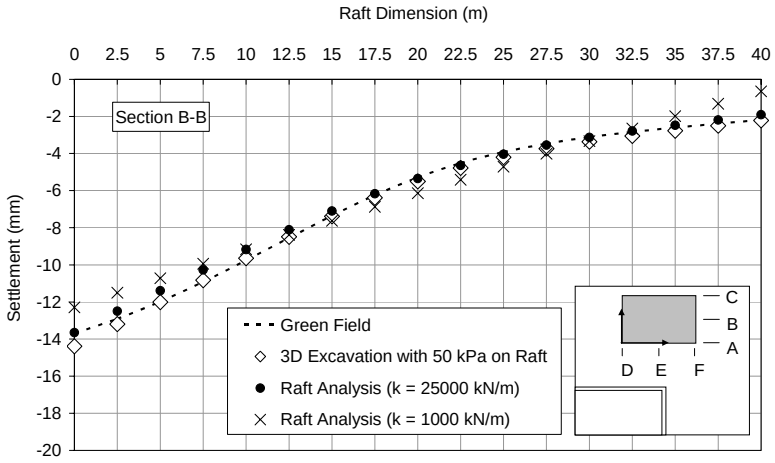

Figure 7.12 Example 2: Comparison of Raft 20x40x1 m Settlement at Section B-B

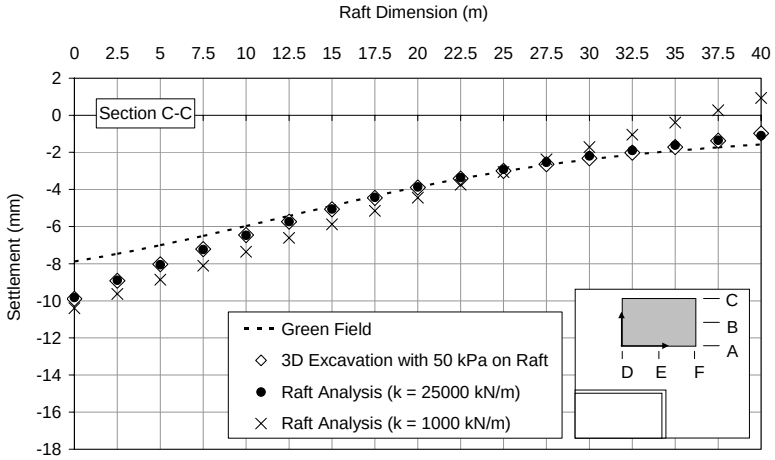

Figure 7.13 Example 2: Comparison of Raft 20x40x1 m Settlement at Section C-C

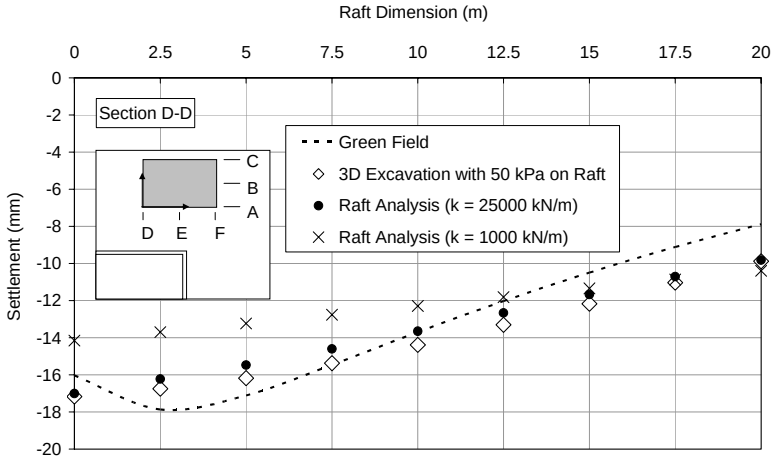

Figure 7.14 Example 2: Comparison of Raft 20x40x1 m Settlement at Section D-D

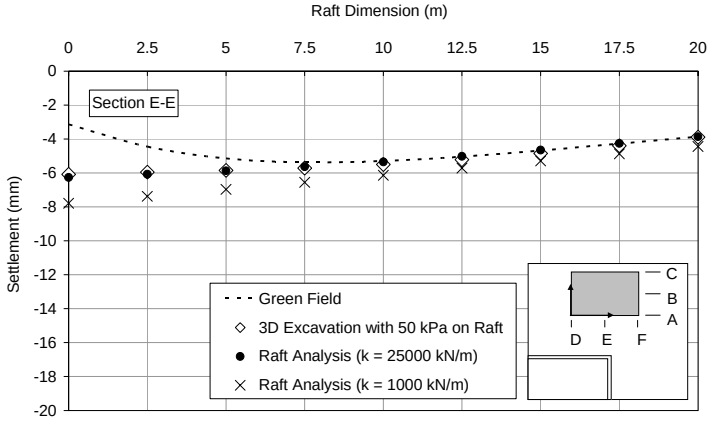

Figure 7.15 Example 2: Comparison of Raft 20x40x1 m Settlement at Section E-E

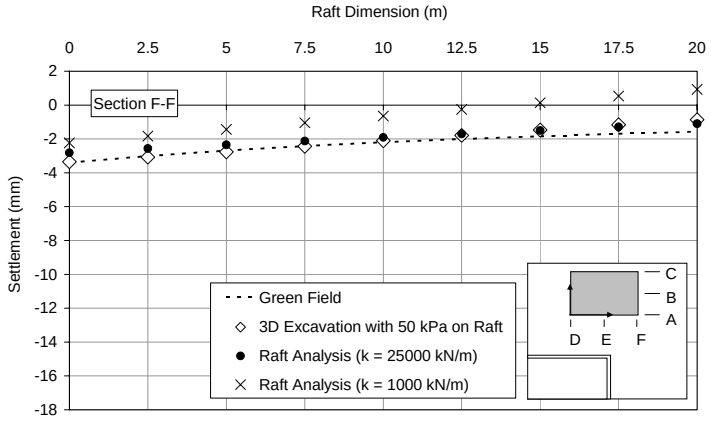

Figure 7.16 Example 2: Comparison of Raft 20x40x1 m Settlement at Section F-F

7.4 Four 3-D Hypothetical Examples

Four examples were analyzed. The calculation procedures are not repeated as they are similar to the first two. Only the results are presented.

7.4.1 Example 3: Flexible Raft

The geometries are the same as those shown in Figures 7.7 and 7.8. Only the raft thickness was changed from 1 to 0.1 m. The results are shown in Figures 7.17 to 7.22. It can be seen that for a flexible raft, the green field settlement and raft settlement are almost identical. The different spring stiffness has no effect on the computed settlement.

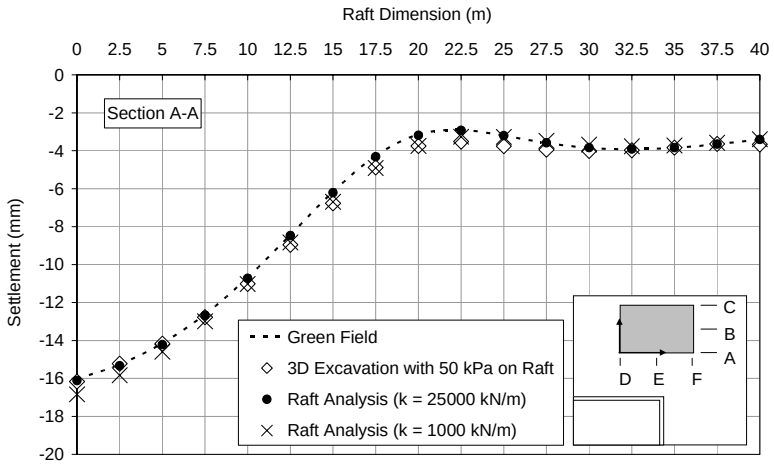

Figure 7.17 Example 3: Comparison of Raft 20x40x0.1 m Settlement at Section A-A

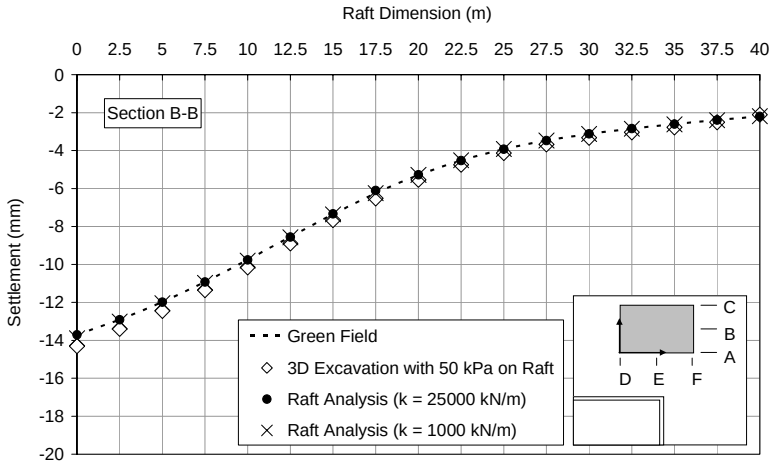

Figure 7.18 Example 3: Comparison of Raft 20x40x0.1 m Settlement at Section B-B

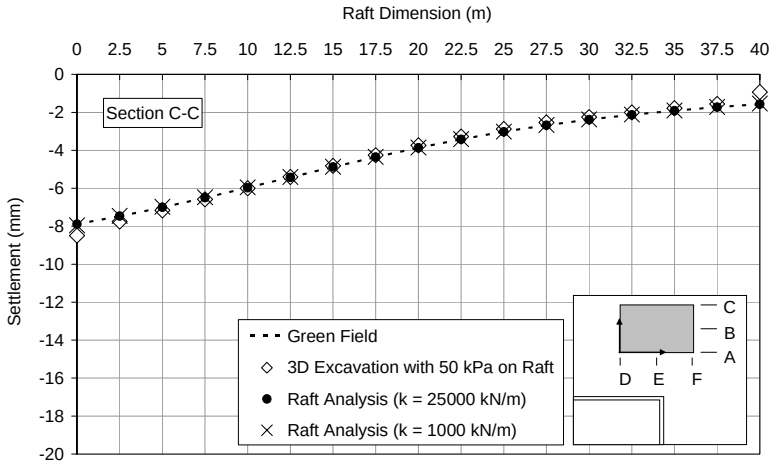

Figure 7.19 Example 3: Comparison of Raft 20x40x0.1 m Settlement at Section C-C

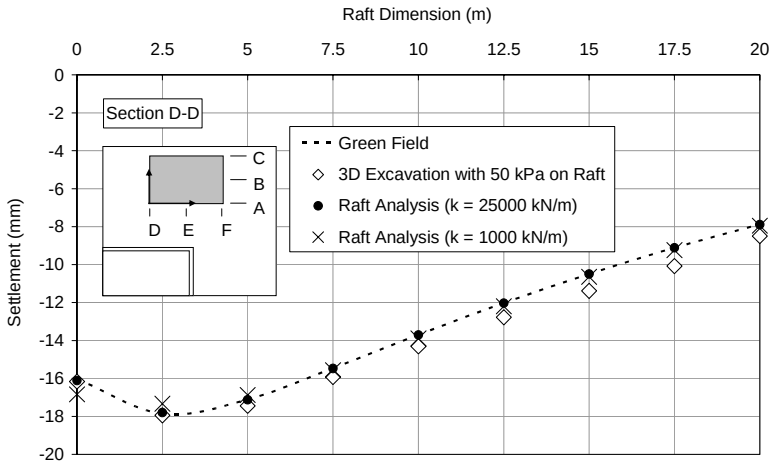

Figure 7.20 Example 3: Comparison of Raft 20x40x0.1 m Settlement at Section D-D

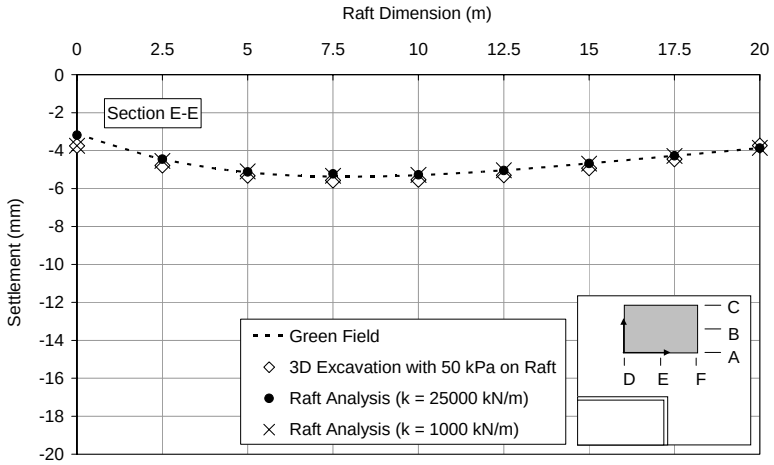

Figure 7.21 Example 3: Comparison of Raft 20x40x0.1 m Settlement at Section E-E

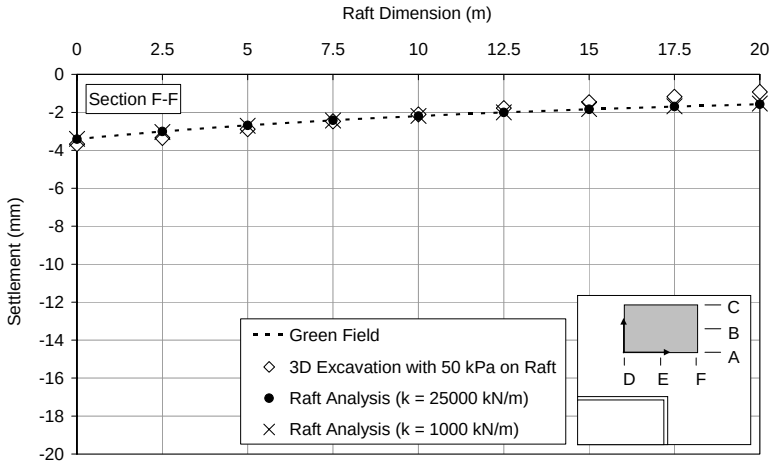

Figure 7.22 Example 3: Comparison of Raft 20x40x0.1 m Settlement at Section F-F

7.4.2 Example 4: Stiff Raft

In this example, the raft is 4 m thick. The cross-section and location of raft is similar to those in Figures 7.7 and 7.8. The results are shown in Figures 7.23 to 7.28. For a stiff raft, the green field and raft settlement are very different. The proposed method was able to produce results that are comparable to those generated from the 3-D analysis. The effect of different spring stiffness is negligible for this case.

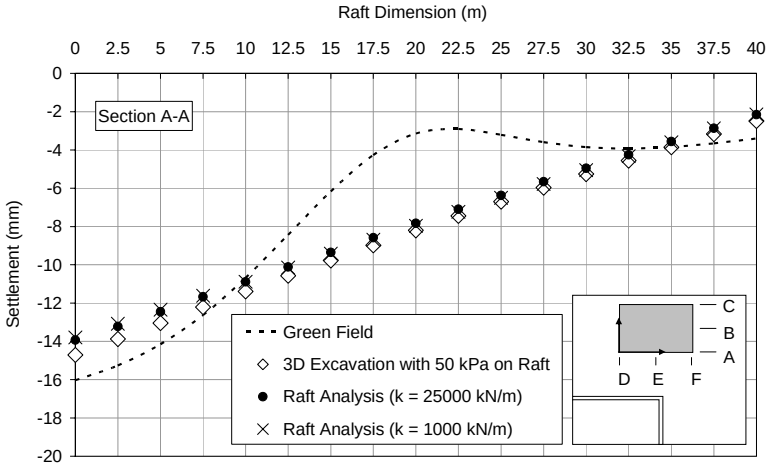

Figure 7.23 Example 4: Comparison of Raft 20x40x4 m Settlement at Section A-A

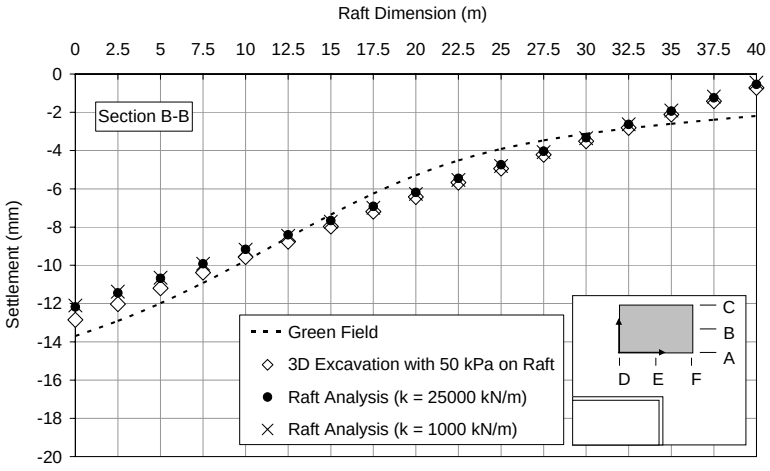

Figure 7.24 Example 4: Comparison of Raft 20x40x4 m Settlement at Section B-B

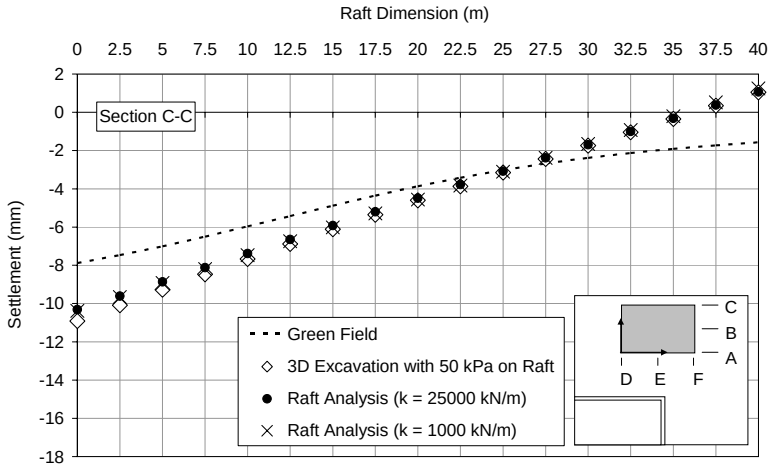

Figure 7.25 Example 4: Comparison of Raft 20x40x4 m Settlement at Section C-C

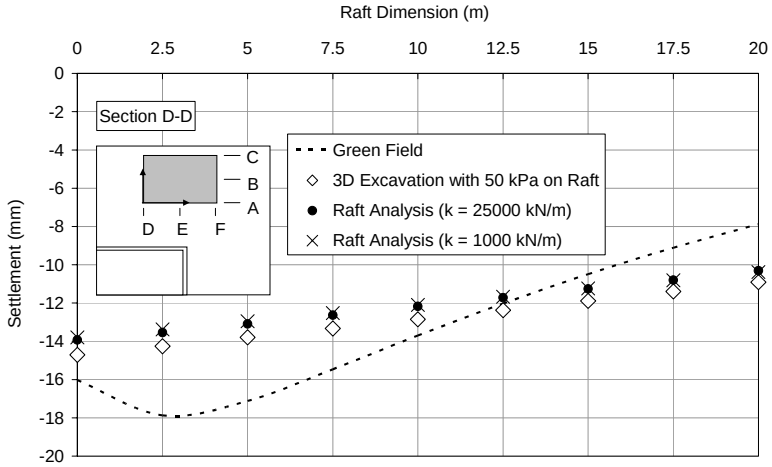

Figure 7.26 Example 4: Comparison of Raft 20x40x4 m Settlement at Section D-D

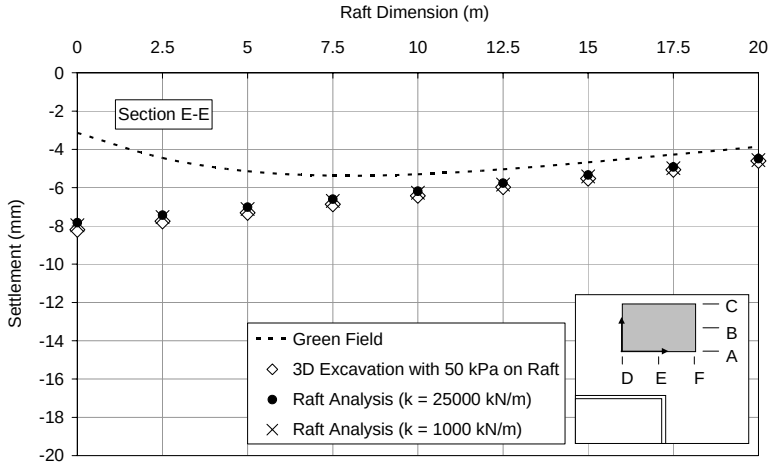

Figure 7.27 Example 4: Comparison of Raft 20x40x4 m Settlement at Section E-E

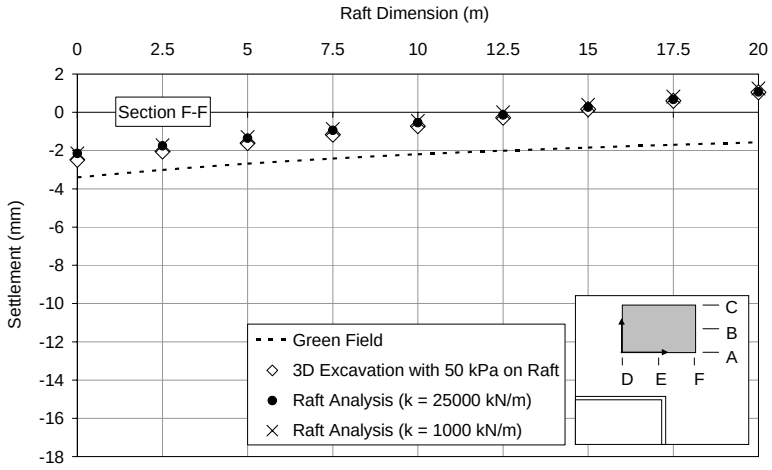

Figure 7.28 Example 4: Comparison of Raft 20x40x4 m Settlement at Section F-F

7.4.3 Example 5: L Shape and Rectangular Raft on Plane Strain Excavation

Two rafts are modeled next to a cut-and-cover tunnel. The excavation is shown in Figure 7.29. The soil properties are similar to the previous examples as shown in Figure 7.7. The thickness of the raft is 1 m. The dimension of the rectangular raft is 20 x 60 x 1 m. The L shape raft is 50 m long in the directions parallel and perpendicular to the excavation wall. The loading on each raft is 50 kPa.

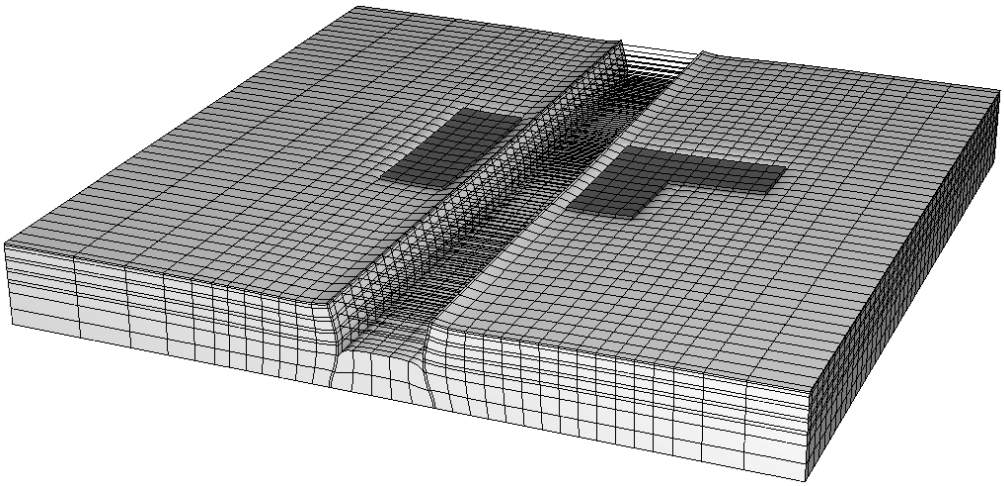

Figure 7.29 Deformed Mesh of Example 5

Results for the L shape and rectangular rafts are shown in Figures 7.30 to 7.35 and 7.36 to 7.41, respectively. The computed settlements from the raft analysis compare favorably with those from 3-D finite element analysis. Again, the effect of spring stiffness is negligible.

7.4.4 Example 6: Rectangular Raft on Different Soil Layers

In the previous examples, the soil had only one stiffness which was 25000 kPa. In reality, the soil stiffness may increase with depth. In order to illustrate this problem, three soil layers with different stiffness are used. The cross-section, soil properties, and structural properties are shown in Figure 7.42, Table 7.5, and 7.6, respectively. The 3-D model is similar to that in Figure 7.8. In the raft analysis, the spring stiffness was chosen as 15000 kN/m. However, the spring stiffness equals to 1000 kN/m was still included in order to investigate the effect. The results are shown in Figures 7.43 to 7.48.

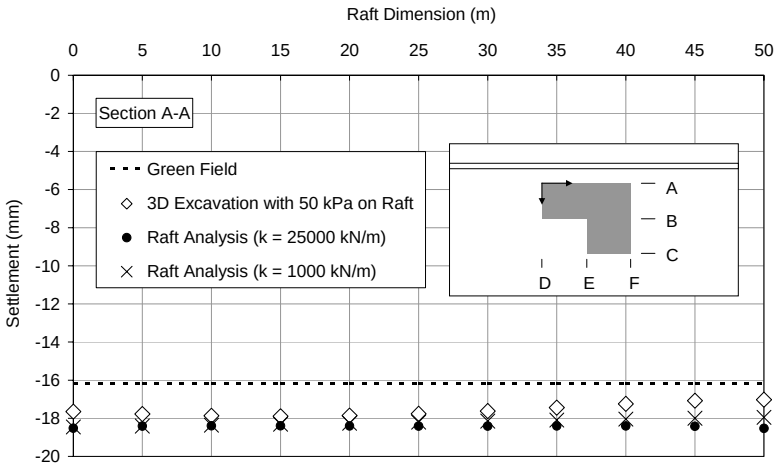

Figure 7.30 Example 5: Comparison of L Shape Raft Settlement at Section A-A

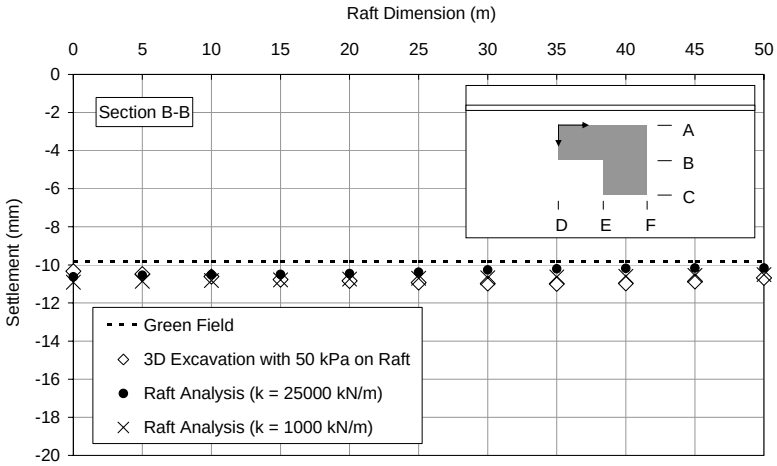

Figure 7.31 Example 5: Comparison of L Shape Raft Settlement at Section B-B

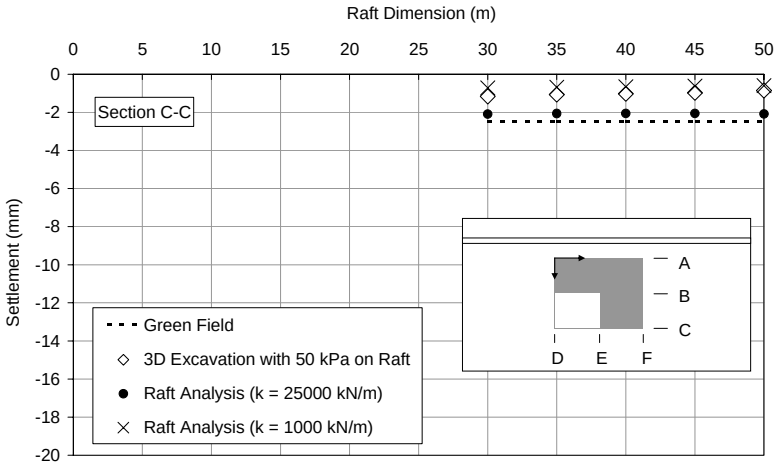

Figure 7.32 Example 5: Comparison of L Shape Raft Settlement at Section C-C

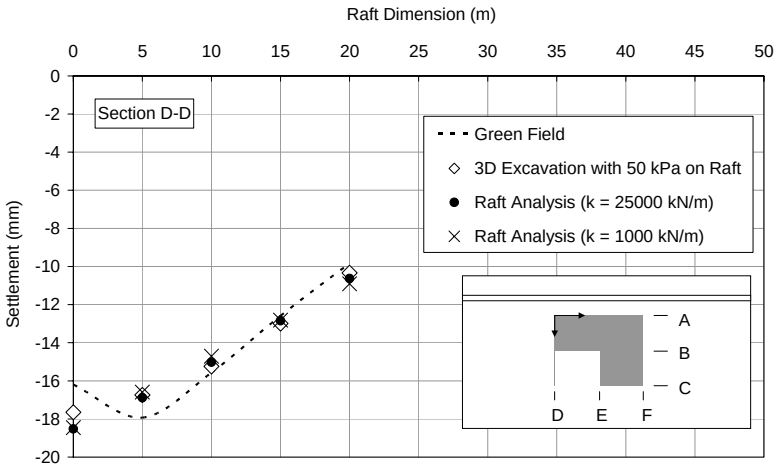

Figure 7.33 Example 5: Comparison of L Shape Raft Settlement at Section D-D

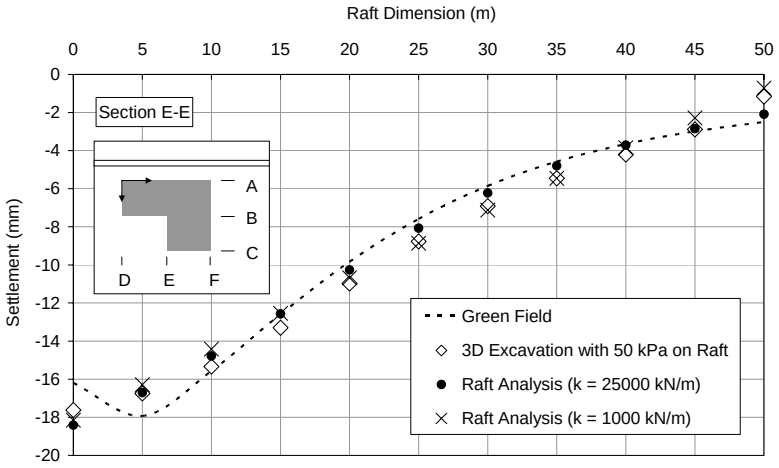

Figure 7.34 Example 5: Comparison of L Shape Raft Settlement at Section E-E

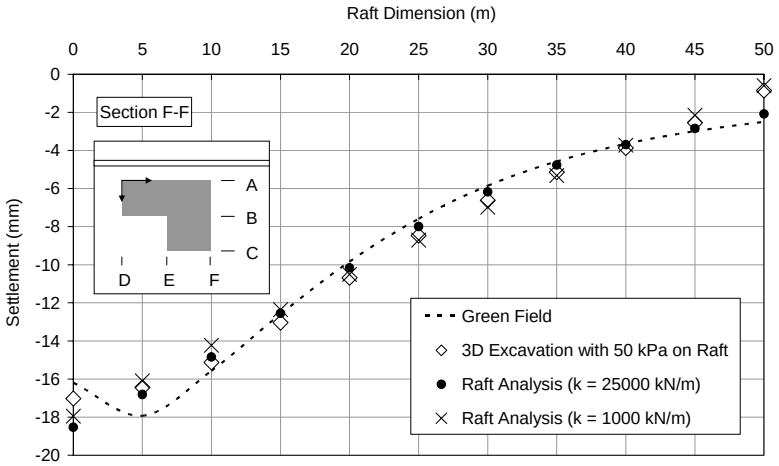

Figure 7.35 Example 5: Comparison of L Shape Raft Settlement at Section F-F

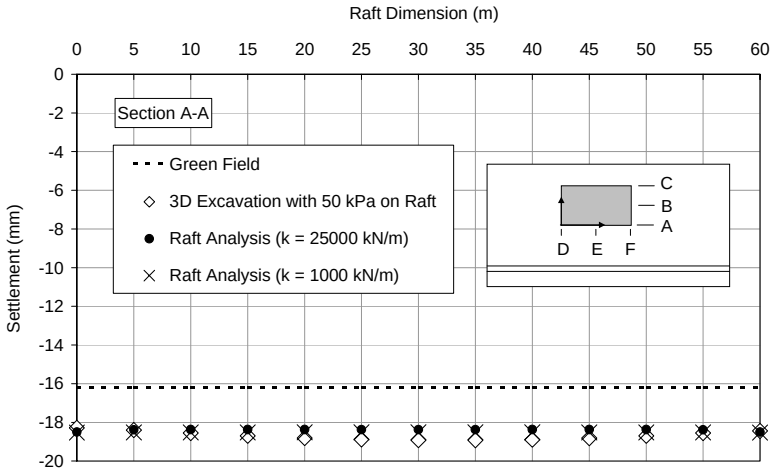

Figure 7.36 Example 5: Comparison of Raft 20x60x1 m Settlement at Section A-A

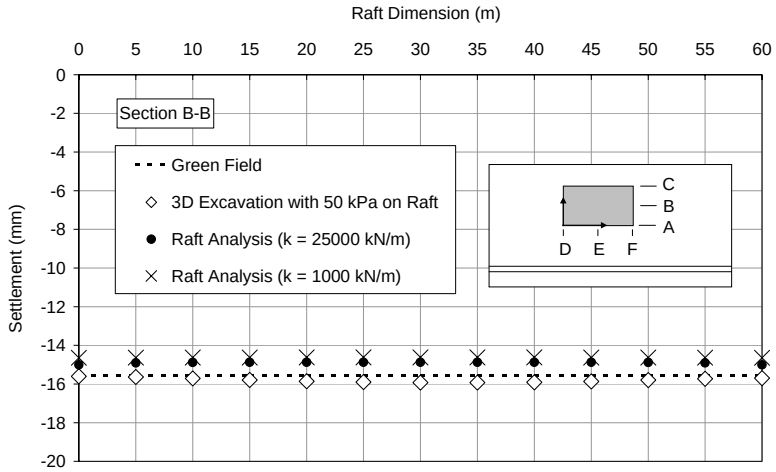

Figure 7.37 Example 5: Comparison of Raft 20x60x1 m Settlement at Section B-B

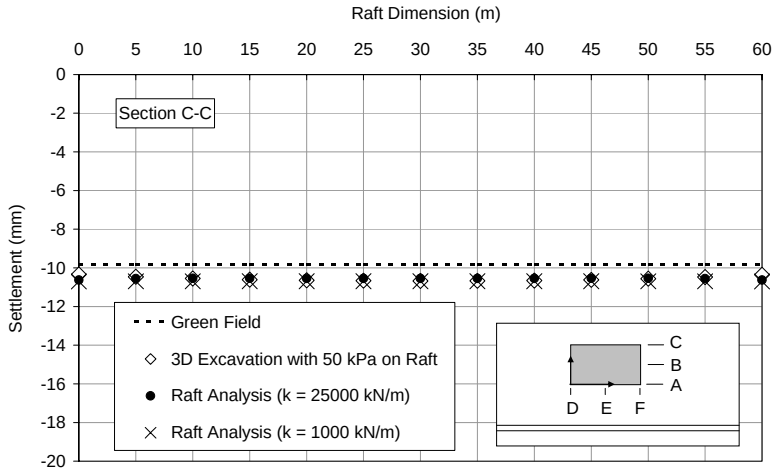

Figure 7.38 Example 5: Comparison of Raft 20x60x1 m Settlement at Section C-C

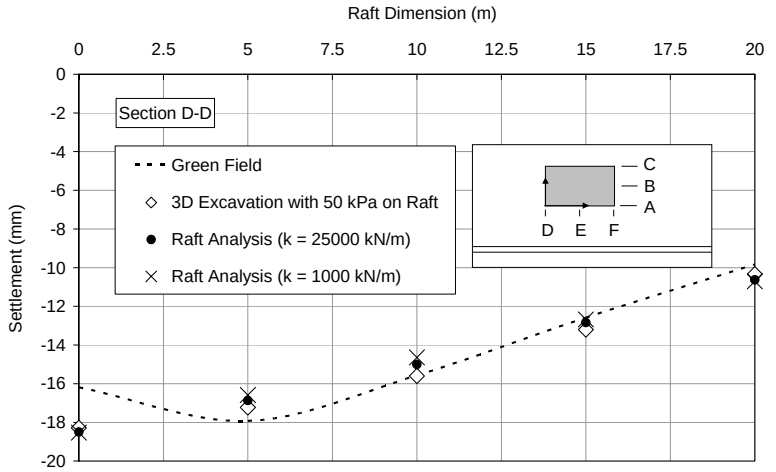

Figure 7.39 Example 5: Comparison of Raft 20x60x1 m Settlement at Section D-D

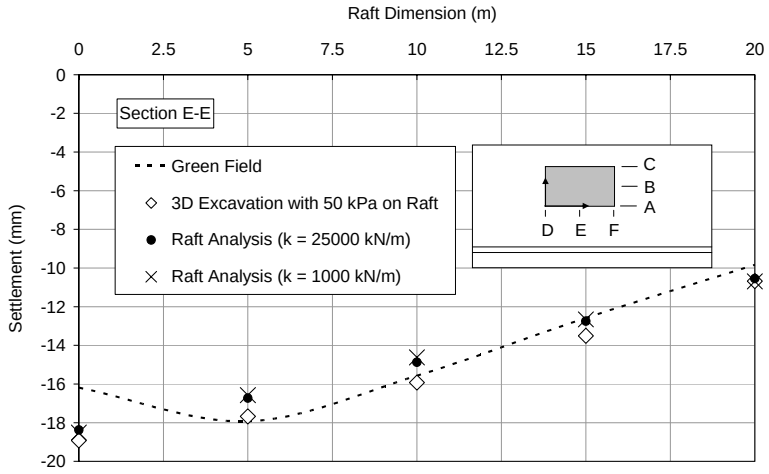

Figure 7.40 Example 5: Comparison of Raft 20x60x1 m Settlement at Section E-E

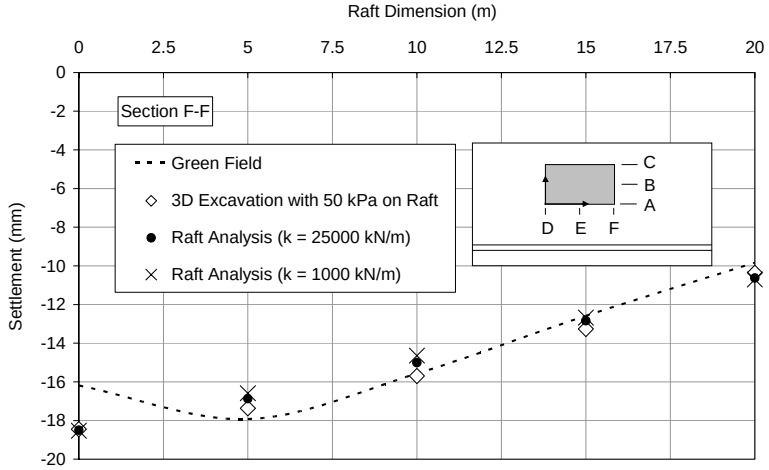

Figure 7.41 Example 5: Comparison of Raft 20x60x1 m Settlement at Section F-F

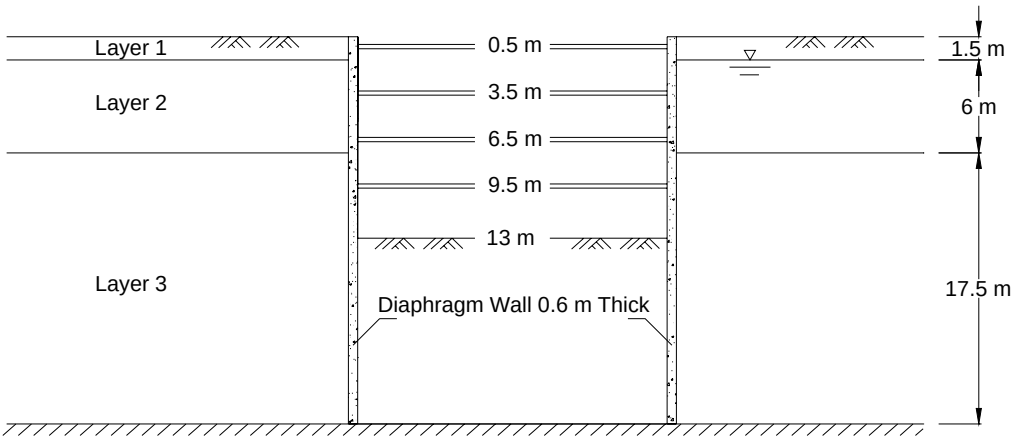

Figure 7.42 Cross-Section of Example 6

Table 7.5 Soil Properties of Example 6

Soil	γ_{dry} (kN/m^3)	γ_{wet} (kN/m^3)	E' (kPa)	ν'	c' (kPa)	ϕ' °	k (m/s)
Layer 1	18	19	20000	0.3	15	34	1x10-5
Layer 2	16	17	15000	0.3	10	33	1x10-8
Layer 3	18	19	25000	0.3	20	35	1x10-8

Table 7.6 Structural Properties of Example 6

Structural Members	E (kN/m^2)	A (m^2/m)	Preload (kN/m)
Strut (all levels)	$2.07x10^8$	0.00518	No preloading
Diaphragm wall (quadrilateral element)	$2.8x10^7$	0.6	-

Figures 7.42 to 7.47 show that the results compare favorably with those from 3-D finite element analysis. Results are also not sensitive to the spring stiffness. Hence, the difficulties in determining the soil stiffness are not an issue.

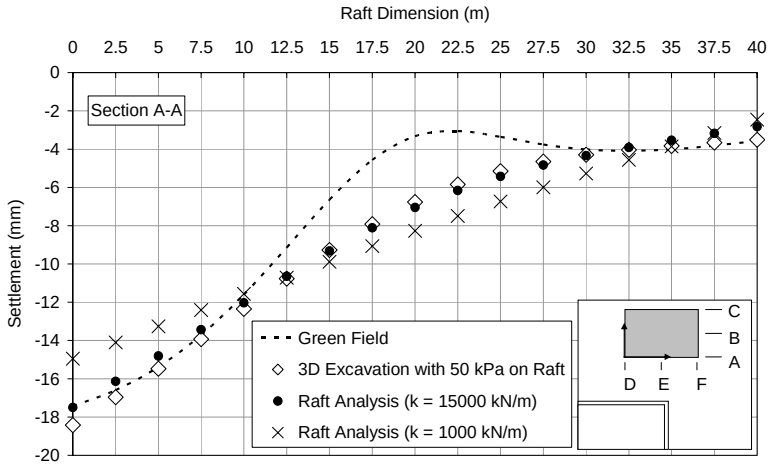

Figure 7.43 Example 6: Comparison of Raft 20x40x1 m Settlement at Section A-A

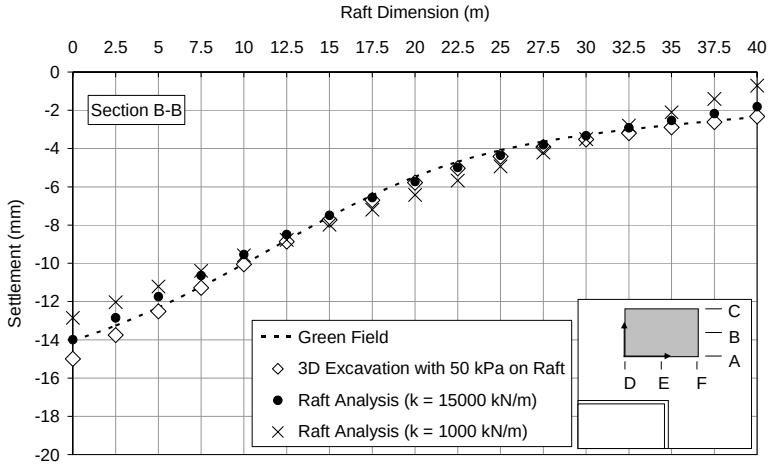

Figure 7.44 Example 6: Comparison of Raft 20x40x1 m Settlement at Section B-B

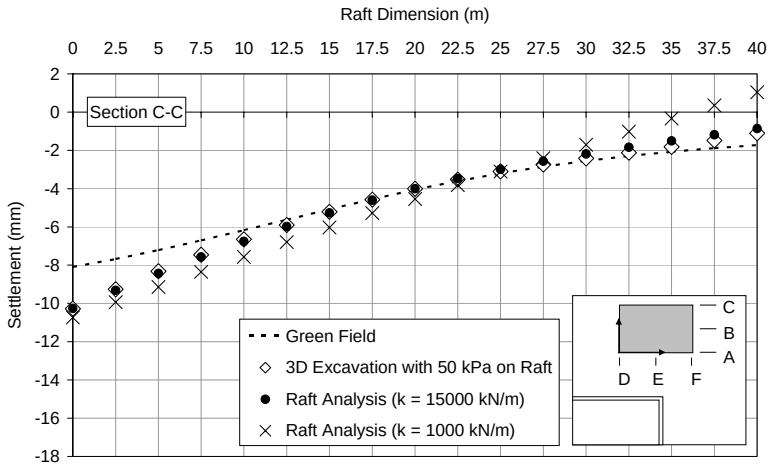

Figure 7.45 Example 6: Comparison of Raft 20x40x1 m Settlement at Section C-C

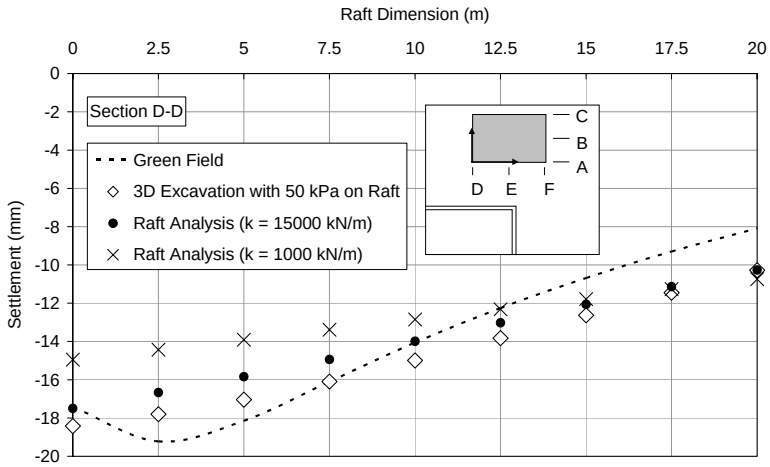

Figure 7.46 Example 6: Comparison of Raft 20x40x1 m Settlement at Section D-D

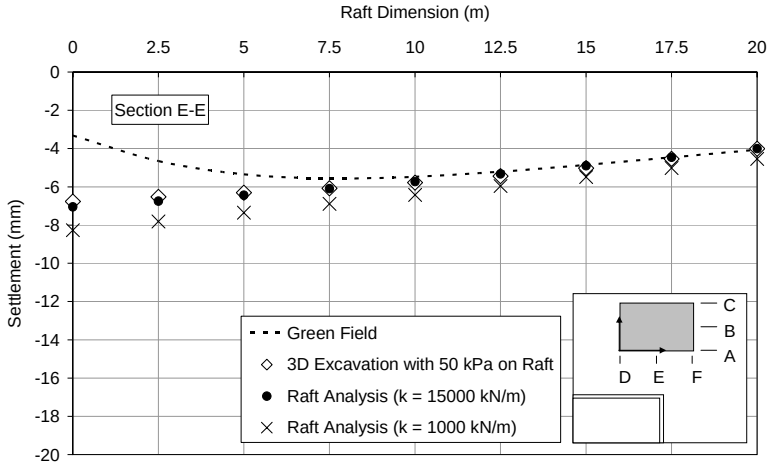

Figure 7.47 Example 6: Comparison of Raft 20x40x1 m Settlement at Section E-E

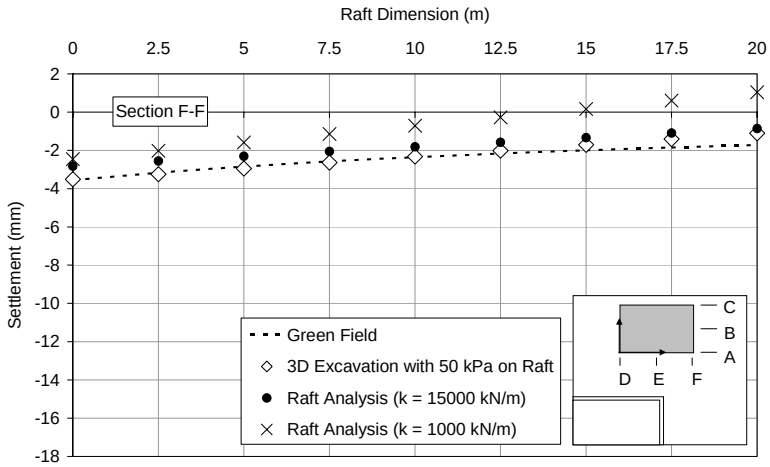

Figure 7.48 Example 6: Comparison of Raft 20x40x1 m Settlement at Section F-F

7.5 Conclusion

A method has been developed that enables one to determine the 3-D raft settlement if the green field settlement is known. This method has been validated against 3-D excavation analysis which includes building weight and raft stiffness. The computed raft settlements using the proposed method compare favorably with those from 3-D analysis.

Results are not very sensitive to the spring stiffness in the Winkler raft analysis. However, a reason estimation of the spring constant using the procedure discussed

in this chapter will produce more accurate results. The proposed method is only applicable to shallow foundation on stiff soils with stresses within the elastic limit. It is not applicable to rafts on soft soils because of the non-linear response and yielding within the soil mass.

CHAPTER 8
POST-EXCAVATION SETTLEMENT

8.1 Introduction

Ground settlement due to excavation can be divided into two phases. The first one occurs during excavation and the second one after excavation. During excavation, the major cause of ground settlement comes from wall deflection. Consolidation also occurs during this phase. Osaimi and Clough (1979) suggested that careful thought needs to be given to use the undrained condition in the design of excavations in clay since pore-pressure dissipation may occur more rapidly than previously thought.

After completion of the excavation, ground settlement may continue. Lambe et al. (1970) showed that two-thirds of the total settlement during the excavation project along Accolon Way constructed with sheet piles wall in Boston occurred after excavation. Experiences (Wen et al., 2001 & Li, 2001) from the construction of MRT North East Line also showed that the post-excavation settlement can exceed 50 mm within the first year.

Field measurements confirm that post-excavation settlements do occur. The reason behind it, unfortunately, is not well understood. In this study, three possible causes are investigated using the finite element software SAGE CRISP. They are (i) under-drainage, (ii) wall leakage, and (iii) base slab leakage.

When the construction of basement is completed, the wall movement more or less ceases. Therefore, the post-excavation settlement comes mainly from consolidation of the soft clay layers. The removal of soil during excavation changes the pore pressure regime in the surrounding soil. Firstly, the stress relief due to excavation causes a reduction in pore pressure in the surrounding soil. There is a possibility that the underlying hard stratum (e.g. Old Alluvium) has a greater reduction in pore pressure than the soft clay above. Wen and Lin (2002) reported large drawdown of

the water pressure head in the Old Alluvium. With a higher negative pore pressure in the hard stratum, it tends to draw or suck water away from the soft clay above resulting in consolidation settlement at the lower portion of the soft clay layer. This phenomenon is locally known as under-drainage. Another possibility of under-drainage is the presence of sand layer or pockets that channel water into the excavation. The extent of the sand layer and pockets will dictate the extent of settlement zone. The effects of these two modes of under-drainage on post-excavation settlement are investigated.

Secondly, the exposed wall will generate a large hydraulic gradient between the front and back faces of the retaining wall. This establishes seepage flow in the soil and through the wall. It leads to an increase in effective stress and hence consolidation settlement. The effects of seepage through the wall or wall leakage on post-excavation settlement are investigated. Several hypothetical studies were conducted.

Thirdly, the base slab leakage is investigated. Cracks or imperfections at the base slab can cause severe leakage. Consequently, seepage flow can occur and lead to ground settlement. Therefore, this effect on post-excavation settlement should be investigated.

Two study cases were back-analysed to investigate the causes of post-excavation settlement. They are: (i) Bugis MRT Station and (ii) cut-and-cover tunnel between Farrer Park and Little India in Singapore. The aim is to gain a better understanding about post-excavation settlement and ground water flow in deep excavation so that preventive measures can be incorporated in the design to minimize post-excavation settlement.

8.2 Diaphragm Wall Leakage

In the design and analysis of temporary earth retaining structures, it is commonly assumed that the diaphragm wall is impervious. This assumption contradicts with field observation. Wong (1997) reported many cases of wall leakage in Singapore.

Figure 8.1 shows the leakage in the cut-and-cover tunnel at Dhoby Ghout MRT Station in Singapore. Even if the wall appears to be dry with no observable leakages, it does not mean that the wall is impervious. It just means that the rate of evaporation is faster than the rate of seepage. Therefore, all diaphragm walls should be treated as pervious rather than impervious.

Figure 8.1 Leakage in Cut-and-Cover Tunnel at Dhoby Ghout MRT Station

Gomes et al. (2003) did an experiment to measure the permeability of concrete as shown in Figure 8.2. The test was conducted on a good sample without cracks. Results show that the permeability decreases with increasing concrete strength. In deep excavations, diaphragm wall with Grade 30 to 40 concrete is commonly used. The corresponding permeability is lower than $1x10^{-10}$ m/s. If this value can be achieved in practice, wall leakage similar to that shown in Figure 8.1 will not occur. The presence of cracks and joints is the main source of leakage. It increases the overall permeability of concrete. Therefore, higher permeability should be used. Unfortunately, it is very difficult to ascertain the overall permeability of diaphragm wall in the field. Therefore, a range of permeabilities from $1x10^{-6}$ to $1x10^{-12}$ m/s were used in hypothetical study.

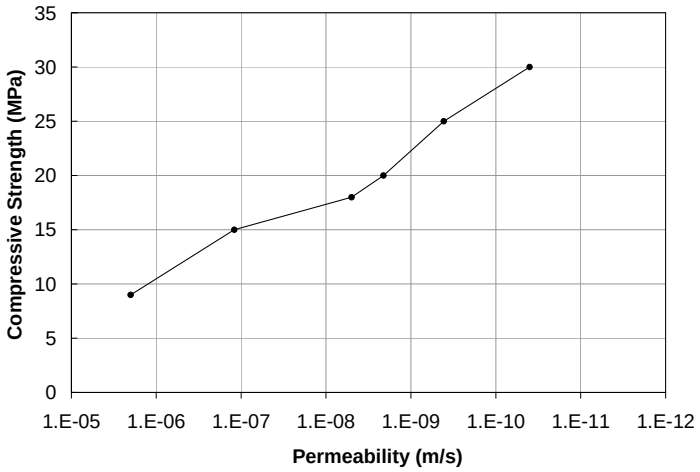

Figure 8.2 Effect of Compressive Strength on Concrete Permeability (Gomes et al., 2003)

8.3 Old Alluvium Permeability

The permeability of Old Alluvium is chosen based on the research by Li (2001). It was divided into three categories depending on the N_{SPT} blowcount. The permeability varied between $1x10^{-6}$ to $1x10^{-10}$ m/s as shown in Figure 8.3. This range was used in the hypothetical analysis.

8.4 A Hypothetical Study

Two models were used in hypothetical study as shown in Figures 8.4 to 8.5. Both figures were used to study the effect of under-drainage. However, Figure 8.4 was used to study the effect of wall leakage and Figure 8.5 was used to study the effect of base slab leakage.

The parameters are given in Tables 8.1, 8.2, and 8.3. Different permeabilities of wall and Old Alluvium (OA) were used. Modified Camclay model was used for the soft clay. Mohr-Coulomb model was adopted for other soil types. Elastic model was used for the diaphragm wall.

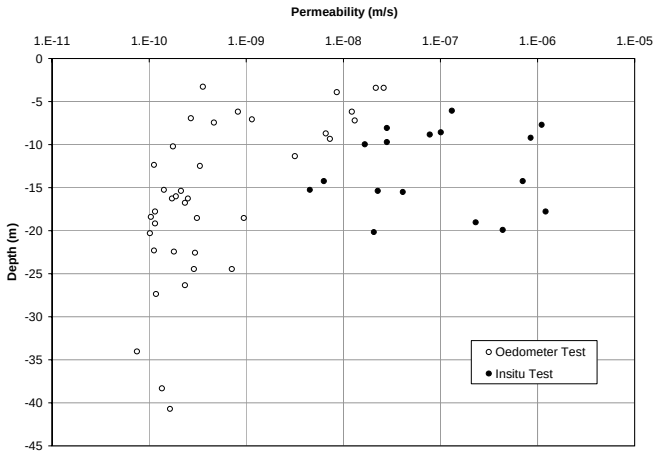

(a) OA I ($N_{SPT} \leq 25$)

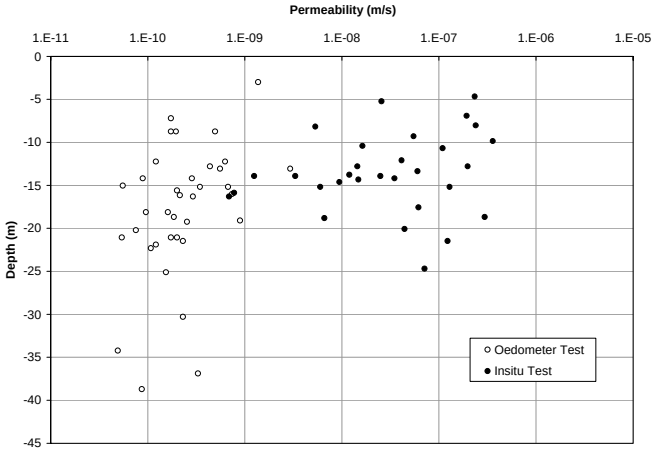

(b) OA II (N_{SPT} 26 to 99)

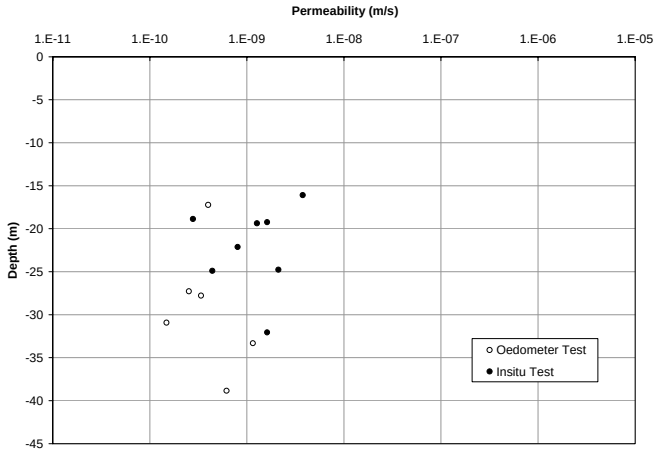

(c) OA III ($N_{SPT} \geq 100$)

Figure 8.3 Permeability of Old Alluvium (Li, 2001)

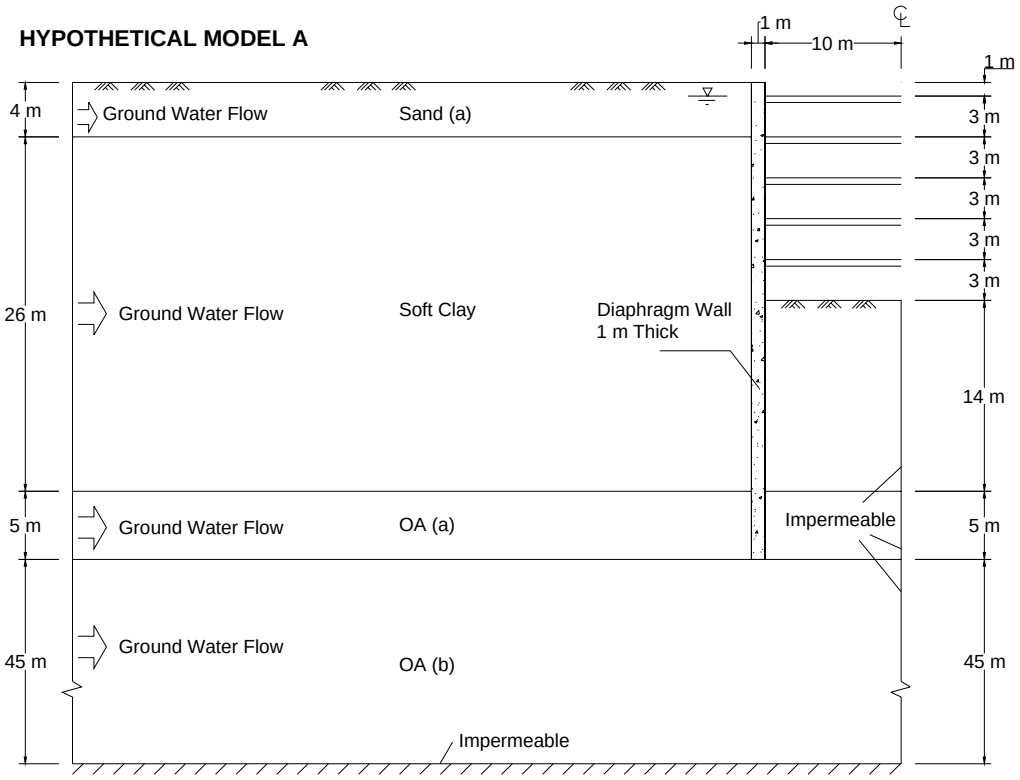

(a) Geometry and Soil Profile of Hypothetical Model A

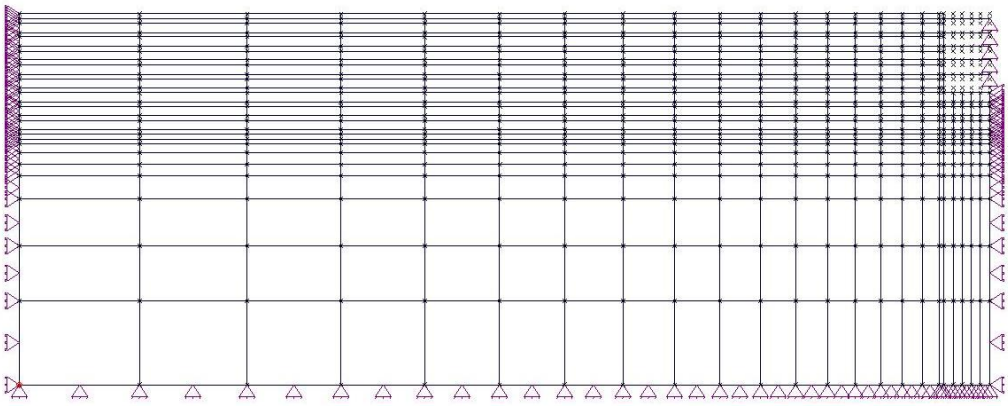

(b) Finite Element Mesh of Hypothetical Model A

Figure 8.4 Geometry, Soil Profile, and Finite Element Mesh of Hypothetical Model A

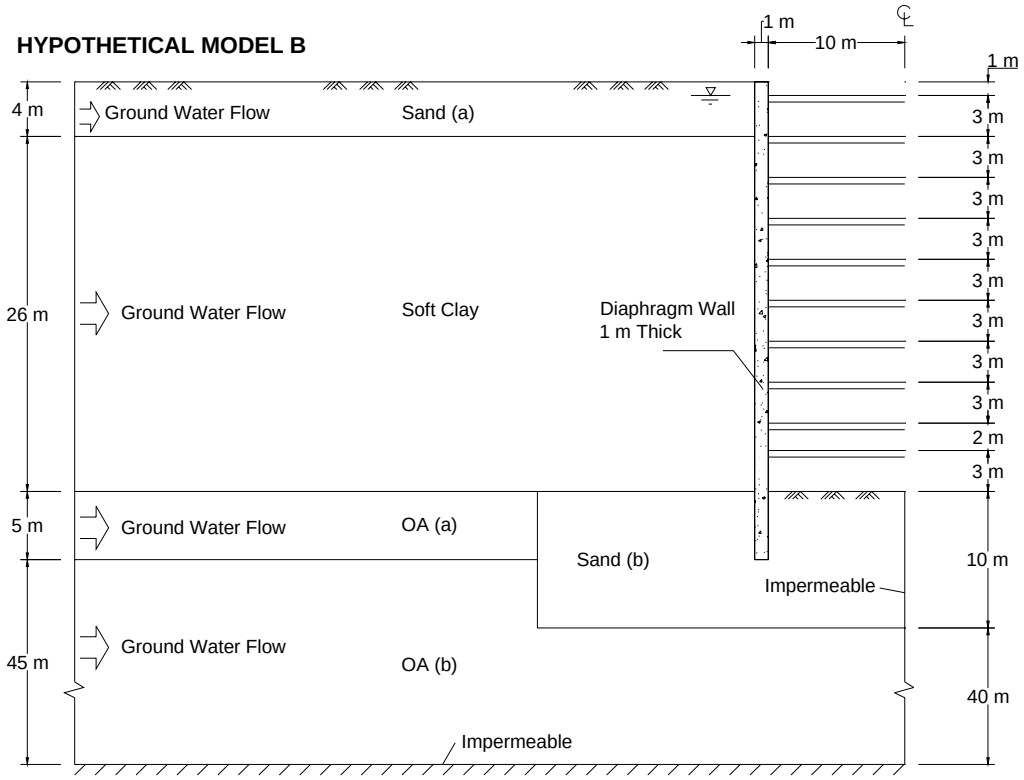

(a) Geometry and Soil Profile of Hypothetical Model B

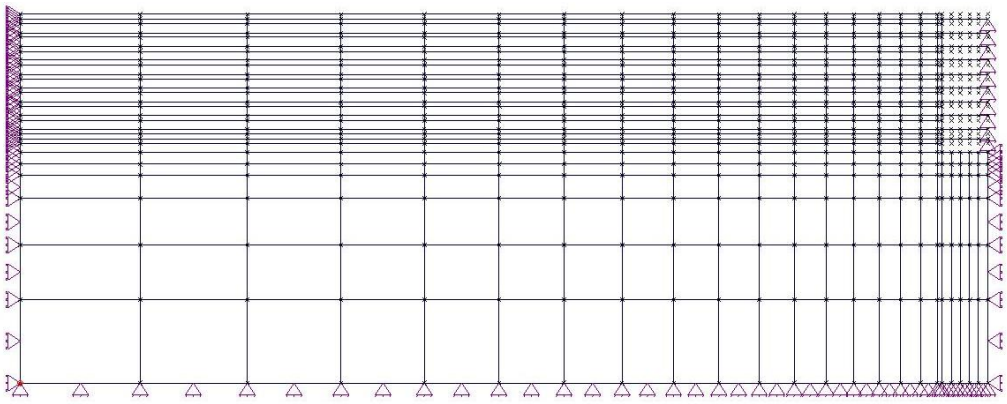

(b) Finite Element Mesh of Hypothetical Model B

Figure 8.5 Geometry, Soil Profile, and Finite Element Mesh of Hypothetical Model B

Table 8.1 Modified Camclay Parameters for Soft Clay

Material Type	γ (kN/m^3)	λ	κ	e_Γ	ϕ' (^{o})	M	ν'	k (m/s)
Soft Clay	16	0.3223	0.0644	2.69	25	0.984	0.33	$1x10^{-9}$

Table 8.2 Mohr-Coulomb Parameters for Sand, OA Soils and Diaphragm Wall

Material Type	γ (kN/m^3)	E' (kPa)	c' (kPa)	ϕ' (^{o})	ν'	k (m/s)
Sand (a)	20	10000	0	35	0.3	$1x10^{-4}$
OA (a)	20	75000	10	37	0.3	$1x10^{-6}$ or $1x10^{-9}$ or $1x10^{-10}$
OA (b)	20	110000	20	37	0.3	$1x10^{-3}$ or $1x10^{-6}$ or $1x10^{-9}$ or $1x10^{-10}$
Sand (b)	20	110000	20	37	0.3	$1x10^{-5}$

Table 8.3 Structural Properties of Model A and B

Structural Members	E (kN/m^2)	A (m^2/m)	Preload (kN/m)
Strut (all levels)	$2.07x10^8$	0.00518	No preloading
Diaphragm wall (quadrilateral element)	$2.8x10^7$	1	-

The excavation sequence adopted in the analysis is as follows.

1. Excavate 2 m of soil for 15 days.
2. Install the struts and excavate 3 m for 15 days in each layer until reaching the formation level.
3. Consolidate for 4 months to simulate the required time for base slab construction.
4. Cast the base slab and consolidate for 5 years.
5. Change the permeability of diaphragm wall and consolidate for 45 years.

In step 4, many assumptions were made in order to simplify the analysis. The permeability of base slab and wall were altered depending on the scenario under consideration such under-drainage, wall leakage, or base slab leakage. The diaphragm wall and base slab were restrained against further movement when the basement construction was completed. At the left boundary of Figures 8.4 and 8.5, the ground water level was kept constant under hydrostatic condition. It was assumed that at that location, there would always be constant water supply and flow to the excavation.

8.5 Effect of Under-Drainage on Post-Excavation Settlement

In this series of analysis, two sources of under-drainage were analyzed. The first one is due to suction in Old Alluvium (Figure 8.4). The second one is due to water flow into the excavation through a sand layer (Figure 8.5). Three different OA permeabilities ($k=1x10^{-6}$, $1x10^{-9}$, and $1x10^{-10}$ m/s) were used. The wall and the base slab were assumed to be impermeable.

8.5.1 Effect of Under-Drainage due to Suction in Old Alluvium

Results of the analysis are shown in Figures 8.6 and 8.7. When the OA had a high permeability of $k=1x10^{-6}$ m/s, no excess negative pore pressure was generated in that layer as shown in Figures 8.6a to 8.6c. The excess negative pore pressure in the soft clay actually draws water from the sand fill above and the OA below. The net result is swelling of 18 mm. Therefore, the post-excavation ground movement is actually a heave rather than settlement. The maximum ground settlements at the end of excavation and 5 years after consolidation were 86 and 76 mm, respectively, as shown in Figures 8.7a and 8.7b.

Figures 8.6d to 8.6f show the excess pore pressure contours for OA with $k=1x10^{-10}$ m/s. The negative excess pore pressure in the OA was higher than that in the soft clay above. In this case that water in soft clay is being drawn to the OA below. The maximum ground settlements at the end of excavation, 5 years and 50 years of consolidation are 80, 84, and 82 mm, respectively, as shown in Figures 8.7a to 8.7c. These figures show that only small changes occur in the settlement. Therefore, post-excavation settlement due to suction by Old Alluvium to draw water from the overlying soft clay is insignificant.

8.5.2 Effect of Under-Drainage due to Water Flow through Sand Layer

Results of the analysis are shown in Figures 8.8 and 8.9 for three different sand pocket sizes: (i) no sand pocket, (ii) short sand pocket, and (iii) long sand pocket. Figure 8.8 shows the ground settlement at various times. Figure 8.9 shows the total pore pressure contours for the long sand pocket case.

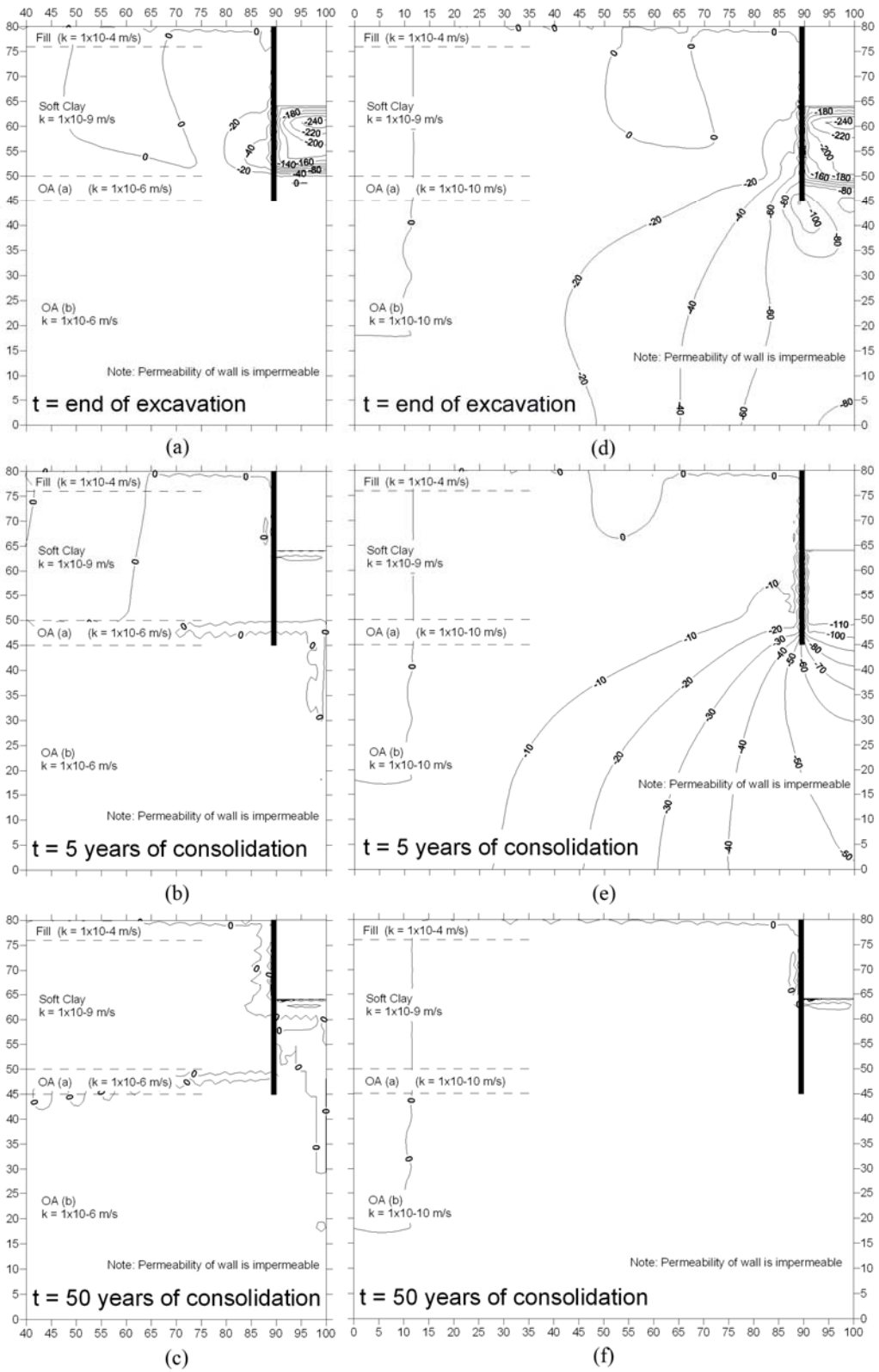

Figure 8.6 Excess Pore Water Pressures for Two Different Permeabilities of OA

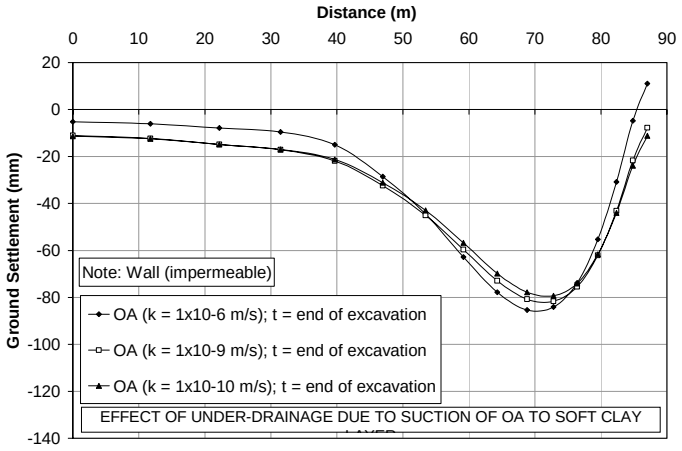

(a) Ground Settlement at End of Excavation

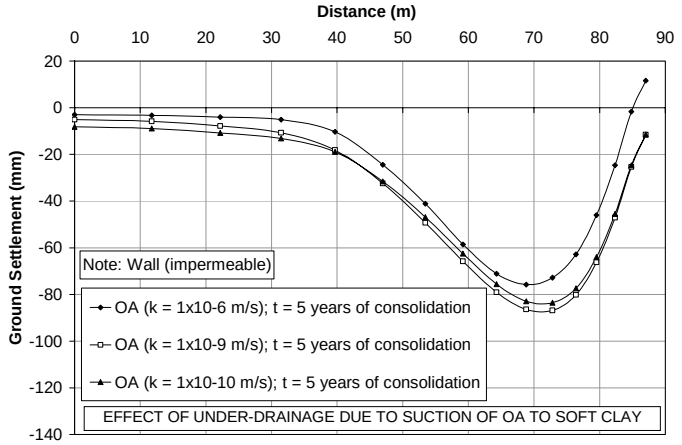

(b) Ground Settlement after 5 Years of Consolidation

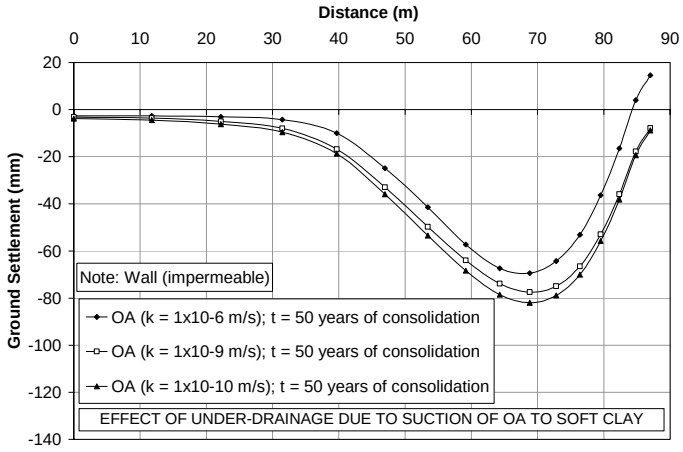

(c) Ground Settlement after 50 Years of Consolidation

Figure 8.7 Ground Settlements for Different Permeabilities of OA

At the end of excavation, significant settlement has occurred if sand pockets are present. The maximum ground settlements with no sand pocket, short sand pocket, and long sand pocket are 80, 160, and 210 mm, respectively. The settlement continues for 4 months until the impermeable base slab was cast. The maximum ground settlement increased to 225 and 340 mm for short and long sand pocket, respectively. However, when there is no sand pocket, the maximum settlement remains unchanged during this 4 months period.

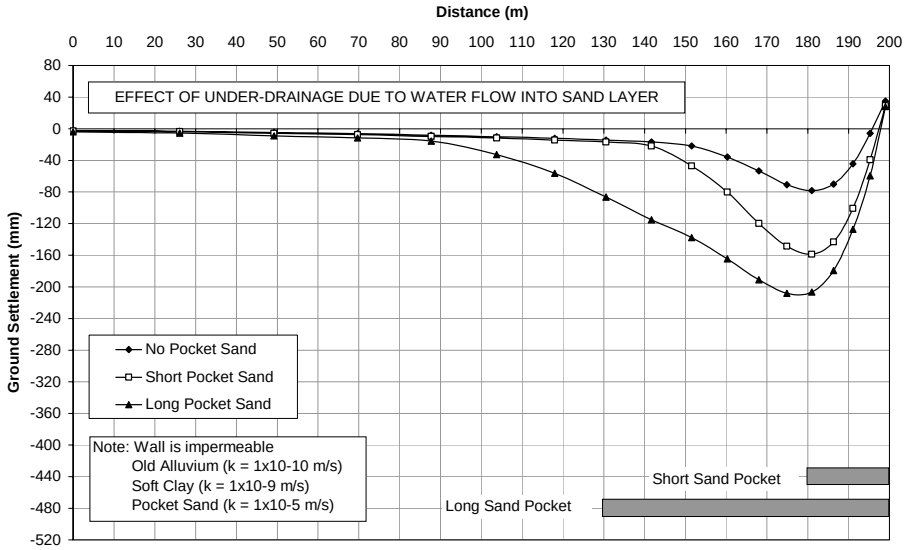

(a) Ground Settlement at End of Excavation

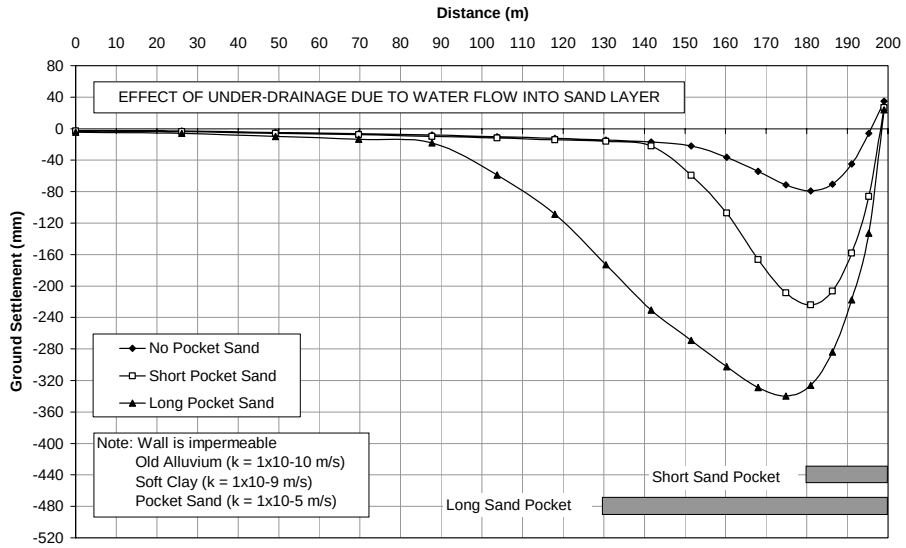

(b) Ground Settlement after 4 Months since End of Excavation

Figure 8.8 Ground Settlement due to Water Flow into Sand Layer *(Continued)*

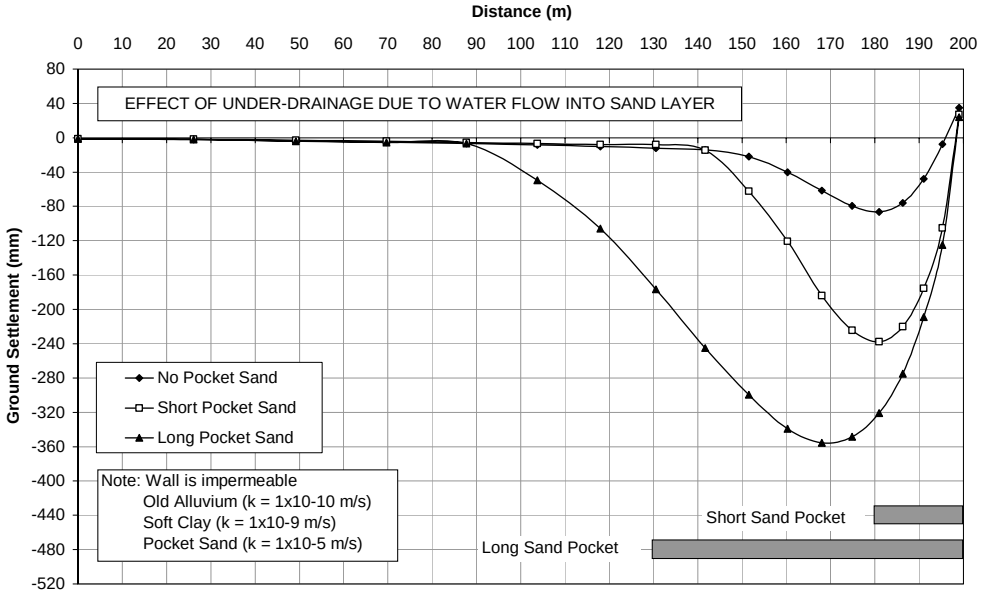

(c) Ground Settlement after 5 Years of Consolidation

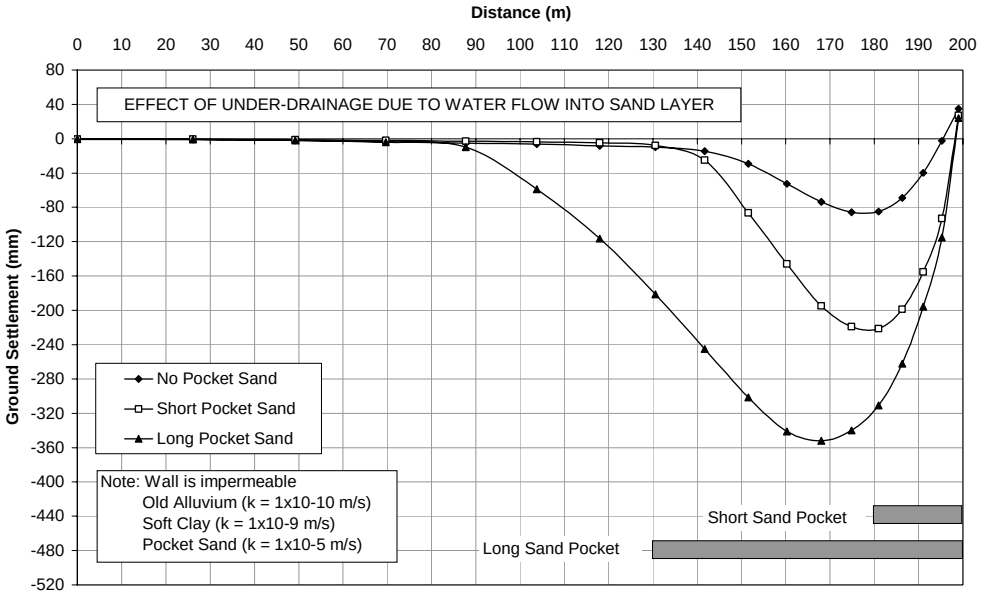

(d) Ground Settlement after 50 Years of Consolidation

Figure 8.8 Ground Settlements due to Water Flow into Sand Layer

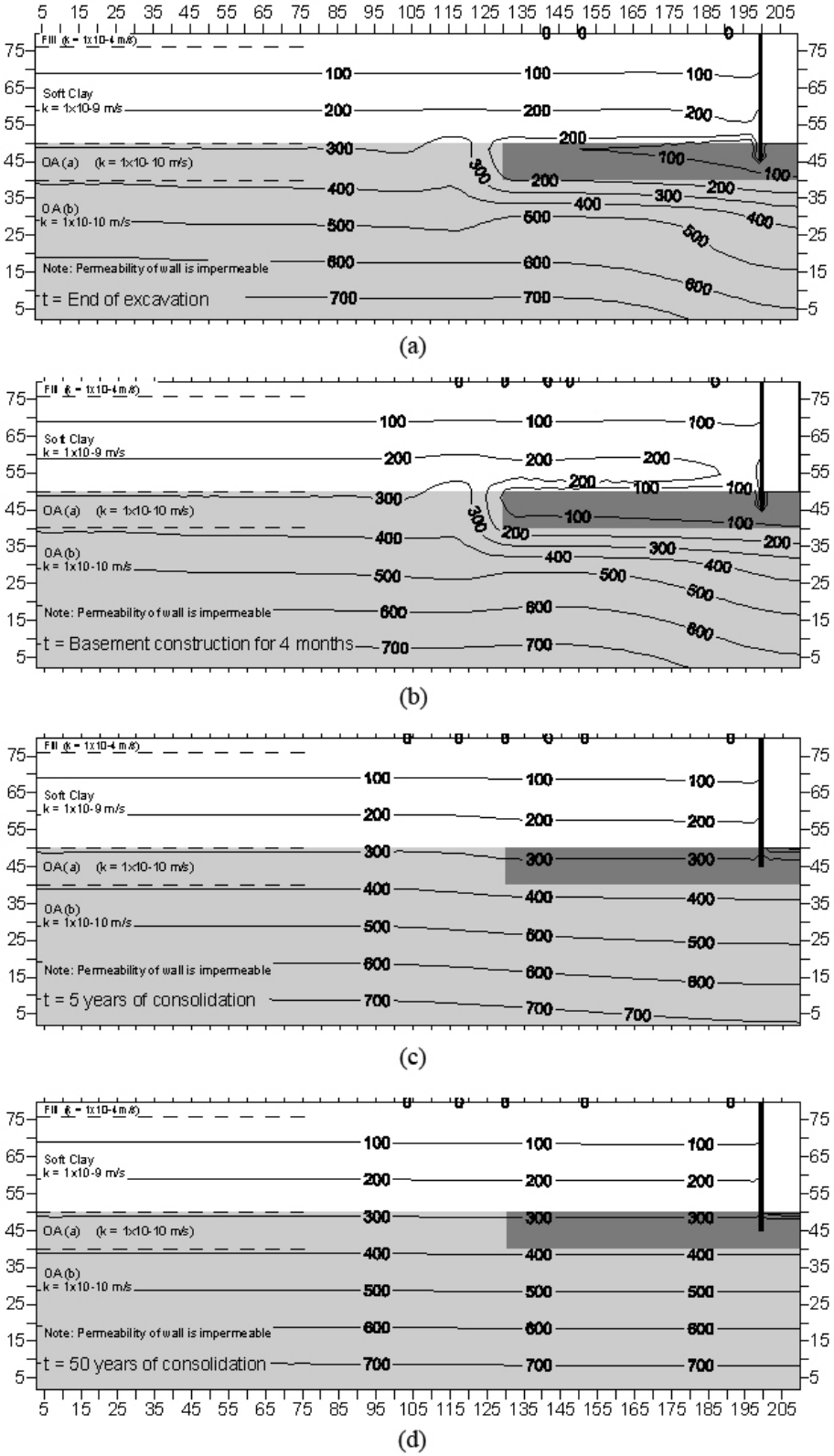

Figure 8.9 Total Pore Pressure Contours for Long Sand Pocket Case

The settlement troughs behind the wall are shown in Figure 8.8. The trough extends a long distance from the wall and is proportional to the length of sand pocket. Therefore it is plausible for settlement to occur a long distance far from the excavation. After the impermeable base slab was cast, the settlement continues to increase in the next 5 years from 225 to 240 mm for the short sand pocket and 340 to 360 mm for the long pocket. After another 45 years, the ground gradually bounced back to 220 and 350 mm for the short and long sand pockets, respectively.

The reason of this post-excavation settlement is due to ground water flow from the soft clay layer to sand pocket. As shown in Figure 8.9a, the pore pressure in the sand pocket is very low as compared to that in the soft clay layer. The high pore pressure gradient caused ground water to flow from soft clay to sand pocket. The increase in effective stress in the soft clay layer resulted in the consolidation settlement. The settlement stopped once the impermeable base slab was cast. Since that time, the total pore pressure in the sand pocket gradually return to hydrostatic. The post-excavation settlement continued in the next 5 years. However, it is very small as compared to that prior to casting the base slab. Fifty years later, the total pore pressure becomes hydrostatic everywhere resulting in a small heave. This hypothetical study shows that under-drainage due to water flowing into sand layer is very significant if the sand layer or pocket is exposed within the excavated area.

8.6 Effect of Wall Leakage on Post-Excavation Settlement

In the study of wall leakage, four wall permeabilities ($1x10^{-6}$, $1x10^{-8}$, $1x10^{-10}$, and $1x10^{-12}$ m/s) were used. The permeabilities of soft clay and OA were set equal to $1x10^{-9}$ and $1x10^{-6}$ m/s, respectively. With OA permeability equals to 10^{-6} m/s, no excess pore pressure was generated in the OA regardless of wall permeability as shown in Figure 8.10. Therefore, the effect of under-drainage can be ignored.

At the end of excavation, the ground settlements are nearly the same regardless of wall permeability as shown in Figure 8.11. This is because the soft clay had a low permeability of $1x10^{-10}$ m/s and the entire excavation process lasted only 90 days. The seepage effect was negligible during this period.

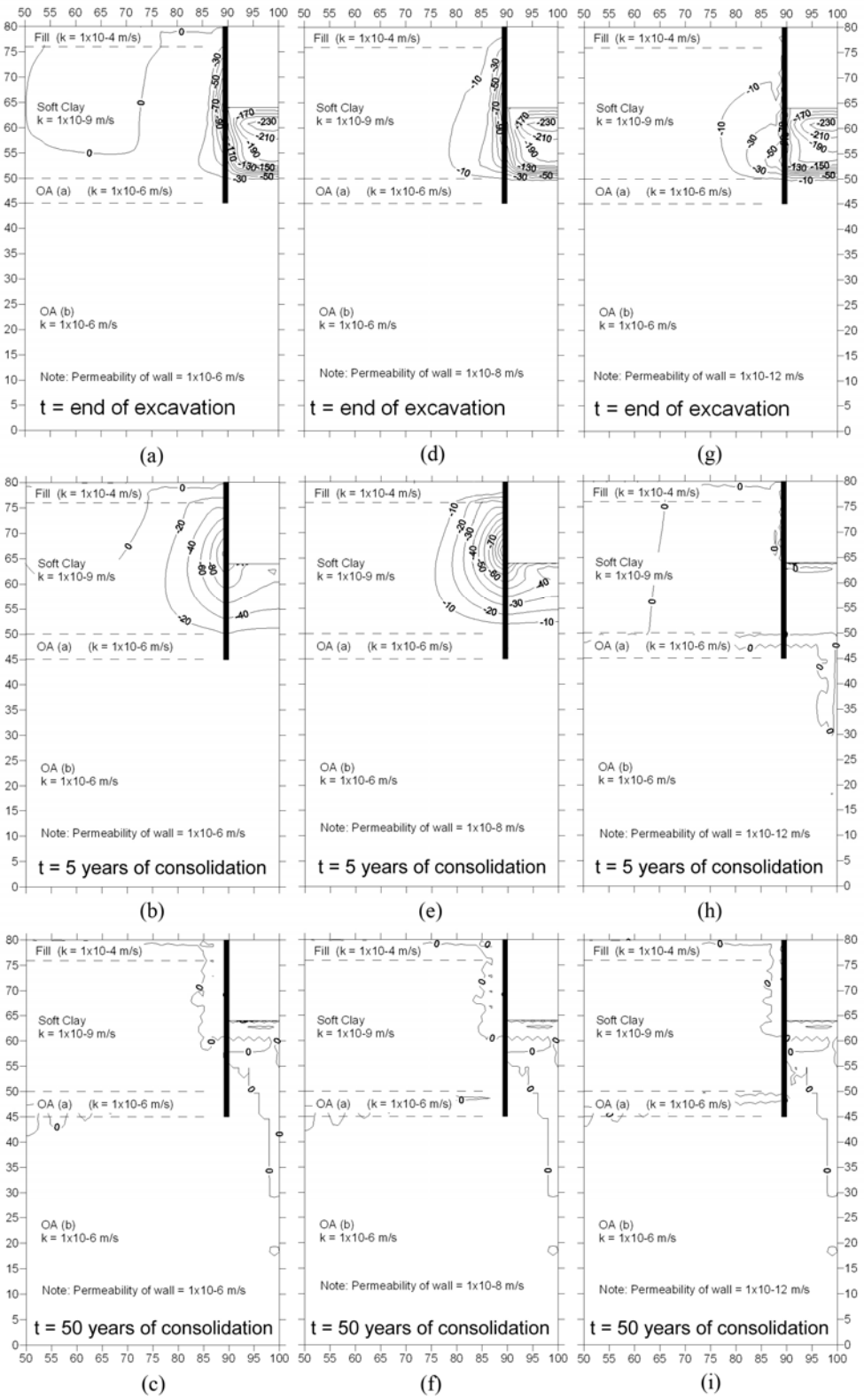

Figure 8.10 Excess Pore Water Pressure Contours for Different Wall Permeabilities

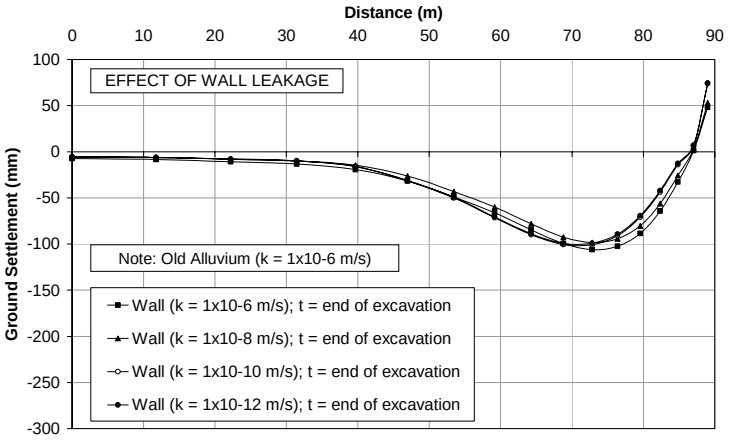

(a) Ground Settlement at End of Excavation

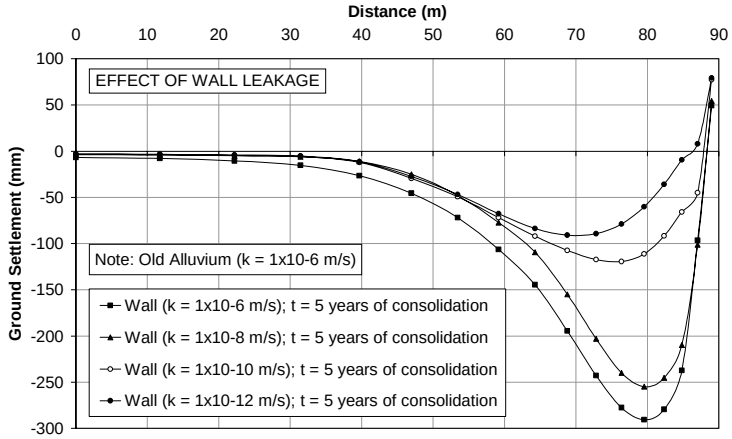

(b) Ground Settlement after 5 Years of Consolidation

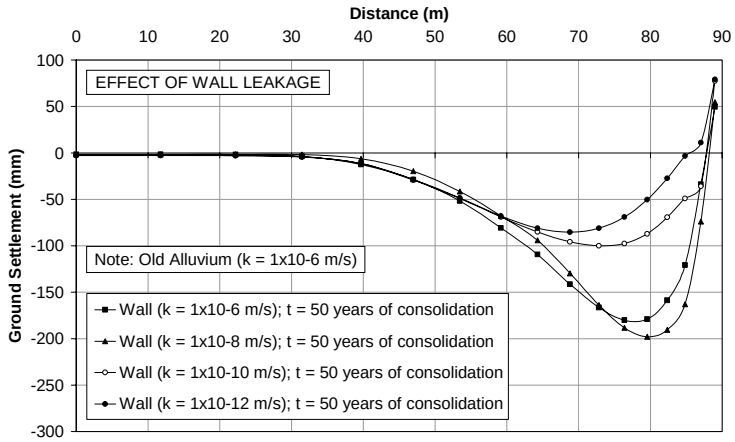

(c) Ground Settlement after 50 Years of Consolidation

Figure 8.11 Ground Settlements for Different Wall Permeabilities

For the wall with k = $1x10^{-6}$ m/s, the excess pore pressure distribution at the end of 5^{th} year is a reflection of near steady state seepage as shown in Figure 8.10. The settlement increased from 100 to 290 mm during this period. After that, drainage through the wall was closed to simulate the fixing of all leakages. The analysis continued for another 45 years to allow gradual return to hydrostatic condition. The net effect was swelling during this 45 years period from 290 to 180 mm as shown in Figure 8.11.

On the other hand, for the wall with a low permeability of $1x10^{-12}$ m/s, Ground heave started to occur once the base slab was cast. This is because the wall is essentially impervious. The ground settlements at the end of excavation, 5 years and 50 years after casting of base slab are 100, 90 and 80 mm as shown in Figure 8.11.

Another series of hypothetical problems was analysed to study the effect of wall leakage. The wall permeability was assumed to be $1x10^{-8}$ m/s up to 5 years after the base slab was cast. After that, the wall permeability was varied and the analysis continued for another 45 years. Results show that the ground may continue to settle or swell after the 5^{th} year depending on the wall permeability. The settlement will continue if the wall permeability is 10^{-9} m/s or higher as shown Figure 8.12. On the other hand, the ground will swell if the permeability is less than 10^{-10} m/s.

Figures 8.13 and 8.14 compare the ground settlements and excess pore pressures of two walls. The first wall is impervious. The second wall has a permeability of $1x10^{-8}$ m/s up to the 5^{th} year after the base slab was cast and then changed to impervious. The portion of wall below formation level remained at k=$1x10^{-8}$ m/s. Results show that the effect of leakage is very significant. Post-excavation settlement does not occur if there is no leakage.

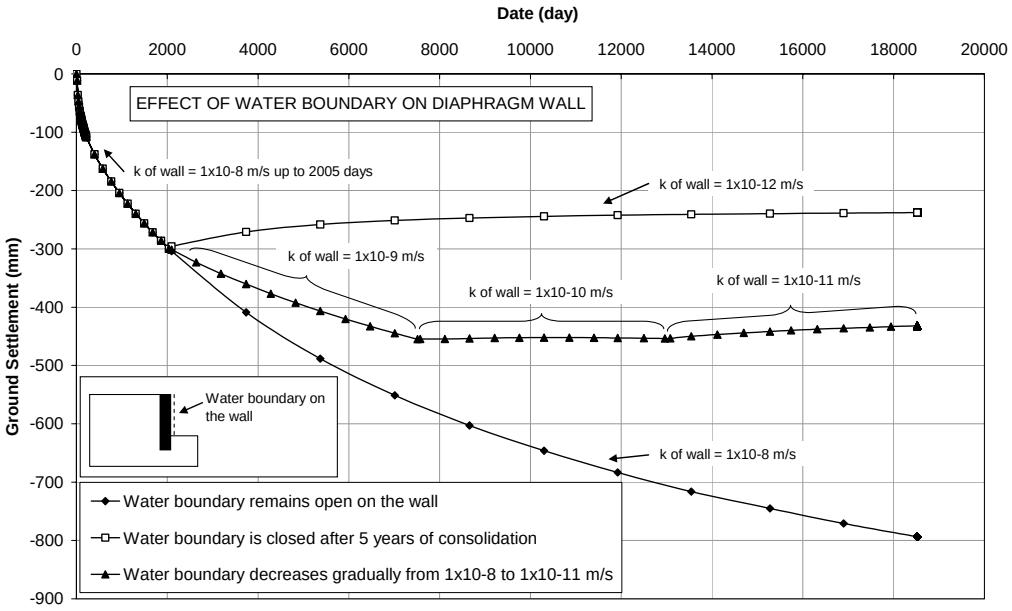

Figure 8.12 Effect of Changing Wall Permeability on Ground Settlement

To illustrate this phenomenon more clearly, the ground settlement at 8 m behind the wall is plotted in Figure 8.15. It can be seen that after the end of excavation, the ground starts to heave if there is no leakage. The heaving is associated with the dissipation of negative pore pressure. In the case where leakage occurs in the wall, the ground continues to settle until the leakage was stopped 5 year later. Subsequently, the ground began to swell.

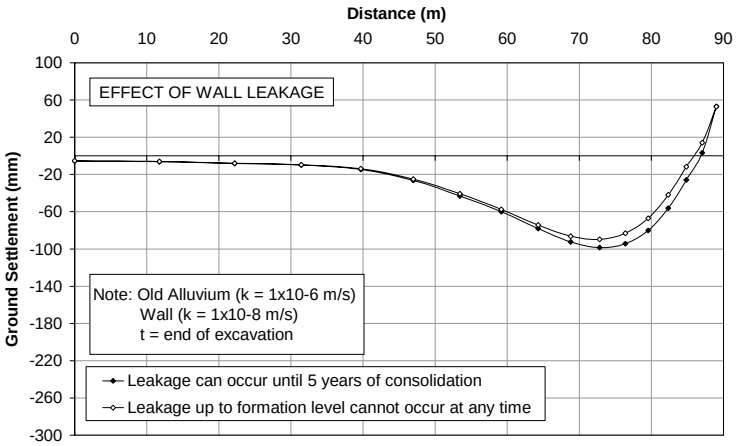

(a) Ground Settlement at End of Excavation

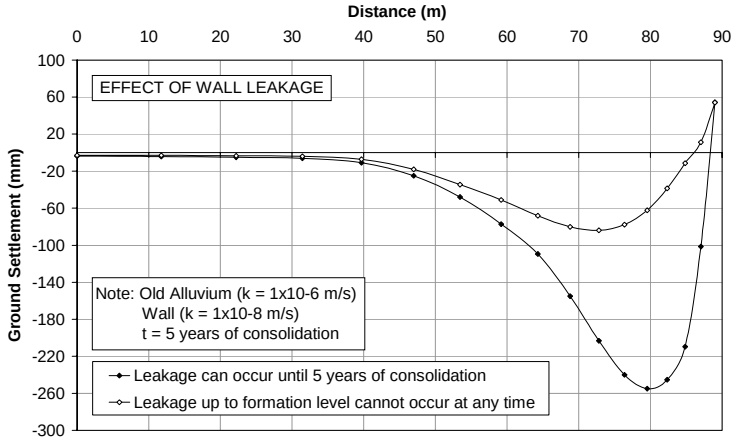

(b) Ground Settlement after 5 Years of Consolidation

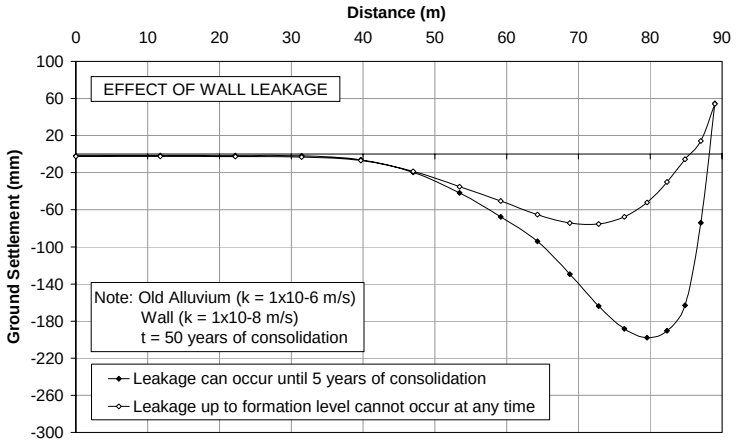

(c) Ground Settlement after 50 Years of Consolidation

Fig. 8.13 Ground Settlements at Different Time and Wall Permeabilities

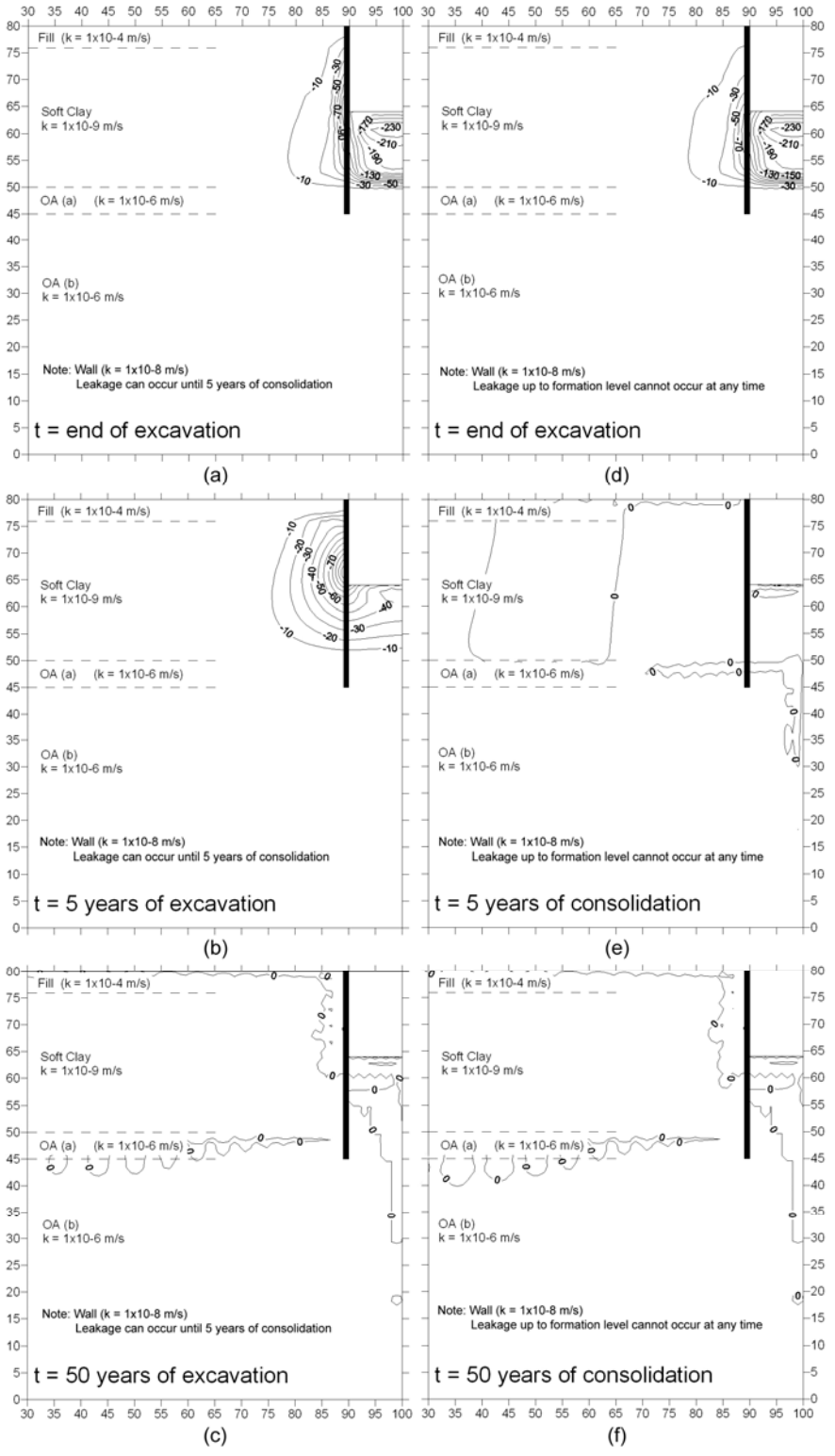

Figure 8.14 Excess Pore Water Pressures at Different Time and Wall Permeabilities

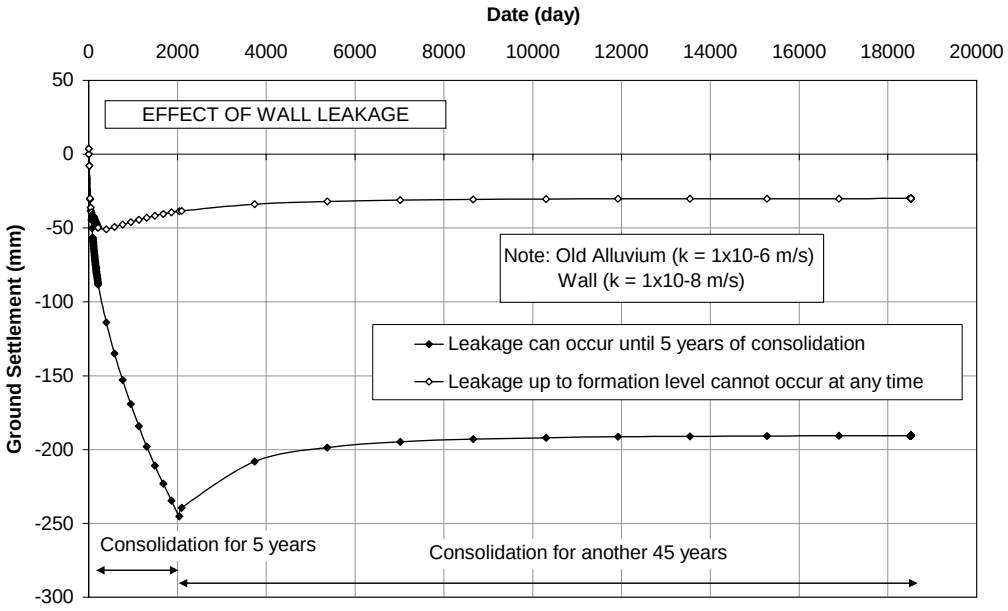

Figure 8.15 Ground Settlements at 8 m behind the Wall versus Time

8.7 Effect of Base Slab Leakage on Post-Excavation Settlement

If there is leakage in the base slab, steady-state seepage can develop which can cause post-excavation settlement. Two permeabilities of Old Alluvium, $1x10^{-6}$ and $1x10^{-10}$ m/s, were chosen in the numerical study. The wall was assumed to be impervious in order to eliminate the effect of wall leakage.

In the first scenario, the OA permeability is $1x10^{-6}$ m/s. Two drainage conditions were considered at the base slab. The first one adopted closed drainage which means the base slab was impervious. The second one adopted open drainage which assumed the base slab was pervious. It is interesting to note that the ground settlements are the same regardless of the drainage boundary condition at the base slab whether it is closed or opened as shown in Figure 8.16. At the end of excavation, the ground settled 85 mm. Four months after reaching the formation level, the base slab was cast. Ever since that time, the ground started to heave. At the end of 5 and 50 years, the ground had heaved 9 and 15 mm, respectively. It is easy to understand why the ground heaved after the impermeable base slab was cast. However, it is not so obvious why the same occurred when the base slab

remained free draining. In order to understand this problem, it is necessary to study the excess pore water pressure for both cases.

Figure 8.17 shows the excess pore water pressure contours. Figures 8.17a to 8.17c are for the case where the water boundary at the base slab was closed. On the other hand, Figures 8.17d to 8.17f are for the case where the water boundary at the base slab remained open. When the water boundary at the base slab was closed, the negative excess pore water pressure would dissipate and the pore pressure regime became hydrostatic with time as shown in Figures 8.17a to 8.17c. Hence, the ground heaved rather than settled.

For the case where the water boundary at the base slab remained open, steady-state seepage began to develop which only affects the soil trapped within the excavated area. It does not affect the marine clay behind the wall. Hence, the post-excavation settlement profile was the same as the one with closed drainage boundary at the bas slab.

In the second scenario, the Old Alluvium had a permeability of $1x10^{-10}$ m/s. The ground settlement is shown in Figure 8.18. At the end of excavation and after 5 years of consolidation, the maximum ground settlements are the same for both drainage boundary conditions at 80 and 84 mm, respectively. However, after 50 years, the results are very different. The maximum ground settlement is 108 mm where the water boundary at the base remained open and 81 mm where the water boundary was closed.

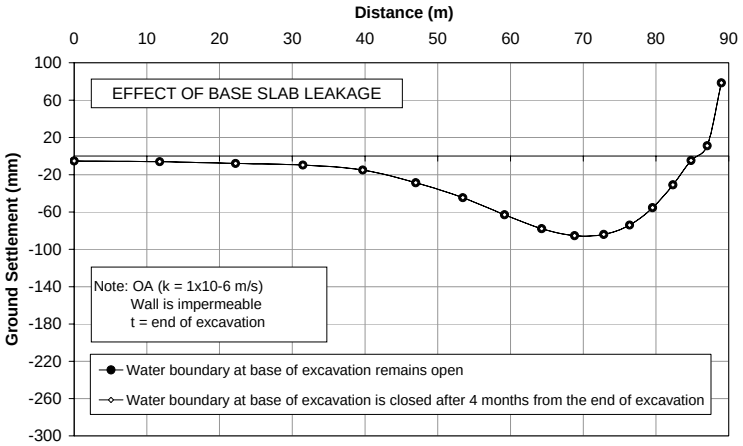

(a) Ground Settlement at End of Excavation

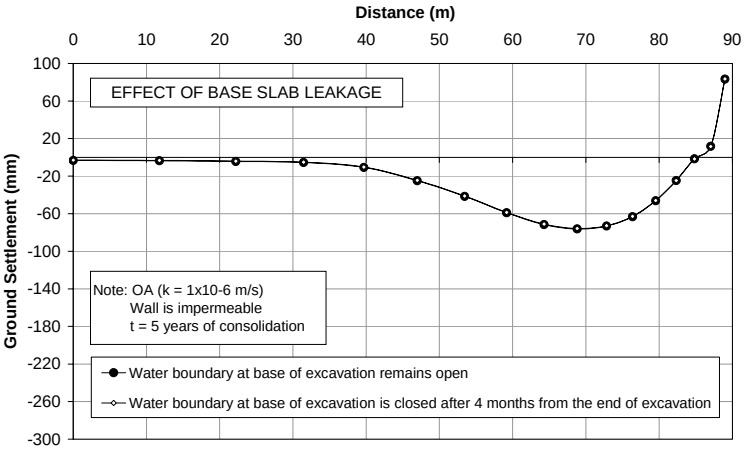

(b) Ground Settlement after 5 Years of Consolidation

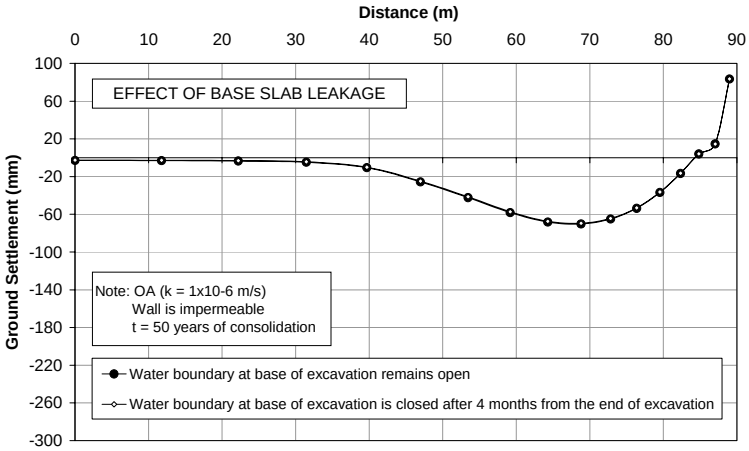

(c) Ground Settlement after 50 Years of Consolidation

Figure 8.16 Ground Settlements for Different Water Boundaries at Base Slab

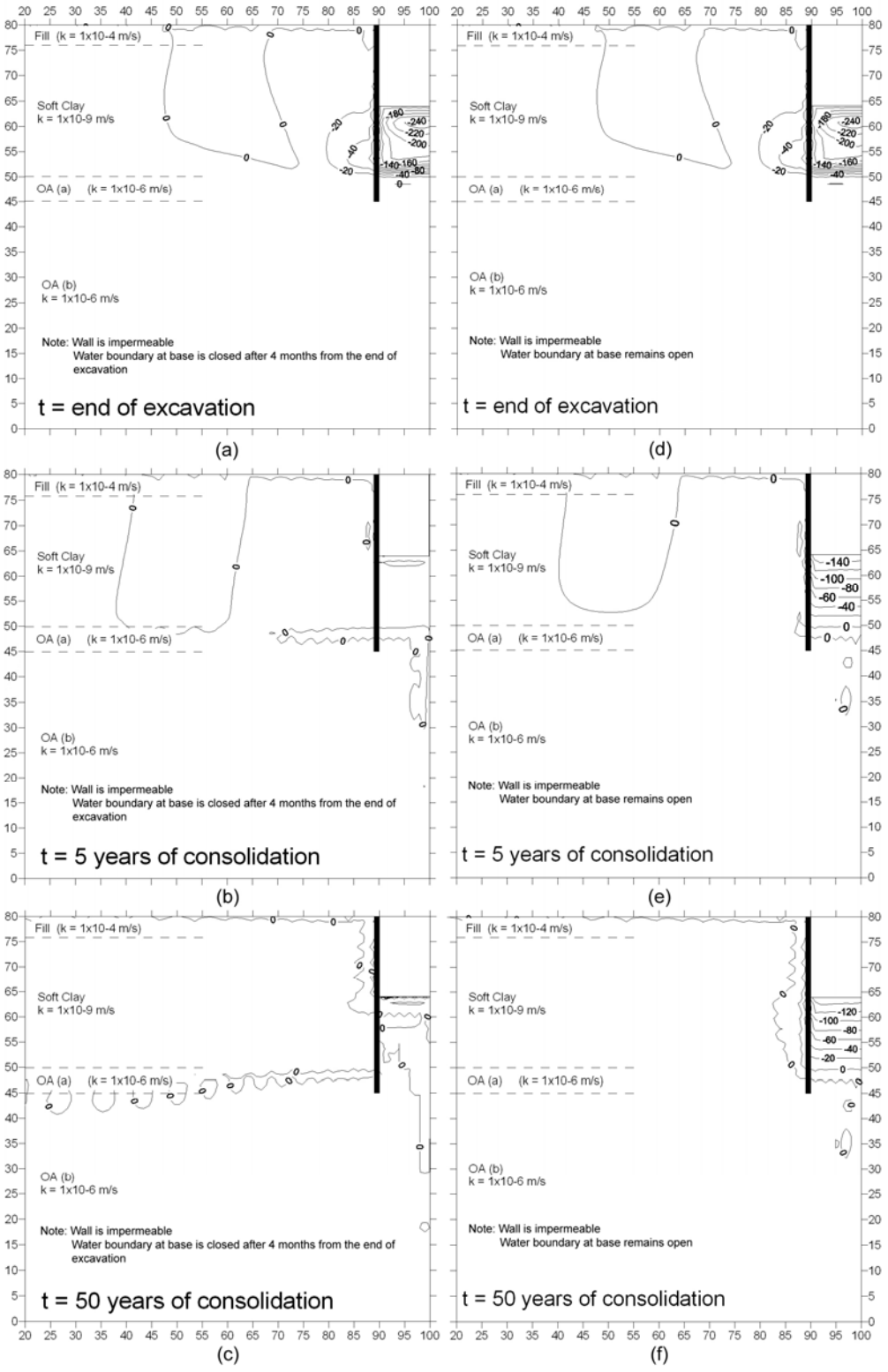

Figure 8.17 Excess Pore Water Pressures for Different Water Boundaries at Base Slab

The reason for the different response can be explained with the aid of excess pore water pressure distribution plots as shown in Figure 8.19. The negative excess pore water pressures are very similar for both cases until 5 years after excavation. Therefore, the ground settlements until that time are very similar as shown in Figure 8.18.

For the case where the water boundary at the base of excavation was closed 4 months after completion of excavation, the dissipation of negative excess pore pressure continue to take place for a long time because of the low permeability of Old Alluvium. Therefore, heaving continued with time.

For the case where the water boundary at the base of excavation remained open, steady state seepage gradually developed with time. Consequently, the increase in effective stress resulted in the consolidation of the soft clay layer. After 50 years of consolidation, the settlement increased from 84 to 108 mm as shown in Figures 8.18b and 8.18c.

Results from this study indicate that there is a strong relationship between water boundary at the base of excavation and under-drainage. As shown in Figures 8.18b and 8.18c, the ground continues to settle from 84 to 108 mm when the permeability of Old Alluvium is low and water boundary at the base of excavation remains open.

This hypothetical study shows that leakage at base slab can cause post-excavation settlement. Once the leakage has been repaired, post-excavation will stop. Therefore, it is important to plug all leakages in the wall and base slab.

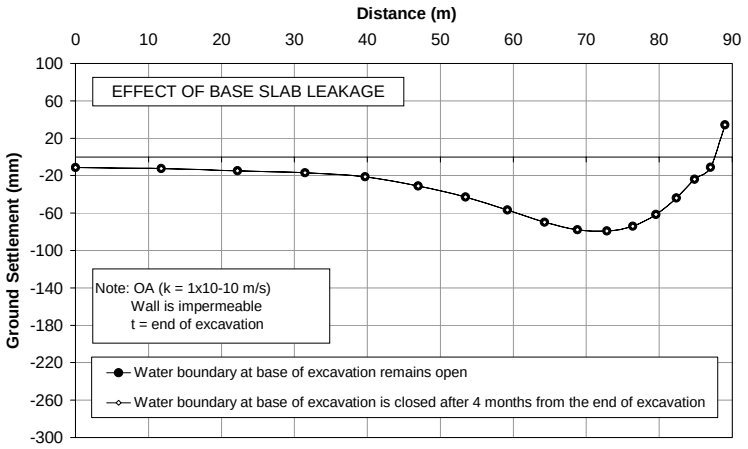

(a) Ground Settlement at End of Excavation

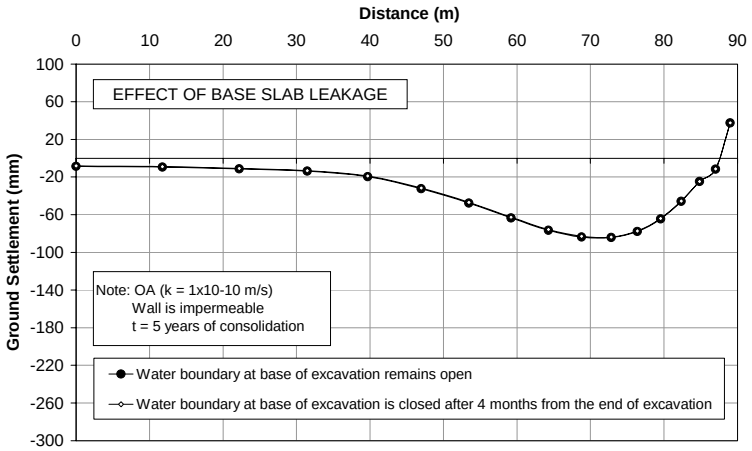

(b) Ground Settlement after 5 Years of Consolidation

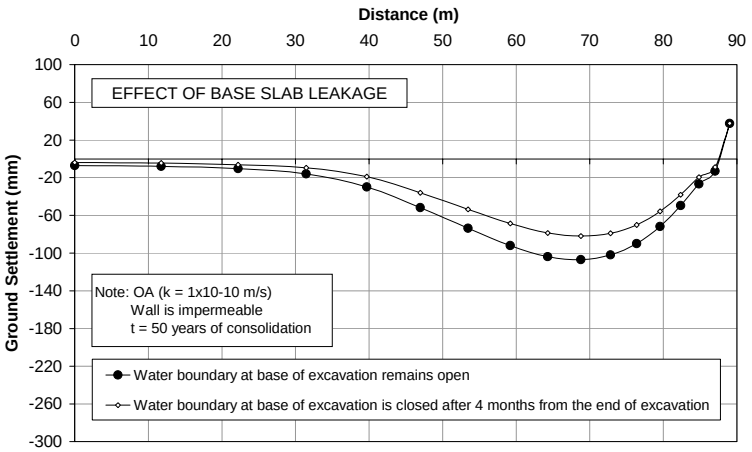

(c) Ground Settlement after 50 Years of Consolidation

Figure 8.18 Ground Settlements for Different Old Alluvium and Water Boundary at the Base of Excavation

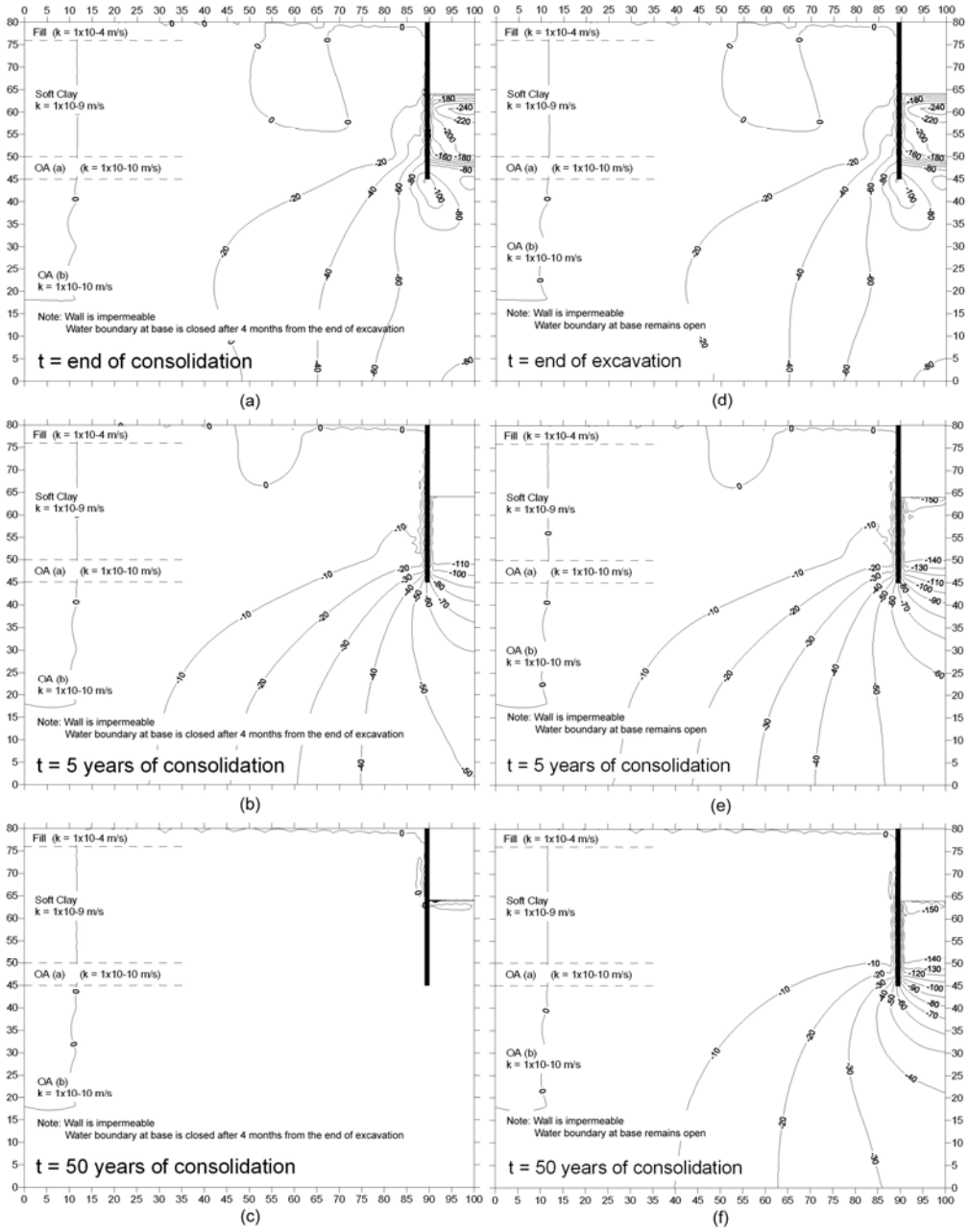

Figure 8.19 Excess Pore Water Pressures for Different Old Alluvium and Water Boundaries at the Base Slab

8.8 Case Study

Two deep excavation cases in Singapore are used to study post-excavation settlement. They are Bugis MRT Station and the cut-and-cover tunnel between Farrer Park and Kandang Kerbau MRT Station.

8.8.1 Bugis MRT Station

Measurements at Bugis MRT Station in Singapore have provided a rare opportunity to study post-excavation settlement. The sectional view and finite element mesh of the excavation are shown in Figure 8.20 and 8.21, respectively. The parameters are shown in Tables 8.4, 8.5, and 8.6. The excavation sequence is shown in Table 8.7.

A series of back-analysis using different wall permeabilities was carried out to match the field settlement. The one that gives the best match involved using values varying from $1x10^{-7}$ to $1x10^{-8}$ m/s. The value of $1x10^{-7}$ m/s was used during excavation. The permeability was gradually reduced to $1x10^{-8}$ m/s during the one year period after the base slab was cast.

Figure 8.22 shows the post-excavation settlement when the permeability remained constant at $1x10^{-7}$ m/s. At the end of one year after the base slab was cast, the computed settlement continued at a relatively constant rate. It contradicted with field measurements which indicated a decreasing rate of settlement.

Figure 8.23 shows the post-excavation settlement where the permeability decreased gradually from $1x10^{-7}$ to $1x10^{-8}$ m/s. This is a realistic scenario as wall leakages were being arrested by grouting. The computed settlements in terms of magnitude and rate are in relatively good agreement with the measured values.

Table 8.4 Modified Cam Clay Parameters for Upper (UMC) and Lower (LMC) Marine Clay at Bugis MRT Station

Soil Type	γ_{sat}	PI	LL	G_s	κ	λ	e_Γ	ϕ_{cs}	M	ν	k
	(kN/m^3)	(%)	(%)					(^{o})			(m/s)
UMC	16	50	70	2.65	0.0585	0.2930	2.25	25.0	0.98	0.33	$1x10^{-10}$
LMC	16	40	60	2.65	0.0468	0.2344	1.9	27.0	1.07	0.33	$1x10^{-10}$

Table 8.5 Mohr-Coulomb Parameters for Sand, Fluvial Clay and OA Soils

Soil Type	γ_{sat} (kN/m^3)	ν	E_{50} (kPa)	E_{ur} (kPa)	c (kPa)	ϕ (^{o})	k (m/s)
Fill (N = 5)	18	0.33	8000	-	26	0	$1x10^{-5}$
Fluvial Clay (PI = 30)	18	0.33	48000	-	80	0	$1x10^{-10}$
Fluvial Clayey Sand (N = 80)	19	0.33	-	150000	0	40	$1x10^{-8}$
OA (N = 130)	20	0.33	-	165000	10	37	$1x10^{-8}$
OA (N > 130)	20	0.33	-	195000	20	37	$1x10^{-8}$

Table 8.6 Structural Properties of Excavation at Bugis MRT Station

Structural Members	E (kN/m^2)	A (m^2/m)	Preload (kN/m)
Strut (at -1.5 m)	2.07×10^8	0.00518	Missing record
Strut (at -4.5 m)	2.07×10^8	0.00518	Missing record
Strut (at -6 m)	2.07×10^8	0.00518	Missing record
Strut (at -9.5 m)	2.07×10^8	0.00518	Missing record
Strut (at -12 m)	2.07×10^8	0.00518	Missing record
Strut (at -14 m)	2.07×10^8	0.00518	Missing record
Diaphragm wall (quadrilateral element)	2.8×10^7	-	-

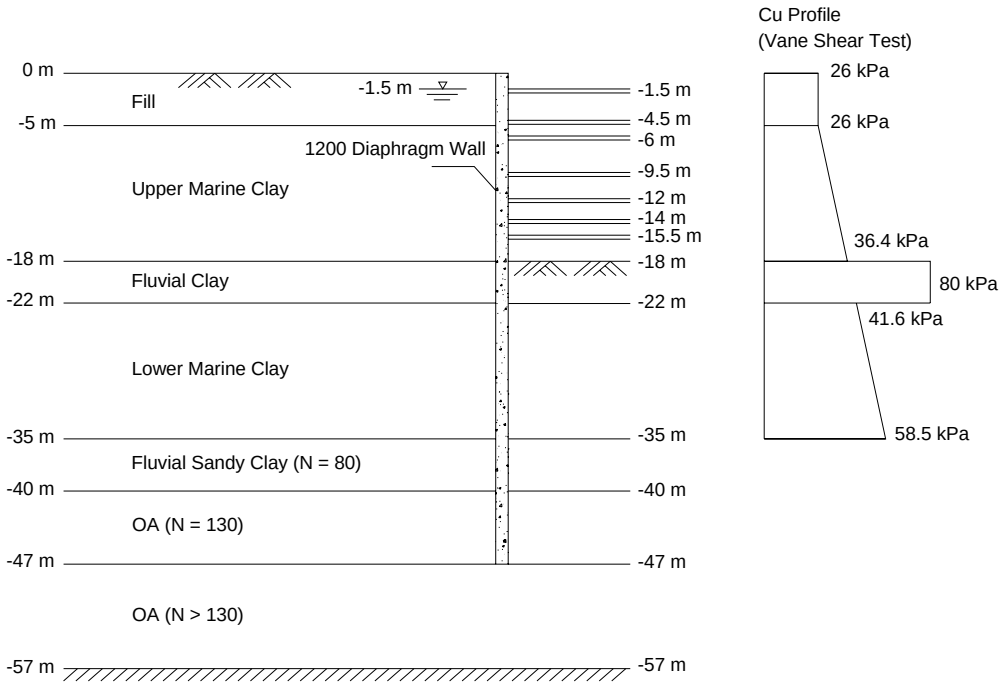

Figure 8.20 Cross-Section at Bugis MRT Station

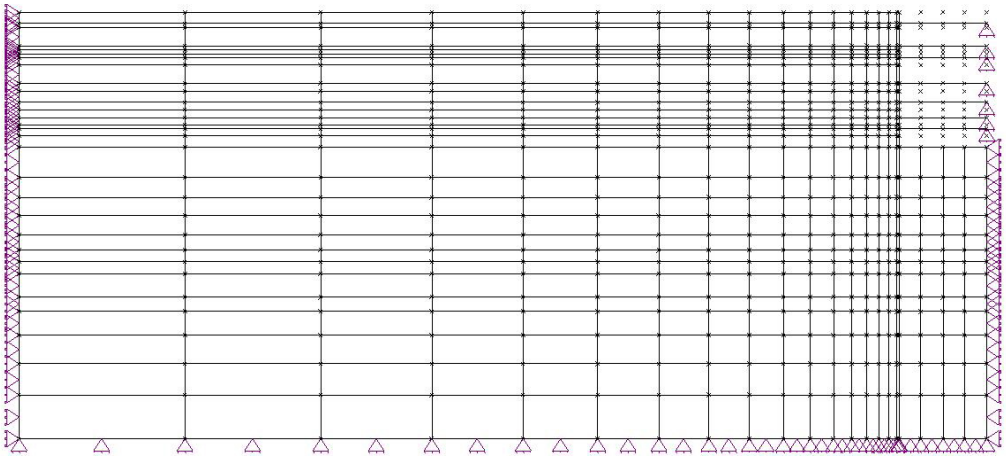

Figure 8.21 Finite Element Mesh of Excavation at Bugis MRT Station

Table 8.7 Construction Sequence at Bugis MRT Station

Stage	Excavation Sequence
1	Excavate to 2.5 m below a ground level (GL)
2	Install first level of strut at 1.5 m below GL
3	Excavate to 5.5 m below GL
4	Install second level of strut at 4.5 m below GL
5	Excavate to 6 m below GL
6	Install third level of strut at 6 m below GL
7	Excavate to 10.5 m below GL
8	Install fourth level of strut at 9.5 m below GL
9	Excavate to 13 m below GL
10	Install fifth level of strut at 12 m below GL
11	Excavate to 16.5 m below GL
12	Install sixth level of strut at 15.5 m below GL
13	Excavate to formation level at 18 m below GL

8.8.2 Cut-and-Cover Tunnel between Farrer Park and Kandang Kerbau MRT Station

The second study case is the cut-and-cover tunnel between Farrer Park and Kandang Kerbau MRT Station in Singapore. The sectional view and finite element mesh of excavation are shown in Figure 8.24 and 8.25, respectively. The parameters are shown in Tables 8.8, 8.9, and 8.10. The construction sequence is shown in Table 8.11.

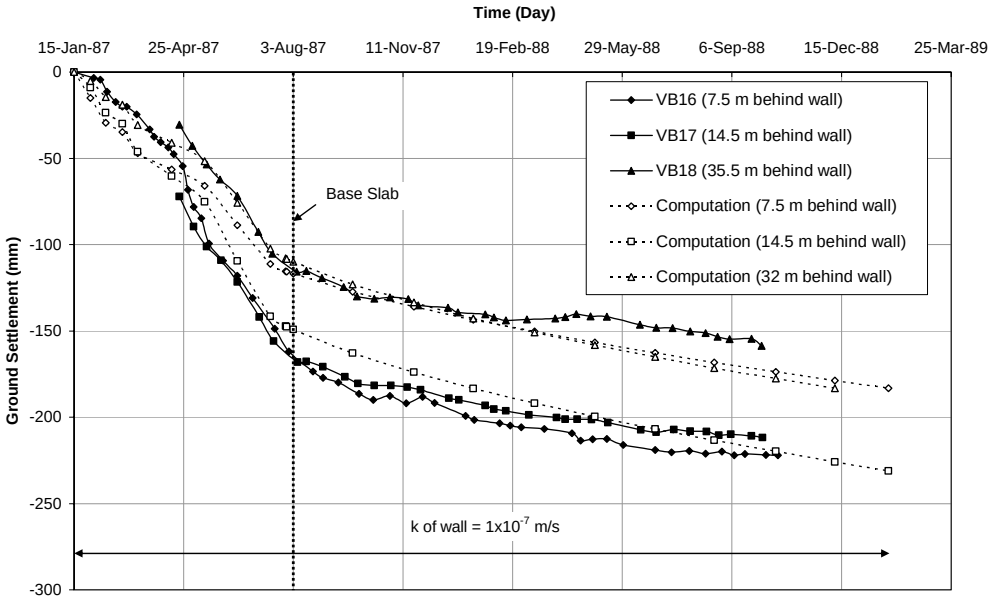

Figure 8.22 Ground Settlements at Bugis MRT Station with Constant Wall Permeability at $1x10^{-7}$ m/s

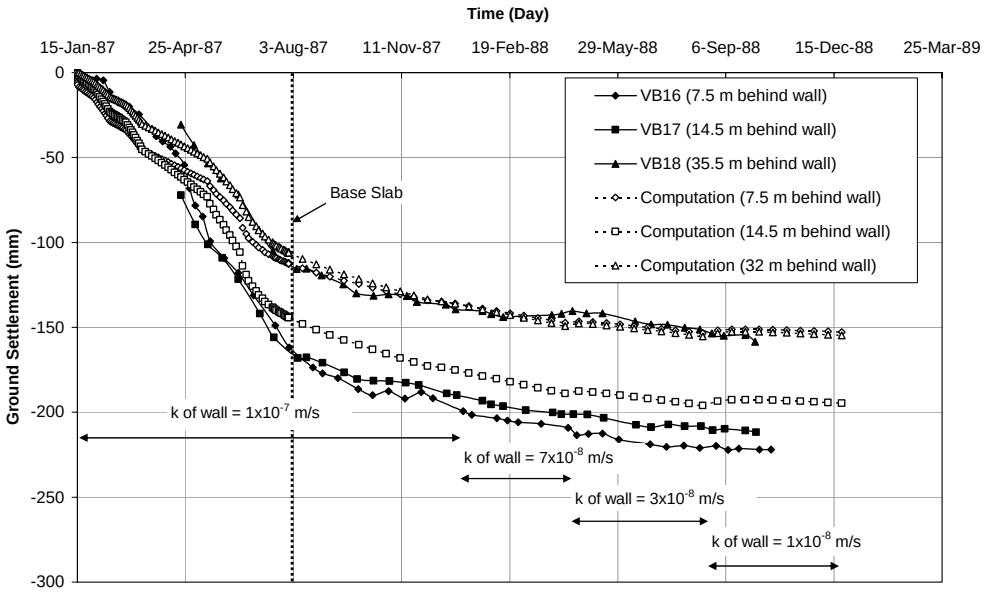

Figure 8.23 Ground Settlement at Bugis MRT Station with Decreasing Wall Permeability from $1x10^{-7}$ m/s to $1x10^{-8}$ m/s

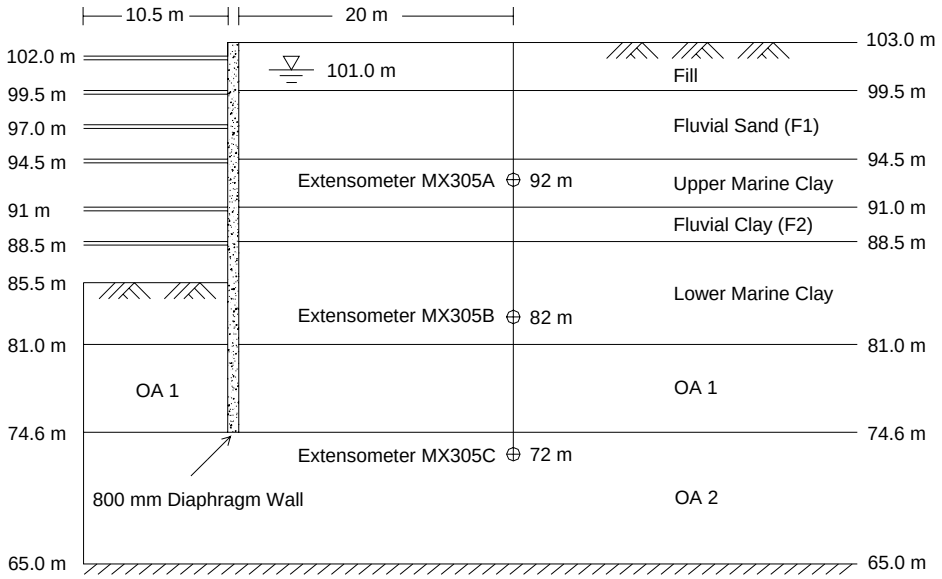

Figure 8.24 Cross Section at Cut-and-Cover Tunnel between Farrer Park and Kandang Kerbau (CH31+895)

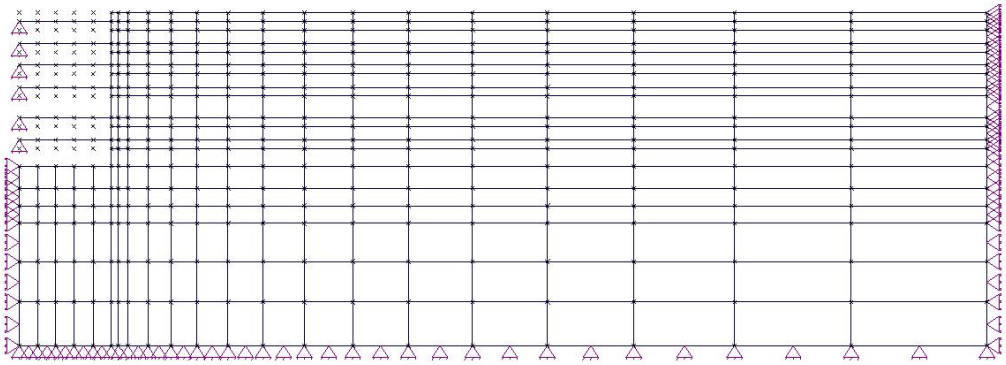

Figure 8.25 Finite Element Mesh at Cut-and-Cover Tunnel between Farrer Park and Kandang Kerbau (CH31+895)

Table 8.8 Mohr-Coulomb Parameters for Other Soils

Soil Type	γ_{sat} (kN/m^3)	ν	E_{50} (kPa)	E_{ur} (kPa)	c (kPa)	ϕ (^{o})	k (m/s)
Fill (Sandy Soil, N = 6)	19	0.33	11000	-	0	38	$1x10^{-4}$
Fluvial Sand (F1) (N = 15)	19	0.33	20000	-	0	39	$1x10^{-5}$
Fluvial Clay (F2) (N = 5, PI = 30)	17	0.33	15000	-	25	0	$1x10^{-8}$
OA 1 (N = 30, PI = 20)	20	0.33	-	337500	150	0	$1x10^{-9}$
OA 2 (N = 100, PI = 20)	20	0.33	-	1125000	500	0	$1x10^{-9}$

Table 8.9 Modified Camclay Parameters for the Upper (UMC) and Lower (LMC) Marine Clay at Farrer Park and Kandang Kerbau MRT Station

Soil Type	γ_{sat} (kN/m^3)	PI (%)	w_L (%)	G_s	κ	λ	e_Γ	ϕ_{cs} (^{o})	M	ν	k (m/s)
UMC	16	55	85	2.65	0.0644	0.3223	2.69	25.0	0.984	0.33	$1x10^{-9}$
LMC	16	45	75	2.65	0.0527	0.2637	2.34	26.2	1.04	0.33	$1x10^{-9}$

Table 8.10 Structural Properties at Cut-and-Cover Tunnel between Farrer Park and Kandang Kerbau (CH31+895)

Structural Members	E (kN/m^2)	A (m^2/m)	Preload (kN/m)
Strut (at RL 102 m)	2.07×10^8	0.019	Missing record
Strut (at RL 99.5 m)	2.07×10^8	0.0228	Missing record
Strut (at RL 97 m)	2.07×10^8	0.0258	Missing record
Strut (at RL 94.5 m)	2.07×10^8	0.0396	Missing record
Strut (at RL 91 m)	2.07×10^8	0.0396	Missing record
Strut (at RL 88.5 m)	2.07×10^8	0.0258	Missing record
Diaphragm wall (quadrilateral element)	2.8×10^7	-	-

Table 8.11 Construction Sequence at Cut-and-Cover Tunnel between Farrer Park and Kandang Kerbau (CH31+895)

Stage	Excavation Sequence
1	Excavate to RL 101 m
2	Install first level of strut at RL 102 m
3	Excavate to RL 98.5 m
4	Install second level of strut at RL 99.5 m
5	Excavate to RL 96 m
6	Install third level of strut at RL 97 m
7	Excavate to RL 93.5 m
8	Install fourth level of strut at RL 94.5 m
9	Excavate to RL 90 m
10	Install fifth levef of strut at RL 91 m
11	Excavate to RL 87.5 m
12	Install sixth level of strut at RL 88.5 m
13	Excavate to formation level at RL 85.5 m

Figure 8.26 shows that the measured post-excavation settlement continued at a relatively constant rate. This is an indication that leakage continued during this period. In the finite element analysis, a constant wall permeability of $1x10^{-7}$ m/s

was used. The computed settlement profiles are in reasonable agreement with the measured profiles.

Figure 8.27 shows the post-excavation settlement obtained from extensometers at locations shown in Figure 8.24. Extensometer MX306C shows that the Old Alluvium did not settle at all. The major source of settlement comes from the marine clay. A comparison between MX306A and MX306B show that the upper marine clay settled more than the lower marine clay.

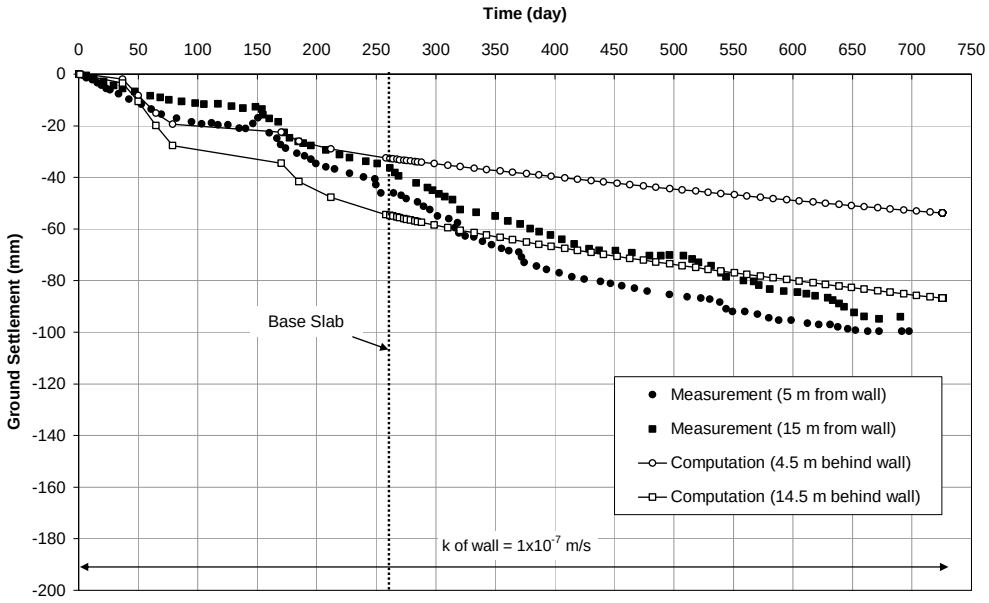

Figure 8.26 Ground Settlement at Cut-and-Cover Tunnel between Farrer Park and Kandang Kerbau MRT Station (CH31+895)

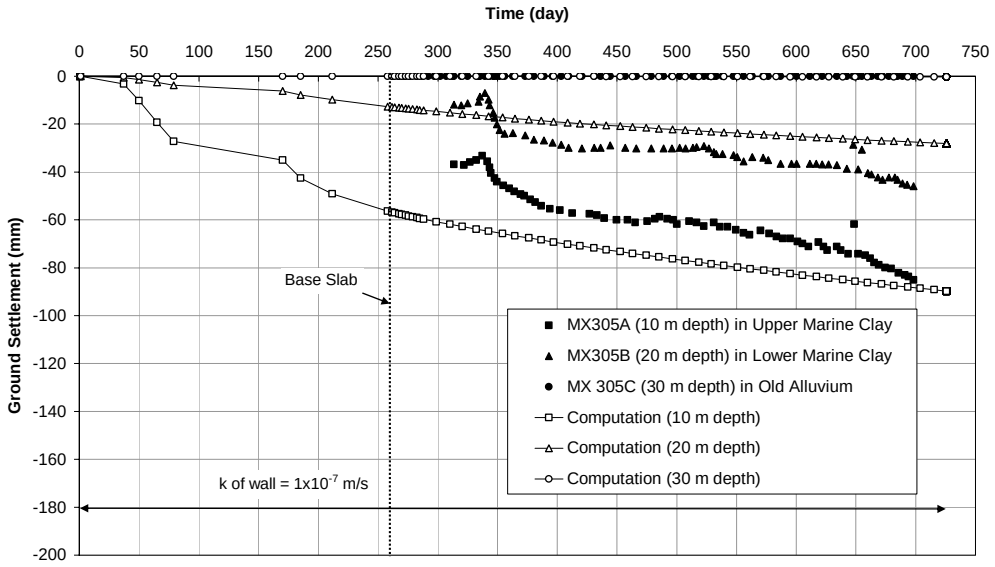

Figure 8.27 Extensometer at Cut-and-Cover Tunnel between Farrer Park and Kandang Kerbau MRT Station (CH31+895) at 20 m from Wall

8.9 Conclusion

Three possible factors affecting post-excavation settlement has been studied in this chapter. They are under-drainage, wall leakage and base slab leakage. The conclusions are as follows:

1. The effect of under-drainage due to suction in Old Alluvium is not significant. Consolidation settlement of the soft marine clay due to this effect is very small.
2. The effect of under-drainage due to water flow into the sand layer can be significant if the sand layer is exposed within the excavated area.
3. The effect of wall leakage on post-excavation settlement is significant.
4. The effect of base slab leakage on post-excavation settlement can be significant.
5. It is important to repair all leakages as soon as possible to prevent post-excavation settlement which can cause damage to surrounding buildings.

CHAPTER 9
SUMMARY AND RECOMMENDATIONS

9.1 Summary

This study has two aims. The first one is to establish a method or procedure to assess the effect of excavation on the performance of adjacent buildings. The second one is to obtain a better understanding on post-excavation settlement. The main findings are summarized below.

9.1.1 Estimation of Mohr-Coulomb and Modified Cam Clay Parameters for Excavation Analysis

Several empirical charts for estimation of Mohr-Coulomb and Modified Cam Clay parameters have been adopted or developed for excavation analysis. Parameters determined using these charts have been validated based on back-analysis of ten case records. It was found that the computed maximum error of wall deflection is about ± 25%. In the absence of quality test data, these charts can provide a reasonable set of parameters. If test data are available, the parameters should be determined directly from these data. However, they should be checked against those obtained from the chart to ensure the values are of the same order of magnitude and comparable.

9.1.2 New Chart for Damage Prediction of Frame Structures

A new chart to predict building damage of frame structure has been developed. The required parameters can be readily determined. The data from the construction of the MRT North East Line and other published data were used to determine the demarcation between the different categories. The chart has been validated against field data. The agreements are quite reasonable.

9.1.3 Transformation of Green Field Settlement of Deep Excavation from 2D into 3D Finite Element Analysis

Two simple equations and nine charts have been developed to convert 2-D green field settlement into 3-D green field settlement. Several hypothetical studies and one case record were back-analyzed to check the accuracy of this method. Results show that this method can produce reliable results.

Two more equations have been developed to predict ground settlement distribution under green field condition. These equations can be used as alternatives to those proposed by Clough and O'Rourke (1990) and Hsieh and Ou (1998). It should be noted that these equations only provide rough estimations since ground settlement can be affected by many factors.

9.1.4 Prediction of Raft Settlement due to Deep Excavation

A new method to predict building damage based on green field settlement has been developed. This method takes into consideration of raft stiffness and raft-soil interaction. Results show that the raft settlement may be quite different from the green field settlement unless the raft is very flexible. The proposed method is applicable to stiff soil with any geometry and raft stiffness. It is not applicable to buildings resting on soft soil.

9.1.5 Factors Affecting Post-Excavation Settlement

There are three main sources contributing to post-excavation settlement.

1. Under-drainage due to suction in Old Alluvium drawing water from the overlying soft clay layer. The post-excavation settlement due to this source is insignificant.
2. Under-drainage due to seepage from soft clay into a pervious layer that extends up to the excavated area. The resulting post-excavation settlement can be significant.
3. Wall and base slab leakage. The resulting post-excavation settlement can be significant.

In order to minimize post-excavation settlement, it is important to repair all leakages as soon as possible. In situations where the pervious layer extends to the bottom of excavation, one can extend the wall to a greater depth to cut off or to minimize the seepage flow. Alternatively, using recharge wells to maintain a high water level in the pervious layer will also minimize the seepage flow. In any case, the base slab should be cast as soon as possible to cut off the seepage.

9.2 Recommendations for Further Research

Further research in the following areas would be useful:

1. To conduct a study on how to efficiently strengthen buildings around an deep excavation.
2. To conduct a study on how to predict raft settlement due to deep excavation in soft soil.
3. To conduct 3-D finite element study for further study in post-excavation settlement.

REFERENCES

American Concrete Institute (ACI). (1999). Building code requirements for masonry. *ACI 530-99*, Detroit.

American Concrete Institute (ACI). (2002). Building code requirements for structural concrete. *ACI 318-02*, Detroit.

Batten, M., Porwie, W., Boorman, R., and Yu, H. (1996). Measurement of proploads in a large braced excavation during construction of the JLE station at Canada Water, East London. *Geotechnical Aspects of Underground Construction in Soft Ground*, London, A. A. Balkema, pp. 57-62.

Bjerrum, L. and Eide, O. (1956). Stability of strutted excavations in clay. *Geotechnique*, London, England, Vol. 6, pp. 32-47.

Bjerrum, L. (1963). Allowable settlement of structures. *Proceedings European Conference on Soil Mechanics and Foundation Engineering*, Wiesbaden, Vol. 2, pp. 135-137.

Bjerrum, L., Clausen, C. J. F., and Duncan, J. M. (1972). Earth pressure on flexible structures. *Norwegian Geotechnical Report*, Oslo, Norwegian, pp. 1-29.

Bono, N. A., Liu, T. K., and Soydemir, C. (1992). Performance of an internally braced slurry-diaphragm wall for excavation support. *Slurry Walls: Design, Construction, and Quality Control*, ASTM Special Topic Publication, Vol. 1129, pp. 347 – 360.

Boone, S. J. (1996). Ground movement related building damage. *Journal of Geotechnical Engineering Division*, ASCE, Vol. 122, No. 11, pp. 886-896.

Boone, S. J., Westland, J., and Nusink, R. (1999). Comparative evaluation of building responses to an adjacent braced excavation. *Canadian Geotechnical Journal*, Vol. 36, pp. 210-223.

Boone, S. J., and Crawford, A. M. (2000). Braced excavations: temperature, elastic modulus, and strut loads. *Journal of Geotechnical and Geoenvironmental Engineering*, ASCE, Vol. 126, No. 10, pp. 870-881.

Borja, R. I. (1992). Free Boundary, fluid flow, and seepage forces in excavations. *Journal of Geotechnical Engineering Division*, ASCE, Vol. 118, No. 1, pp. 125-146.

Boscardin, M. D. (1980). Building response to excavation induced ground movements. *Ph.D. Thesis*, University of Illinois, Urbana-Champaign, USA.

Boscardin, M. D., and Cording, E. J. (1989). Building response to excavation induced settlement. *Journal of Geotechnical Engineering Division*, ASCE, Vol. 115, No. 1, pp. 1-21.

Bowles, J. E. (1988). Foundation analysis and design. 4th Edition, McGraw-Hill Book Company, New York.

Breymann, H., Fuchsberger, M., and Schweiger, H. F. (1996). Deep open excavation in soft plastic ground in Salzburg, Austria. *Geotechnical Aspects of Underground Construction in Soft Ground*, A. A. Balkema, Rotterdam, pp. 69-74.

Broms, B. B. and Bennermark, H. (1967). Stability of clay at vertical openings. Journal of the Soil Mechanics and Foundations Division, ASCE, Vol. 93, No. SM1, pp. 71-94.

Broms, B. B., Wong, I. H., and Wong, K. S. (1986). Experience with finite element analysis of braced excavation in Singapore. *Proceedings of Second International Symposium on Numerical Models in Geomechanics*, A. A. Balkema, Rotterdam, The Netherlands, pp. 309-324.

Broms, B. B. (1988). Design and construction of anchored and strutted sheet pile walls in soft clay. *Proceedings Second International Conference on Case Histories in Geotechnical Engineering*, St. Louis, pp. 1515-1550.

Burd, H. J., Houlsby, G. T., Augarde, C. E., and Liu, G. (2000). Modelling tunneling-induced settlement of masonry buildings. *Proceedings Institute of Civil Engineers Geotechical Engineering*, Vol. 143, pp. 17-29.

Burland, J. B. and Wroth, C. P. (1974). Settlement behavior of buildings and associated damage. *Proceedings Conference on Settlement of Structures*, Cambridge University, Cambridge, pp. 611-654.

Burland, J. B. and Hancock, R. J. R. (1977). Underground car park at the House of Common, London: geotechnical aspects. *The Structural Engineer*, Vol. 55, No. 2, pp. 87-100.

Burland, J. B., Broms, B. B., and de Mello, V. F. (1977). Behavior of foundations and structures, *Ninth International Conference on Soil Mechanics and Foundation Engineering*, Tokyo, State-of-the-Art Report, Vol. 2, pp. 495-546.

Burland, J. B., Simpson, G. B., and John, H. D. (1979). Movements around excavations in London Clay. *Design Parameters in Geotechnical Engineering*. London, Vol. 1, pp. 13-29.

Burland, J. B. (1997). Assessment of risk of damage to buildings due to tunneling and excavation. *First International Conference on Earthquake Geotechnical Engineering*, pp. 1189 – 1201.

Chan, L. F. amd Yap, Teck. F. (1992). Effects of construction of a diaphragm wall very close to a masonry building. *Slurry Walls: Design, Construction, and Quality Control*, ASTM, Philadelphia pp. 129-139.

Chang, C. S. and Abas, M. H. B. (1982). Deformation analysis for braced excavation in clay. *Application of Plasticity and Generalized Stress-Strain in Geotechnical Engineering, ASCE Special Publication*, pp. 205-226.

Charles, W. W. Ng and Martin, L. L. (1993). Effects of modeling soil nonlinearity and wall installation on back-analysis of deep excavation in stiff clay. *Journal of Geotechnical Engineering Division*, Vol. 121, No. 10, pp. 687-695.

Clough, G. W., Weber, P. R., and Lamont, J. (1972) Design and observation of a tied-back wall. *Proceedings ASCE Conference on Performance of Earth and Earth-Supported Structures*, Purdue University, Vol. I, pp. 1367-1389.

Clough, G. W. and Tsui, Y. (1974). Performance of tied-back walls in clay. *Journals of Geotechnical Engineering*, Vol. 100, pp. 1259-1274.

Clough, G. W. and Davidson, R. R. (1977). Effects of construction on geotechnical performance. *Stanford University Civil Engineering Research Report*, 1977, pp. 1-39.

Clough, G. W. and Denby, G. M. (1977). Stabilizing berm design for temporary walls in clay. *Journal of the Geotechnical Division*, ASCE, Vol. 103, No. GT2, pp. 75-90.

Clough, G. W., Hansen, L. A., and Mana, A. I. (1979). Prediction of supported excavation movements under marginal stability conditions in clay. *Third International Conference on Numerical Methods in Geomechanics*, Aachen, pp. 1485 – 1502.

Clough, G. W., and Hansen, L. A., (1981). Clay anisotropy and braced wall behavior. *Journal of the Geotechnical Engineering Division*, ASCE, Vol. 107, pp. 893-914.

Clough, G. W. and O'Rourke, T. D. (1990). Construction induced movements of in situ walls. *In Proceedings, Design and Performance of Earth Retaining Structures*, ASCE Special Conference, Ithaca, New York, pp. 439-470.

Clough, G. W. and Schmidt, B. (1981). Design and performance of excavations and tunnels in soft clay. *Soft Clay Engineering*, Elsevier Scientific Publishing Company, pp. 569-634.

Clough, G. W., Smith, E. M., and Sweeney, B. P. (1989). Movement control of excavation support systems by iterative design. *Proceeding of ASCE on Foundation Engineering: Current Principles and Practices*, Vol. 2, pp. 869-884.

Cook, D. (1994). Studies of settlements and crack damage in old and new facades. *Proceedings of the British Masonry Society Third International Masonry Conference*, London, October, 1992. pp. 203-211.

Cook, D. A., Ledbetter, S., and Wenzel, F. (2000). Masonry crack damage: its origins, diagnosis, philosophy and a basis for repair. *Proceedings Institution of Civil Engineering in Structures and Buildings*, Vol. 140, pp. 39-50.

Cording, E. J., O'Rourke, T. D., and Boscardin, M. (1978). Ground movements and damage to structures. *International Conference Evaluation and Prediction of Subsidence*, Florida, pp. 516-537.

Dames and Moore (1983). Mass rapid transit system, Singapore: Detailed geotechnical study – interpretive report. *Provisional Mass Rapid Transit Authority*, Singapore.

Das, B. M. (2002). Principles of Geotechnical Engineering, *Brooks/Cole*, California.

De Moor, E. K. and Stevenson, M. C. (1996) Evaluation of the performance of a multi-propped diaphragm wall during construction. Geotechnical Aspects of Underground Construction in Soft Ground, A. A. Balkema, Rotterdam, pp. 111-116.

Dowding, C. H. and McKenna, L. M. (2005) Crack response to long-term environmental and blast vibration effects. Journal of Geotechnical and Geoenvironmental Engineering, ASCE, Vol. 131, No. 9, pp. 1151-1161.

Duncan, J. M. and Chang, C. Y. (1970). Nonlinear analysis of stress and strain in soils. *Journal of the Soil Mechanics and Foundations Division*, ASCE, Vol. 96, No. SM5, pp. 1629-1653.

Duncan, J. M. and Buchignani, A. L. (1976). An engineering manual for settlement studies. *Geotechnical Engineering Report*, Department of Civil Engineering, University of California, Berkeley, 94 pp.

Duncan, J. M., Byrne, P., Wong, K. S., and Mabry, P. (1980). Strength, stress-strain and bulk modulus parameters for nonlinear finite element analyses of stresses and movements in soil masses. Geotechnical Engineering Report, No. UCB/GT/80-01, Department of Civil Engineering, University of California, Berkeley.

Fang, M. L. (1987). A deep excavation in Taipei Basin. *Ninth Southeast Asian Geotechnical Conference*, Bangkok, Vol. 1, pp. 35-42.

Finno, R. J., Atmatzidis, D. K., and Nerby, S. M. (1988). Ground response to sheet-pile installation in clay. *Proceedings of the Second International Conference*

of Case Histories in Geotechnical Engineering. University of Missouri-Rolla, St. Louis, MO, pp. 121-126.

Finno, R. J., Nerby, S. M., and Perkins, S. B. (1988). Soil parameters implied by braced cut observations. *Soil Properties Evaluation from Centrifugal Models and Field Performance, Geotechnical Special Publication*, No. 17, pp. 71-87.

Finno, R. J., Atmatzidis, D. K., and Perkins, S. B. (1989). Observed performance of a deep excavation in clay. *Journal of Geotechnical Engineering*, ASCE, Vol. 115, No. 8, pp. 1045-1064.

Finno, R. J. and Harahap, I. S. (1991). Finite element analyses of HDR-4 excavation. *Journal of Geotechnical Engineering Division*, ASCE, Vol. 117, No. 10, pp. 1590-1609.

Finno, R. J. (1992). Deep cuts and ground movements in Chicago clay. *Excavation and Support for The Urban Infrastructures*, Geotechnical Special Publication, Vol. 33, pp.119-143.

Finno, R. J., and Bryson, L. S. (2002). Response of building adjacent to stiff excavation support system in soft clay. *Journal of Performance of Constructed Facilities*, ASCE, Vol. 16, No. 1, pp. 10-20.

Finno, R. J., Voss, F. T., Rossow, E., and Blackburn, J. T. (2005) Evaluating damage potential in buildings affected by excavations. *Journal of Geotechnical and Geoenvironmental Engineering*, ASCE, Vol. 131, No. 10, pp. 1199-1210.

Fjeld, S. (1963). Settlement damage to a concrete-frame structure. *Norwegian Geotechnical Institute*, Oslo, Norway, pp. 37-45.

Frischmann W., Hellings J., and Snowdon C. (1994). Protection of the mansion house against damage caused by ground movemens due to the Docklands Light Railway Extension. *Proceedings of the Institution of Civil Engineers, Geotechnical Engineering*, Vol. 107, No.2, pp. 65 – 76.

Gere, J. M. and Timoshenko, S. (1997). Mechanics of materials, Fourth Edition, PWS Publication, 912 pp.

Gibbs, H. J. and Holtz, W. G. (1957). Research on determining the density of sands by spoon penetration testing. *Proceedings of the Fourth International Conference on Soil Mechanics and Foundation Engineering*, Vol. 1, pp. 35-39.

Gill, S. A. and Lukas, R. G. (1990). Ground movement adjacent to braced cuts. *Design and Performance of Earth Retaining Structures*, ASCE Geotechnical Special Publication, Vol. 25, pp. 471-488.

Goh, A. T. C. (1994). Estimating basal heave stability for braced excavations in soft clay. *Journal of Geotechnical Engineering Division*, ASCE, Vol. 120, No. 8, pp. 1430-1436.

Goldberg, D. T., Jaworski, W. E., and Gordon, M. D. (1976). Lateral support systems and underpinning, *Report FHWA-RD-75-128, Federal Highway Administration*, Washington.

Gomes, A. M., Costa, J. O., Albertini, H., and Aquiar, J. E. (2003). Permeability of concrete: a study intended for the "in situ" valuation using portable instrumentations and traditional techniques. *International Symposium on Non-Destructive Testing in Civil Engineering 2003*, NDT-CE 2003, GZIP/BAM, Berlin.

Gould, J. P., Tamaro, G. J., and Powers, J. P. (1992). Excavation and support for the urban infrastructure. *ASCE Geotechnical Special Publication*, No. 33, pp. 144-171.

Grant, R., Christian, J. T., and Vanmarcke, E. H. (1974). Differential settlement of building. *Journal of Geotechnical Engineering Division*, ASCE, Vol. 100, No. GT9, pp. 973-991.

Harris, C. W., and O'Rourke, T. D. (1983). Response of jointed cast iron pipe lines to parallel trench construction. *Geotechnical Engineering Report*, Vol. 83, No. 5, School of Civil and Environmental Engineering, Cornell University, Ithaca, New York.

Harris, D. I., Mair, R. J., Love, J. P., Taylor, R. N., and Henderson, T. O. (1994). Observations of ground and structure movements for compensation grouting during tunnel construction at Waterloo station. *Geotechnique*, Vol. 44, No. 4, pp. 691-731.

Hashash, Y. M. A. and Whittle, A. J. (1996). Ground movement prediction for deep excavation in soft clay. *Journal of Geotechnical Engineering Division*, ASCE, Vol. 122, No. 6, pp. 474-486.

Henkel, D. J. and Wade, N. H. (1966). Plain strain tests on a saturated remolded clay. *Journal of the Soil Mechanics and Foundation Division*, ASCE, Vol. 92, No. SM6, pp. 67-80.

His, J. P. and Small, J. C. (1992). Ground settlement and drawdown of the water table around an excavation. *Canadian Geotechnical Engineering*, Vol. 29, pp. 740-756.

Ho, D. K. H. and Smith, I. M. (1993). Modelling of soil nailing by 3 dimensional finite element analysis. *Conference on Retaining Structures*, Cambridge, pp. 515-528.

Hong, W. P. and Yun, J. M. (1996) Lateral earth pressures acting on anchored excavation retention walls for building construction. *Twelfth Southeast Asian Geotechnical Conference*, Kuala Lumpur, pp. 373-378.

Horiuchi, T. and Shimizu, M. (1996) Settlement of soft ground and damage of wooden houses by braced excavation. *Geotechnical Aspects of Underground Construction in Soft Ground*, A. A. Balkema, Rotterdam, pp. 149-154.

Hsieh, P. G. and Ou, C. Y. (1998). Shape of ground surface settlement profiles caused by excavation. *Canadian Geotechnical Journal*, Vol. 35, pp. 1004-1017.

Jardine, R. J., Potts, D. M., Fourie, A. B., and Burland, J. B. (1986). Studies of the influence of non-linear stress-strain characteristics in soil-structure interaction. *Geotechnique*, Vol. 36, No. 3, pp. 377-396.

Jamiolkowski, M., Ladd, C. C., Germaine, J. T., and Lancellotta, R. (1985). New developments in field and laboratory testing of soils. *Proceedings of 11th International Conference on Soil Mechanics and Foundation Engineering*, San Fransisco, Vol. 1, pp. 57-153.

Jennings, J. E. and Kerrich, J. E. (1962). The heaving of buildings and the associated economic consequences, with particular reference to the Orange Free State Goldfields, *The Civil Engineers in South Africa*, Vol. 5, No. 5, 122 pp.

Kjellman, W. (1936). Report on an apparatus for consummate investigation of mechanical properties of soils. *Proceedings First International Conference on Soil Mechanics and Foundation Engineering*, Cambridge, Massachusetts, Vol. 1, pp. 16-20.

Kulhawy, F. H. & Mayne, P. W. (1990). Manual on estimating soil properties for foundation design. *Report EL-6800, Electric Power Research Institute, Palo Alto, CA.*

Kok, C. Y. (1985). *A brace sheet pile excavation in very soft Singapore marine clay, the MOE building at Scotts Road*. Geotechnical Publications by Public Works Department, Singapore, 45 pp.

Koutsoftas, D. C., Frobenius, P., Ching, L.W., Meyersohn, D., and Kulesza, R. (2000). Deformations during cut-and-cover construction of MUNI Metro Turnback project. *Journal of Geotechical and Geoenvironmental Engineering*, ASCE, Vol. 126, No. 4, pp. 344-359.

Ladd, C. C., Foott, R., Ishihara, K., Schlosser, F., and Poulos, H. G. (1977). Stress deformation and strength characteristics. *Proceedings Ninth International Conference on Soil Mechanics and Foundation Engineering*, Tokyo, Vol. 2, pp. 421-494.

Lambe, T. W., (1970). Braced excavations. *Proceedings of Special Conference on Lateral Stresses in the Ground and Design of Earth Retaining Structures*, Ithaca, N. Y., pp. 149–218.

Lambe, T. W., Wolfskill, L. A., and Wong, I. H. (1970). Measured performance of braced excavation. *Journal of Geotechnical Engineering Division*, ASCE, Vol. 96, No. 3, pp. 817-836.

Lambe, T. W., Wolfskill, L. A., and Jaworski, W. E. (1972). The performance of a subway excavation. *Proceedings on the Specialty Conference on Performance of Earth and Earth-Supported Structures*, Purdue University and ASCE, pp. 1403-1424.

Lee, K. L. (1970). Comparison of plain strain and triaxial tests on sand. *Journal of the Soil Mechanics and Foundations Division*, ASCE, Vol. 96, No. SM3, pp. 901-923.

Lee, F. H., Yong, K. W., Quan K. C. N., and Chee K. T. (1998). Effect of corners in strutted excavations: field monitoring and case histories. *Journal of Geotechnical and Geoenvironmental Enginnering*, ASCE, Vol. 124, No. 4, pp. 339-349.

Lee, S. L., Yong, K. Y., Karunaratne, G. P., and Chua, L. H. (1986). Field instrumentation for a strutted deep excavation in soft clay. *Fourth International Geotechnical Seminar Field Instrumentation and In Situ Measurements*, Nanyang Technological Institute, Singapore. pp. 183 – 186.

Leonard, G. A. (1975). Discussion of "Differential Settlement of Buildings" by Grant, R., Christian, J. T., and Vanmarcke, E. H., *Journal of Geotechnical Engineering Division Division*, ASCE, Vol. 101, No. GT7, pp. 700-702.

Leussink, H., and Wittke, W. (1964). Difference in triaxial and plane strain shear strength. *Special Technical Publication*, ASTM, No. 361, pp. 77-89.

Li, W. (2001). Braced Excavation in Old Alluvium in Singapore. *Ph.D. Thesis*, Nanyang Technological University, Singapore.

Li, W. and Wong, K. S. (2001). Geotechnical properties of old alluvium in Singapore. *Journal of Institution of Engineers*, Singapore, 2001.

Liao, S. S. C. and Whitman, R. V. (1986). Overburden correction factors for SPT in sand. *Journal of Geotechnical Engineering*, ASCE, Vol. 112, No. 3, pp. 373-377.

Lim, K. W., Wong, K. S., Orihara, K. & Ng, P. B. (2003). Comparison of results of excavation analysis using WALLAP, SAGE CRISP, and EXCAV97, *Underground Singapore 2003*, Singapore, pp. 83-94.

Lings, M. L., Nash, D. F. T., Ng, C. W. W., and Boyce, M. D. (1991). Observed behaviour of a deep excavation in Gault clay, a preliminary appraisal. *Proceedings of The Tenth European Conference on Soil Mechanics and Foundation Engineering*, Vol. 10, No. 2, pp. 467-470.

Little, M. E. R. (1969). Discussion, Session 6. *Proceedings Symposium on Design for Movement in Buildings*, The Concrete Society, London.

Long, M. (2001). Database for retaining wall and ground movements due to deep excavations. *Journal of Geotechnical and Geoenvironmental Engineering*, ASCE, Vol. 127, No. 3, pp. 203-224.

MacLeod, I. A. and Littlejohn, G. S. (1974). Discussion on Session 5. *Conference of Settlement of Structures*, Cambridge, Pentech Press, London, pp. 792-795.

MacLeod, I. A. and Abu-El-Magd, S. (1980). Estimation of Stiffness of Building Façade Walls Undergoing Differential Settlement. *International Journal of Masonry Construction*, Vol. 1, No. 2, pp. 46-51.

MacLeod, I. A. and Paul, J. G. (1984). Settlement monitoring of buildings in Central Scotland. *Geotechnique*, Vol. 34, No. 1, pp. 99-117.

Mana, A. I., (1979). Behaviour of Deep Excavations in Soft Clay. *Ph.D. Thesis*, Stanford University, California, USA.

Mana, A. I., and Clough, G. W. (1981). Prediction of movement for braced cuts in clay. *Journal of Geotechnical Engineering Division*, ASCE, Vol. 107, No. GT6, pp. 759-777.

Mitchell, A. R., Izumi, C., Bell, B. C., and Brunton, S. (2000). Semi top-down construction method for Singapore MRT, NEL. *Tunnels and Underground Structures*, A. A. Balkema, Rotterdam, pp. 431-436.

Mitchell, J. K. (1976). *Fundamentals of Soil Behavior*. New York: John Wiley and Sons.

Miyoshi, M. (1977). Mechanical behavior of temporary braced wall. *Proceedings of the 6th International Conference on Soil Mechanics and Foundation Engineering*, Tokyo, Vol. 2, No. 2/60, pp. 655-658.

Morton, K., Leonard, M. S. M., and Cater, R. W. (1980). Building settlements and ground movements associated with construction of two stations of the modified initial system of the mass transit railway, Hong Kong. *Ground Movements and Structures*, Pentech Press, London, pp. 788-802.

National Coal Board. (1975). Subsidence Engineers Handbook. *National Coal Board Production Department*, U. K.

Ng, C. W. W. and Lings, M. L. (1995). Effects of modeling soil nonlinearity and wall installation on back-analysis of deep excavation in stiff clay. *Journal of Geotechnical Engineering Division*, ASCE, Vol. 121, No. 10, pp. 687-695.

Ng, C. W. W. and Yan, R. W. M. (1998). Stress transfer and deformation mechanisms around a diaphragm wall panel. *Journal of Geotechnical and Geoenvironmental Engineering*, ASCE, Vol. 124, No. 7, pp. 638-647.

NGI (1962). Measurements at a strutted excavation, Oslo Subway, Vaterland 1, km 1373, Technical Report 6, *Norwegian Geotechnical Institute*, 76 pp.

NGI. (1962). Measurements at a strutted excavation, Oslo Subway, Vaterland 3, km 1450, Technical Report 8, *Norwegian Geotechnical Institute*, 56 pp.

Nicholson, D. P. (1987). The design and performance of the retaining wall at Newton Station. *In Proceeding of Singapore Mass Rapid Transit Conference*, Singapore, pp. 147-154.

Niu, J. X., Wong, I. H., and Makino, M. (2005). Temperature effects on strut loads and ground movements for a 31 m deep excavation in Singapore. *Underground Singapore*, National University of Singapore.

O'Rourke, T. D., Cording, E. J., and Boscardin, M. (1976). The ground movements related to braced excavation and their influence on adjacent buildings. *U.S. Department of Transportation, Report DOT-TST 76T-23.*

O'Rourke, T. D. (1981). Ground movements caused by braced excavations. *Journal of Geotechnical Engineering Division*, ASCE, Vol. 107, No. 6, pp. 1159-1178.

O'Rourke, T. D. (1985). Ground movements from a deep excavation in sands and interbedded clay. Failures in Earthworks, Thomas Telford Ltd, London, pp. 371-381.

Osaimi, A. E. and Clough, G. W. (1979). Pore pressure dissipation during excavation. *Journal of Geotechnical Engineering Division*, ASCE, Vol. 105, No. 4, pp. 481-498.

Osman, A. S. and Bolton, M. D. (2006). Ground movement predictions for braced excavations in undrained clay. *Journal of Geotechnical and Geoenvironmental Engineering*, ASCE, Vol. 132, No. 4, pp. 465-477.

Ou, C. Y., Hsieh, P. G., and Chiou, D. C. (1993). Characteristics of ground surface settlement during excavation. *Canadian Geotechnical Journal*, Vol. 30, No. 5, pp. 758-767.

Ou, C. Y., Chiou, D. C., and Wu, T. S. (1996). Three dimensional finite element analysis of deep excavations. *Journal of Geotechnical Enginnering*, ASCE, Vol. 122, No. 5, pp. 337 – 345.

Ou, C. Y. and Shiau, B. Y. (1998). Analysis of the corner effect on excavation behaviors. *Canadian Geotechnical Journal*, Vol. 35, pp. 532-540.

Ou, C. Y., Liao, J. T., and Lin, H. D. (1998). Performance of diaphragm wall constructed using top-down method. *Journal of Geotechnical and Geoenvironmental Engineering*, ASCE, Vol. 124, No. 9, pp. 987-1008.

Ou, C. Y., Liao, J. T., and Cheng, W. L. (2000). Building response and ground movements induced by a deep excavation. *Geotechnique*, Vol. 50, No. 3, pp. 209-220.

Padfield, C. J. and Sharrock, M. J. (1983). Settlement of structures on clay soils. *Construction Industry Research and Information Association*, London, 133 pp.

Peck, R. B. (1969). Deep excavations and tunneling in soft ground. *Proceedings of 7th International Conference on Soil Mechanics and Foundation Engineering*, Mexico City, State of the Art Volume, pp 225-290.

Peck, R. B., Hanson, W. E., and Thornburn, T. H. (1974). *Foundation Engineering*, 2nd ed., Wiley, New York, 514 pp.

Poh, T. Y., Wong, I. H., and Chandrasekaran, B. (1997). Performance of two propped diaphragm walls in stiff residual soils. *Journal of Performance of Constructed Facilities*, ASCE, Vol. 11, No. 4, pp. 190-199.

Poh, T. Y. and Wong, I. H. (1998). Effects of construction of diaphragm wall panels on adjacent ground: field trial. *Journal of Geotechnical and Geoenvironmental Engineering*, ASCE, Vol. 124, No. 8, pp. 749-756.

Poh, T. Y., Goh, A. T. C., and Wong, I. H. (2001). Ground movements associated with wall construction: case histories. *Journal of Geotechnical and Geoenvironmental Engineering*, ASCE, Vol. 127, No. 12, pp. 1061-1069.

Polshin, D. E. and Tokar, R. A. (1957). Maximum allowable non-uniform settlement of structures. *Fourth International Conference on Soil Mechanics and Foundation Engineering*, Vol. 1, pp. 402.

Potts, D. M. and Fourie, A. B. (1985). The effect of wall stiffness on the behaviour of a propped retaining wall. *Geotechnique*, Vol. 35, No. 3, pp. 347-352.

Raju, G. V. R., Lim, K., and Endicott, L. J. (2000). Geotechnical design and construction aspects of the Clarke Quay station. *Tunnels and Underground Structures*, A. A. Balkema, Rotterdam, pp. 405-412.

Rampello, S., Tamagnini, C., and Calabresi, G. 1993. Observed and predicted response of a braced excavation in soft to medium clay. *Predictive soil mechanics*, Thomas Telford, London, 1993.

Rankin, W. J. (1988). Ground movements resulting from urban tunneling; predictions and effects. *Engineering Geology of Underground Movement, Geological Society*, Engineering Geology Special Publication, No. 5, pp. 79-92.

Saji, S., Murata, J., and Sugimoto, T. (2000) Surface settlement due to walled excavation on 200 projects in Tokyo. *Geotechnical Aspects of Underground Construction in Soft Ground*, A. A. Balkema, Rotterdam, pp. 705-710.

Schmertmann, J. H. (1978). Guidelines for cone penetration test performance and design. *Report FHWA-TS-78-209*, U.S. Department of Transportation, Washington, 145 pp.

Seng, Y. K. (1985). Three cases of deep excavations in soft clay in Singapore. *Geotechnical Publications by Public Works Department*, PWD Technical Seminars 1975 to 1985, Vol. 3, pp. 1-25.

Shirlaw, J. N. and Wen, D. (1999). Measurements of pore pressure changes and settlements due to a deep excavation in Singapore marine clay. *Field Measurements in Geomechanics, Proceeding of the 5th International Symposium on Field Measurements in Geomechanics*, Singapore, pp. 241-246.

Shirlaw, J. N., Jeyarajah, R., Yong, B., and Seetoh, H. H. (2001). Damage to geotechnical instruments during the construction of the North East Line. *Underground Singapore*, Singapore.

Skempton, A. W. and MacDonald, D. H. (1956). Allowable settlement of buildings. *Proceedings Institution of Civil Engineers*, Part III, Vol. 5, pp. 727-768.

Sliwinski, Z. and Fleming, W. G. K. (1975). Practical considerations affecting he construction of diaphragm walls. *Diaphragm Walls and Anchorages*, Institution of Civil Engineers, London, pp. 1-10.

Stroud, M. A. (1974). The standard penetration test in insensitive clays and soft rocks. *Proceedings European Conference on Penetration Tests*. Vol. 2. No. 2. Stockholm, pp. 367-375.

Tan, S. B. and Lee. K. W. (1977). Engineering geology of the marine member of the Kallang Formation in Singapore. *Proceedings of the International Symposium on Soft Clays*, Bangkok, pp. 75-88.

Tan, S. B., Loy, W. C., and Lee, K. W. (1980). Engineering geology of the Old Alluvium in Singapore. *Proceedings of the 11th South East Asian Conference on Soil Engineering*, Taipei, Vol. 1, pp. 673-684.

Tan, S. B., Tan, S. L., Chin, T. K. (1985). A braced sheetpile excavation in soft Singapore marine clay. *In Proceedings of the 11th International Conference on Soil Mechanics and Foundation Engineering*, San Francisco, California, Vol. 3, pp. 1671-1674.

Taylor, D. W. (1939). A comparison of results of direct shear and cylindrical compression tests. *Proceedings Symposium on Shear Testing of Soils*, ASTM, Vol. 39, pp. 1059-1070.

Tedd, P., Chard, B. M., Charles, J. A., and Symons, I. F. (1984). Behaviour of a propped embedded retaining wall in stiff clay at Bell Common tunnel, *Geotechnique*, Vol. 34, No. 4, pp. 513-532.

Terzaghi, K. (1943). Theoretical Soil Mechanics, Wiley, New York, 510 pp.

Terzaghi, K. and Peck, R. (1967). Theoretical and applied soil mechanics, Wiley, New York.

Timoshenko, S. (1957). Strength of Materials – Part 1, *D van Nostrad Co Inc*, London.

Torp-Peterson, G. E. and Black, M. G. (2001) Geotechnical investigation and assessment of potential building damage arising from ground movements: CrossRail. *Proceedings of the Institution of Civil Engineer*s, London, Transport 147, Issue 2, pp. 107-119.

Tschebotarioff, G. P. and P. Brown. (1948). Lateral earth pressure as a problem of deformation or of rupture. *Proceedings International Conference on Soil Mechanics and Foundation Engineering*, Vol. 2. Rotterdam, pp. 81-86.

Wahls, H. E. (1981). Tolerable settlement of buildings. *Journal of the Geotechnical Engineering Division*, ASCE, Vol. 107, No. GT11, pp. 1489-1504.

Ward, W. H. (1956). Discussion on paper by Skempton, A. W. and MacDonald, D. H. The allowable settlements of buildings. *Proceedings Institution of Civil Engineers*, Part III, Vol. 5, pp. 782.

Ward, W. H. (1961). Displacement and strains in tunnels beneath a large excavation in London. *Proceedings Fifth International Conference on Soil Mechanics and Foundation Engineering*, Vol. 2. Paris, pp. 749-753.

Ward, W. H. and Burland, J. B. (1973). The use of ground strain measurements in civil engineering. *Phil Trans Royal Society*, London, A274, pp. 421-428.

Wen, D., Ow, N. C., and Yoon, S. I. (2001). The monitoring of cut and cover tunnel construction at the Race Course Road next to Foochow Methodist Church. *Underground Singapore*, pp. 261-271.

Wen, D. and Lin, K. Q. (2002). The effect of deep excavation on pore water pressure changes in the Old Alluvium and under-drainage of marine clay in Singapore. *Geotechnical Aspects of Underground Construction in Soft Ground*, pp. 447-451.

Whittle, A. J., and Hashash, Y. M. A. (1993). Analysis of the behaviour of propped diaphragm walls in a deep clay deposit. *Proceedings on Retaining Structure*, Thomas Telford, Cambridge, England, pp. 131-139.

Whittle, A. J., Hashash, Y. M. A., and Whitman, R. V. (1993). Analysis of deep excavation in Boston. *Journal of Geotechnical Engineering Division*, ASCE, Vol. 119, No. 1, pp. 69-90.

Winkler, E. (1867). Die Lehre von Elastizitat und Festigkeit (On Elasticity and Fixity), H. Dominicus, Prague.

Wong, I. H. (1997). Experience with waterproofness of basements constructed of concrete diaphragm walls in Singapore. *Tunneling and Underground Space Technology*, Vol. 12, No. 4, pp. 491-495.

Wong, I. H., Poh, T. Y., and Chuah, H. L. (1997). Performance of excavations for depressed expressway in Singapore. *Journal of Geotechnical Engineering Division*, ASCE, Vol. 123, No. 7, pp. 617-625.

Wong, I. H. and Chua, T. S. (1998). Ground movements due to pile driving in an excavation in soft soil. *Canadian Geotechnical Journal*, Vol. 36, pp. 152-160.

Wong, I. H. and Poh, T. Y. (1999). Comparison of retaining walls for basement construction in stiff clays. *Tunneling and Underground Space Technology*, Vol. 14, No. 4, pp. 461-468.

Wong, K. S. and Duncan, J. M. (1974). Hyperbolic stress-strain parameters for nonlinear finite element analyses of stresses and movements in soil masses. *Report no. TE 74-3*, University of California, Berkeley, California, USA.

Wong, K. S. and Broms, B. B. (1989). Lateral wall deflections of braced excavation in clay. *Journal of Geotechnical Engineering Division*, ASCE, Vol. 115, No, 6, pp. 853-870.

Wong, K. S., Li, J. C., Goh, A. T. C., Poh, K. B., and Oishi, E. (1990). Effect of jet grouting on performance of a deep excavation in soft clay. *Proceedings of the 5th International Symposium on Field Measurements in Geomechanics*, Singapore, December 1999, pp. 279-284.

Wong, K. S. (2003). Observational approach to avoid failures in temporary works. *Seminar on Avoiding Failures in Excavation Works*, Building & Construction Authority, Singapore, 11 July 2003.

Wong, K. S. (2004). How to avoid failures in deep excavation. *Proeedings of International Conference on Structural and Foundation Failures*, Singapore, pp. 384-397.

Wood, D. M. (1990). Soil behavior and critical state soil mechanics. Cambridge: Cambridge University Press.

Xanthakos, P. P., Abramson, L. W., and Bruce, D. A. (1994). Ground control and improvement, Wiley, New York, 510 pp. 910.

Yong, K. Y., Lee, F. H., Parnploy, U., and Lee, S. L. (1989). Elasto-plastic consolidation analysis for strutted excavation in clay, *Computer and Geotechnics*, Vol. 8, No. 4, pp. 311-328.

Young, D. K. and Ho, E. W. L. (1994). Observational approach to design of a sheet-piled retaining wall. *Geotechnique*, Vol. 44, No. 4, pp. 637-654.